Title

Controlling Charge-Transfer Interactions in Doped Semiconducting Polymers and Directly Measuring Charge Carrier Localization with the Vibrational Stark Effect

Author

Stanfield, Dane Andrew

Publication Date

2021

UNIVERSITY OF CALIFORNIA
Los Angeles

Controlling Charge-Transfer Interactions in Doped Semiconducting Polymers and Directly Measuring Charge Carrier Localization with the Vibrational Stark Effect

A dissertation submitted in partial satisfaction
of the requirements for the degree
Doctor of Philosophy in Chemistry

by

Dane Andrew Stanfield

2021

ABSTRACT OF THE DISSERTATION

Controlling Charge-Transfer Interactions in Doped Semiconducting Polymers and Directly Measuring Charge Carrier Localization with the Vibrational Stark Effect

by

Dane Andrew Stanfield
Doctor of Philosophy in Chemistry
University of California, Los Angeles, 2021
Professor Benjamin J. Schwartz, Chair

Semiconducting polymers show promise for use in a variety of applications such as photovoltaic cells, light emitting diodes, and thermoelectric generators. For many of these devices, the electronic properties are tuned through the introduction of chemical dopants. This dissertation is focused on understanding several key aspects of the chemical doping process. The first chapter gives an overview of semiconducting polymers, introduces doping by sequential processing methods and looks at how the chemical doping process works on a basic level. We also explore dopant transport methods, discuss the electrical and thermoelectrical characterization of these materials, and finally consider the structural morphology of conjugated polymer thin films. Chapter 2 takes an analytical approach to understanding how the underlying morphology and electrical/thermoelectrical properties of doped polymer films are affected when introducing the dopant either via the solution phase or using vapor transport. Chapter 3 explores the fundamental charge transfer interactions that occur between polymer and dopant. We introduce a novel processing technique that enables the tunable production of dopant-polymer charge transfer complexes (CTCs), which represent a poorly understood but widely seen doping mechanism in these materials. We provide the first comprehensive picture of the forces that drive CTC formation and offer guidelines for limiting CTC occurrence in doped conjugated polymers as their electrical properties are usually undesirable. Finally, in Chapter 4 we solve a long-standing mystery in the literature of the highly variable vibrational spectra of certain dopant molecules, which should nominally show consistent and predictable frequencies. We show that the wide range of vibrational energies observed for these

dopant molecules can be fully understood through the framework of the vibrational Stark effect. Our experimental evidence shows a clear and predictable shift for these modes as a function of their locally experienced electric field, which arises due to Coulomb interactions with the charge carriers on the polymer. Thus, the vibrational shifts of these dopant molecules are actually exquisite reporters on the local environment of the charge carriers in doped conjugated polymers. We use our experimentally-measured shifts to quantitatively estimate the change in polaron coherence length, the extent to which the charge carriers on the polymer spread over multiple polymer repeat units. These chapters cover a variety of themes which highlight the sometimes unexpected path from experiment to manuscript. I sincerely hope they can be of use to others who study similar systems and motivate additional works in the future.

The dissertation of Dane Andrew Stanfield is approved.

Justin Caram

Stuart Brown

Qibing Pei

Benjamin J. Schwartz, Committee Chair

University of California, Los Angeles

2021

To my parents, Megan & Perry.

To my wonderful wife, Allison.

Ad astra per aspara

TABLE OF CONTENTS

LIST OF FIGURES

LIST OF TABLES

ACKNOWLEDGMENTS

I would like to begin by acknowledging my wife, Ali. In our junior year of college I remember you were the first person I confided in that I was beginning to consider if a PhD was the right path for me after college. It was becoming clear to me that an undergraduate degree in chemistry really wasn't going to satiate my appetite for this area, and a PhD seemed to represent the exact kind of deep dive into the natural sciences that I was looking for. Back then, you fully supported that path and all its implications. You moved across the country for me, married me, and even financially supported me through graduate school. None of this really would have been possible without you by my side so 'acknowledging' that support I think puts it in fairly mild terms.

I also wouldn't have made it very far without my parents, Megan & Perry. They may be some of the only people who realize the full context of my academic journey going back to the very beginning. I was diagnosed with dyslexia at a very young age and subsequently had difficulties with reading and math (which is easy to forget is also a symbolic writing system we all learn). I'm not sure if there's anything my mom wouldn't do to ensure I got the support I needed in school, and I also spent many evenings with my dad, who helped me to decode the basics of long division and algebra homework. You guys were the clear reason for my successful development in those early years, and it is no exaggeration to say that none of this would have been possible without your never-ending support and dedication. I hope some day I can pay it forward.

For my more recent educational endeavors, I have to acknowledge my research advisor and life mentor, Ben Schwartz. Where to begin… Even before coming to UCLA, I was fairly certain I wanted to join your group, just from reading a subset of your recently published papers. In that sense, I suppose we share the same basic common research interests. But beyond that, I'm not sure there was really any way I could have prepared for the lessons I'd learn in your group and how they would shape me into the person I am today. You taught me what it means to think like a scientist, how to defend your ideas with data and vigor, and how to construct a scientific story that really hits with a 'pop'. While I still have much to do in the years ahead, I can confirm that you've set me on the right path and taught me the 'how' for achieving the 'what'. I'll be sad to lose VPN access to the polymer doping literature, but I look forward to keeping tabs on where the field is headed in the years to come, so feel free to forward me any interesting doping related papers you come across.

I have to make a shout out to the ghosts of grad students past, who I never got to work with directly, but certainly influenced my experiments and equipment through myriad LabVIEW programs and questionably soldered electrical wiring. We have a giant beaker filled with recycled ITO substrates from the days of fabricating polymer solar cells, and back then it was customary to score the sample ID on the back using the grad student's initials. Having used countless ITO substrates over the years, I'd like to list an array of ITO sample IDs here, alongside the grad students who I believe etched them (but never had a chance to work with directly). AA118I – Alex Ayzner, now associate professor at UC Santa Cruz. BTV159 – Bertrand Tremolet de Villers, who is now a researcher at the National Renewable Energy Laboratory in Golden, CO. GZ45ZG – Guangye Zhang, currently an assistant professor at the Shenzhen Technology University. SW20 – Monica So, who is now a professor at CSU Chico. JCA42G – Jordan Aguirre, engineering technology development manager at Intel. Finally, Steve Hawks who is now a staff scientist at Lawrence Livermore National Lab, is notably missing from the ITO sample IDs. I'm told he was influential in moving the lab over to the much cheaper process of recycling old substrates, hence explaining why he never had to etch his initials into brand new (and very expensive) ITO.

The more recent elder grad students that I *did* directly work with helped immensely with getting me on my feet in the early days. Tyler Scholes, you gave me my first project over the summer in the CELIV doping experiments, as well as my second project with F_4TCNQ doping. I hope I was able to do you justice in keeping at least one of those projects alive. It's too bad we never published that dopant electromigration or spray coating work. Things may have taken a different direction from what you expected but there's no doubt the F_4TCNQ sequential doping project is alive and strong.

Matt Fontana, you were always a vast spring of optimism. I worked very closely with you on my first paper in the Schwartz group and that certainly wouldn't have been possible without your dedication, hard work and leadership. I nostalgically remember many conversations with you in lab concerning the simple principles of index fund investing. You and Tyler showed me the ropes learning LaTeX on the vapor doping paper, which proved to be a worthwhile investment. It has made the process of assembling my thesis a total snap. Thank you for that gift that keeps on giving.

Taylor Aubry–or as I like to think, The Last Jedi of the polymer solar cell project–when you finally chose to join the dark side of polymer doping, you absolutely crushed it. It was really amazing to watch a more senior grad student take on polymer doping with the boron cluster dopants and swiftly navigate your way to ground breaking science. It was, and still is, inspiring work, and I feel very lucky to have worked side by side with you, even if we never got to publish together.

On the ultrafast laser side of the lab, Matthew Voss and Erik Farr, you two were my first introduction to the ways of the spectroscopist, and I feel lucky to have gotten to see what you guys were up to in the dark and spooky laser lab. You also did a great job of showing me the lab culture of the Schwartz group, which I hope I was able to carry on to the younglings.

To the boron cluster Padawan turned Jedi Master, Omar Leon, you saved me from the fate of Matt Damon in The Martian, growing potatoes by myself in the polymer lab. For a time, it seemed that after Taylor graduated, I was going to be the lone scientist telling jokes to my three friends Nathan Jr., Nexdep, and Dektak. You proved to be an inspiring new grad student and it has been an honor to get to work with you and manage the day to day lab work together. I can't imagine a more thoughtful and dedicated lab partner. I still don't know your secret sauce for quick mental math, but every time I reach for a calculator, you inspire me to consider working it out in my head.

To the people on the theory side of our group, particularly Wil Narvaez and Andy Vong, we all started the same year and took Ben's grad quantum class together in Fall 2016. Sitting in the front row was like being in the Shamu splash zone since Ben would attack the chalk board with enough vigor to send splintered off chalk flying with an unknown ballistic trajectory. If Ben *taught* our class, then you guys helped demystify it and showed me how to tango. I will forever be in awe of your technical prowess, and I always think of you guys when I run into anything quantum related.

To the next generation: Quynh Duong, Mariah Gomez, Zerina Mehmedović, Ken Mei, and Reid Wilson, you guys are all great additions to continue the experimentalists tradition in the Schwartz group (except you Ken! but I'm sure you'll keep the theorists happy). You each have a unique set of skills that I can see being honed on a daily basis into your very own super powers. I am sad that I won't be around to watch you all graduate, because it is going to really be something special, and it's clear to me that in the process you will take our lab to yet loftier heights. I look forward to seeing the science you publish, and please forward me your work if you remember me when you're famous.

I also need to make a shout out to our resident postdoc, Eric Wu. I feel like a good post-doc keeps a research group hygienic and healthy, and you are truly everything that a lab looks for and needs in a postdoc. You have been a great role model for all of us as we navigate grad school, and your vast knowledge on a range of topics from ultrafast lasers to simulations and ionic liquids, just to name a few, is simply inspiring. If I ever become as well versed as you on half the range of topics, I think I will be very satisfied.

To those I've collaborated with over the years, K.J. Winchell, and Patrick Yee from the Tolbert group, you guys set a great example and introduced me to the group culture during solar meetings as well as during my visitation weekend even before coming to UCLA. More recently, I collaborated with Yutong Wu and Charlene Salamat from the Tolbert group. I was lucky enough to co-author a paper with Yutong on charge transfer complex doping which turned out to be a much more interesting topic than expected, and her GIWAXS analysis proved critical to pinning down a unique packing structure for that doping mechanism which really rounded out that work into something that I feel lucky to have been a part of.

Charlene, I am sure is going to do incredible things. We have worked very closely on a wide range of experiments, but regrettably our timelines did not match up to publish anything just yet. Nevertheless, you introduced us all to the new direction of the doping project with a journal club for the ages back in early 2020. I very much look forward to seeing the fruits of that work which are still working their way through the pipeline.

To the Schwartz group as a whole, may the Schwartz be with you, and if you haven't seen Spaceballs you should definitely watch the movie so you can fully appreciate that reference.

Chapter 2 and Appendix A are versions of Reference 11, reprinted (adapted) with permission from J. Fontana, M. T.; Stanfield, D. A.; Scholes, D. T.; Winchell, K. J.; Tolbert, S. H.; Schwartz, B. J. J. Phys. Chem. C 2019, 123, 37, 22711–22724. Copyright 2019 American Chemical Society. The full article can be accessed at https://pubs.acs.org/doi/abs/10.1021/acs.jpcc.9b05069 This work was supported by the National Science Foundation under grant numbers CBET-1510353 and CHE-

1608957. All of the GIWAXS measurements for this project were performed by K. J. Winchell at the Stanford Synchrotron Radiation Lightsource on beamline 11-3. The co-first-authors for the publication are Matthew Fontana and Dane Stanfield. Tyler Scholes helped immensely with the design of experiments, constructing the instrument for measuring Seebeck coefficients, and writing the LabVIEW code for taking the measurements. Matthew Fontana carried out many of the thermal evaporations and was invaluable to the development and drafting of the manuscript. All coauthors assisted in the editing of the manuscript. The PIs and/or project directors were: Benjamin Schwartz and Sarah Tolbert.

Chapter 3 and Appendix B are versions of Reference 12, Reprinted (adapted) with permission from Stanfield, D. A.; Wu, Y.; Tolbert, S. H.; Schwartz, B. J. Chem. Mater. 2021, 33, 7, 2343–2356. Copyright (2021) American Chemical Society. The full article can be accessed at https://pubs.acs.org/doi/10.1021/acs.chemmater.0c04471?ref=pdf This work was supported by the National Science Foundation under grant number CHE-20003755. Use of the Stanford Synchrotron Radiation Lightsource, SLAC National Accelerator Laboratory, is supported by the U.S. Department of Energy, Office of Science, Office of Basic Energy Sciences under Contract No. DE-AC02-76SF00515. All of the measurements and fitting of GIWAXS data for this project were performed by Yutong Wu at the Stanford Synchrotron Radiation Lightsource, SLAC National Accelerator Laboratory using beamline 11-3. Jonathan Onorato synthesized the highly regioregular P3HT, UV-Vis-NIR and FTIR data for the varied crystallinity study was acquired and provided by Tyler Scholes. Inspiration for this project arose from conversations with Tyler Scholes, who's interpretations of preliminary data turned out to be spot on the target, and were highly influential in steering the project down the right path in those early days. All coauthors assisted in editing the manuscript. The PIs and/or project directors were: Benjamin Schwartz and Sarah Tolbert.

Chapter 4 and Appendix C are versions of unpublished work and will be submitted to Advanced Materials for publication shortly after filing this dissertation. Jonathan Onorato synthesized the highly regioregular P3HT. The FTIR dataset on varied crystallinity was acquired and provided by Tyler Scholes. Inspiration for this project arose out of conversations with Sarah Tolbert and Yutong Wu during a visitation to a Tolbert group meeting, when additional peak fitting for the F_4TCNQ vibrational spectra was suggested. Countless conversations with Ben Schwartz were critical to the development of the vibrational Stark effect analysis. Zerina Mehmedović spent considerable time calculating the vibrational spectrum for the F_4TCNQ anion, and at the time of submitting this dissertation continues working towards an estimation of the Stark tuning rate parameters for both the B_{1u} and B_{2u} vibrational modes. These were regrettably not finished in time to include here but will be included in the manuscript upon submission for publication. Benjamin Schwartz assisted in editing the manuscript. The PIs and/or project directors were: Benjamin Schwartz.

VITA

2021	James D. McCullough Dissertation Award Recipient
2021	Michael E. Jung Excellence in Teaching Award Recipient
2020	UCLA Chemistry & Biochemistry Excellence in Research Fellow
2020	Michael E. Jung Excellence in Teaching Award Recipient
2019–2020	Joint Research Safety Initiative, Founding Member – UCLA
2016–2018	M.S. in Chemistry, University of California, Los Angeles
2017–2019	Science & Policy Group, Founding Member – UCLA
2011–2016	B.S. in Chemistry, Western Washington University

PUBLICATIONS AND PRESENTATIONS

Stanfield, D. A., Mehmedović, Z., and Schwartz, B. J. “Measuring the Vibrational Stark Effect in Chemically Doped Semiconducting Polymers **(2021)** *preparing manuscript for submission*.

Stanfield, D. A., Wu, Y., Tolbert, S. H., and Schwartz, B. J. “Controlling the Formation of Charge Transfer Complexes in Chemically Doped Semiconducting Polymers” **(2021)** Chem. Mater. 33 (7), 2343-2356 DOI: 10.1021/acs.chemmater.0c04471

Fontana, M. T., **Stanfield, D. A.**, Scholes, D. T., Winchell, K. J., Tolbert, S. H., and Schwartz, B. J. “Evaporation vs Solution Sequential Doping of Conjugated Polymers: F_4TCNQ Doping of Micrometer-Thick P3HT Films for Thermoelectrics" **(2019)** J. Phys. Chem. C. 123 (37), 22711-22724 DOI: 10.1021/acs.jpcc.9b05069

Stanfield, D. A., Fontana, M. T., Scholes, D. T., Winchell, K. J., Tolbert, S. H., and Schwartz, B. J. "Comparing Chemical Doping Methods for Preparing Micron-Thick Films of Semiconducting Polymers for Thermoelectric Applications" Presented at the 2019 Materials Research Society Spring Meeting, April **(2019)**, Phoenix, AZ, *poster*

Schaaf, C., Jenkins, M., Morehouse, R., **Stanfield, D. A.**, McDowall, S., Johnson, B. L., and Patrick, D. L. "Predictive Modeling of Nanoscale Domain Morphology in Solution-Processed Organic Thin Films" **(2017)** Phys. Rev. Mater. 1, no. 4 : 043404. DOI: 10.1103/PhysRevMaterials.1.043404

Morrison, L. A., **Stanfield, D. A.**, Jenkins, M., Baronov, A. A., Patrick, D. L., and Leger, J. M. "High Performance Organic Field-Effect Transistors Using Ambient Deposition of Tetracene Single Crystals" **(2016)** Org. Electron. 33 : 269–273. DOI: 10.1016/j.orgel.2016.03.021

Stanfield, D. A. "Observing Semiconductor Growth Towards Better Theory & Devices" **Fall 2015**, *Poster*, Murdock College Science Research Conference - Vancouver, WA

Stanfield, D. A., Baranov, A. "Delayed Burst Nucleation" **Spring 2014**, *Poster*, Western Washington University Scholars Week - Bellingham, WA

Stanfield, D. A., Baranov, A. "Organic Vapor-Liquid-Solid Deposition for Growth of Molecular Crystalline Films" **Fall 2013**, *Poster*, American Vacuum Society, Pacific Northwest Chapter - Portland, OR

CHAPTER 1

Introduction

Chemical doping is a straightforward method for tuning the electrical properties of polymeric semiconductors.[1–57] A comprehensive picture that describes this process is critical to the performance of many types of organic electronics. In the traditional picture of inorganic semiconductors, the electronic properties may be modulated by atomic substitution of dopant impurity atoms, giving rise to conduction at the bulk level. In analogy with these materials, polymeric semiconductors may also be doped in a similar way by introducing 'impurity' molecules, better known in the chemical literature as strong oxidizing agents for the case of *p*-type doping. When a molecular *p*-type dopant is introduced to a polymer film, it may remove an electron from the extended π conjugation network along the polymer backbone, leaving behind a positively-charged hole (Figure 1.1). It is sometimes useful to describe this hole as a quasiparticle, referred to as a polaron.[13] The concept of a polaron includes not only the net charge and spin, but also the distortion of the chemical bonds of the surrounding material that accompany the charged region, as depicted in Figure 1.1b. Because these materials have extended π conjugation along the polymer backbone, resonance contributions mean that polarons may delocalize along the polymer chain as well as between adjacent π orbital stacks. The polaron is the basic charge transport unit in organic semiconductors, which gives rise to conduction of mobile carriers at the bulk level.[2,40,43,44,46,58–61]

In this dissertation, we study *p*-type doping of the archetypal conjugated polymer poly(3-hexylthiophene-2,5-diyl) (P3HT) using the commonly studied small molecule electron acceptor 2,3,5,6-tetrafluoro-7,7,8,8-tetracyanoquinodimethane (F_4TCNQ) as the dopant (Figure 1.2). Chapters 2-4 are each focused on understanding a specific and unique aspect of the chemical doping process for this polymer-dopant pair, and this introduction serves as an overview of the key concepts and themes that are shared between them.

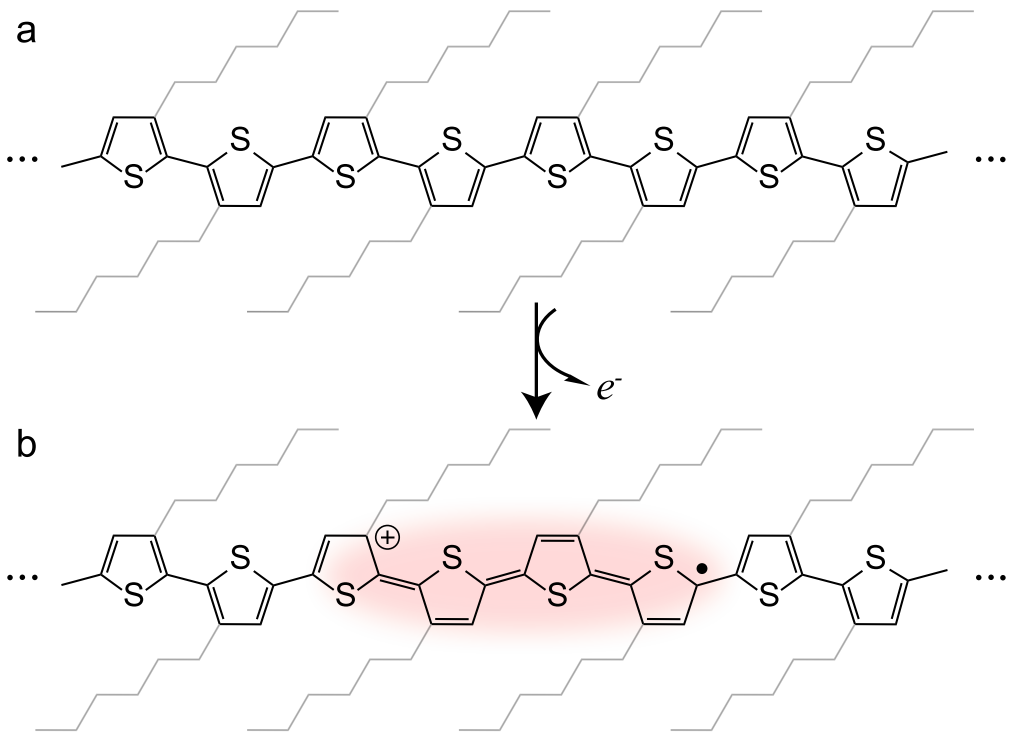

Figure 1.1: (a) Depiction of a single P3HT chain, and (b) the subsequent changes in bond order as a result of removing an electron during the doping process. Side-chains are semitransparent to highlight the changes to the conjugated backbone. The polaronic hole is the quasiparticle indicated by the blurred area in red which describes the positive charge and radical electron left behind on the polymer, along with the associated quinoidal bond distortions. The polaron is the fundamental charge transport unit in doped conjugated polymers.

1.1 Semiconducting Organic Molecules

Due to the chemical versatility of carbon-based molecules, there exists a virtually limitless number of possible organic electronic materials, in contrast to atomic or compound semiconductors, for which the periodic table only offers a finite number of possible combinations. Organic semiconductor materials can roughly be divided into two groups: (i) small molecule and (ii) polymeric organic semiconductors (Figure 1.3). Although both sets of these materials offer their own unique advantages and drawbacks, this thesis will principally focus on semiconducting polymers.

There are several advantages to working with polymeric semiconductors. For example, relatively early on in their development, the insight to add solubilizing side-chain groups to the monomer

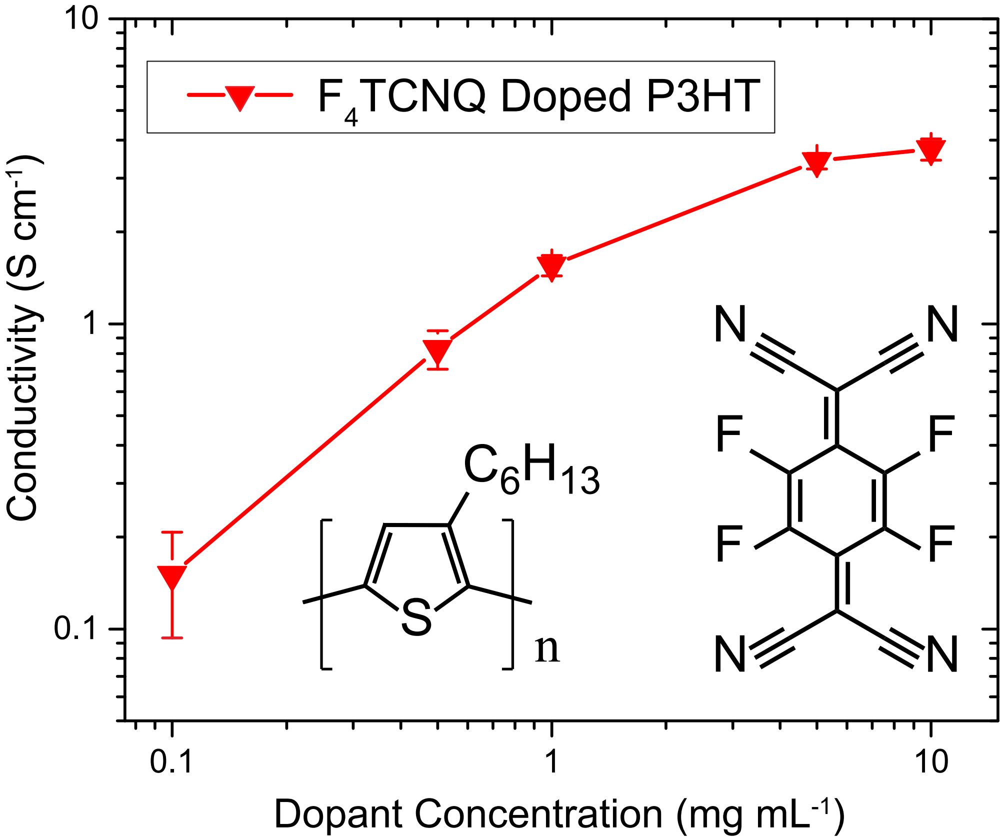

Figure 1.2: Electrical conductivity of doped P3HT polymer films plotted against F_4TCNQ concentration in the *n*-butyl acetate (*n*BA) solution used to intercalate the dopant.

units significantly improved their processability into thin film devices while largely preserving the electronic structure of the π conjugation network on the polymer backbone.[62] Indeed, it is a relatively straightforward process to form these materials into bulk heterojunction (BHJ) solar cells,[63] light emitting diodes,[64] and thermoelectric generators[22] among other applications.[65] In chapter 3 and appendix B of this dissertation, we explore how the presence of these side-chains affects the resulting packing structure of the material, influencing the type of doping mechanism that takes place.[12]

Solution processable semiconducting polymers also benefit from mechanical flexibility, and the formation of smooth films with nanometer-scale roughness over centimeter length scales. From the standpoint of structural morphology, conjugated polymers have an intrinsic amount of entropic disorder, which gives them a mix of crystalline domains surrounded by disordered or amorphous polymer regions. The size of these crystalline domains (typically a few tens of nanometers) are many orders of magnitude smaller than the length scales of devices so that the resulting bulk properties are predictable and isotropic. This ultimately means that device properties like electrical conductivity and thermoelectric power factor are highly reproducible between samples using straightforward solution processing techniques.

These materials also benefit from the relatively straightforward process of spin-coating, where the polmyer solution is deposited on a rotating substrate so that the centripetal forces pull the liquid over the entire substrate and the evaporating solution leaves behind a solid polymeric thin film. Considering how simple this process is, it is capable of producing exceptionally uniform polymer layers, whith nanometer level reproducibility across many samples. In the section that follows, we will discuss several spin-coater based techniques developed by our group that enable the fabrication of polymer thin films containing a wide range of structural morphologies.

1.1.1 Sequential Processing

For many polymer-based devices, it is desirable to mix the conjugated polymer with some guest species, such as a dopant. The method of sequential processing, developed here at UCLA, has become quite popular.[2, 11, 19, 43, 44, 61, 66, 67] In this method, a pristine polymer layer is first laid down on the substrate, and then the guest species is intercalated inside the pre-cast polymer film in a subsequent processing step. This technique is quite versatile in that the guest species may be deposited from the solution phase, or for small molecules of requisite stability, intercalated via thermal evaporation. The differences between these two methods will be explored in detail chapter 2 and appendix A. Additionally, the underlying structure of the polymer film can be finely controlled by sequential processing, either in the first step when the pristine polymer layer is laid down, or in the subsequent step when intercalating the guest species. In either case, the structural order of the polymer can be controlled by the solvent choice. To manipulate polymer order in the first processing step, solvent evaporation kinetics can be exploited, where slower drying times yield a higher fraction of crystalline polymer domains. It is straightforward then to subsequently intercalate the guest species using a weakly-interacting solvent that swells but does not dissolve the pre-cast polymer layer to preserve the underlying film morphology. To manipulate the polymer structure in

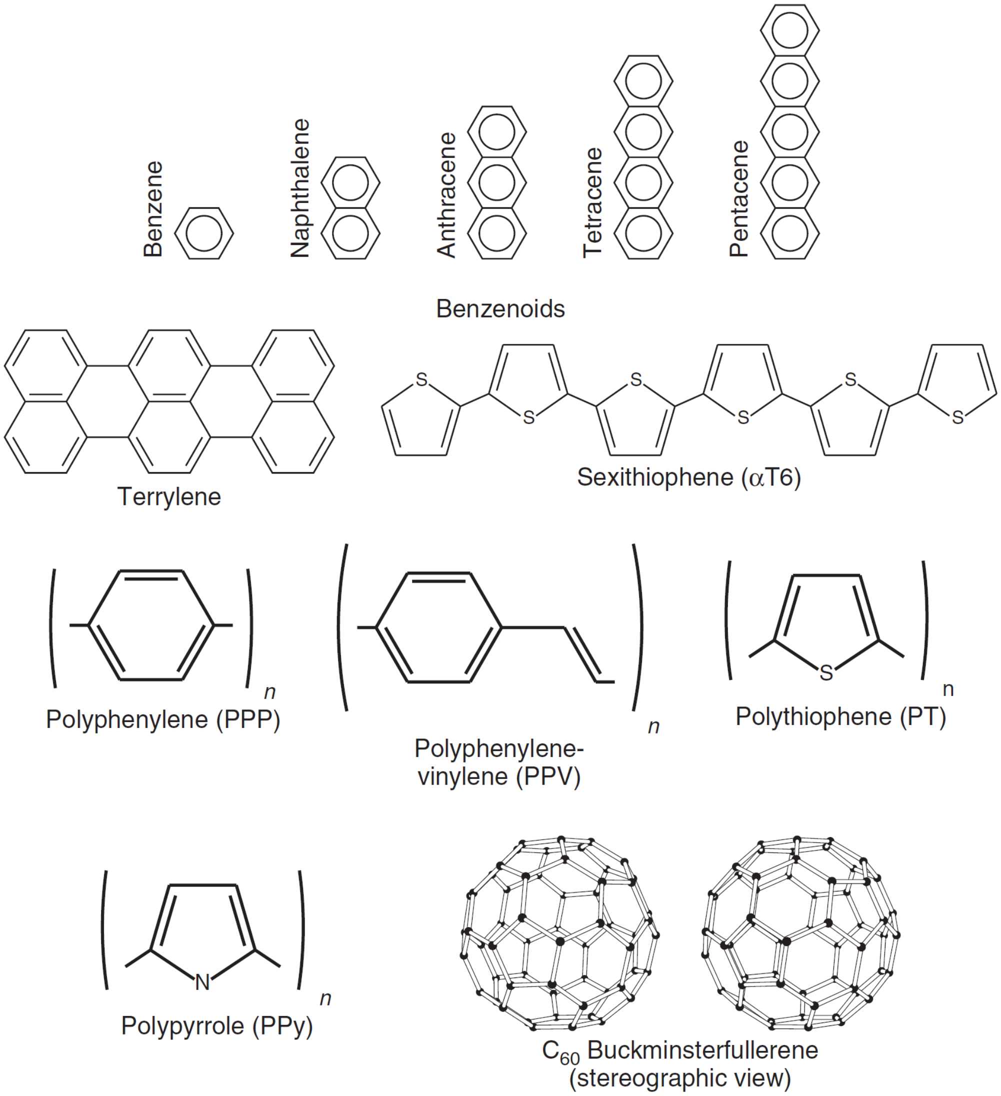

Figure 1.3: A depiction of some common classes of organic semiconductors. The top row shows the oligo-acene progression, a series of small molecule semiconductors comprised of an increasing number of fused benzene rings. These molecules form a molecular crystal in the solid phase, held together by weakly interacting Van der Walls forces. The second row depicts some common larger small molecule oligomers. Bottom two rows show some commonly seen polymeric semiconductors as well as buckminsterfullerene C_{60}. (This figure borrowed from reference 1.)

the subsequent intercalation step, solvent blends with tailored solubility towards the polymer layer can be used, where greater dissolving power tends to create more amorphous polymer domains, but the dissolution/reprecipitation from such solvent blends means that the ordered domains that remain in the polymer layer are on average more crystalline. This technique of manipulating the intercalation solvent to control polymer structure will be explored in detail in chapter 3 and appendix B.

1.2 Chemical Doping of Conjugated Polymers

The fundamental goal of the chemical doping process is to introduce equilibrium free charge carriers into a semiconducting polymeric material. In the case of *p*-type doping, these are generated through the oxidation of the conjugated polymer backbone by the dopant guest species. In this way, the integer transfer of charge from polymer to dopant generates (i) a polaronic hole on the polymer backbone and (ii) an anionically-charged guest species, which must remain somewhere inside the film to maintain charge neutrality. Due to the extended π conjugation network, the polaronic hole is delocalized across the polymer backbone over several repeat units, and possibly between adjacent polymer backbones. In the crystalline polymer domains, the dopant anion is typically situated within the side-chain lamellar regions between vertically-adjacent polymer π-stacks (Figure 1.4a).[7,11,21,29,34,42,44–46,53,55,57,61,68,69]

The distance between a dopant molecule and the hole polaron, d_{anion}, is crucially important, because shorter d_{anion} values lead to a stronger Coulomb interaction between the two charges.[2,40,43,44,46,58–61] This, in turn, serves to localize the polaronic charge carriers, a topic that is discussed in detail in chapter 4 and appendix C. The hole on the polymer backbone is associated with the loss of an electron from the valence band, and so Figure 1.4c shows that for a highly doped film, the polymer band-gap transition becomes heavily bleached as a result of the doping process. Doping is also associated with the formation of two new mid-gap states between the valence and conduction bands, as depicted in Figure 1.4b. Because these mid gap states are close to the valence and conduction bands, the lowest energy transition, P1, is located in the mid-IR (Figure 1.4c). The other two transitions, P2 and P3, are numbered in order of increasing energy and can be seen near 1.5 eV and

1.9 eV for P3HT in the spectrum shown in Figure 1.4c. The doped film here was produced via an anion-exchange doping process, where the dopant F_4TCNQ was used to initiate electron transfer and then replaced with a secondary salt anion, bis(trifluoromethane)sulfonimide ($TFSI^-$), from the same solution. In addition to the exceptionally high charge carrier densities obtained, exchange doping with the $TFSI^-$ anion is also very useful for spectroscopic purposes, because this anion does not absorb light in any locations of interest for the doped P3HT spectrum. It is otherwise rare to observe a doped conjugated polymer spectrum that does not contain overlapping absorbance(s) from the chemical dopants inside the film.

1.3 Charge Transport Properties and Electrical/Thermoelectrical Characterization

The doping process introduces free charge carriers into a thin polymer film, so measuring the film's electrical conductivity yields basic insights into the charge transport characteristics of a given doped conjugated polymer. The electrical conductivity, σ, is related to the charge carrier mobility, μ, and charge carrier density, n, through equation 1.1. The charge carrier mobility is a measure of how easily charge carriers migrate through the material in the presence of an externally-applied electric field. Equation 1.2 highlights the relationship between the electric field, E, the charge carrier mobility, μ, and the drift velocity of the charge carriers, υ_d. Thus, the charge carrier mobility can be viewed as the parameter that relates a given field strength to the corresponding drift velocity of free charge carriers in a material.

$$\sigma = p\mu n \tag{1.1}$$

$$\upsilon_d = \mu E \tag{1.2}$$

In Eq. 1.1, the charge carrier density n is simply a measure of the volumetric concentration of free charge carriers present in a material, and p represents the elementary unit of charge. Thus, measur-

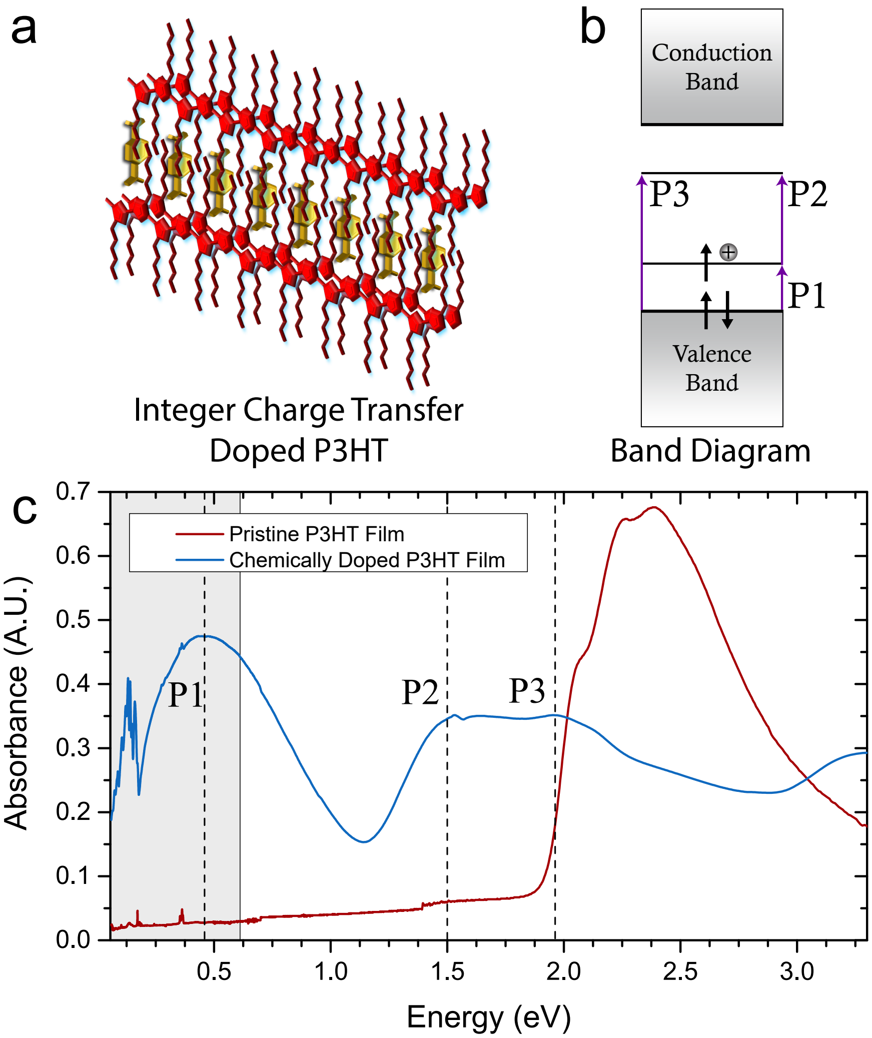

Figure 1.4: (a) Depiction of the structural arrangement for integer charge transfer doped P3HT. The cationic hole on the polymer is spatially separated from the electron which resides on the dopant molecule in the side-chain lamellar regions. The two species are separated by a distance d_{anion}. The Coulomb interaction between the two species, and thus the d_{anion} distance control the spectral shape and position for the P1 mid-gap transition. (b) Band diagram depicting the new mid gap states that arise as a result of the doping process. The transitions depicted by arrows in purple correspond to the spectroscopic features labeled in panel a. (c) UV-Vis-NIR / FTIR composite spectrum of a pristine, undoped P3HT film (maroon curve) and strongly chemically doped P3HT using bis(trifluoromethane)sulfonimide (TFSI$^-$) as the dopant anion (blue curve). Dashed lines indicate peak locations for the mid-gap transitions between the valence and conduction bands. The area in gray corresponds to the FTIR acquired spectrum.

ing the electrical conductivity gives the product of p, μ, and n. Since p is known, measurement of either μ or n allows determination of the other, which completely characterizes the charge carrier landscape of a given polymer-dopant pair. In chapter 3 and appendix B we will use a spectroscopic analysis, paired with the measured electrical conductivity, to obtain estimates of both the charge carrier concentration, n, and mobility, μ.

1.3.1 Measuring Electrical Conductivity

When the resistance of a material is sufficiently low, as with doped semiconducting polymer films, a two-terminal DC measurement is not sufficient for determining the resistivity. This is because the series resistance between the electrode contacts and cables become non-negligible in this regime, and the electrode contact resistance can vary from sample to sample. To navigate this, it is considered best practice to employ a four-point probe measurement, such as that depicted in Figure 1.5.[1] In the co-linear geometry, shown in panel a, current is sourced between the outside electrodes A and D. The voltage drop that is induced across electrodes B and C is then measured to determine the resistivity. The advantage here over the two terminal measurement is that the quantity of sourced current can be measured very accurately by the source meter, independent of the cable resistance. Similarly, electrodes B and C are only sensing a voltage drop, and thus receive no current, so that the contact resistances are negated in this measurement, allowing the resistance to be calculated according to equation 1.3.

A slightly more sophisticated four-point probe measurement can be taken in the so-called van der Pauw geometry. This has the advantage of sampling the sheet resistance across the entirety of a 2-D thin film rather than only in a line as with the co-linear geometry. When carried out correctly, this method gives remarkably good reproducibility between samples (Figure 1.2), since the source and sense electrodes are arranged across the full area of the sample. In this geometry, electrodes are situated according to the scheme depicted in Figure 1.5b. Two measurements are carried out, first sourcing current between points A and D, and measuring the induced voltage at points B and C. The electrode geometry is then rotated by 90° so that the current is subsequently sourced between points A and B, and the ensuing voltage drop is measured at points C and D. The result of these measurements yields values R_a and R_b, which then can be inserted into equation 1.4 to solve for R_{sheet}.

The sheet resistance, R_{sheet}, which has units of $\Omega/\square$, is an intrinsically thickness-independent parameter related to the resistivity, ρ, according to equation 1.5. Thus, to obtain the resistivity from a material's measured sheet resistance, the thickness, d, of the thin film must also be known. This is usually straightforward to measure using surface profilometry techniques, or under more stringent circumstances, atomic force microscopy (AFM). Of course, resistivity is just the reciprocal of conductivity, σ, which is much more commonly quoted in the field of doped organic semiconductors.

$$R = \frac{V_B - V_C}{I_{AD}} \tag{1.3}$$

$$\exp\left(-\frac{\pi R_a}{R_{sheet}}\right) + \exp\left(-\frac{\pi R_b}{R_{sheet}}\right) = 1 \tag{1.4}$$

$$R_{sheet} = \frac{\rho}{d} \tag{1.5}$$

1.3.2 The Seebeck Coefficient and Thermoelectric Power Factor

One exciting application for doped semiconductors is thermoelectric power generation, a process that is capable of converting waste heat into usable electricity. These devices operate on the principle of the thermoelectric effect, which is the direct conversion of a temperature difference into an electric voltage. Because this principle is reversible, it is also possible to use a sourced voltage to induce a temperature difference across the same material.

The Seebeck coefficient, S, is an important parameter for evaluating thermoelectric performance. Observationally, S is the measured induced voltage across a material per unit temperature difference that is applied across the same distance (Eq. 1.6) So, the greater the voltage drop for a given temperature difference, the higher the Seebeck coefficient. In more precise terms, the Seebeck coefficient can be represented as the average amount of entropy that each charge carrier transports from the hot to cold side of the material, which depends on the density of states at the fermi level.

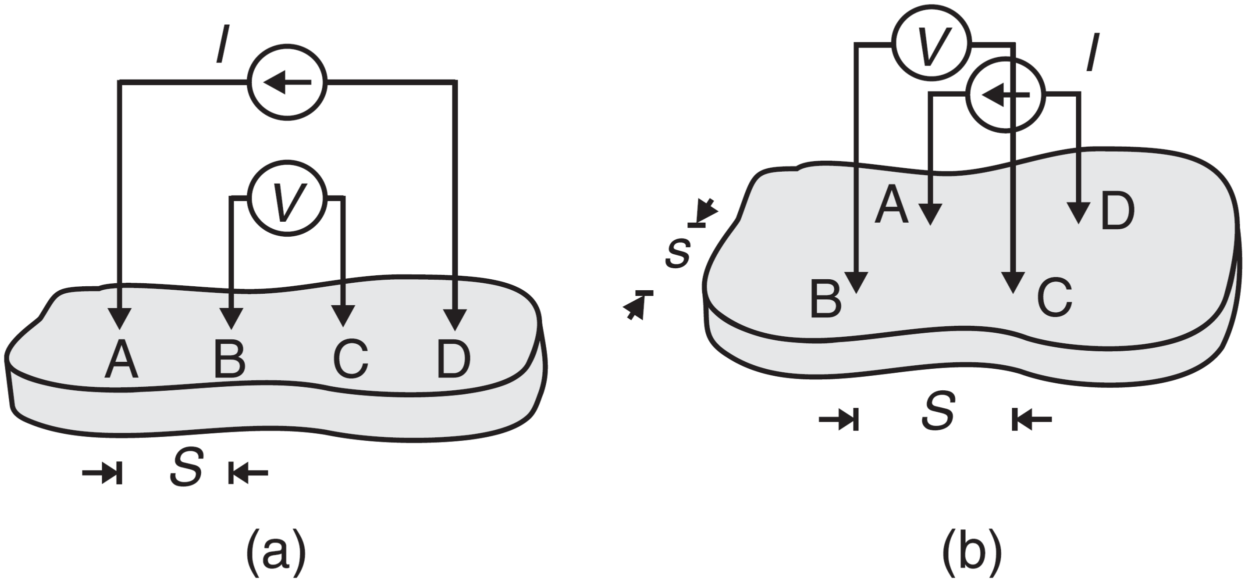

Figure 1.5: The four-point probe resistivity measurement in the (a) co-linear geometry with electrode spacing, S. Current is sourced from points D to A and the corresponding voltage that is induced is sensed across points B and C. (b) The van der Pauw geometry. Current is sourced across points D to A and the corresponding induced voltage is sensed across points B and C. (This figure borrowed from reference 1.)

Thus, at low charge carrier densities, the average entropy per carrier is high, and at increased carrier densities, the average entropy per carrier becomes reduced.

$$S = -\frac{\Delta V}{\Delta T} \tag{1.6}$$

The thermoelectric effect arises due to the migration of charge carriers from the hot side of a material to the cold side, however because the charge carriers in a semiconductor can be either p-type or n-type, the sign of the charge carrier determines which direction the current is flowing; in either case, however, the carriers will always migrate from hot to cold. The efficiency of thermoelectric materials can be evaluated according to the figure of merit, ZT, which is described in equation 1.7. We can see that the thermoelectric efficiency is proportional to the electrical conductivity, σ, the square of the Seebeck coefficient, S^2, the average temperature, T, and is inversely proportional to the thermal conductivity, κ. Thus, the ideal thermoelectric generator will have the largest possible electrical conductivity and Seebeck coefficient and the smallest possible thermal conductivity. Unfortunately, thermal and electrical conductivities tend to move in tandem as a material's properties are varied. Moreover, when increasing the conductivity of a material by doping, the Seebeck coefficient is empirically seen to fall as $\sigma^{-\frac{1}{4}}$ across a wide range of doped materials. Because of these factors, developing high performance thermoelectric generators made from readily available materials has remained an elusive goal for materials scientists.

In general, polymeric materials have fairly low thermal conductivities, so one approach to solving this problem has been to develop organic thermoelectric generators (OTGs).[22] The fundamental goal is to raise the electrical conductivity as much as possible for doped semiconducting polymers, without mitigating these gains through too much reduction in the Seebeck coefficient.

$$ZT = \frac{\sigma S^2 T}{\kappa} \tag{1.7}$$

Given the empirical trade-off that exists between the Seebeck coefficient and electrical conductivity, one parameter that is useful for measuring these two quantities collective contribution to the thermoelectric figure of merit is, σS^2, a parameter referred to as the thermoelectric power factor (PF). In chapter 2 and appendix A, we will explore how the differences in dopant deposition method affect the resulting performance of organic thermoelectric materials by characterizing the electrical conductivity and the Seebeck coefficient, which determine the thermoelectric power factor.

1.4 Structural Morphology of Conjugated Polymers

Fundamentally, the charge transport properties in doped conjugated polymers are related to the underlying structural morphology of the material. In previous sections we discussed how Coulomb interactions between the dopant anion and hole contribute to the degree of hole delocalization. In this section, we will show how the distance between the two oppositely-charged species is controlled by the structure of the polymer.[7, 11, 29, 44, 55, 57, 61, 68, 69] In addition, the intrinsic structural order of the polymer can also control the extent of polaron delocalization. This means that a description of charge carrier transport in these doped materials is not complete without an understanding of the underlying structural morphology.

Through an ongoing collaboration with the Tolbert group at UCLA, we have studied the structure-function relationships of doped conjugated polymers. Most commonly, this was done using 2-D grazing incidence wide-angle X-ray scattering (GIWAXS), which requires the use of a synchrotron light source. Figure 1.6 summarizes the data acquisition geometry, where a grazing incident X-ray beam is directed at the sample of interest. Incident X-rays interact with and scatter off of the electrons inside the sample, and subsequently strike the detector. For an ordered material, certain repeat distances or ‘d-spacing’s’ will cause the scattered X-rays to interfere constructively, forming peaks on the 2-D detector that contain information about the stacking distance for a given plane. In addition to this, because GIWAXS is a 2-D measurement, it also records the relative orientations of these stacking distances, either out-of-plane (Figure 1.6c), or in-plane (Figure 1.6d). P3HT adopts a so-called ‘edge-on’ geometry, meaning that the aliphatic side-chains which are added to confer favorable solubility properties tend to be oriented perpendicular to the substrate on which the polymer film is cast. Many conjugated polymers that are capable of forming ordered crystals adopt this edge-on geometry, and as a result, the lamellar side-chain stacking distance is reflected in the out-of-plane peaks in Figure 1.6b and c. The edge-on geometry also shows the crystallographic $\pi-\pi$ stacking direction from scattering in the in-plane direction.

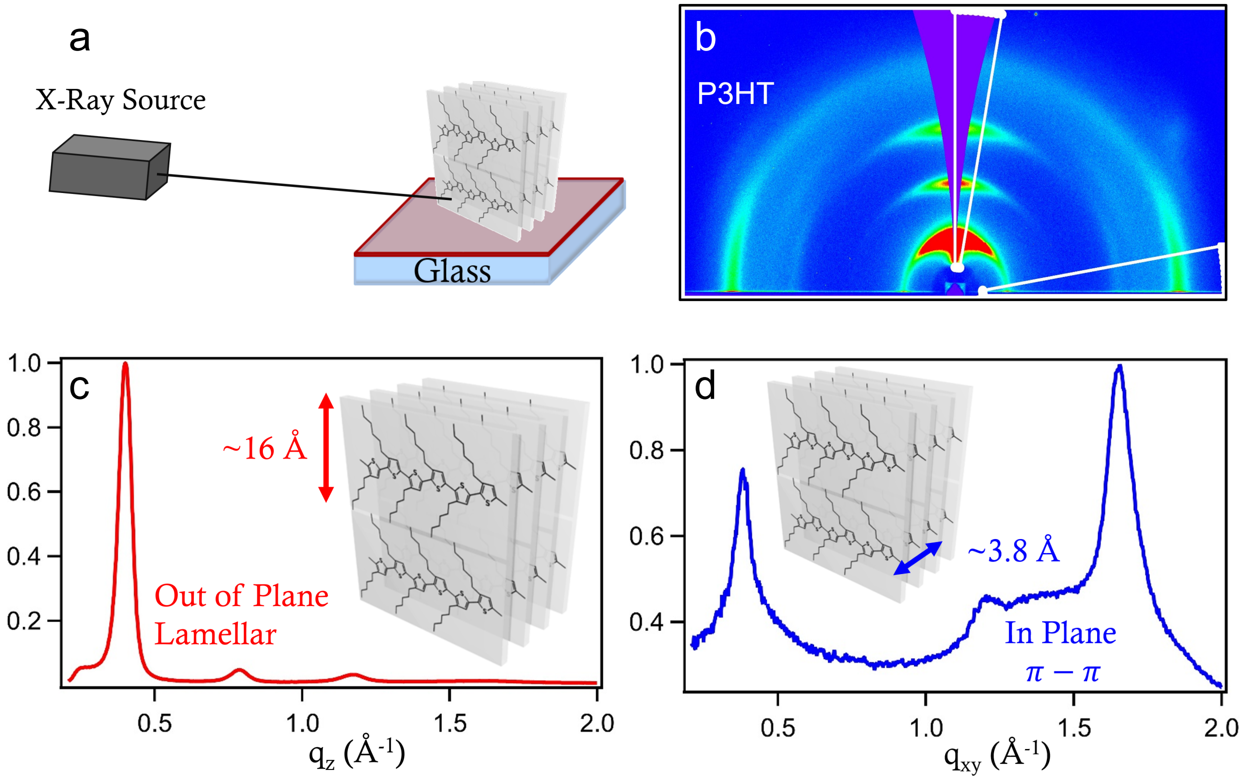

Figure 1.6: (a) A depiction of the 2-D grazing incidence wide-angle X-ray scattering (GIWAXS) geometry. (b) The corresponding 2-D diffractogram acquired from a pristine P3HT polymer thin film. (c) Integration of the out-of-plane wedge shown in panel b in white. The edge-on orientation of the P3HT crystallites means that the side-chain lamellar regions interact with each other in vertically layered structures. (d) Integration of the in-plane wedge shown in panel b in white. Again, the edge-on orientation of P3HT here shows that the $\pi - \pi$ stacking interaction occurs in the plane of the substrate.

In chapter 2 and appendix A, we will use this technique to evaluate the structural order of the doped polymer, comparing the effects of vapor vs. solution processing of the dopant molecule. In chapter 3 and appendix B, we will use structural insights gleaned from GIWAXS experiments to build an understanding of the preferred charge transfer interaction in doped crystalline polymer regions, including identifying a rare polymer-dopant polymorph that was previously difficult to study.

1.5 Overview of Thesis

This thesis is comprised of four chapters, each with a specific focus on aspects of the chemical doping process.

1.5.1 Chapter 2: Evaporation vs. Solution Sequential Doping of Conjugated Polymers: F_4TCNQ Doping of Micrometer-Thick P3HT Films for Thermoelectrics

The work in this chapter has been previously published as reference 11. For thermoelectric and other device applications, there has been great interest in the chemical doping of conjugated polymer films. Blending the polymer and dopant together before deposition generally yields poor quality films, but this issue can be alleviated by sequential doping: a pure polymer film is deposited first and the dopant is then added as a second processing step, preserving the quality and structure of the original polymer film. In this chapter, we compare two methods for sequential doping of conjugated polymer films: evaporation doping, where a controlled thickness of dopant is added via thermal sublimation to a temperature-controlled polymer film, and sequential solution doping, where the dopant is spin-cast from a solvent chosen to swell but not dissolve the underlying polymer film. To compare these two different types of sequential doping, we examine the optical, electrical, and structural properties of P3HT films doped by each method with the small-molecule dopant F_4TCNQ as a function of the polymer film thickness. Although each method intercalates the dopant in fundamentally unique ways, we find that both vapor and solution doping methods produce films that share many of the same properties. Interestingly, both methods can produce doped P3HT films with conductivities of $\sim 5\,\mathrm{S\,cm^{-1}}$ and comparable thermoelectric properties, even for films as thick as 400 nm. For the evaporation method, an ‘overhead’ dopant film thickness of $\sim$6 nm is required, either to promote reorganization of existing crystallites or to fill preexisting trap states in the polymer film. After the overhead amount has been deposited, the thickness of the dopant layer that must be evaporated to reach the optimal electrical conductivity is $\sim$1/3 that of the underlying polymer film. For a given P3HT film thickness, the amount of evaporated dopant needed to produce the highest conductivity corresponds to a thiophene monomer to ionized dopant ratio of $\sim$8.5:1. For solution processing, with the appropriate choice of solvent and dopant concentration, we show that P3HT films as thick as 2 µm can be doped to achieve conductivities of $\sim 5\,\mathrm{S\,cm^{-1}}$ and thermoelectric power factors approaching $2\,\mathrm{\mu W\,m^{-1}\,K^{-2}}$. For either method, if excess dopant is applied, it remains in neutral form either in the amorphous regions or on top of the film, reducing the conductivity by increasing the film thickness. For both methods, UV-Visible absorption can be used as a quick proxy to easily monitor whether saturation doping levels have been reached or exceeded. Fourier-transform infrared spectroscopy (FTIR) and grazing-incidence wide-angle x-ray scattering (GIWAXS) both show that vapor-doped films and thicker solution-doped films have improved morphologies that result in more mobile carriers. Overall, we demonstrate that it is a straightforward process to select a sequential doping method for a desired application: evaporation doping is more amenable to large-area films while solution-doping is lower cost and better suited for polymer films with µm thicknesses.

1.5.2 Chapter 3: Controlling the Formation of Charge Transfer Complexes in Chemically Doped Semiconducting Polymers

The work in this chapter was previously published as reference 12. Chemical doping of semiconducting polymers predominantly takes place via integer charge transfer (ICT), where an electron is entirely removed from the host conjugated polymer and transferred to reside on the dopant guest species. In contrast, chemical doping of small conjugated molecules and oligomers often leads to the formation of charge transfer complexes (CTCs), which have significant orbital overlap and shared electron density between the host and guest species. To date, the observation of fractional charge transfer in doped conjugated polymers is relatively rare, occurring only under extreme processing conditions that can be difficult to achieve, which is fortunate given that CTC formation generally yields fewer mobile carriers per dopant. In this work, we use the classic conjugated polymer/dopant pair of P3HT and F_4TCNQ to demonstrate how simply adjusting the casting solvent for the dopant in sequential processing can fundamentally alter the nature of doping in this well-studied system, leading to tunable production of CTCs. Using solvent blends of dichloromethane and chloroform, selected for their low and high solubility towards P3HT, respectively, we show that the relative amount of polymer-dopant CTCs can be readily controlled over an order of magnitude. Increasing the amount of chloroform in the dopant solvent blend favors the creation of CTCs, while increasing the dichloromethane content results in doping by the more standard ICT mechanism; the results allow us to explain why CTC formation is common in charge-transfer salts but generally less so in doped conjugated polymers. We also explore the role of the doping method and the crystallinity of P3HT films in controlling the relative amounts of ICT and CTC formation. We find that the use of evaporation doping and higher-crystallinity material discourages CTC formation, but that even in the most favorable case of evaporation doping with high polymer crystallinity, fractional charge transfer always occurs to some extent. Finally, we show that brief thermal annealing can convert CTCs to integer charge transfer species, indicating that ICT is the thermodynamically-preferred doping mechanism in conjugated polymers, and that fractional charge transfer is the result of kinetic trapping. With this understanding, we offer guidelines for limiting the occurrence of charge transfer complexes during sequential doping of conjugated polymers, thus avoiding the deleterious effects of CTCs on charge transport.

1.5.3 Chapter 4: Measuring The Vibrational Stark Effect in Chemically Doped Semiconducting Polymers

The work in this chapter is currently unpublished, but will be submitted soon. The nitrile stretching vibrational modes of the 2,3,5,6-tetrafluoro-7,7,8,8-tetracyanoquinodimethane (F_4TCNQ) anion can occur across a range of different frequencies in doped P3HT films. In this paper we show that these shifts can be predicted using the vibrational Stark effect (VSE). F_4TCNQ^- serves as a sensitive vibrational Stark probe and the nitrile stretching modes shift as a function of the locally experienced electric fields from the nearby polaron on the polymer backbone. The shift of the F_4TCNQ^- B_{1u} mode and broadening of the B_{2u} mode show conclusively that the anion's long axis is oriented perpendicular to the P3HT backbone. These vibrational shifts also prove that the anion-polaron distance in F_4TCNQ^- doped P3HT films is 6 Å, and that the intrachain polaron coherence varies between 3-4 P3HT monomer units with increasing local polymer order. We also show that attempting to increase polaron delocalization through enhancing the local order only works to an extent, where polaron delocalization eventually becomes limited by the minimum intrinsic strength of the anion-polaron Coulomb interaction. This provides the first direct experimental measurement of polaron delocalization in doped conjugated polymer films, and verifies theoretical models relating polaron coherence increases to changes in the mid-IR electronic absorption spectrum.

CHAPTER 2

Evaporation vs. Solution Sequential Doping of Conjugated Polymers: F_4TCNQ Doping of Micrometer-Thick P3HT Films for Thermoelectrics

2.1 Introduction

Conjugated polymers are of considerable interest since they are semiconducting,[70–72] low-cost,[73,74] have mechanical flexibility,[75,76] are easily solution processed,[73,77] and have properties that are readily tuned synthetically.[73,78] As a result, these materials are ideally suited for a wide variety of device applications.[79–82]

As with inorganic semiconductors, it is possible to dope conjugated polymers to increase their equilibrium carrier density and thus modify their electrical properties. Unlike inorganic semiconductors, which are doped by atomic substitution, organic semiconductors are usually doped chemically by adding a strong oxidizing (or reducing) agent. When doped, semiconducting polymers show particular promise as active materials for thermoelectrics[29,70,83–88] due to their reasonably high electrical conductivities and generally poor thermal conductivities.[22,83,86,89] This explains the recent surge of research on the multiple ways to produce molecularly-doped conjugated polymers; this research includes studies on the methodologies used to produce doped polymer films as well as studies on the performance of devices fabricated from such materials.[16,19,44,61,90–93]

It is well established that the electrical conductivity of semiconducting polymers can be effectively tuned over several orders of magnitude by changing the amount of dopant used.[34,91,94,95] What is less clear, however, is the maximum possible degree of doping that can be achieved. Part of the reason for this is that there are multiple different methods for producing doped polymer films.

The most common method involves casting a film of pre-doped polymer created by co-blending the polymer and dopant in solution, which we refer to as blend-cast doping.[19,22,34,39,84,87,90,96] This method makes it difficult to produce high doping levels, however, because as conjugated polymers become charged in solution, they generally become much less soluble, making it difficult to cast high-quality films.[19,28,84,97–99] Because of this, there has been a great deal of recent effort aimed at starting with undoped conjugated polymer films and then exposing the pre-cast films to the dopant in a secondary step.

Different groups implemented this latter approach, which we term sequential doping, in various ways. Some researchers expose the polymer film to the dopant molecules in the vapor phase,[21,21,34,35,37,42] as outlined schematically in Fig. 2.1a. Alternatively, some groups, including ours, pursued a solution-based technique where the dopant is directly spin-coated from solution onto a pre-cast polymer film,[19,23,29,44,61,90,100] represented in Fig. 2.1b. The purpose of this paper is to compare in detail the evaporation and solution-based sequential doping methods to determine which method, if either, is better for particular applications, such as thermoelectrics. This is accomplished through a head-to-head comparison of the films' optical, electrical, and structural properties. As far as we are aware, this is the first study performed to-date that compares the two doping methods side-by-side on identical pre-cast polymer films. Furthermore, our comparison extends to films that are hundreds of nm thick, a thickness regime that is largely uncharacterized in the literature.

Evaporation sequential doping has been the subject of many recent reports, most of which have focused on the doping of poly(3-hexylthiophene-2,5-diyl) (P3HT) by 2,3,5,6-tetrafluoro-7,7,8,8-tetracyanoquinodimethane (F_4TCNQ).[34,42] These reports attributed the high electrical conductivities observed after doping to the idea that the crystalline order of the pre-cast polymer films is preserved after doping. Similar conclusions have been reached upon evaporation doping of poly(2,5-bis(3-alkylthiophen-2-yl)thieno[3,2-*b*]thiophene) (PBTTT).[24] Although evaporation sequential doping yields high conductivities, most reports focus on films that are only a few tens of nm thick.[21,24,35,42]

Another open question with evaporation doping is how to reproducibly control the amount of dopant delivered. This is because most experimental evaporation doping setups add the dopant by sublimation in a home-built chamber with no way to precisely monitor the amount of dopant deposited on the polymer film.[34,35,37,42] An additional issue is the fact that the sublimation process

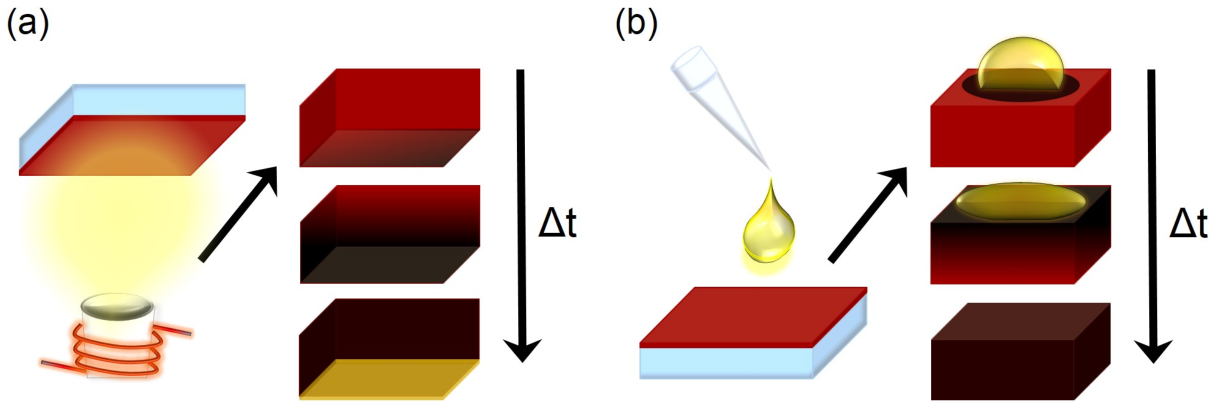

Figure 2.1: Schematic showing sequential doping of conjugated polymer films using (a) evaporation sequential doping and (b) solution sequential doping; after the initial step, the arrows in each panel indicate the changes that take place as a function of time. Panel a shows that for evaporation doping, the crucible is resistively heated, producing dopant vapor (yellow) that can intercalate into a pre-cast polymer film (red). With additional time, a greater amount of dopant intercalates within the polymer film (doped film is indicated with black color). If evaporation continues, the dopant is added in excess, eventually coating the exposed side of the film. Panel (b) shows that for solution doping, a dopant solution (yellow) is spin-cast onto a pre-cast polymer film (red). The solvent for the dopant solution is chosen to swell but not dissolve the polymer, allowing mass action to drive the dopant from the solution into the swollen film. Films can be more strongly doped (increasing black color) by increasing the concentration of the dopant in solution.

tends to heat polymer films: heating promotes increased diffusion of dopant species, and heating-induced diffusion may vary among different polymer/dopant systems. This leads to potential difficulties with reproducibility if the temperature of the film cannot be precisely controlled.[35,42] Very few studies have focused on more quantitative methods for delivering a precise amount of dopant, such as using a thermal evaporator with thickness monitoring.[21]

Solution sequential doping has also been the focus of much recent work.[19,23,29,37,44,61,87,90,100–102] Methods for solution sequential doping include 1) immersing the film in a dopant solution, 2) drop-casting the dopant solution onto the polymer film, and 3) spin-coating the dopant solution onto the polymer film. Although film immersion and drop-casting can effectively dope polymer films, we focus here on doping by spin-coating due to its facility in producing high-quality films.[19,44,61] With spin-coating, the dopant is dissolved in a solvent that is chosen to optimally swell but not dissolve the polymer of interest. When the dopant solution is spin-coated onto a pre-cast polymer film, mass action drives the dopant from the solution into the swollen polymer underlayer.[19,44,61,90,90,103,104] As with evaporation doping, solution sequential doping maintains much of the pre-cast polymer film's morphology, leading to excellent film quality and high electrical conductivities.[19,44,61,90] Moreover, because the method involves the spin-coating of a dopant solution with a precisely defined concentration, the reproducibility of the method is high.[19,23,44,61,90]

Solution sequential processing is limited, however, by the need to find solvents that simultaneously dissolve the dopant and optimally swell the polymer, but do not dissolve the polymer underlayer. Since it is generally straightforward using solvents or solvent blends to optimally swell a conjugated polymer film,[90,104] the limiting factor for dopant intercalation with solution sequential doping is usually the solubility of the dopant in the selected swelling solvent.[105]

Despite the widespread and increasing application of sequential doping via evaporation and solution processing, no head-to-head comparison between the two methods has been carried out. In this work, we consider the similarities and differences between the evaporation and solution sequential doping methods, focusing on the well-studied P3HT/F_4TCNQ materials combination. Of particular interest is the way each method scales for doping conjugated polymer films of increasing thicknesses. For our evaporation-sequential-doping experiments, we employ a thermal evaporator to intercalate the F_4TCNQ dopant into films of P3HT. The films are actively held at a fixed temperature and the extent of deposition is calibrated using a quartz crystal microbalance (QCM) thickness monitor, providing quantitative and reproducible dopant delivery. Our solution sequential doping measurements rely on spinning F_4TCNQ from dicholormethane (DCM), which is a near-optimal solvent for swelling P3HT.[19,44,61,90,90,104,106,107] Since both techniques are sequential, we are able to make detailed comparisons between the two methods by doping identical pre-cast films of P3HT.

Using these two methods, we find that the electrical conductivities and thermoelectric performance of doped films are comparable if each method is properly applied. For evaporation doping, after an "overhead" thickness of $\sim$6 nm of F_4TNCQ is deposited, the optimal degree of doping is achieved when a thickness ratio of $\sim$1:3 dopant:polymer is reached, corresponding to a thiophene monomer:ionized dopant species ratio of $\sim$8.5:1 for all film thicknesses studied. For solution doping, the dopant solution concentration must be adjusted depending on the polymer film thickness.

We also find that both solution and evaporation sequential doping can effectively dope very thick semiconducting polymer films. When we started this study, we expected that evaporation doping would be ineffective for thicker films because the vertical distribution of the dopant would be limited by molecular diffusion, yielding high dopant concentrations near the top surface and a deficit of doping near the substrate. Surprisingly, however, our UV-Vis, conductivity, and QCM measurments all indicate that for a wide range of polymer film thicknesses, the extent of uniform chemical doping by evaporation only levels off after a monomer unit:dopant ratio of $\sim$8.5:1 is reached.

Both the evaporation and solution methods can create 400-nm-thick doped P3HT films with electrical conductivities of $\sim$5 S/cm and thermoelectric power factors near $2\,\mu\mathrm{W\,m^{-1}\,K^{-2}}$; these same properties can be maintained for films as thick as $2\,\mu\mathrm{m}$ when doped via the solution method.

In addition, we find using grazing-incidence wide-angle x-ray scattering (GIWAXS) that doping by either method increases P3HT crystalline coherence lengths, particularly for the evaporation-doped films: crystallinity of the doped film is important with dopants such as F_4TCNQ in order to keep the dopant anion as far as possible from the polaron on the polymer backbone.[43,61] When the doping process is optimized by either the solution or evaporation sequential methods, we see that the amplitude ratio of the P3HT neutral to F_4TCNQ anion/P2 polaron optical absorption peaks is near 1:1, providing a simple guideline to achieve optimal doping when the evaporation thickness cannot be easily controlled. Overall, we conclude that both solution- and evaporation-based doping methods are well-suited to achieve high doping concentrations for applications across a wide range of polymer film thicknesses.

2.2 Experimental Methods

All materials and solvents were purchased commercially and used as received. Electronic-grade P3HT was purchased from Rieke Metals and F_4TCNQ was purchased from TCI America. Please see appendix A for more details.

P3HT solutions at concentrations of 0.5%, 2%, and 5% weight/volume (w/v) were prepared by dissolving 5 mg, 20 mg, and 50 mg P3HT in 1 mL of *o*-dichlorobenzene, respectively. The solutions were heated and stirred at 65 °C to fully dissolve the polymer and the solutions were cooled to room temperature before use. Films were prepared in a N_2 atmosphere by spin-casting the P3HT solutions onto glass substrates at 1000 rpm for 60 s followed by 3000 rpm for 5 s. With this spin-casting condition, the 0.5%, 2%, and 5% w/v P3HT solutions yielded 25-nm, 110-nm, and 400-nm thick films, respectively. Films that were 2 µm thick were prepared by drop-casting 30 µL of a 2% w/v P3HT solution onto glass substrates, which were then slow-dried by being placed onto a small, covered Petri dish for two days. Thickness measurements were carried out using a Dektak 150 profilometer. UV-visible absorption spectra were collected using a Lambda 25 UV-visibile spectrophotometer and Fourier-transform infrared (FTIR) spectroscopy data were acquired for films prepared on KBr plates using a Jasco FT/IR-420 spectrophotometer.

We performed our evaporation sequential doping via controlled thermal evaporation. F_4TCNQ was thermally evaporated onto pre-cast P3HT films using an Angstrom Engineering Nexdep thermal evaporator, in which the F_4TCNQ powder was placed into an alumina crucible that was resistively heated at pressures below 1×10^{-6} Torr to induce sublimation. The pre-cast P3HT films were fixed to a rotating sample stage that was actively cooled using $\sim$15 °C chilled water. The evaporation rate was held constant at $0.5\,\text{Å}\,\text{s}^{-1}$ and the thickness of evaporated dopant was monitored using a quartz crystal microbalance located next to the sample holder. For all the data presented here, the doped polymer films were characterized immediately ($\leq$ 1 hr) after treating with dopant from either the vapor or solution phases; however, no changes in conductivity, spectroscopy or other factors were observed as a function of time after doping, indicating that subsequent diffusion of the dopant did not take place.

Determination of the P3HT monomer to dopant ratio required measuring the mass density of both pristine P3HT films and pure evaporated films of F_4TCNQ, which was carried out using a previously reported method.[108] The mass density of evaporated F_4TCNQ also was verified using a fresh quartz crystal microbalance (QCM) and surface profilometer. We found that the mass density of evaporated F_4TCNQ is only $0.77 \pm 0.06\,\mathrm{g\,cm^{-3}}$, about half that of the single-crystal density; a more detailed discussion of how we determined the precise amount of F_4TCNQ deposited by evaporation can be found in appendix A. Solution sequential doping proceeded via spin coating solutions of F_4TCNQ dissolved in dichloromethane (DCM) at specified concentrations onto pre-cast P3HT films at 4000 rpm for 10 s.

Grazing incidence wide angle X-ray scattering (GIWAXS) experiments were performed at the Stanford Synchrotron Radiation Lightsource on beamline 11-3 using an X-ray wavelength of 0.9742 Å, an incident angle of 0.12°, and a sample to 2-D charge-coupled device distance of 250 mm. All samples were irradiated for 90 s. 2-D diffractograms were radially integrated from 0-180° for full integration, 0-10° for in-plane curves, and 80-90° for out-of-plane curves. Curves were thickness normalized based on the pre-doping film thickness. This normalization was chosen because only the polymer thickness contributes to the diffraction intensity.

Four-point-probe based electrical conductivity measurements were performed under ambient conditions on samples fabricated as described above using the Van der Pauw geometry,[109] with silver paste electrodes placed at the corners of the $1.5 \times 1.5\,\mathrm{cm^2}$ square samples as in our previous work.[19,61] Electrical conductivities were determined by measuring the film thickness and sheet resistance, and the electrical conductivity was determined by dividing the reciprocal of the measured sheet resistance by the measured thickness of the doped film in centimeters.

For measurements of the thermovoltage/Seebeck coefficient, the samples were prepared in the same way as for the electrical conductivity measurements except the electrodes were fabricated by evaporating 15 nm of molybdenum oxide (MoO_3) to reduce the contact resistance followed by 60 nm of silver; these electrodes had a 6.6-mm spacing. The samples were placed at the interface of two commercial thermoelectric devices to establish a temperature difference between the two electrodes, generating a thermovoltage. We measured the thermovoltage generated at applied temperature differences ranging from 2 to 9 °C, and calculated the Seebeck coefficient as the slope of the best-fit line of the thermovoltage vs. temperature difference. Details of our home-built thermoelectric characterization setup and data analysis are further described in appendix A.

2.3 Results & Discussion

The main goal of this work is to understand the evaporation and solution sequential doping methods by comparing them on the same pre-cast conjugated polymer films using the same dopant. We seek to better understand any trade-offs that may exist between the two doping methods, and describe under what conditions if any, one method may be favored over the other. For both types of sequential doping, we investigate the limit of thick films, which are expected to function better for many applications, including thermoelectrics. The evaporation doping literature has only explored film thicknesses of a few tens of nm, and it is not yet clear if thick polymer films can be fully saturated with dopant by this method. Solution doping has been explored for thicker films using a multi-layer method,[100] and more recently, very thick P3HT films (10-40 µm) were demonstrated to be homogenously doped by soaking in solutions of dopant dissolved in acetonitrile for 72 hours.[110] It is still unclear if the method of soaking in a completely orthogonal solvent is reproducible, and how this method would extend to solution spin-coating which relies on semi-orthogonal swelling solvents in a single, concerted processing step. Here, we show that when properly tuned, both the evaporation and solution sequential doping methods are capable of doping films of surprisingly large thicknesses, yielding comparable conductivities and thermoelectric performance.

2.3.1 Sequential-Doping of P3HT by Thermal Evaporation

We begin our comparison by studying doping via thermal evaporation. For this method, we tracked the extent of doping via the thickness of F_4TCNQ deposited, as measured by a calibrated QCM. For the 25-nm thick polymer films, we explored a range of evaporated dopant thicknesses between 5 and 50 nm. For 110-nm thick P3HT films, we examined dopant thicknesses from 25 to 50 nm. Finally for 400-nm thick polymer films, our dopant deposition ranged from 25 to 200 nm. The evaporated doping thickness ranges were chosen to span a similar ratio of evaporated dopant thickness to pre-existing polymer film thickness.

The electrical conductivities of our evaporation-doped P3HT films are explored in Fig. 2.2 and Table 2.1. The blue circles/lines in Fig. 2.2a show that the conductivity of 25-nm pre-cast P3HT films is low when only small amounts of evaporated F_4TCNQ are employed, reaches a maximum with 15 nm of evaporated F_4TCNQ, and then decreases upon the evaporation of additional dopant. For 110-nm-thick P3HT films, the red circles/lines in panel b show that the optimal conductivity is reached using 40 nm of evaporated dopant. The increased thickness of dopant required to achieve the optimal conductivity makes sense given the greater pre-cast polymer film thickness: additional dopant is clearly required to optimally dope the additional polymer in the thicker film. For 400-nm-thick pre-cast P3HT films, the green circles/lines in Fig. 2.2c show that 150 nm of evaporated F_4TCNQ is needed to achieve the optimal conductivity. As far as we are aware, this represents the first time a P3HT film of this thickness has been successfully doped to saturation levels by the evaporation method. Previous work has shown that evaporated bulky dopants that are larger than F_4TCNQ can effectively diffuse through P3HT at room temperature, but only for 50-nm-thick P3HT films.[111] Our results here show that this diffusion holds for films at least eight times as thick.

Although we could have explored thicker films via evaporation sequential doping, we did not examine this limit since reaching the optimal conductivity would likely require evaporating hundreds of nm of F_4TCNQ, which becomes cost-prohibitive. Additionally, previous work indicates that evaporated F_4TCNQ better penetrates P3HT films if the temperature of the film is raised during the evaporation, although it is important to note that excessive heat can de-dope polymer films.[7,112] The data in Fig. 2.2 were taken on films that were actively cooled and held at 15 °C during evaporation. This suggests that evaporation doping should be readily applicable to even thicker films if heating were applied to increase the solid-state diffusion of the dopant into the polymer.

The conductivity values shown in Fig. 2.2 were calculated from the measured electrical sheet resistance using the measured film thickness after doping. In the limit of evaporating a large amounts of dopant, enough material was added that the thickness of the film increased significantly after doping. For example, Table 2.1 shows that the pre-cast 400-nm-thick P3HT with the optimal 150 nm of evaporated F_4TCNQ becomes 512 nm thick after doping. We surmise that at the highest evaporated doping thicknesses, not all of the dopant participates in the electrical conduction of the films; thus, in some sense, the ‘conductive thickness’ of the doped film is at most only that of the original pre-cast P3HT polymer. This strongly suggests that at the point of maximum conductivity, the largest possible number of P3HT units are doped, and that the addition of more dopant accomplishes little other than increasing the film thickness. As a result, the conductivity begins to decrease past the optimal evaporated dopant thickness simply because of the change in thickness.

Figure 2.2 and Table 2.1 also show that we obtain higher maximum conductivities with increasing thickness of the pre-cast P3HT films. As we will discuss further below, this is because the doped thicker films have a larger crystalline coherence length: this produces more delocalized carriers with higher mobilities by helping to increase the distance between the dopant counterion and the conductive hole on the polymer backbone.[43,61]

To gain further insight into the changes taking place in our P3HT films upon evaporation doping, Fig. 2.3 shows the UV-visible absorption spectrum of each of the films whose conductivities were explored in Fig. 2.2. The spectroscopy of F_4TCNQ-doped P3HT films has been explored previously by many groups,[19,23,29,35,61,113] and we show a reference spectrum of a doped film assigning the various features in appendix A. For purposes of the discussion here, we will focus on the P3HT neutral exciton absorption peak spanning the region from 2.0 to 2.8 eV and the overlapping P3HT P2 polaron and F_4TCNQ anion peaks near 1.6 eV.[19,113]

Figure 2.3 shows that for all three pre-cast P3HT film thicknesses, as the amount of evaporated dopant is increased, the amplitude of the P3HT neutral exciton absorption decreases while the amplitude of the overlapping P2 polaron and dopant anion absorption bands concomitantly increases. Moreover, the data also show that once we have passed the point of optimal conductivity for each film, a broad absorption centered near $\sim$3.1 eV appears due to the presence of neutral F_4TCNQ; appendix A shows the absorption spectrum of a pure film of evaporated F_4TCNQ for comparison. Figure 2.3 thus indicates that once the optimal conductivity is achieved, additional F_4TCNQ does

pre-cast P3HT (nm)	evaporated F_4TCNQ (nm)	doped P3HT film thickness (nm)	conductivity ($\mathrm{S\,cm^{-1}}$)	monomer : dopant ratio
25	5	25 ± 5	0.26 ± 0.02	N/A
	10	26 ± 5	0.67 ± 0.07	17 ± 1
	15	27 ±5	1.04 ± 0.07	8 ± 1
	20	33 ± 5	0.47 ± 0.03	5 ± 1
	25	45 ± 5	0.43 ± 0.04	4 ± 1
	35	53 ± 5	0.34 ± 0.02	2 ± 1
	50	70 ± 5	0.22 ± 0.03	2 ± 1
110	25	142 ± 5	0.57 ± 0.03	16 ± 1
	35	145 ± 5	1.74 ± 0.13	11 ± 1
	40	149 ±5	2.75 ± 0.14	9 ± 1
	50	154 ± 5	1.50 ± 0.14	7 ± 1
400	25	403 ± 5	0.00041 ± 0.00004	58 ± 4
	35	407 ± 5	0.019 ± 0.003	38 ± 3
	50	430 ± 5	0.18 ± 0.02	25 ± 3
	75	441 ± 5	1.52 ± 0.06	16 ± 1
	100	480 ± 5	2.22 ± 0.14	12 ± 1
	150	512 ± 5	4.20 ± 0.17	8 ± 1
	200	564 ± 5	3.52 ± 0.10	6 ± 1

Table 2.1: Summary of the conductivity for sequential doping of pre-cast P3HT films with different thicknesses. The conductivity values were calculated using the measured sheet resistance and thickness of the doped films. [1]These values calculated after subtracting initial 6 nm of overhead.

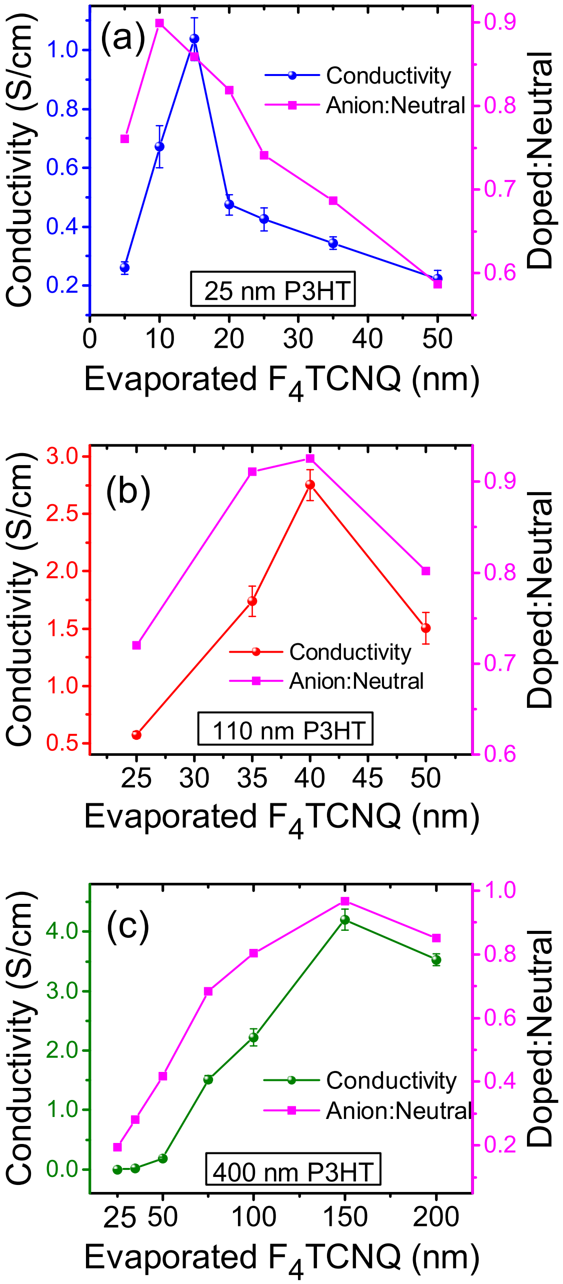

Figure 2.2: Conductivity (circles) measurements for (a) 25-nm pre-cast P3HT films (blue), (b) 110-nm pre-cast P3HT films (red), and (c) 400-nm pre-cast P3HT films (green) doped with different evaporated thicknesses of F_4TCNQ. The ratio of the optical absorbance at 1.6 eV to that at 2.4 eV (corresponding roughly to the amount of neutral material) for each film is plotted as the magenta squares (right axis); cf. Fig. 2.3. The optical absorption ratio empirically tracks the conductivity and reaches a peak of ∼0.9 at the optimal conductivity.

little except cake onto the surface of the film.

Figure 2.3 also shows that for all three pre-cast P3HT film thicknesses, the absorption spectra of the doped films with the optimal amount of evaporated F_4TCNQ for the best conductivity are essentially identical (other than their absolute absorptivities). In particular, we empirically see that the optimally-doped films always have a roughly 0.9:1 ratio of the absorbance at 1.6 to 2.4 eV: these two energies, respectively, correspond roughly to the amounts of doped and neutral material in the film. We note that deconvoluting the overlapping absorbances in this region[37] can be challenging because the spectrum and absorptivity of the polaron and anion species are environment-dependent,[19] but we see that the absorption ratio at these two wavelengths serves as an excellent proxy for determining the optimal degree of doping. We plot the ratio of the absorbance at 1.6 and 2.4 eV for each of our evaporated doped films as the magenta squares/lines in Fig. 2.2. Below, we will show that optimally-doped films created by solution sequential doping also have a similar absorbance ratio at these two energies. This indicates that this ratio corresponds to optimal doping in all situations for this materials combination. This suggests that when the amount of evaporated dopant cannot be readily controlled (such as in a home-made sublimation set-up), one could use the empirically-determined absorbance ratio at these two wavelengths as a useful proxy for determining the optimal amount of F_4TCNQ needed to dope a given P3HT film.

As summarized in Table 2.1, the 25-nm, 110-nm, and 400-nm pre-cast P3HT films require 15, 40, and 150 nm of evaporated F_4TCNQ, respectively, in order to achieve their optimal conductivity. When we examine the ratio of optimal evaporated dopant thickness to pre-cast polymer film thickness, we see that it is 0.36 and 0.38 for the 110-nm and 400-nm pre-cast films, respectively. This strongly suggests that there is an optimal doping ratio that is independent of the polymer film thickness. The 25-nm-thick pre-cast film, however, has a much higher evaporated dopant:polymer thickness ratio ($\sim$0.6) at the optimal conductivity point.

This discrepancy in dopant/polymer thickness ratio for the 25-nm P3HT film likely results from structural transitions that occur when P3HT is doped with F_4TCNQ.[29] As dopant is introduced into the polymer, it is well documented that the P3HT lamellar spacing becomes larger and the π-π stacking distance decreases,[19,61] a change that can be attributed to a reorientation of the P3HT chains with respect to the unit cell to accommodate the presence of the dopant in the lamellar

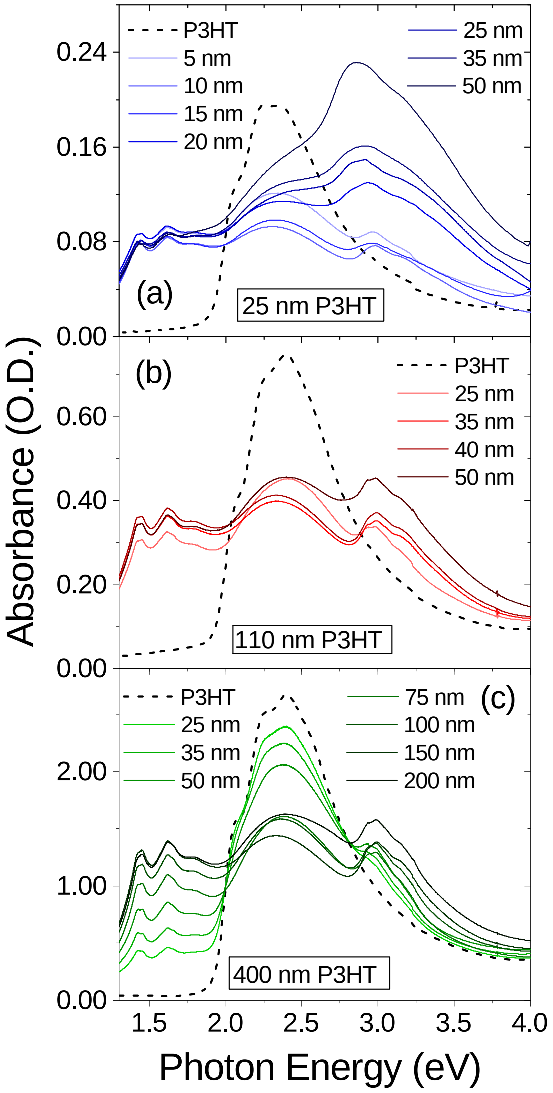

Figure 2.3: UV-visible absorbance spectra for (a) 25-nm pre-cast P3HT films (blue), (b) 110-nm pre-cast P3HT films (red), and (c) 400-nm pre-cast P3HT films (green) doped with varying thicknesses of evaporated F_4TCNQ; more saturated/darker colors correspond to thicker amounts of evaporated dopant. As the pre-cast P3HT film thickness is increased, an increasing thickness of evaporated F_4TCNQ is required to effectively dope the film. At the F_4TCNQ thickness for optimal electrical conductivity, the ratio of the absorbance at these two energies (plotted in Fig. 2.2) is ∼0.9:1. For all three P3HT film thicknesses, once the optimal conductivity point is passed, a new absorbance feature at 3.1 eV due to presence of neutral F_4TCNQ grows in, indicating that the ability to dope the film is saturated.

region of the film.[29] This makes it possible that there exists a threshold or "overhead" thickness of evaporated dopant that is required to induce or nucleate this structural transition, as discussed further in appendix A. It is also possible that this overhead thickness is required for filling trap states in the polymer film before an appreciable number of free carriers can be formed, although this would suggest that the overhead thickness would depend on the film thickness. An explanation in better agreement with our observations is that structural reorganization proceeds in a way similar to seeded crystal growth, where a minimum crystal size is required to initiate the process, at which point the structural reorganization may self-propagate as new dopants are added. We find that if the required "overhead" thickness of evaporated F_4TCNQ is 6 nm, we obtain an identical dopant-to-polymer thickness ratio of $\sim \frac{1}{3}$ for all three P3HT film thicknesses, as shown in appendix A.

We can take this idea of an optimal thickness ratio a step further and analyze the ratio of thiophene monomer units to ionized dopant molecules at the optimal doping concentration. Typically, this ratio has only been determined at very low doping levels when the dopant and polymer species were co-dissolved at carefully prescribed concentrations. At higher dopant concentrations, this ratio has been estimated based on the optical absorption of the polaron in the infrared region of the spectrum (the so-called P1 absorption).[23,58] Unfortunately, as mentioned above, the spectral position, shape and intensity of the P1 polaron absorption band changes with the degree of P3HT crystallinity because of a change in the average distance between the polaron and the counterion,[43,61] and the P2 polaron absorption overlaps with that of the F_4TCNQ anion. This makes the reliable determination of stoichiometric dopant ratios by optical methods a challenging task. This is especially true near the limit of saturation doping levels when both trapped and free polarons can be present.[19,114]

However, because our vapor-doping process uses a QCM thickness monitor *in-situ*, we have explicit knowledge of the mass of the added dopant during thin-film deposition. As described in appendix A, by measuring the evaporated F_4TCNQ and spin-coated P3HT film mass densities, we are able to determine the dopant/polymer stoichiometry based on the evaporated dopant thickness. The stoichiometric ratios for each evaporation are summarized in Table 2.1. We find that when excluding the measured "overhead" thickness of 6 nm, the optimum ratio of P3HT thiophene units to ionized F_4TCNQ dopants is ~8.5:1 for all P3HT film thicknesses.

Based on this information, we can draw two important conclusions about the evaporation doping process. First, it appears that small molecule dopants like F_4TCNQ are capable of interpenetrating films of P3HT of essentially any thickness. Second, it appears that there is little point to further doping beyond the optimal ratio of $\sim$8.5:1 thiophene units per ionized F_4TCNQ molecule. For dopant densities higher than optimal, we see an increase in absorption of the neutral F_4TCNQ species located at $\sim$3.1 eV, suggesting once saturation doping levels are reached, much of the additional F_4TCNQ does not undergo charge transfer. This observation is consistent with previous work that suggests at higher doping levels there is an increase in the creation of trapped carriers, suggesting that the optimal ratio is where the polymer crystallites become full with dopant.[114]

2.3.2 Sequential-Doping of P3HT by Solution-Processing

We continue our comparison of sequential doping methods in this section by exploring the properties of P3HT films doped via solution sequential doping. This involves spin-coating solutions of F_4TCNQ dissolved in dichloromethane at different concentrations on top of pre-cast P3HT films of different thicknesses. DCM is known to swell P3HT films without dissolving them, and it also has a reasonable solubility for F_4TCNQ, allowing mass action to drive the dopant into the swollen polymer underlayer.[90] In previous work, we have successfully used this method to dope P3HT films of roughly 100-nm thickness with F_4TCNQ,[19,44,61,90] and another group has developed a layer-by-layer version of solution doping to produce thicker doped films for thermoelectrics.[100]

We begin by investigating how the use of different F_4TCNQ solution concentrations (0.01 $\mathrm{mg\,mL^{-1}}$, 0.1 $\mathrm{mg\,mL^{-1}}$, and 1.0 $\mathrm{mg\,mL^{-1}}$) influence the resultant electrical conductivity of doped P3HT films with different thicknesses. Figure 2.4 shows that when using a 0.01 $\mathrm{mg\,mL^{-1}}$ F_4TCNQ solution (orange diamond), we are able to measure the conductivity of a pre-cast 25-nm-thick P3HT film, but thicker films show no measurable conductivity as they are exhaustively under-doped. When we increase the dopant concentration to 0.1 mg/mL (maroon squares), we see respectable conductivities ($\leq$1 $\mathrm{S\,cm^{-1}}$ for pre-cast 25-nm, 110-nm, and 400-nm thick P3HT films. Not until we use a 1.0 $\mathrm{mg\,mL^{-1}}$ F_4TCNQ solution, which is close to the F_4TCNQ solubility limit in DCM, we can effectively dope P3HT films with thicknesses ranging from 25 nm to 2 µm; these films all have conductivities above 1 $\mathrm{S\,cm^{-1}}$.

These results demonstrate that solution sequential doping can be used in a single step to optimize the conductivity of even very thick conjugated polymer films. Similar to our evaporation results, the thickest pre-cast P3HT films have the highest electrical conductivities, which we attribute below to greater polymer ordering and thus hole mobility. Although $\sim$1 µm-thick films of P3HT have previously been doped with tetrabutylammonium salts,[36] our results here represent, to the best of our knowledge, the thickest reported films of P3HT doped with F_4TCNQ.

Figure 2.5 presents the UV-visible absorption spectra of the solution-doped films, which show noticeably similar trends compared to the evaporation-doped films (Fig. 2.3): as the dopant concentration increases, the neutral P3HT peak intensity decreases while that of the F_4TCNQ anion/P2 polaron peak increases. Figure 2.5a shows that 25-nm-thick pre-cast P3HT films are already highly doped even when using a low solution F_4TCNQ concentration of 0.01 $\mathrm{mg\,mL^{-1}}$. When the dopant solution concentration is increased to 1.0 $\mathrm{mg\,mL^{-1}}$, we observe significant absorbance at 3.1 eV from neutral F_4TCNQ, indicating we are past the optimal doping point and have over-saturated the films with F_4TCNQ. For 110-nm-thick pre-cast P3HT films, Fig. 2.5b shows a similar trend, but at low dopant concentrations, the extent of doping is reduced. This fits with our expectation that additional polymer material requires additional dopant to achieve the same doping levels. Figure 2.5c indicates for 400-nm-thick pre-cast P3HT films, the extra polymer material necessitates the higher-concentration 1.0 $\mathrm{mg\,mL^{-1}}$ dopant solution to achieve sufficient doping levels. We were unable to perform UV-visible spectroscopy on 2 µm-thick P3HT films because their optical density exceeds 10. Although the concentration range investigated here is more coarse grained than that explored for vapor doping, it is worth discussing some final similarities and difference between the two methods. First, in the case where dopant is in high excess relative to the polymer, we see very similar absorption features in UV-Visible spectra. This is most clearly illustrated in panel a of Figures 2.3 and 2.5, where excess dopant produces very similar absorption profiles, independent of doping method. One marked difference we might expect between the two methods concerns the need for the overhead thickness to induce structural reordering, as in the case of vapor doping. Because polymer films swell during the solution doping process, it is plausible that the swelling solvent instead provides the impetus for the needed structural reordering, negating the need for an

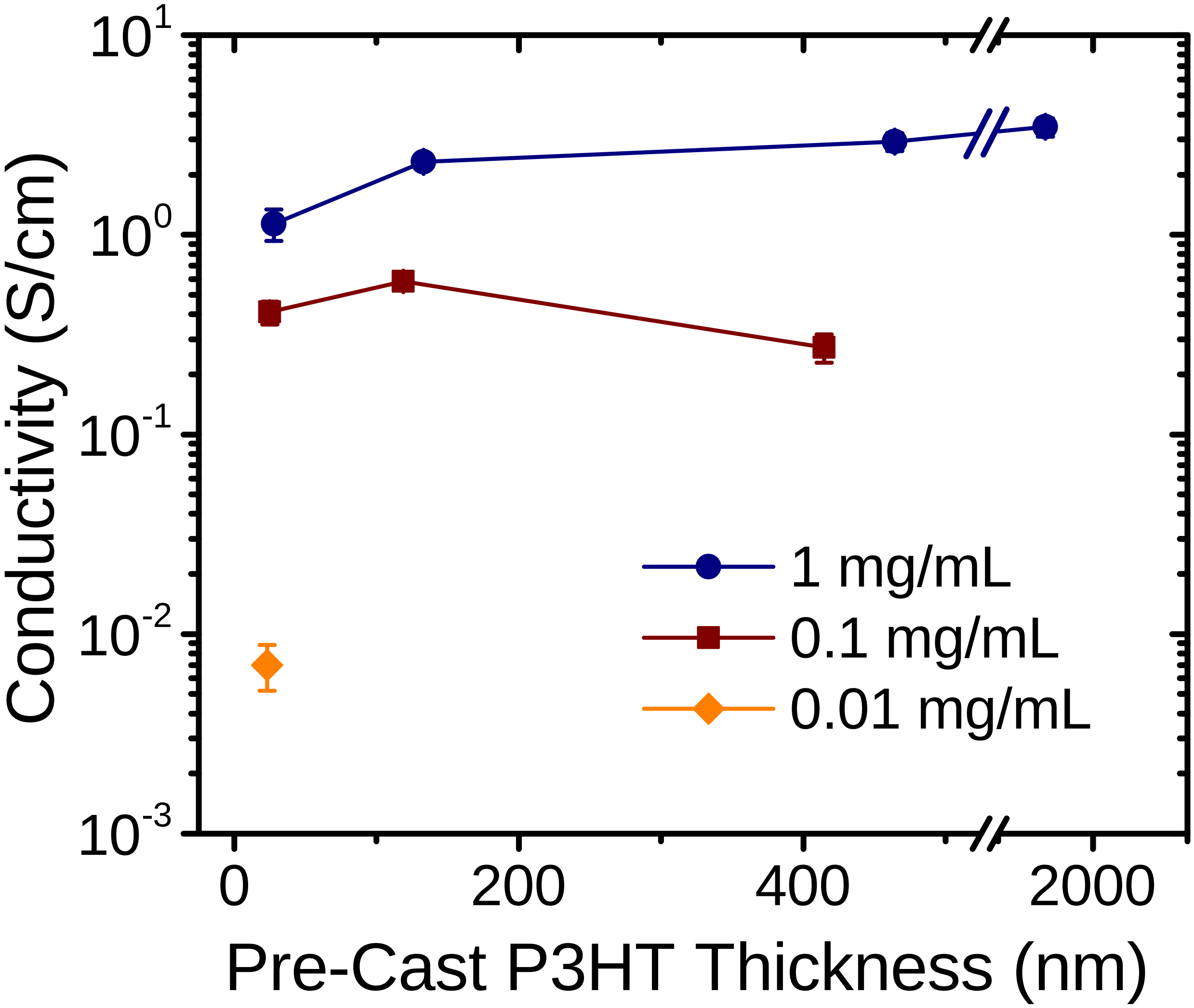

Figure 2.4: Conductivity measurements for solution-doped pre-cast P3HT films ranging in thickness from 25 nm to 2,000 nm. The films are solution-doped with $0.01\,\mathrm{mg\,mL^{-1}}$ **(orange diamond),** $0.1\,\mathrm{mg\,mL^{-1}}$ **(maroon squares), or** $1.0\,\mathrm{mg\,mL^{-1}}$ **(navy circles) solutions of** F_4**TCNQ in DCM. Film conductivity increases with increasing** F_4**TCNQ concentration until an optimal value is reached. Note the** *x***-axis scale break between 525 and 1,900 nm.**

overhead amount of dopant material. Again, adequately exploring the analogous doping regime for solution processing would require investigating a more finely spaced concentration range, and we leave this open to future work.

When we examine the UV-visible spectra in more detail, we see that the ratio of the doped material absorption peak at 1.6 eV to the neutral P3HT absorption peak at 2.4 eV is $\sim$1.1:1, which is very similar to the optimal ratio of $\sim$0.9:1 that we saw with evaporation doping. We note that the absorbance peak ratio for the 25-nm-thick film is lower, but this likely results from overlap of the neutral P3HT peak with the tail of the neutral F_4TCNQ absorption. Thus, the UV-visible absorption spectrum can serve as a guide to finding the optimal doping concentration for electrical conductivity by roughly matching the intensities of the neutral and doped P3HT absorbance peaks. This result follows in the same manner as our UV-visible results for evaporation-doped films, where the same ratio was observed for optimal electrical conductivity.

2.3.3 Structural & Infrared Characterization of Vapor & Solution-Doped P3HT Films

In order to better understand the relationship between film structure and the conductivity of our doped and undoped P3HT films, we used 2-D grazing-incidence wide-angle X-ray scattering (GIWAXS) to study films doped by both evaporation and solution sequential doping. In the data shown below, we study P3HT films at their optimal doping level for conductivity, as determined by the data in Figures 2.2 and 2.4.

Undoped P3HT is well known to prefer an edge-on orientation in films: the π-stacking or (010) diffraction peak appears in the in-plane direction and the lamellar or side-chain spacing (100) peak appears in the out-of-plane direction. Figure 2.6 shows representative 2D diffractograms for 110-nm-thick P3HT films. The data demonstrate that, as expected, the pre-cast films (panel a), solution-doped (panel b), and evaporation-doped (panel c) films have a preferentially edge-on orientation. We also show in Figs. A.5, A.7, and A.8 of appendix A that edge-on orientation is maintained for all other P3HT thicknesses of pre-cast and sequentially-doped films.

Previous work has shown that increased P3HT relative crystallinity (as measured by the (100) peak intensity) is correlated with increased conductivity in F_4TCNQ-doped films.[19,35,37,44,61] The

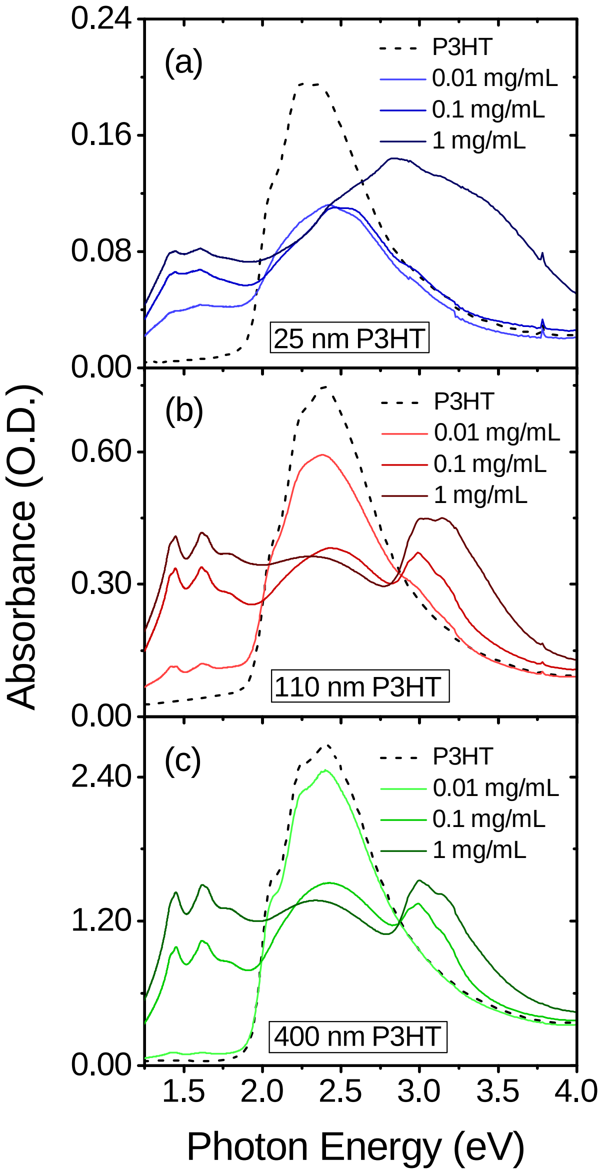

Figure 2.5: UV-visible absorption spectra for (a) 25-nm pre-cast P3HT films (blue), (b) 110-nm pre-cast P3HT films (red), and (c) 400-nm pre-cast P3HT films (green); as with Fig. 2.3, more saturated/darker colors correspond to increased dopant concentrations of $0.01\,\mathrm{mg\,mL^{-1}}$, $0.1\,\mathrm{mg\,mL^{-1}}$, and $1.0\,\mathrm{mg\,mL^{-1}}$. As the thickness of P3HT increases, an increasing concentration of F_4TCNQ is required to effectively dope the film, as indicated by the decrease of the P3HT neutral peak near 2.4 eV and the increase of the F_4TCNQ anion/polaron P2 peak near 1.6 eV. As with the evaporated doped films, the optimal electrical conductivity occurs when the doped:neutral ratio is $\sim$1.1. For all films in this thickness range, the doping becomes saturated at higher concentrations, as evidenced by the appearance of absorbance due to neutral F_4TCNQ peak near 3.1 eV.

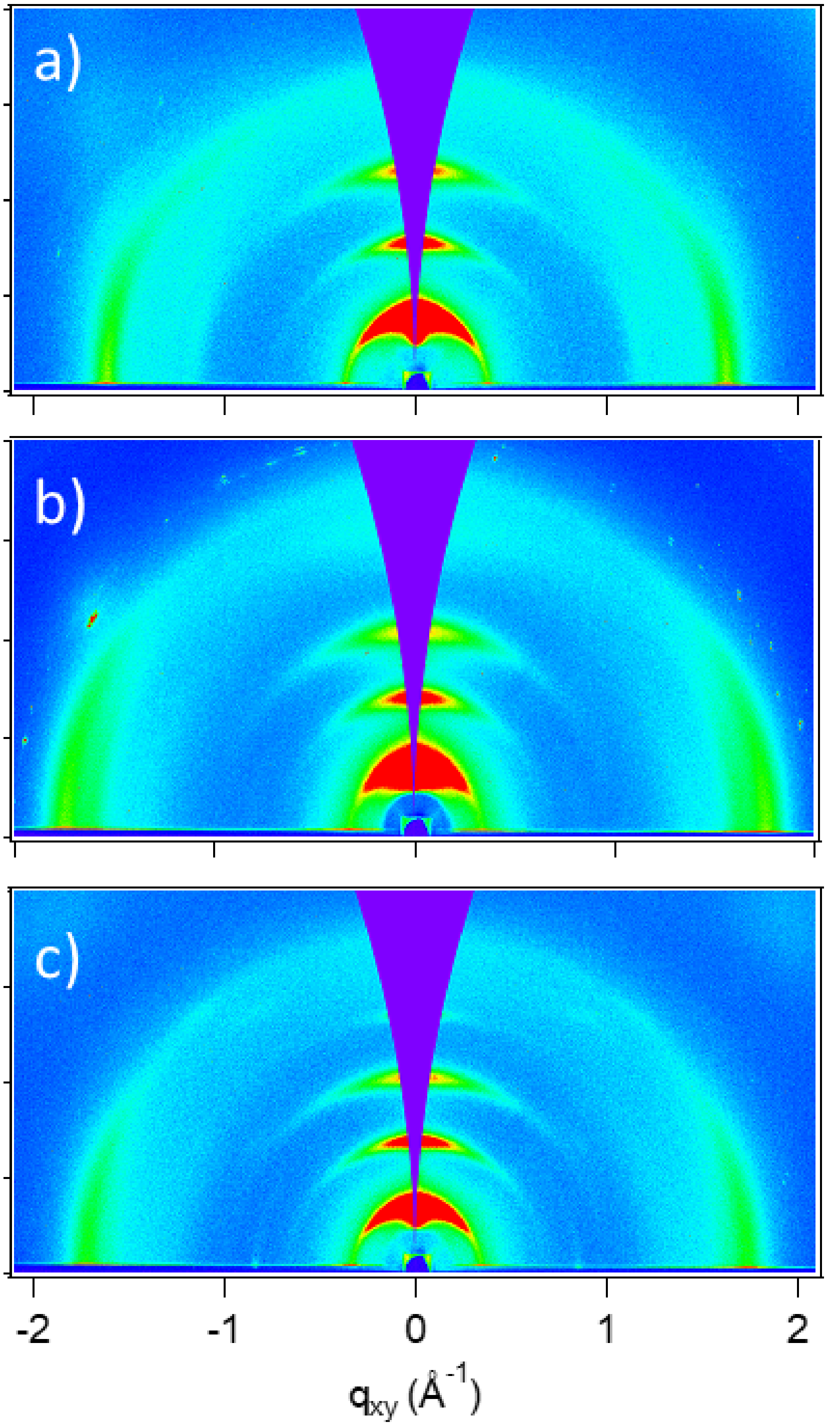

Figure 2.6: Representative 2-D diffractograms of 110-nm-thick P3HT films that are (a) undoped, (b) doped with F_4TCNQ via solution sequential processing, and (c) doped with F_4TCNQ via thermal evaporation. These results demonstrate that the natural edge-on orientation of the P3HT chains in undoped films is maintained following both methods of sequential doping.

origin of this increase lies in the fact that F_4TCNQ molecules located within crystalline domains sit between the side chains in the lamellar region, and are thus held fairly far from the polaron on the P3HT backbone. This distance decreases coulomb attractions between the polaron and the counterion, which is particularly important given the low dielectric constant of most conjugated polymers, thereby resulting in more mobile charge carriers.[43]

We note that simply integrating the (100) scattering peak is not the ideal way to determine the relative crystalline fraction of a P3HT film because other effects (overall structure factor, etc.) can modify this value, particularly for films with very different thicknesses. Table 2.2 summarizes the GIWAXS data for all of our pristine and sequentially-doped P3HT films. These data show that based simply on the thickness-normalized integrated (100) peak areas, the thicker and more conductive doped films in fact have less relative crystallinity. Moreover, the vapor-doped films show lower integrated (100) peak areas than the thickness-matched solution-doped films, despite the fact that vapor doping produces more conductive films (Figs. 2.2 and 2.4).

Since diffraction peak area alone cannot explain the conductivity trends we observe with the doping method or film thickness, we also investigated the relative degree of order of the crystalline regions, which is reflected in the GIWAXS crystalline coherence length and relative overtone strength.[115–117] Figure 2.7 shows that doping by either sequential method causes the lamellar (h00) peaks to shift to lower q, which corresponds to a larger d-spacing that better accommodates the F_4TCNQ anion, as expected.[29] However, the insets of Figure 2.7a and b demonstrate that vapor doping of P3HT also causes a (400) lamellar overtone to appear, which is particularly evident in thicker films. There is no sign of a new (400) peak for the equivalent solution-doped P3HT samples, in agreement with previously-published work,[19,34,35,42,44,61] indicating that this additional order is induced only by the vapor doping process.

Using the widths of the (h00) overtones, we calculated crystallite size or crystallite coherence lengths from the Scherrer equation.[118,119] The results in Table 2.2 show that for films thicker than 25 nm, vapor doping results in an increase in domain sizes compared to both solution-doped P3HT films and the original undoped P3HT films; for example, the vapor-doped samples where the (400) peak is observed have a crystalline coherence length calculated from the diffraction peak width of 14 nm, while our solution-doped films of equivalent thickness demonstrate a coherence

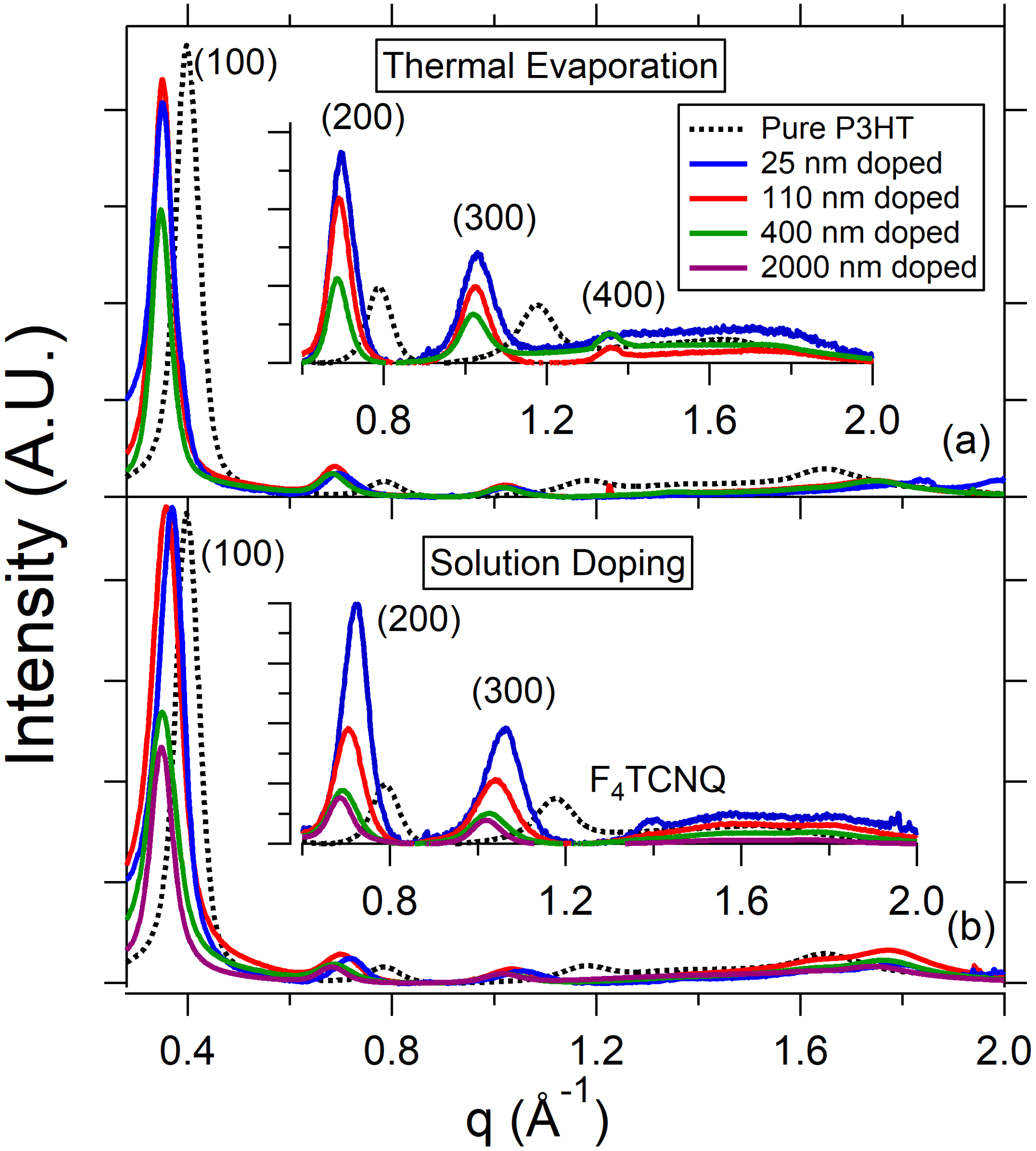

Figure 2.7: Full integrations of thickness-normalized 2-D GIWAXS diffractograms of P3HT films doped with F$_4$TCNQ via (a) thermal evaporation and (b) solution sequential processing. The data for undoped P3HT (dashed black curve) is shown for reference. Out-of-plane integrations are included in the expanded insets for clarity. The data show that 25-nm (blue) and 110-nm (red) films both largely maintain their original crystallinity after doping. For the 110-nm and 400-nm (green) vapor-doped films, a (400) overtone appears, indicating improved long-range order that correlates with higher carrier mobility and thus conductivity.

length of only 9 nm. This increased coherence length further corroborates the conclusion that the vapor-doped samples are more ordered than the solution-doped samples. The decrease in peak width and the increase in the number of observable overtones together indicate that doping increases the long-range order of P3HT films and that evaporative doping increases the long-range order of P3HT to a greater extent than solution doping.

pre-cast P3HT (nm)	doping method	(100) location (Å^{-1})	relative (100) area	(200) location (Å^{-1})	relative (200) area	coherence length	(100):(200) peak area ratio
25	None	0.39	1.0	0.78	1.0	9.3	29:1
	Solution	0.37	1.2	0.72	2.0	8.8	17:1
	Vapor	0.35	0.92	0.70	2.1	9.2	12:1
110	None	0.40	0.73	0.78	1.1	13	20:1
	Solution	0.36	0.97	0.70	3.0	9.0	10:1
	Vapor	0.35	0.55	0.69	1.8	14	8:1
400	None	0.40	0.83	0.78	1.3	11	18:1
	Solution	0.35	0.55	0.69	1.9	9.2	8:1
	Vapor	0.35	0.36	0.69	1.4	14	7:1
2000	None	0.40	0.51	0.80	0.83	13	17:1
	Solution	0.35	0.34	0.69	1.3	12	8:1

Table 2.2: Summary of the thickness-normalized GIWAXS data for pure P3HT, solution-doped P3HT, and vapor-doped P3HT films.

Figure 2.7 and Table 2.2 also show that although the peak widths are somewhat broader for solution-doped films compared to both undoped and vapor-doped films, the relative intensities of the overtone peaks is even higher than those from the vapor-doped material. This suggests that for the the P3HT/F$_4$TCNQ system, it is not the overall crystalline fraction that contributes to increased conductivity, but rather increased long-range ordering within the crystalline regions that correlates with increased conductivity, presumably because this best increases the average polaron-to-counterion distance.

To better explore the correlation between film structure and the resultant carrier properties, we measured the IR absorption spectrum of the P1 polaron transition for our 110-nm and 400-nm pre-cast P3HT films. We chose conditions for both solution and evaporation doping to achieve the optimal electrical conductivity at each thickness. Figure 2.8 shows that for the 400-nm-thick pre-cast P3HT films (blue curves), the main P1 band is red-shifted and the IR-active vibrations (IRAVs, which occur below 0.18 eV) have a higher intensity compared to the 110-nm-thick pre-cast films (red curves), independent of processing method.[120] A red-shifted P1 band and higher-absorption IRAV band are known to correlate with increased polaron delocalization and hence higher carrier mobility.[40,43,61,121,122] Thus, we see a direct correlation between the degree of polaron delocalization and conductivity, explaining why thicker films in general have higher conductivities.

2.3.4 Thermoelectric Properties of P3HT Films Prepared by Evaporation & Solution Sequential Doping

Having compared two methods for effectively sequentially doping P3HT films of varying thickness, we now turn to investigating how F_4TCNQ-doped P3HT films fabricated by the different routes function as thermoelectric materials up to 2 µm thick. Figure 2.9 presents the thermoelectric properties of the evaporation (black squares) and solution (red circles) doped P3HT films that yielded the highest electrical conductivities for each pre-cast film thickness. Panel a shows that the electrical conductivity increases with increasing pre-cast P3HT film thickness for both doping methods. As mentioned above, this is because the thicker P3HT films have a higher degree of delocalization, yielding higher-mobility carriers. The evaporation doped samples yield slightly higher conductivities at the same film thickness, which is due to slightly increased long-range order in the evaporation-derived materials. The UV-visible absorption spectra of these optimal-conductivity films are all quite similar, as shown in appendix A.

Figure 2.9b shows the Seebeck coefficients of the doped polymer films, which are determined by the magnitude of the thermovoltage produced for a given temperature gradient. The data show that the Seebeck coefficient decreases for the thicker, more conductive films. This trend agrees with the well-known anti-correlation between electrical conductivity and Seebeck coefficient, where the Seebeck coefficient is seen empirically to vary as electrical conductivity to the $-\frac{1}{4}$ power,[22,83] as shown in more detail in appendix A. Indeed, the Seebeck coefficients for the solution-doped films are higher than those for the evaporation-doped films, as expected from their slightly lower electrical conductivities. Furthermore, we note that the Seebeck coefficients we measure in the tens of $\mu V\,K^{-1}$ range are consistent with those found in other studies on thinner films of doped polythiophenes.[22,96]

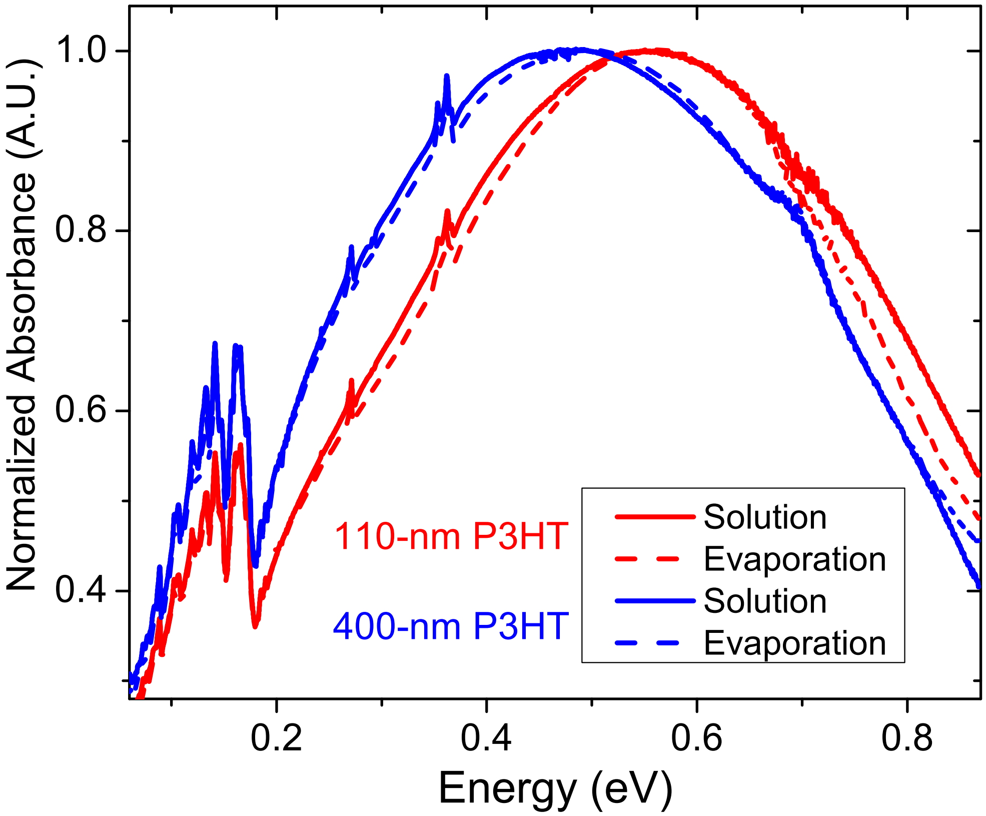

Figure 2.8: Absorption spectra of the P1 polaron transition for the doped 110-nm (red) and 400-nm (blue) pre-cast P3HT films. The films are doped by solution (solid lines) and evaporation (dashed lines) sequential doping; the doping conditions were selected to optimize the electrical conductivity. The P1 band for both the solution and evaporation sequentially-doped 400-nm pre-cast P3HT films are red-shifted, indicating greater polymer ordering that is correlated with a higher hole mobility.

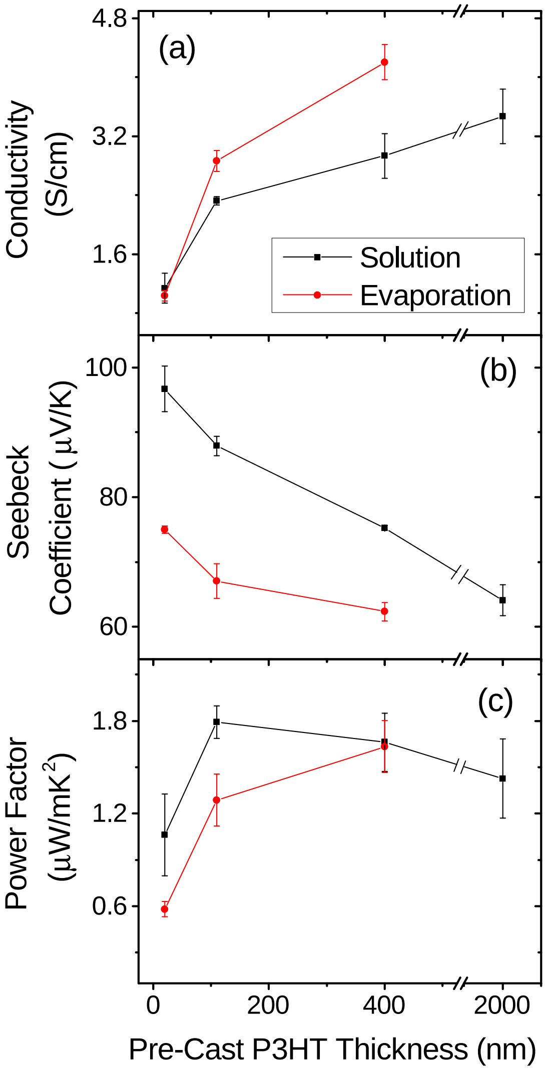

Figure 2.9: Thermoelectric properties of 25-nm, 110-nm, 400-nm, and 2000-nm pre-cast P3HT films doped with F_4TCNQ by solution (black squares) and evaporation (red circles) sequential processing. The processing conditions for each method were chosen to produce the most conductive films. For evaporation doping, the 25-nm, 110-nm, and 400-nm-thick pre-cast P3HT films were doped with 15 nm, 40 nm, and 150 nm of F_4TCNQ, respectively. For solution doping, all P3HT films were doped with a $1.0\,\mathrm{mg\,mL^{-1}}$ F_4TCNQ solution. (a) Thicker P3HT films have higher electrical conductivities than thinner films, and evaporation doping produces slightly higher conductivities than solution doping. (b) The Seebeck coefficient of doped P3HT films decreases with increasing film thickness, and solution doping yields slightly higher values than evaporation doping. (c) The thermoelectric power factors of all our doped P3HT films are similar, indicating that both processing techniques produce films equally well-suited for use in thermoelectrics. Note the scale break on the *x*-axis between 525 and 1,900 nm.

Finally, we calculated the thermoelectric power factor, which is the product of the electrical conductivity and the square of the Seebeck coefficient. The power factor, along with the thermal conductivity and the temperature, is the main measure of thermoelectric efficiency; we show the power factor for our doped P3HT films in Fig. 2.9c.[22,83] For all film thicknesses that we investigated, the devices show similar power factors on the order of 1–2 $\mu W\,m^{-1}\,K^{-2}$. The fact that the power factor holds for the 2 µm-thick film shows that solution sequential processing is an effective method for producing organic thermoelectric active layers.

Overall, we see that regardless of doping methodology, the thermoelectric properties of solution- and evaporation-doped polymer films are quite similar. Even though the two methods deliver the dopant in different ways, they both preserve the original P3HT film structure by doping in a sequential manner[19,34,42,61,90] and thus both offer potential for creating active layers for organic thermoelectrics. Overall, both evaporation and solution doping methods have distinct advantages, and our results show that one can use whichever method best suits the particular device fabrication needs: solution processing benefits from lower cost while evaporation methods might be more amenable for larger device areas.

2.4 Conclusions

In this paper, we demonstrate that sequential processing is a highly effective method for chemically doping conjugated polymer films by performing a direct comparison between identically-prepared evaporation and solution doped films. Sequential doping starts with a pre-cast polymer film, which is then doped either by thermally evaporating dopant or by spin-casting a solution of dopant on top of the polymer film. Both methods have the advantage of leaving the structure of the pre-cast polymer film roughly intact, and thus the methods give similar electrical conductivities with similar degrees of doping.

One key aspect of this work is our demonstration that both methods can be used to dope very thick semiconductor polymer films. For evaporation sequential doping, we demonstrated the ability to dope films up to 400 nm thick, and the doping of thicker films should be readily possible (particularly if heating is employed to improve diffusion of the dopant into the film), limited only by cost of evaporating large amounts of dopant. For solution sequential doping, we have shown that films up to 2 µm thick can be doped via spin-coating in a single processing step.

Evaporation doping results in improved long-range crystallinity, as evidenced by the development of a (400) lamellar overtone in GIWAXS, and increased crystalline coherence lengths, explaining why evaporation doping achieves slightly higher electrical conductivities than solution doping. Evaporation doping requires an "overhead" thickness of $\sim$6 nm, possibly to induce restructuring of the polymer crystal lattice to accommodate the dopant; once the overhead is complete, the optimal evaporated F_4TCNQ thickness is $\sim \frac{1}{3}$ the P3HT film thickness, resulting in a thiophene monomer:ionized dopant molecule ratio of $\sim$8.5:1. Solution doping, on the other hand, allows access to the doping of thicker films with a far more cost efficient use of material. However, finding the optimal solvent to dissolve the dopant and swell, but not dissolve the polymer may not be so straightforward with every polymer:dopant combination.

For both sequential doping methods, we find empirically that UV-visible absorption spectroscopy provides a good indication of when the optimal electrical conductivity has been achieved. Here we define optimal as the point where the ratio of the doped to neutral P3HT absorption approaches 1:1. When less dopant than the optimal is used, the films have poor conductivity because much of the polymer remains undoped. When more dopant than optimal is employed, the film conductivity decreases slightly, due to the fact that additional dopant either creates trapped carriers or does not dope at all. The increase in thickness that results from the presence of excess dopant causes a drop in conductivity. Thicker pre-cast P3HT films demonstrate higher electrical conductivities due to greater polymer long-range ordering, which increases the hole mobility.

Upon fabricating thermoelectric devices by both sequential doping methods, we find that their thermoelectric properties are quite similar regardless of which method is employed. For each polymer film thickness studied, the power factors fall across only a narrow range. This demonstrates that processing techniques that operate on fundamentally different principles can both be successfully applied to the fabrication of thermoelectric devices. Finally, although we have pushed the limit of sequential doping to 2 µm-thick films, it is clear that either technique could potentially be extended to still thicker films, which is something worth exploring in the future.

2.5 Supporting Information

Details on the device materials, doping fabrication procedures, UV–visible spectra, grazing incidence wide-angle X-ray scattering (GIWAXS) experiments and analysis, calculation of the F_4TCNQ overhead thickness, determination of the monomer:dopant ratio in evaporation-doped films, conductivity measurements, thermoelectric measurements, and Seebeck empirical power law fitting can all be found in appendix A.

2.6 Acknowledgements

This work was supported by the National Science Foundation under grant numbers CBET-1510353 and CHE-1608957.

CHAPTER 3

Controlling the Formation of Charge Transfer Complexes in Chemically Doped Semiconducting Polymers

3.1 Introduction

Conjugated organic semiconductors offer great promise as the active materials for applications in flexible electronics, including light emitting diodes, photovoltaics and thermoelectric devices.[22,63,64,123,124] For many of these applications, it is necessary to introduce equilibrium charge carriers into the π-systems of these materials. This is often achieved by chemical doping, which involves the introduction of a strong oxidizing (or reducing) agent to remove (or add) electrons from (to) an organic semiconductor. In organic light emitting diodes and photovoltaic cells, for example, chemical doping of an interfacial conjugated polymer layer can lower barriers and enhance charge injection. Additionally, for organic thermoelectric materials, doping dramatically affects both the Seebeck coefficient and the electrical conductivity, two of the factors that comprise the thermoelectric figure of merit.[22,55,125] Most organic semiconductors are *p*-type materials, so they are best doped by using strong oxidizing agents to remove electrons from the π-conjugated backbone.

The idea of chemical doping of organic semiconductors has its roots in the study of charge-transfer salts, which dates back to the 1970's.[126–128] The classic example of a charge-transfer salt is a mixture of tetrathiafulvalene (TTF) and 7,7,8,8-tetracyanoquinodimethane (TCNQ).[129] In such charge-transfer salts, acceptor molecules like TCNQ act as oxidizing agents, removing part of an electron from conjugated donors like TTF. The co-crystals are characterized by charge-transfer complexes (CTCs), which result in delocalized electronic states with a band structure that has the valence band predominantly derived from the donor HOMO and the conduction band from the acceptor LUMO.[130] Such charge-transfer salts can exhibit metallic behavior if they form in the right co-crystal structure and have sufficient driving force for charge separation (i.e., the energetic offset between the oxidation potential of the donor and the reduction potential of the acceptor is sufficiently large), both of which determine the fraction of an electron that is locally transferred from the donor to the acceptor.[128, 131]

Unlike the donors in small molecule charge-transfer salts, when solution-processable conjugated polymers are mixed with small-molecule oxidizing agents, the result is nearly always integer charge transfer (ICT);[2, 16, 17, 19, 21, 23, 29, 43, 61, 95, 132] the types of CTCs that are readily observed with small conjugated molecules in charge-transfer salts have been less commonly seen.[4, 6, 8, 9, 52, 133] In fact, one needs to go to great lengths to produce CTCs from chemically-doped conjugated polymers. For example, CTCs can be observed when the polymer and dopant are spun from a hot solution onto a pre-heated substrate,[6] or when branched side chains are employed to force the dopant counterion into specific locations in the polymer crystal lattice.[133] CTC's are usually not desirable for most doped conjugated polymer applications, since they produce a smaller fraction of doping-induced carriers than ICTs; thus, their relative rarity is generally advantageous.[134] But it is still not clear why ICT is favored when chemically doping conjugated polymers. This leads to the central question explored in this work: why do mixtures of acceptors with small-molecule donors, including the oligomers of many common conjugated polymers, usually produce CTCs,[5] while mixtures of conjugated polymers with the same acceptors usually lead to ICT?

To address this question, in this paper we re-examine the well-studied conjugated polymer, poly(3-hexylthiophene-2,5-diyl) (P3HT) doped with the strong electron acceptor 2,3,5,6-tetrafluoro-7,7,8,8-tetracyanoquinodimethane (F_4TCNQ) to gain new insights into the process of how conjugated polymers produce CTCs or undergo ICT upon chemical doping. We track the degree of charge transfer using a combination of UV-Visible spectroscopy, to monitor the electronic transitions produced following doping, and FTIR spectroscopy, to determine the amount of charge transferred from the polymer to the F_4TNCQ acceptor; we also monitor the structure of the doped films using 2-D grazing-incidence wide-angle x-ray scattering (GIWAXS). We find that we can control the relative amounts of CTCs and ICT that take place upon F_4TCNQ-doping of P3HT by using a tunable blend of solvents (dichloromethane, DCM, and chloroform, CF) to infiltrate the dopant into the polymer layer via sequential processing. Using pure DCM to deposit F_4TCNQ onto pre-cast

P3HT films, we see relatively little CTC formation, whereas the use of pure CF increases CTC formation by over an order of magnitude. Sequentially depositing the dopant from blends of DCM and CF allows the amount of CTC formed to be tuned anywhere in between.

With this control in hand, we now have a toolkit for studying CTC formation without resorting to extreme processing conditions or synthetically-modified conjugated polymers. This allows us to explore how different aspects of the materials and processing conditions affect the tendency to undergo CTC formation. In particular, we compare the use of evaporation doping (i.e., subliming the F_4TCNQ dopant onto pre-cast conjugated polymer film)[11] to the typical solution-based sequential doping method to investigate the role of dopant transport on CTC formation. We then study the role of the pre-formed polymer film crystallinity to elucidate the preference of crystalline and amorphous polymer domains to participate in CTC formation.

P3HT films are always comprised of some combination of crystalline and amorphous regions, we find that the more crystalline a P3HT film is prior to sequential doping, the smaller the fraction of CTC states generated. However, we also find that CTC doping cannot be entirely eliminated, even for the most crystalline P3HT films, showing that there is still room to improve sequential doping methods. We also show that doping via vapor transport produces a smaller fraction of CTC states relative to solution sequential doping, providing significant clues to the role of kinetics in forming CTC states.

The structure of most conjugated polymers consists of semi-crystalline regions characterized by a π-stacking spacing between the polymer backbones and a lamellar spacing along the polymer side chains. We and other research groups have argued in previous work that dopant molecules prefer to reside in the polymer lamellae, as the barrier to dopant insertion into the easily disordered side-chains is lower than breaking up the polymer π-stacks to insert the dopant.[2,19,29,55,61] Placing dopants in the lamellae, where they reside far from the polymer backbone, leads to ICT, as there is insufficient wave function overlap between the donor and acceptor for CTC formation to take place. Instead, CTC states only occur when the F_4TCNQ dopant is able to π-stack with the conjugated polymer.[6,8,9,52,133] These results lead us to an improved picture of the kinetic competition between the two doping mechanisms, where the choice of processing conditions can alter the kinetic barrier for placing dopants in the polymer π-stacks. All the results explain how solvent blends and polymer crystallinity can control the preference for ICT vs. CTC formation in doped conjugated polymers, and why CTC is the preferred doping mechanism in small-molecule charge-transfer salts.

Finally, we show that ICT is not only kinetically preferred, but is also thermodynamically favored for the F_4TCNQ/P3HT combination of dopant and conjugated polymer. By exposing doped films to brief thermal annealing treatments, we find that the fraction of CTCs produced upon doping can be converted to ICT, further indicating that CTCs are kinetically trapped in doped conjugated polymer films. Overall, our work shows the steps that can be taken to minimize CTC formation for electronic applications (or to enhance CTC formation for study), including increasing the polymer crystallinity and using dopants that physically cannot π-stack or have wave function mixing with the conjugated polymer backbone.[43, 61]

3.2 Experimental Section

3.2.1 Materials

Electronic-grade P3HT (4002-EE; 91-94%, M_w = 46-57 kg/mol, PDI = 2.3) was purchased from Rieke Metals and sublimation-grade F_4TCNQ (purity >98%) was purchased from TCI America. The synthesis and preparation of the P3HT denoted "100% RR" has been described by us in prior work.[61] All materials and solvents were used as received without any further purification.

3.2.2 Fabrication and Doping of Polymer Films

Glass and silicon substrates were first degreased by sequentially sonicating for ten minutes in a detergent solution, deionized water, acetone, and finally isopropyl alcohol. Substrates were then dried and stored in a nitrogen glove box where all subsequent solution processing steps takes place. For experiments using doping solvent blends, thin films of P3HT were prepared by spin-coating a polymer solution ($20\,\mathrm{mg\,mL^{-1}}$) out of *o*-dichlorobenzene (ODCB)) at 1000 rpm for 20 s. Directly after spin-coating, the still wet films were moved to an open petri dish until finished drying. All dopant solutions of F_4TCNQ ($1\,\mathrm{mg\,mL^{-1}}$) for the set of solvent blends containing chloroform (CF) and dichloromethane (DCM) were generated by adding the desired volume of each solvent to a vial with F_4TCNQ powder. Sequential doping was carried out by pipetting dopant solution solvent blends (100 µL) onto pristine P3HT films and spin-coating at 4000 rpm for 10 s to remove excess material. Additional experimental details can be found in appendix B.

For the experiments comparing the vapor and solution sequential doping methods, 110 nm and 400 nm thick pristine P3HT films were prepared by spin-coating from 20 $\mathrm{mg\,mL^{-1}}$ and 50 $\mathrm{mg\,mL^{-1}}$ ODCB solutions respectively at 1000 rpm for 60 s followed by 3000 rpm for 5 s. Sequential solution doping with F_4TCNQ was carried out by pipetting 100 µL of dopant solution out of DCM (1 $\mathrm{mg\,mL^{-1}}$) onto pristine P3HT films and spin-coating at 4000 rpm for 10 s to remove excess material. Sequential vapor doping with F_4TCNQ was carried out using an Angstrom Engineering Nexdep Physical Vapor Deposition System. F_4TCNQ powder was placed in an alumina crucible and evaporated at 0.5 $\mathrm{Å\,s^{-1}}$ with a base pressure $< 1 \times 10^{-6}$ Torr. Pristine P3HT films were placed on a rotating stage that was actively cooled to 15 °C during deposition. Doping levels for the vapor process were optimized to produce the highest conductivity and to show comparable doping levels to the solution-processed samples. A more detailed discussion can be found in chapter 2 and appendix A.

For our work comparing doped P3HT films with tunable crystallinity, we used solvent evaporation kinetics to control the rate of P3HT film formation, where higher-boiling point solvents yield higher-crystallinity polymer films. To obtain P3HT films with relatively low crystallinity, P3HT solutions (10 $\mathrm{mg\,mL^{-1}}$) were spin-coated from chloroform (CF) (b.p. = 61.2 °C) at 1000 rpm for 60 s. For films of intermediate crystallinity, P3HT solutions (20 $\mathrm{mg\,mL^{-1}}$) were spin-coated from *o*-dichlorobenzene (ODCB) (b.p. = 180 °C) at 1160 rpm for 20 s. These still wet films were then placed in a covered petri dish to further extend the drying period. Finally for films with the highest degree of crystallinity, an in-house batch of P3HT with a regioregularity of essentially unity was employed. The same spin-coating procedure was used for this material as for the commercial material cast from ODCB with the exception that solutions were spincoated out hot at 60 °C to prevent aggregation. Additional details on film preparation, synthesis and characterization can be found in our earlier work[61] and its supporting information.

3.2.3 GIWAXS Measurements of Doped Polymer Films

2-D GIWAXS data were collected at the Stanford Synchrotron Radiation Lightsource using beamline 11-3. The beam wavelength was 0.9742 Å and the incidence angle was 0.12 °. The sample chamber was flowed with helium to reduce noise and the sample holder was 250 mm away from the detector. All the samples were irradiated for 90 s. To reduce the 2-D diffractograms, we used the WAXStools in Igor Pro. The diffractograms were radially integrated to reduce to 1-D diffraction curves (0-10° for out-of-plane, 80-90° for in-plane and 0-90° for full). All the samples at a given doping condition were made and measured in triplicate to ensure the reproducibility and absolute scattering intensity. All diffractograms were thickness-normalized (after background subtraction) to the polymer film thickness prior to doping with F_4TCNQ since only the polymer contributes to the diffraction intensity. Additional details can be found in appendix B.

3.3 Results & Discussion

One of the most common ways to produce chemically-doped polymer films is by solution sequential processing, where the dopant is infiltrated into a pre-cast conjugated polymer film using a semi-orthogonal solvent that swells but does not dissolve the underlying morphology.[19,61] Sequential doping is generally preferred because simply mixing the polymer and dopant together results in solution-phase charge transfer, creating a salt with unfavorable solubility in the non-polar organic solvents typically used to dissolve conjugated polymers. The resulting blend solutions are usually highly aggregated, leading to poor quality when cast into films.[19] Sequential processing avoids this difficulty because the doped films largely have the same morphology as the original pre-cast films, providing the added advantage that the pre-cast polymer film can be created with different degrees of crystallinity[19,61] or rubbed to produce alignment of the polymer chains.[29,55,68] Sequential doping can also involve thermally evaporating the dopant onto a pre-cast polymer film,[21,34,35,37,42,51] which allows for effective infiltration of the dopant, even into polymer films that are hundreds of nm thick.[11]

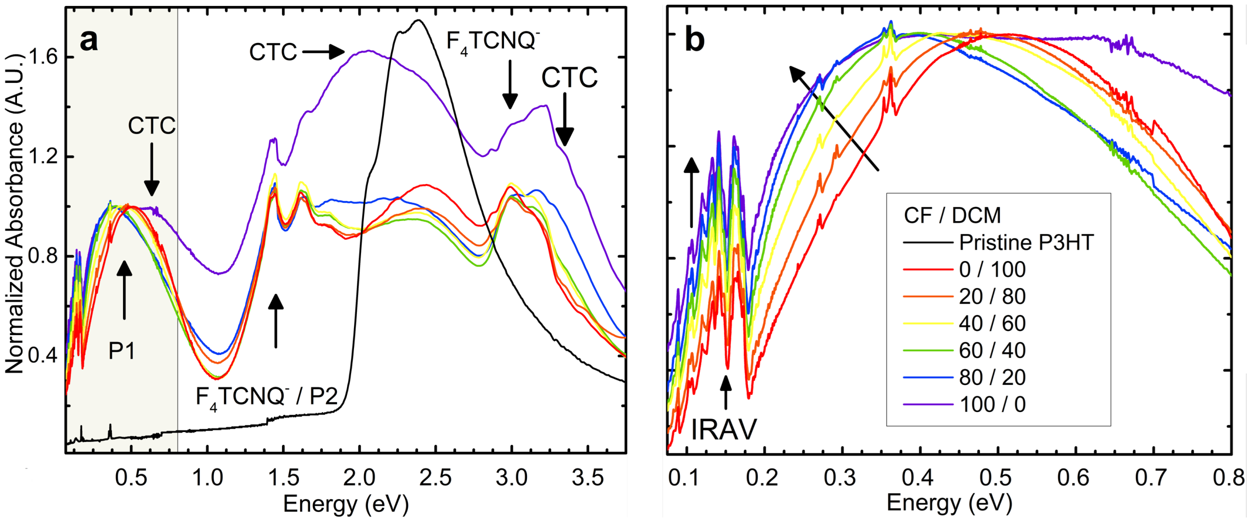

Figure 3.1: (a) UV-vis-NIR absorption spectrum of 1 mg mL^{-1} F$_4$TCNQ sequentially-doped P3HT films with the dopant deposited from solvent blends with different CF/DCM ratios, normalized to the peak absorption for the main P1 band near 0.4 eV. The electronic transitions from the CTC phase are labelled, along with the standard absorption features that appear with ICT. For comparison, the black curve shows the absorption of a P3HT film prior to doping, scaled to the correct relative absorption intensity of the film doped using 100% DCM (red curve). (b) Zoom-in of the NIR P1 polaron absorption of P3HT films sequentially doped with F$_4$TCNQ from solvent blends with the indicated CF/DCM ratio by volume; this data corresponds to the section shaded in gray in panel a. The black arrows highlight the increased intensity of the IRAV band and the monotonic redshift of the main P1 peak absorption with increasing CF content of the dopant casting solvent, indicative of increased polaron delocalization. The absorbance for pristine P3HT is essentially zero in this part of the spectrum and has thus been omitted for clarity.

3.3.1 Optical Transitions of P3HT:F_4TNCQ Charge-Transfer Complexes

When using solution sequential processing to dope a conjugated polymer, the solvent selected to introduce the dopant is usually chosen to have poor solubility for the underlying polymer; however, in principle, any solvent with a reasonably high solubility for the dopant can be used. For the P3HT/F_4TCNQ system, we have shown that DCM is a particularly good solvent for solution sequential processing due to its reasonably high solubility towards F_4TCNQ and relatively low solubility ($0.818\,\mathrm{mg\,mL^{-1}}$) towards P3HT.[11, 19, 44, 61, 135]

Based on this idea, it would seem that a solvent like CF, which has one of the highest known solubilities towards P3HT ($38\,\mathrm{mg\,mL^{-1}}$),[135] would be a poor choice for doping via solution sequential processing. This is because at first glance, CF would be expected to dissolve the underlying polymer and thus remove the entire P3HT film from the substrate during the doping process. What we will show below, however, is that when sequentially doping P3HT, the high dissolving power of CF does put some of the underlying P3HT film into solution while the F_4TCNQ is being introduced, effectively removing any kinetic barriers to placing the dopant in the polymer π-stacks. At the same time, the rapid change in polymer solubility that occurs upon doping still allows most of the polymer material to remain intact on the substrate through a dynamic dissolution and reprecipitation process during doping.

Our first sign that using CF to sequentially dope P3HT with F_4TCNQ produces a different electronic species comes from UV-Vis-NIR spectroscopy. Figure 3.1 shows the results when DCM, CF and various blends of the two solvents (which are miscible) are used to expose pre-cast films of P3HT to $1\,\mathrm{mg\,mL^{-1}}$ solutions of F_4TCNQ. The full spectra are plotted in Fig. 3.1a, with the IR region focusing on the so-called P1 band (lowest-energy electronic transition) of the P3HT polaron shown on an expanded scale in Fig. 3.1b. The spectra in both panels are normalized to the height of the absorption maximum near 0.4 eV and further experimental details can be found in appendix B.

The red curves in Fig. 3.1 show the results when pure DCM is used as a dopant processing solvent. As is well known, doping P3HT this way leads to a reduced intensity of the neutral P3HT exciton absorption near 2.3 eV (black curve) as electrons are removed from the polymer valence band. Doping also leads to the appearance of a new band with two sharp vibronic features near

1.5 eV, which are representative of the F_4TCNQ anion produced by ICT, along with the so-called P2 absorption band of the oxidized polymer that appears in the same energetic location. Finally, doping and ICT lead to a new absorption with peaks at 0.16 and $\sim$0.4 eV, corresponding to the infrared active vibrations (IRAV band) and the P1 band of the hole (or polaron) on the polymer, respectively. The relative intensities of the P2/F_4TCNQ^{-1} peak, the P1 band, and the remaining neutral P3HT absorption are all comparable in magnitude. In previous work, we found that with sequential doping, there is a maximal amount of F_4TCNQ that can be intercalated into a pre-existing polymer film, no matter how high the doping solution concentration. The spectral signature for reaching this 'saturation doping' is seen when the P1, P2/F_4TCNQ^- and neutral P3HT bands are all comparable in absorbance, as is the case for these samples.[11]

With the exception of the film doped using pure CF, the other colored curves in Fig. 3.1 show that using blends of DCM and CF to dope the P3HT film with F_4TCNQ leads to the generally-accepted ICT doping behavior. However, for the solvent blend comprised of 80% CF and 20% DCM (blue curves), there is a noticeable increase in absorption near 0.7, 2.0 and 3.3 eV, which further increase when casting F_4TCNQ from pure CF (purple curves). The three new features all match well with what has been observed previously for CTC formation by Jacobs et al. for this system when hot solution mixtures of P3HT and F_4TCNQ and hot substrates and pipette tips were used to create doped films.[6] These workers were able to isolate a structurally novel polymorph associated with these electronic features,[6] which we show below is also present in our films doped sequentially from CF. Thus, Fig. 3.1 shows that changing the solvent blend used for doping allows for control over the relative amount of CTC formation.

The results in Fig. 3.1 can further be compared to work from Thomas et al., who showed that F_4TCNQ doping can produce CTC states in a polythiophene derivative whose conjugated backbone is identical to that of P3HT, but with branched ethyl-hexyl side chains.[133] The bulkier side chains prevent F_4TCNQ molecules from residing in their typically preferred location in the lamellar regions of the P3HT crystallites, leading to an absorption spectrum that resembles that seen with hot solvent casting by Jacobs et al.[6] and that of the purple curve in Fig. 3.1. Thus the UV-Vis-NIR spectrum in Fig. 3.1a strongly suggests that the elevated solubilzing power of CF has a similar effect to high-temperature-prolonged solvation of both species, allowing them to assemble into a polymorph with π-stacked charge transfer interactions that are separate from the typical ICT geometries seen for doped conjugated polymers. In addition, the relative intensity of the CTC absorption features to the P1 polaron peak seen for the pure CF processed condition further indicates a substantial fraction of the F_4TCNQ molecules in the film are no longer undergoing ICT and are instead doping via CTC formation. It is tempting to attempt to use the measured spectra to quantitatively extract information about the overall doping level and/or the ratio of ICT to CTC carriers for each set of processing conditions. However, because these films are doped via sequential deposition, we do not quantitatively know the overall doping level. We have established previously[19] that there is overlapping peak intensity of the F_4TCNQ anion with other absorbing species, and unfortunately, we do not know the cross-section for any of the absorbing species in doped P3HT films. This makes it problematic to use absorption spectroscopy directly to quantify the doped species. Despite this, we will show in Section 3.3.2 below, that we can obtain good estimates of carrier concentrations from spectroscopy via a more indirect method.

Figure 3.1b also shows that increasing CF content produces a monotonic redshift of the main P1 absorbance peak near 0.4 eV that is concomitant with an increase in the relative intensity of the IRAV modes located near 0.16 eV, as highlighted by the black arrows. These two spectral features are hallmarks of greater polaron delocalization and increased carrier mobility.[40, 61, 122] We believe that this results from a solvent annealing effect. CF (b.p. = 61.2 °C) has a higher boiling point than DCM (b.p. = 39.6 °C), and the extra drying time and increased P3HT solubility during spin coating likely gives P3HT crystallites more time to order, as we will demonstrate using GIWAXS data in Section 3.3 below. It is also possible that the more soluble disordered polymer regions, corresponding to more blue-shifted P1 absorption, are the most likely to be dissolved away upon exposure to CF. Together, this means that increasing CF content when depositing F_4TCNQ both increases the formation of CTCs but also makes those remaining carriers produced via ICT even more mobile.

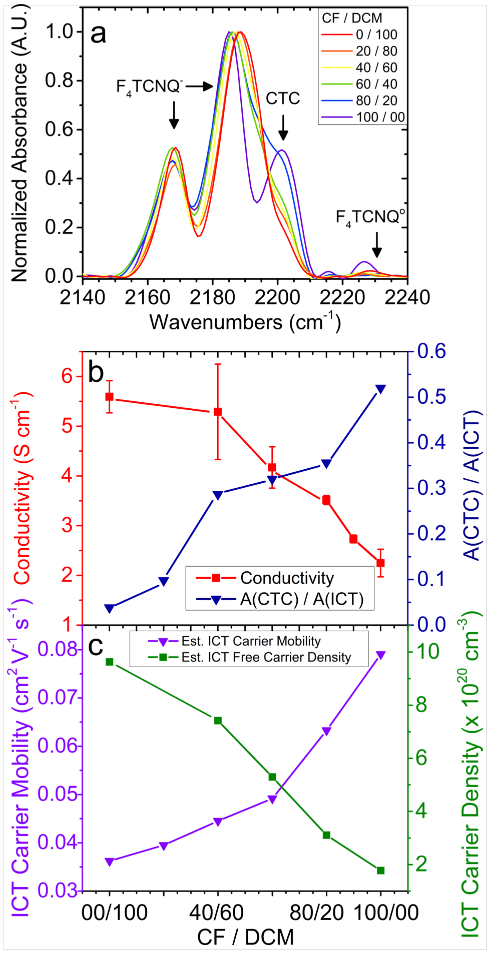

Figure 3.2: (a) Infrared absorbance of the C≡N stretching modes of F_4TCNQ-doped P3HT films as the dopant is introduced sequentially from solvent blends containing various CF/DCM ratios. The CTC peak at $2201\,\mathrm{cm}^{-1}$ shows a monotonic increase in relative amplitude as the fraction of CF is increased for the doping solvent. (b) Electrical conductivity (red squares) plotted against the fraction of CF in the doping solvent blend. A monotonic decrease in conductivity is observed as an increasing proportion of CF is used in the doping solvent, despite the fact that the carriers produced by ICT are becoming more mobile. The ratio of integrated infrared peak area for the CTC peak at $2201\,\mathrm{cm}^{-1}$ to that of the integrated peak area of the central ICT infrared band located near 2185 cm^{-1} (blue triangles), both taken from the data in panel a. (c) Estimated ICT carrier mobility (purple triangles), calculated as described in appendix B and Ref. 2 using the energy of the P1 polaron band peak absorbance. The estimated ICT carrier density (green squares) was calculated from the estimated mobility and electrical conductivity. Clearly, the presence of CTC states is strongly anticorrelated with the doped film ICT carrier density.

3.3.2 Quantifying CTC Formation Using the F_4TCNQ C≡N IR Stretching Modes

Two features make the F_4TCNQ C≡N vibrational modes particularly well suited for studying CTC formation: (1) the fact that the frequency of C≡N stretches are known to be highly sensitive to the local coulombic environment,[10,136] and (2) the fact that the C≡N stretch frequencies occur near 2200 cm^{-1}, which places them in an IR spectral window that is largely absent of other vibrational modes. Although neutral F_4TCNQ has a vibration that weakly absorbs near 2227 cm^{-1}, the fully anionic species produced by ICT undergoes a mode softening, bringing the vibrational frequency down to $\sim$2190 cm^{-1}, as shown in Fig. 3.2a. Because the energy of the C≡N stretching mode is highly dependent on the charge state of the dopant molecule, FTIR is better suited than UV-Vis-NIR for quantifying the abundance of partial charge transfer states since the F_4TCNQ stretching vibrational energy associated with CTCs appears at intermediate stretching frequencies just above 2200 cm^{-1}.[6,8,9] For the case when pure CF is used as the casting solvent, the purple curve in Fig. 3.2a shows a well-defined peak at 2201 cm^{-1}, clearly revealing the presence of a large fraction of CTC states for this dopant casting condition.

Consistent with the electronic indications of CTC formation from the UV-Vis-NIR in Fig. 3.1, Fig. 3.2a shows that as the fraction of CF is increased in the dopant casting solvent blend, the fraction of CTC states in the doped films also increases. Surprisingly, however, even when using pure DCM as the dopant casting solvent, the presence of the CTC peak near 2201 cm^{-1} never disappears. The ratio of CTC to ICT states, taken from the integrated peak areas in the IR spectrum and plotted as the blue curve in Fig. 3.2b, reaches 0.04, but never zero. This suggests that for sequential solution doping, there is always a small population of CTC states formed alongside the more predominant ICT phase when doping P3HT with F_4TCNQ.

It is worth pointing out that the corresponding electronic transitions for the small fraction of CTC states produced at low CF fractions are not readily identifiable in the corresponding UV-Vis-NIR spectra. This is due to the already-crowded nature of the electronic spectrum, the small population of CTCs generated for these doping conditions, and the fact that the CTC electronic absorption features likely have lower cross-sections than the corresponding ICT features. However, using the integrated area peak fits from the FTIR spectra, we find that the CTC content can be controllably varied in these doped films by a factor of just over 10 as the fraction of CF in the dopant casting solvent is tuned from zero to 100%.

To better understand how the presence of CTCs affects the electronic properties of F_4TCNQ-doped P3HT films, we also probed the in-plane conductivity of the various doped P3HT films. Fig. 3.2b (red squares) shows the electrical conductivity of the films as a function of CF composition in the doping solvent blend. A monotonic decrease in electrical conductivity is observed, going from 5.6 ± 0.3 S cm^{-1} when using pure DCM, down to 2.3 ± 0.3 S cm^{-1} when using pure CF as the casting solvent, a $\sim$60% reduction in electrical conductivity.

It is well known that the electrical conductivity is given by, $\sigma = pe\mu$, where μ is the free carrier mobility, p is the free carrier density and e is the fundamental charge. Recently, we performed an analysis based on AC Hall effect measurements to show that for P3HT, the energetic location of the P1 polaron band is strongly correlated with the free charge carrier mobility.[2] Thus, we can use this correlation, along with the measured electrical conductivity and P1 peak position, to estimate the free carrier density and mobility in our doped P3HT films as a function of CF fraction in the solvent used to infiltrate the F_4TCNQ dopant. The precise way we accomplish this is described in both Ref. 2, and appendix B, and the results are shown in Fig. 3.2c

The purple triangles in Fig. 3.2c show that as the fraction of CF in the dopant solution is increased, the estimated free carrier mobility actually increases from $0.036\,\mathrm{cm^2V^{-1}s^{-1}}$ for pure DCM, up to $0.8\,\mathrm{cm^2V^{-1}s^{-1}}$ when using pure CF. These values are well within the range of Hall mobilities that have been measured previously for similarly doped P3HT films.[2,43,61] Given that the electrical conductivity decreases with increasing CF fraction, the increase in free carrier mobility reflects a strong decrease, over 80%, in the density of free carriers produced by ICT, shown as green squares/right axis in Fig. 3.2c. We note that we spent a great deal of time attempting to quantify the CTC carrier concentration in these films from absorption, but this is challenging to do accurately because we do not know the cross-sections of either the vibrational or electronic transitions of either the F_4TCNQ anion or the CTCs. However, if we assume a similar total dopant loading density across this series of doped P3HT samples, then the drop in free carrier concentration suggests a CTC dopant concentration of roughly 8×10^{20} cm^{-3}. Thus, free carriers created by ICT become more mobile with the use of CF as a doping solvent, but the overall electrical conductivity still drops due to the fact that free carriers produced by integer charge transfer are lost via conversion into CTCs.

Overall, IR spectroscopy and electrical conductivity shows that the use of solvent blends in seqential doping affords a high degree of control over the relative population of CTCs compared to ICTs. Simply changing the amount of CF in the solvent used to infiltrate F_4TCNQ into a P3HT film is enough to control the amount of CTCs present, allowing us to study their electronic, vibrational and structural properties. The fact that we cannot entirely eliminate CTC formation, however, even using pure DCM as the dopant casting solvent, means that there is still significant room to improve the electrical properties of doped conjugated polymer films.

3.3.3 The Structure of P3HT:F_4TCNQ CTCs via Grazing Incidence Wide Angle X-ray Scattering

To understand the local structures of the crystalline ICT and CTC states, we used 2-D GIWAXS to probe films sequentially doped from different-composition CF/DCM solvent blends. P3HT is well-known to lie edge-on to the substrate, with its side chains oriented normal to the substrate and its π-π stacking oriented in the plane of the film (Fig. 3.3a). Pristine P3HT has a monoclinic crystal structure where the angle of π-π stacking is tilted with respect to unit cell *b* axis (Fig. 3.3g).[137]

Upon doping P3HT with F_4TCNQ, Fig. 3.3b shows that the overall edge-on orientation is preserved, while Fig. 3.3d (red curve labelled ICT) shows that the lamellar scattering peak shifts to lower q. The red curve in Fig. 3.3e shows that the π-π stacking peak splits into two, with one peak remaining near the original location and a new peak appearing at higher q.[2,29,34,43,55,61] All of these shifts result from a rearrangement of the P3HT crystal structure upon doping, caused by the incorporation of F_4TCNQ into the side-chain regions of the P3HT crystallites. The added F_4TCNQ volume causes a reduction in the tilting of the π-π stacking direction with respect to the *b* axis and thus a reduction in the π spacing, as shown in Fig. 3.3h.[29]

The fact that the dopants prefer to reside in the polymer lamellae (even for dopants that are physically larger than the lamellar spacing)[2,43] is important for helping to physically separate polarons from their counterions following ICT. This is because the low dielectric constant of organic semiconductors does a poor job of screening the interaction between the charge carriers on the polymer backbone and the dopant counteranion. When the dopant counterion in a crystallite is located among the polymer side chains, it is physically as far from the holes on the polymer backbone as possible, allowing the holes to move more freely.[40,43,61,122] Despite the preference for dopants to occupy the lamellae and thus be physically separated from the polaron, it has been estimated that only 5 to 10% of holes generated by doping P3HT with F_4TCNQ become free charge carriers.[2,16]

In contrast to the ubiquitous formation of ICT states when paired with semiconducting polymers, F_4TCNQ usually shows fractional charge transfer when combined with small organic donor molecules, forming CTCs as mentioned earlier.[138–140] Depending on the packing geometry and driving force for charge transfer, the degree of charge transfer can vary from 0 to 1.[131] Similarly, both experimental[5] and theoretical[141] work show that conjugated oligomers also have a tendency to π-stack with F_4TCNQ, which means that oligomers show very different structural behavior when compared to their polymeric counterparts comprised of the same monomer.[142]

This leads us again to the question of why CTCs form readily in charge-transfer salts, but much less so in doped conjugated polymers.[6,8,9,52,133] As discussed above, increasing the polymer solubility by casting at high temperatures[6] or forcing dopants out of the lamellae with branched side chains[133] can facilitate CTC formation. Moreover, Neelamraju et al. found that CTC formation can be the preferred doping mechanism in regiorandom P3HT, which is a highly amorphous material compared to the regioregular P3HT material studied in this work.[8]

The spectroscopic characterization presented above shows evidence for the co-existence of ICT and CTC states in P3HT films sequentially doped with F_4TCNQ using CF/DCM solvent blends. Here, we draw similar conclusions based on structural evidence derived from GIWAXS. We find that changes in the diffraction patterns emerge as the CF ratio of the doping solvent increases, as seen in Figures 3.3a-c, (intermediate CF/DCM ratios are shown in Fig. B6 in appendix B). As the fraction CF in the doping solvent is increased, both the peak positions and widths evolve. In particular, when P3HT is doped using CF (Fig. 3.3c), the scattering shows unusual broadening of both the lamellar and π-stacking peaks. In addition, thickness-normalized data in Fig. S8 shows that the films become less edge-on with higher CF ratios in the doping solvent.

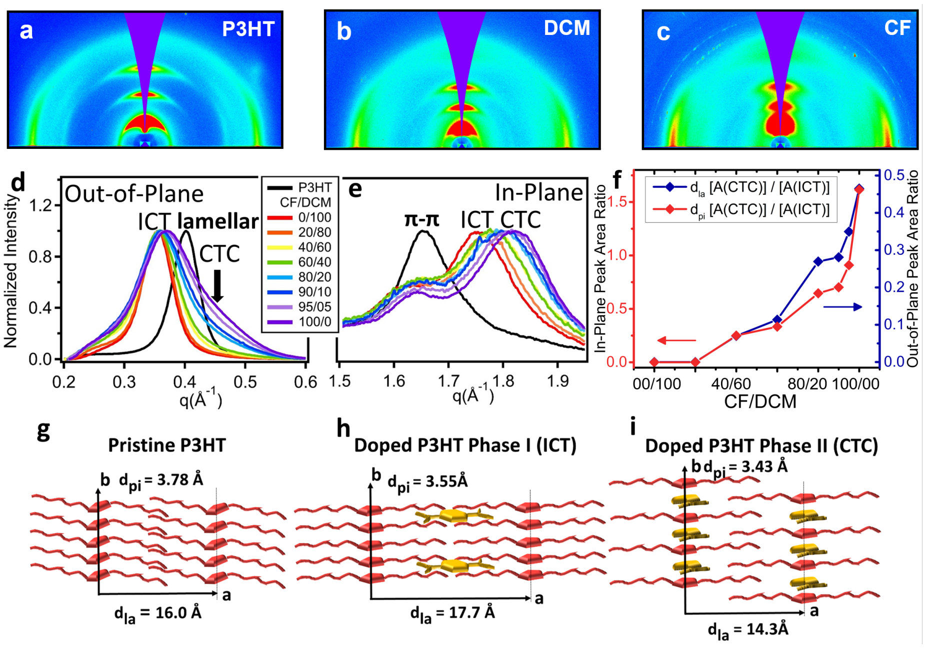

Figure 3.3: 2-D GIWAXS diffractograms for films of: (a) pristine P3HT, (b) P3HT sequentially doped with F_4TCNQ from 100% DCM, (c) and doped from 100% CF. All samples maintain their edge-on orientation, but the peak positions, widths and texture all change with doping and with the particular doping solvent composition. (d) Normalized out-of-plane and (e) in-plane integrations of thickness-normalized 2-D GIWAXS diffractograms of P3HT sequentially doped with F_4TCNQ from blend solvents with different ratios of CF and DCM. The in-plane scattering from the π-stacking region in panel (e) shows a continuous shift to higher q and a broadening of the peak width as the CF fraction is increased. The out-of-plane scattering in the lamellar region in panel (d) shows that with increasing CF ratio, a new peak appears at higher q. (f) Integrated GIWAXS peak area ratios for the CTC (phase II) relative to the ICT (phase I) structures, for both the out-of-plane lamellar (blue points) and in-plane π-stacking (red points) peaks. The structural trends match with what we deduced from the infrared C≡N stretch vibrations in Fig. 3.2b. (g) Cartoon of the pristine P3HT crystal structure showing that the b direction is not precisely parallel to the π-stacking direction. (h) Cartoon of the ICT (phase I polymorph) structure of doped P3HT, showing how F_4TCNQ resides in the lamellar region of the crystallites and rearranges the unit cell, resulting in a decreased π distance (d_{pi}) and increased lamellar distance (d_{la}). (i) Cartoon of the CTC (phase II polymorph) structure of P3HT doped with F_4TCNQ. Because the incorporation kinetics are changed when CF is used as the dopant solvent, F_4TCNQ is capable of π stacking with the P3HT backbone, forming an interdigitated lamellar structure with decreased lamellar and tighter π-stacking distances.

To better display the structural changes that take place upon doping, Figs. 3.3d and e show radially-integrated 1-D curves from the corresponding 2-D scattering patterns. Panel d shows normalized out-of-plane integrations for the lamellar peak for different doping solvent blends. When P3HT is doped with F_4TCNQ using DCM as the casting solvent (red curve), the peak from the pristine material (black curve) shifts to lower q (higher d spacing), as expected for intercalation of F_4TCNQ into the crystalline lamellae.[29,61] As the fraction of CF in the doping solvent increases, the ICT lamellar peak remains in the same shifted position, but a shoulder grows in at higher q, which fits best to a single new peak appearing around 0.44 $Å^{-1}$ (see Fig. B7a in appendix B for more details on fitting). This new peak can be assigned to the fundamental lamellar spacing of the CTC phase.[6]

Figure 3.3e shows the normalized in-plane integration in the π-stacking region for the same series of doped P3HT films. Here, we see that when pure DCM is used as the doping solvent (red curve), the original undoped π peak (black curve) decreases in intensity while a new π peak rises at 1.66 $Å^{-1}$, as expected when F_4TCNQ occupies the lamellar region of the crystallites.[29,61] As the fraction of CF in the doping solvent increases, the doped-phase π-stacking peak appears to shift to higher q and slightly broadens. A detailed analysis shows that this results from changes in intensity of two underlying peaks: the original doped lower-q peak at 1.66 $Å^{-1}$ (ICT peak) decreases in intensity while a second peak from the CTC phase appears at 1.84 $Å^{-1}$ when high fractions of CF are used (see Fig. B7b in appendix B for fits).

Both the out-of-plane lamellar peak at 0.44 $Å^{-1}$ and the in-plane π-stacking peak at 1.84 $Å^{-1}$ closely resemble those of the CTC polymorph described by Jacobs et al.[6] This provides structural confirmation that tuning the fraction of CF in the doping solvent controllably introduces a second polymorph of doped P3HT (labelled phase II in Fig. 3.3i), which co-exists with the more familiar ICT phase I structure (Fig. 3.3h). Since the new phase II shows a decrease in lamellar packing distance as well as a further decrease in π-π distance, we assign it to a CTC structure where F_4TCNQ π-stacks with thiophene rings on the P3HT backbone and the side chains become further interlocked.[6]

We note that in previous works, ICT was incorrectly postulated to take place via a π stacking arrangement.[17,143] This makes the structural data presented here and in Ref. 6 interesting in that we can definitively correlate P3HT polymorphs with the F_4TCNQ dopant occupying either the lamellar or the π stacks to two unique charge transfer interactions with distinct spectroscopic and electronic properties.

With the caveat that GIWAXS only reports on the crystalline regions of a sample (and we know there can be significant amounts of F_4TCNQ in the amorphous regions at high doping concentrations),[43,67,114] we can use the ratio of the integrated peak areas for each of the two phases to estimate their relative abundance. Figure 2.7f shows the ratio of the CTC and corresponding ICT peaks for both the lamellar (blue data points) and π-stacking (red data points) regions. The ratios of the two different peaks change in a similar fashion with increasing CF fraction, verifying that they are indeed reporting on the same new phase.

We believe that this results from the fact that CF's high dissolving power is capable of swelling and disrupting the P3HT crystallite structure to a much greater extent than DCM during the sequential doping process. This disruption allows F_4TCNQ to intercalate between the P3HT π-stacks, producing the phase II polymorph associated with CTC doping. The appearance of the new phase monitored by GIWAXS also closely matches that monitored by the infrared absorbance of the C≡N stretch of the F_4TCNQ, as shown in Fig. 3.2b. Interestingly, the diffraction peak area ratio in Fig. 3.3f rises somewhat more gradually than the IR peak area ratio, suggesting that CTC states formed at lower CF fractions occur with higher probability in disordered regions of the polymer, and thus affect the GIWAXS data less strongly than the IR absorption.

One additional question is whether the red shift in the P1 band observed in Fig. 3.1b can be correlated with structural changes observed in GIWAXS. Figures B.6 and B.7 in appendix B show a systematic decrease in ICT scattering intensity with increasing CF fraction at all compositions below 100% CF. This decrease is likely due to the conversion of ICT states to CTC states. At 100% CF, the intensity jumps up, indicating that despite significant CTC formation, the total crystallinity is also increasing. The fact that high CF fractions can dramatically crystallize formerly amorphous regions of the polymer is compatible with the idea that smaller amounts of CF can more subtly increase order in the already-crystalline regions, helping to explain the red shift of the P1 peak observed in Fig. 3.1b.

3.3.4 Dopant Infiltration Method & CTC Formation

Now that we have established that CF content can be used to tune the relative amounts of ICT and CTC formation in F_4TCNQ-doped P3HT films, we next explore the effects of different dopant infiltration methods. In previous work, our group performed a head-to-head comparison of sequential doping using solution vs. evaporation deposition.[11] Evaporation, or vapor doping, involves exposing a pre-cast polymer film to a flux of dopant vapor created by sublimation. We found that vapor doping is every bit as effective as solution doping, even for very thick polymer films, and that vapor doping does a slightly better job of preserving the underlying crystallinity of the polymer film than solution doping.[11]

Figure 3.4 shows the IR absorption of two sets of sequentially-doped P3HT films; one set based on underlying films of 110-nm thickness (red curves) and a second set based on underlying films of 400-nm thickness (blue curves). We have shown previously that due to the spin-coating conditions for the pure material, the 400-nm-thick films have a higher total crystallinity compared to the 110-nm-thick films.[11] We then doped each set of films with F_4TCNQ both by solution processing (solid curves), using 100% DCM as a casting solvent ($1\,\mathrm{mg\,ml^{-1}}$), as well as by vapor deposition (dashed curves) in an evaporator equipped with a QCM thickness monitor to achieve comparable doping levels. The increased IRAV absorption and red-shift of the P1 band of the 400-nm-thick films seen in Fig. 3.4a makes clear that the thicker films have a greater degree of polaron delocalization, and thus increased degree of order.[40,122] Figure 3.4a also shows that choice of sequential doping method has almost no effect on the degree of delocalization.

Figure 3.4b shows the FTIR spectra of these same films in the F_4TCNQ C≡N stretching region. Unlike the electronic absorption, the FTIR data shows pronounced differences depending on the sequential processing method employed. The biggest difference is in the relative amplitude of the CTC band at $2201\,\mathrm{cm^{-1}}$, which is significantly higher for solution doping with DCM compared to evaporation doping. This suggests that evaporation doping goes further toward eliminating undesirable CTC formation than solution doping, independent of the initial degree of film crystallinity. From the perspective of kinetics, solution doping is much more effective at disrupting the existing P3HT π stacks and thus at facilitating the insertion of CTC dopants. On

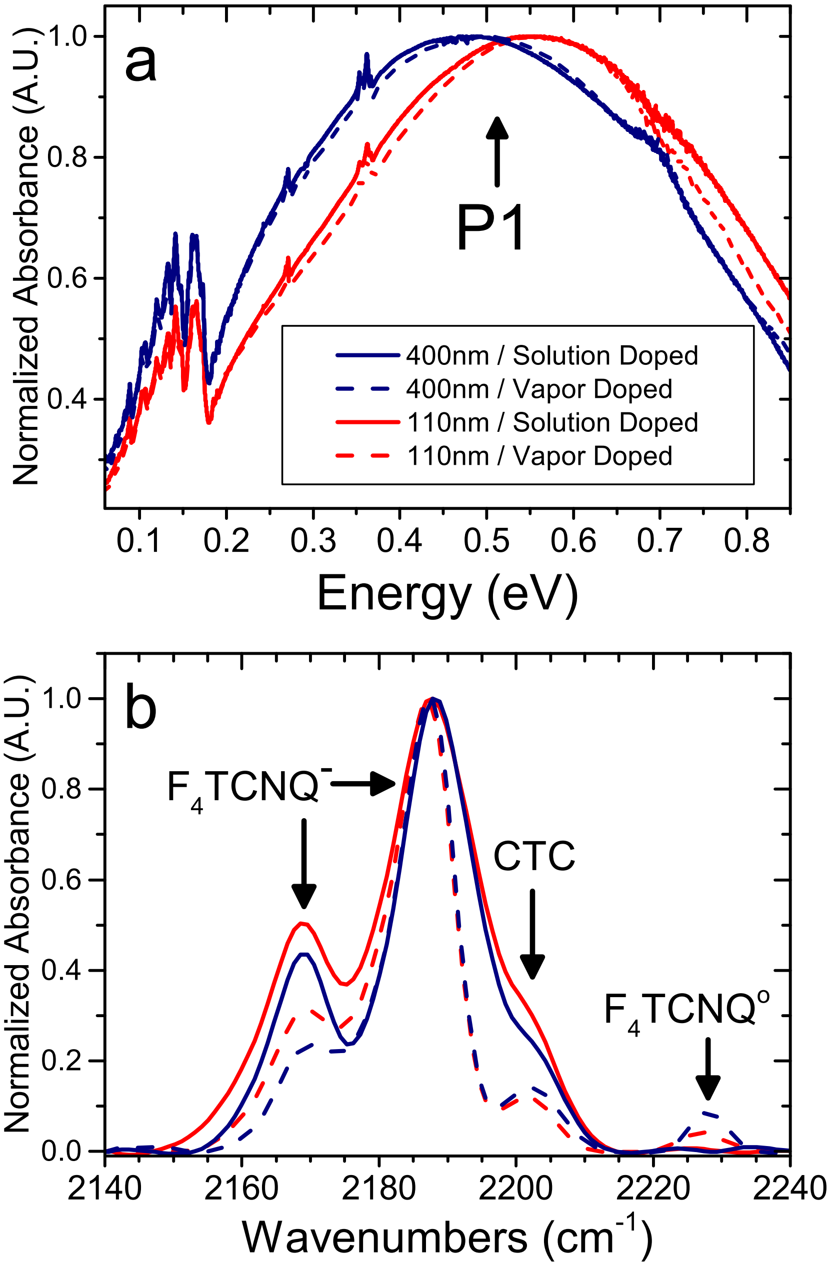

Figure 3.4: **(a) FTIR absorption spectra normalized against max P1 intensity for a set of 400 nm thick (blue curves) and 110 nm thick (red curves) doped P3HT samples. Solid curves designate films treated by sequential solution doping with F_4TCNQ at $1\,\mathrm{mg\,mL^{-1}}$ from DCM. Dashed curves designate films doped with F_4TCNQ by vapor transport. (b) An inset view of the same set of spectra shown in a) replotted in the wavenumber range for the C≡N stretching modes. In panel a, the small set of peaks centered near $\sim 0.27\,\mathrm{eV}$ on the P1 spectrum correspond to absorption of the F_4TCNQ vibrational modes.**

the other hand, vapor transport is a minimally invasive processing technique during which P3HT π stacks are less likely to be disrupted, causing CTC doping to be largely relegated to the amorphous polymer regions. In addition, the vapor-doped films show remarkably narrow ICT C≡N stretching modes, suggesting a more homogeneous population of ICT states. Overall, the data show that the choice of doping method can also control the extent of CTC formation, which may be important for many applications.

3.3.5 The Role of P3HT Crystallinity in CTC Formation

One of the strongest advantages of sequential doping is that it allows for a degree of control over the total crystallinity of a doped polymer film.[11,61] Since the polymer layer is deposited first in sequential doping, the processing conditions (choice of solvent, spin speed, thermal annealing, etc.) can be chosen to enhance or reduce crystallinity as desired. In previous work, we examined how controlling the crystallinity of pre-cast P3HT films affected the electrical and optical properties after sequentially doping with F_4TCNQ.[61]

Here, we follow those same methods to prepare P3HT films of identical thickness with three different degrees of crystallinity, whose (undoped) UV-Visible absorption spectra are shown in Fig. 3.5a. First, we cast the initial P3HT film from CF (prior to doping), which is a rapidly-evaporating solvent that produces substantially more disordered, lower crystallinity films than traditional aromatic solvents used for polymer deposition (teal curve). The relatively low crystallinity is easily verified by the lack of vibronic structure in the UV-Vis[144,145] as well as by GIWAXS.[61] Second, we cast the P3HT films using our standard high boiling point solvent *o*-dichlorobenzene (ODCB) (orange curve), producing higher-crystallinity films, as evident by both GIWAXS[61] and by the presence of vibronic structure in the UV-Visible absorption spectrum. Finally, very high crystallinity films were obtained using a specially-synthesized batch of P3HT with nearly 100% regioregularity,[146] also cast from ODCB (blue curve).

Figure 3.5b shows the UV-Vis-NIR absorption spectra of the same three films as panel a after solution sequential doping with F_4TCNQ using pure DCM ($1\,\mathrm{mg\,mL^{-1}}$) as a casting solvent. As expected, the films with higher crystallinity show a red-shifted main P1 band near 0.4 eV and an increased relative IRAV band intensity near 0.16 eV.[2,40,43,61,122] The electrical conductivity, carrier mobility, free carrier concentration and GIWAXS of films produced this way all have been discussed in our previous work; the electrical conductivity of the most crystalline film conditions is roughly seven times higher than that of the least crystalline, as a direct result of improved carrier mobility with increased crystallinity.[61]

Figure 3.5c shows the corresponding FTIR absorption spectrum of the F_4TCNQ C≡N stretching modes in these same three doped P3HT films. Interestingly, the main (ICT) anion absorption band shifts position from 2191 cm^{-1} in the least-crystalline film (P3HT cast from CF) to 2185 cm^{-1} in the most crystalline film (100% RR P3HT). This suggests that the position of the ICT vibronic absorption band depends directly on the degree of overall crystallinity, with the more ordered environments producing a red-shifted vibronic band; we will explore this observation in more detail in future work.

In addition to the shift of the anion absorption associated with ICT, the data in Fig. 3.5c show the distinct presence of the CTC peak in all three films, as evidenced by its vibronic absorption near 2201 cm^{-1}. The correlation is clear: the film with the lowest overall crystallinity has the largest fraction of CTCs, and vice-versa for the most crystalline film. Given that the CTC requires π-stacking of the dopant and polymer, which is kinetically difficult to achieve in crystallites, it makes sense that CTC formation is favored in more disordered, amorphous films, where the requisite π-stacking geometry is easier to achieve.

3.3.6 Thermal Annealing and the Stability of CTC States

The question of the relative thermodynamic stability of CTC and ICT phases in doped conjugated polymer films has also been a topic of considerable interest. Watts et al. recently argued that CTC states in P3HT films are thermodynamically preferred[9] while Jacobs et al. showed that the CTC polymorph in their samples rapidly degraded when exposed to light or air, suggesting that the CTC states are kinetically unstable.[6] More recently, Zapata-Arteaga et al. investigated CTC formation following extended thermal annealing of vapor-doped conjugated polymer films, and ultimately concluded that samples rich in the CTC phase are more thermally stable.[52]

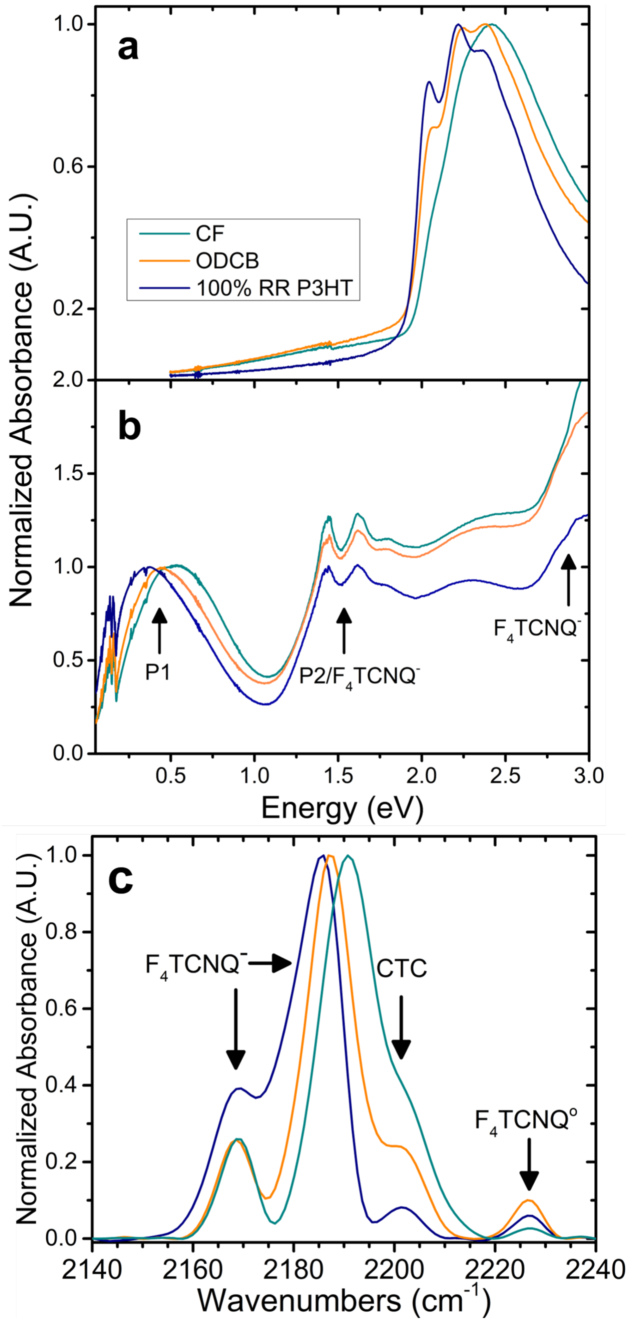

Figure 3.5: (a) UV-vis absorption spectrum of three different P3HT films with increasing crystallinity controlled by the evaporation kinetics of the solvent used to cast the film or the degree of polymer regioregularity. (b) UV-vis-NIR/FTIR combined spectrum for the same set of films after sequential solution doping with F_4TCNQ from DCM ($1\,\mathrm{mg\,mL^{-1}}$), normalized at the P1 band. (c) Vibrational spectra for the F_4TCNQ C≡N stretching mode for the same three films. The CTC peak near $2201\,\mathrm{cm^{-1}}$ clearly shows that lower polymer cyrstallinity is associated with forming more CTC states.

Because of the control over CTC production afforded by our solvent blend method, we have also addressed this question here by exploring the effects of thermal annealing. Our goal is to understand if the CTC phase, once formed, is only kinetically stable or is in fact the thermodynamically preferred phase. It is known that F_4TCNQ can thermally desorb from doped P3HT films upon exposure to higher temperatures, leading to chemical dedoping of these films.[31] Thus, to test the stability of the CTC phase, we employed only modest heating for a short duration. Utilizing the full span of CF/DCM solvent blend ratios, films were placed on a hot plate at 80 °C for one to five minutes in a nitrogen atmosphere. The samples were removed promptly after the indicated time and allowed to cool to room temperature prior to analysis.

Figure 3.6 shows the results of thermally annealing our pure-CF-doped films, which contain the highest fraction of CTC states, for different durations of time.

Upon heating at 80 °C for 1 minute, the two vibronic absorption peaks near 1.5 eV, and an additional peak near 3.0 eV all from the F_4TCNQ anion actually increase in intensity. This result is contrary to what is usually seen when annealing doped polymer films, since heating typically leads to dedoping, resulting in a loss of all absorption features associated with the doped species.[31] The fact that we see increased absorption upon heating indicates that heating reverts the metastable CTC phase back to ICT. It's worth pointing out that if CTC states were simply being converted to ICT, we might expect to see isosbestic points in the spectra following different degrees of thermal annealing. However, because the thermal annealing process also causes a net dedoping of the P3HT film, the overall absorption of F_4TCNQ^- and neutral P3HT are also changing. As such if we continue thermal annealing at this temperature for 5 minutes, the resulting UV-Vis spectrum loses overall intensity. More importantly however, the spectrum obtained after 5 minutes of annealing looks quite similar to that obtained when using pure DCM as the doping solution, indicating that at least at the level of sensitivity provided by electronic absorption, we can remove the CTC states while still leaving the majority of the ICT states intact.

Remarkably, GIWAXS patterns of the doped P3HT films (Fig. 3.7a and b) show that the new CTC phase II polymorph reverts entirely back to the phase I P3HT ICT crystal structure upon thermal annealing. Both the lamellar peak (Fig. 3.7a) and the π-stacking peak (Fig. 3.7b) lose all signatures of the CTC structure. These data provide direct structural evidence that the phase II

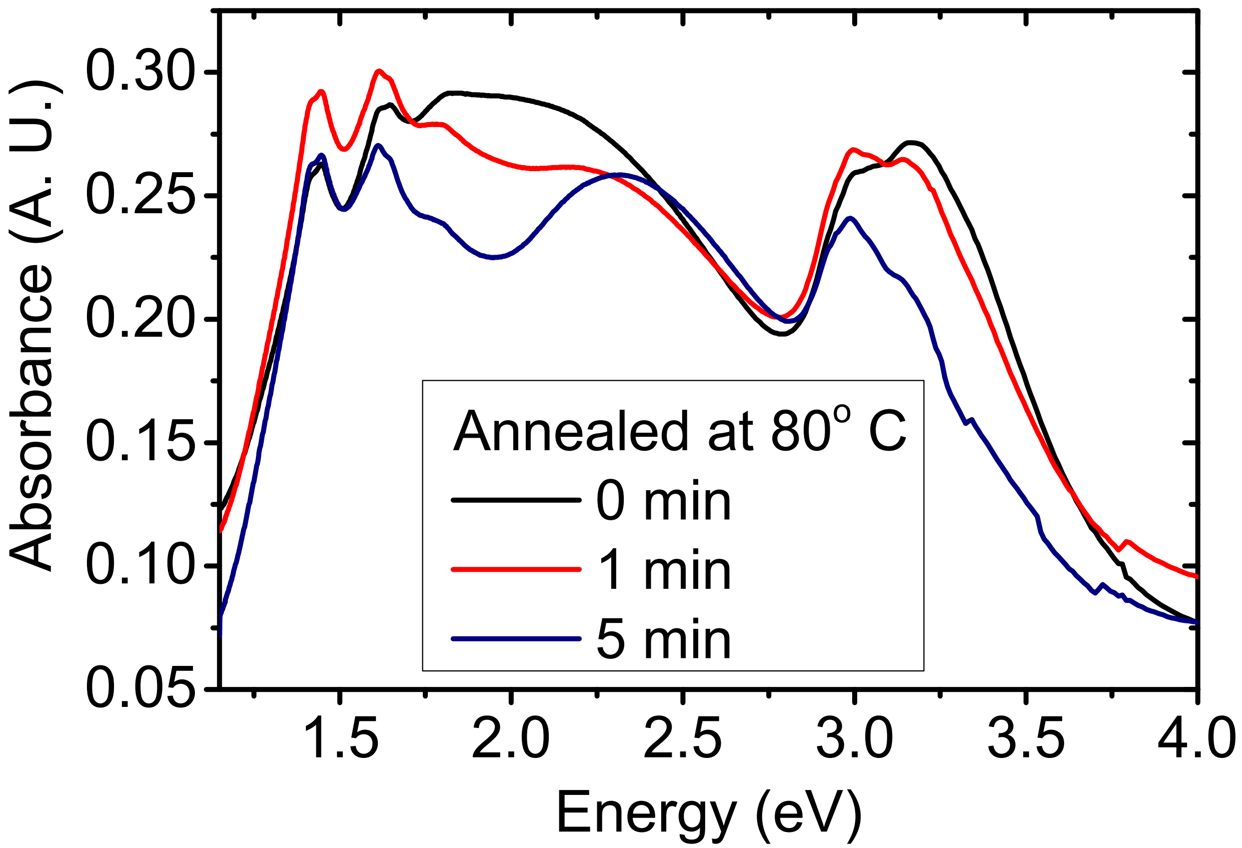

Figure 3.6: UV-Visible absorption spectra of P3HT films sequentially solution doped with F_4TCNQ (1 mg mL^{-1}) using 100% CF as the dopant casting solvent. Red curve represents a short annealing time of 1 minute, while the blue curve represents annealing for 5 minutes. Thermal annealing at 80 °C was carried out in a nitrogen glovebox. Brief annealing for 1 minute shows increased absorbance of the F_4TCNQ anion peaks near 1.5 eV, 3.0 eV and decreased CTC absorption near 2.0 eV, indicating a conversion of the CTC phase to the ICT phase without a significant loss of total doping. More extended annealing times lead to overall dedoping as well as a complete loss of the CTC phase.

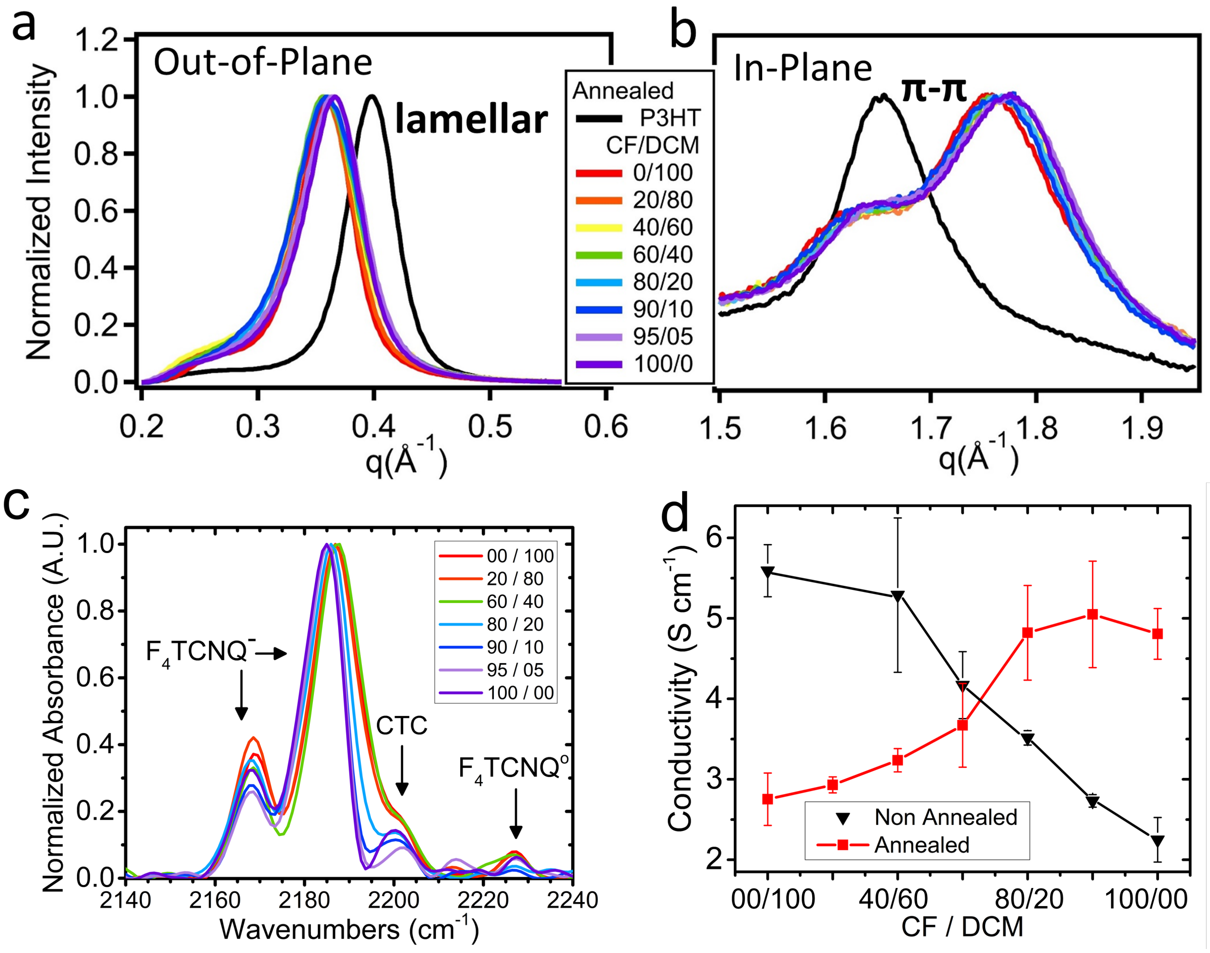

Figure 3.7: (a) Normalized out-of-plane and (b) in-plane integrations of thickness-normalized 2D GIWAXS diffractograms of P3HT films sequentially doped with F_4TCNQ from different ratio solvent mixtures of DCM and CF, subsequently annealed for 5 minutes at 80 °C. (c) Vibrational spectrum for the C≡N stretching mode after annealing. (d) In-plane conductivity of blend doped P3HT films prior to (black) and after annealing (red).

CTC polymorph is a kinetically-trapped phase. Upon thermal annealing, the dopants responsible for CTC formation physically relocate in the P3HT film and revert to the more preferred integer charge transfer doping mechanism. Moreover, the thickness-normalized GIWAXS data (appendix B Figs. B.8c-d and B.9b) show that after low-temperature thermal annealing, both the lamellar and π-stacking peak intensities for samples doped using CF are higher than those for films processed from DCM. Even more surprising, the GIWAXS intensities for these annealed conditions are also higher than the pristine P3HT intensity. Doped P3HT films usually show decreased lamellar peak intensities because doping usually induces some disordering.[43,61] The increased peak intensity we see after removing the CTC state (Figs. B8a,b and B9a in appendix B) by thermal annealing indicates that the original loss of peak intensity after doping from solvents with increasing CF fraction is due to conversion of ICT states to CTC states and not to induced disorder upon doping. Indeed, it appears that fundamentally, CF serves as an annealing solvent during the doping process which favorably rearranges the polymer microstructure. In the ICT state, this increased order can be observed in the P1 band (Figure 3.1b), and upon thermal conversion of the CTC states to ICT states, the increased order also can be clearly observed in the diffraction intensity.

Figures B.8c-d in appendix B also show that after thermal annealing, P3HT films doped from CF become more edge-on than the unannealed films. Since the edge-on geometry is beneficial for in-plane conductivity, this could also help to explain the conductivity change after thermal annealing in Fig. 3.7d.

The changes in structure seen by GIWAXS are directly reflected in the optical and electrical properties of the thermally-annealed doped films. In the FTIR C≡N stretching region, shown in Fig. 3.7c, the thermally-annealed samples produced with DCM-rich doping solvent mixtures show little change relative to their unannealed counterparts (shown above in Fig. 3.2a). This suggests that CTC states formed from CF-poor solvents may be isolated doping sites in amorphous regions that can more favorably form the CTC π-stacked structure. In contrast, samples fabricated with CF-rich doping solvents almost entirely lose their CTC vibrational signature at $2201\,\mathrm{cm}^{-1}$ after thermal annealing. In fact, the vibrational spectra for these CF-rich, thermally-annealed samples most closely resemble what was seen for our highest-crystallinity predominantly ICT-doped films; in other words, annealing the samples doped from CF ultimately produces a film whose properties match the solution-doped 100% RR P3HT (Fig. 3.5c) or the commercially-available P3HT that was doped from the vapor phase (Fig. 3.4b). The characteristic narrowing of the principal absorption peak and relatively small intensity for the CTC peak is a common feature shared across each of these processing methods and confirms that using CF as a doping solvent actually improves the overall crystallinity for the remaining P3HT. This also provides additional evidence that ICT is thermodynamically preferred: modest heating causes a marked reduction in the CTC peak at 2201 cm^{-1} where dopant molecules that π-stack with the P3HT backbone become free to diffuse until they can find a more stable configuration in the lamellae to undego ICT.

Finally, Fig. 3.7d shows the electrical conductivity of two series of identical samples doped from different solvent blends with one series subsequently being thermally annealed. As is typical for samples that use pure DCM as the doping solvent, thermal annealing decreases the electrical conductivity from 5.6 ± 0.3 S cm^{-1} to 2.8 ± 0.3 S cm^{-1}, because thermally-driven desorption of the F_4TCNQ species leads to de-doping.[7,132] In contrast, for the samples sequentially doped from pure CF, annealing actually causes an increase in electrical conductivity from 2.3 ± 0.3 S cm^{-1} to 4.8 ± 0.3 S cm^{-1}, nearly the same value measured for unannealed DCM solvent-doped films. This behavior is also consistent with the idea that brief annealing causes F_4TCNQ molecules that were kinetically locked in the metastable CTC π-stacking phase to revert back to the ICT doping mechanism, as corroborated by the C≡N stretching spectrum and the structural changes seen with GIWAXS. The drop in conductivity from any F_4TCNQ lost to desorption appears to be more than compensated for by the increased ICT carrier density and mobility due to enhanced crystallinity. Further annealing leads to additional dedoping, lowering the conductivity of all the films. An interesting crossover point exists near the 60/40 (CF/DCM) samples, which can be interpreted as a steady-state regime where the annealing-induced desorption of F_4TCNQ, the thermal conversion of CTC states into the ICT phase, and any annealing-induced changes in carrier mobility all compensate to cancel each other out.

In combination, the X-ray, FTIR and electrical conductivity data make clear that the application of modest heating can convert the CTC phase to the more desirable ICT phase. This shows that the CTC phase is kinetically accessible only under special processing conditions, but is not thermodynamically preferred, which means that the application of small amounts of heat for short treatment times may greatly improve the performance of devices based on chemically-doped conjugated polymers.

3.4 Conclusions

Overall, our work shows that even though ICT is the preferred mechanism of charge transfer in doped conjugated polymers, fractional charge transfer – i.e., CTC formation – also plays a significant, though sometimes hidden, role. Methods like UV-Vis-NIR and X-ray diffraction are incapable of detecting the presence of CTC species when they exist in small quantities: the electronic absorption of CTCs is likely weaker than those of the ICT states, and CTCs may also be associated with primarily amorphous regions in the polymer film, making them hard to detect via X-ray scattering. Here, we show clearly that even in the most crystalline P3HT films, produced either using vapor doping or with 100% regioregular material, we consistently see the presence of at least some charge transfer complexes after doping with F_4TCNQ.

Why are CTCs generally harder to make and study in doped conjugated polymers than in small molecule/oligomeric charge-transfer salts? The donor species in these charge transfer salts do not have the large aliphatic side chains needed to confer solubility on most conjugated polymers. Thus, small molecules and oligomers tend to form co-crystals with electron acceptors that allow for the close spatial contact needed for wave function overlap and CTC formation. For conjugated polymers, there is not only much more space to place acceptors in the lamellae, but lamellar placement leads to much less disruption of the polymer crystal structure and polymer-polymer π-stacking than insertion into the π-stacks, as outlined in Figs. 3.3g-i.

The propensity for CTCs to form in doped conjugated polymers is directly related to the degree of polymer swelling that takes place during the doping process, which in turn is linked to the fraction of amorphous regions. Indeed, we see that the relative abundance of CTCs in doped polymers increases with film swellability (and is minimized with evaporation doping), strongly suggesting that CTCs primarily reside in the disordered regions of the polymer film. This explains why CTC phases are rarely seen via GIWAXS, since it is difficult to form them in large crystallites without specially controlling the processing, such as our use of CF, or via high temperature processing as demonstrated by Jacobs et al.,[6] or by specifically preventing lamellar intercalation through the use of branched side chains.[133]

The key observation in this work is that simple adjustment of the composition of the sequential processing solvent used to introduce the dopant can greatly influence the observed doping mechanism. The use of CF as a doping solvent likely redissolves the underlying polymer film and thus provides a route for the thermodynamically-disfavored CTC state to form by initiating π-stacking between the dopant and the polymer in the disordered, partly dissolved state, and then preserving the kinetically-trapped π-stacked structure into the solid state. This is likely the same mechanism that occurs in the high-temperature processing employed by Jacobs et al.,[6] but should prove much easier to control for others to reproduce and further study. Moreover, we also presented a recipe – modest thermal annealing for a brief period of time – to remove CTC states and convert them to the ICT phase without significant dedoping, providing a simple way to improve the electrical performance of doped conjugated polymer films.

Moreover, our results are reassuring in that they confirm that for conjugated polymers, doping overwhelmingly takes place by integer charge transfer. This is because under normal sequential doping conditions, the dopants prefer the lamellae, where they remain far from the extended π-system of the polymer. Thus, the addition of side chains to conjugated polymers meant to confer favorable solubility also happens to control the preferred type of charge transfer interaction. This is consistent with conclusions we drew when exploring the doping of P3HT films with dodecaborane acceptors that are larger in size ($\sim$2 nm) than the polymer lamellar spacing ($\sim$1.6 nm) but still prefer to reside in the lamellar region.[2]

Finally, when comparing dopant infiltration methods, vapor doping showed the smallest fraction of CTC states generated, independent of the degree of pre-formed polymer crystallinity. In a certain sense, vapor doping provides the absolute minimum kinetic facilitation for CTC doping, helping to explain why this method produces a notably smaller quantity of CTC states. Additionally, it seems clear that under normal solution sequential doping conditions, the majority of CTC states are located in the amorphous polymer regions, and that the fraction of amorphous polymer will, in fact, also dictate the overall fraction of doping that takes place via the CTC mechanism. This work suggests that to minimize the occurrence of CTC states when sequentially doping with F_4TCNQ, one should strive for the highest crystallinity polymer possible, and carry out the sequential doping process by thermal evaporation, followed by brief low-temperature thermal annealing. These processing guidelines create the most conducive environment for maximizing both the equilibrium free carrier concentration as well as charge carrier mobility in these materials.

3.5 Supporting Information

Supporting Information includes detailed information on materials used, fabrication & doping of polymer films, optical & electrical measurements, F_4TCNQ C≡N vibrational spectrum & peak fitting details, and GIWAXS measurements of doped polymer films. These can all be found in appendix B.

3.6 Acknowledgements

This work was supported by the National Science Foundation under grant number CHE-2003755.

CHAPTER 4

Measuring the Vibrational Stark Effect in Chemically Doped Semiconducting Polymers

4.1 Introduction

Chemical doping of conjugated polymers has emerged as a viable method for tuning the electronic properties of organic electronic devices such as thermoelectrics and photovoltaics.[22,63,64,123,124] In the simplest case, *p*-type doping of polymer-based semiconductors can be achieved through the introduction of strong oxidizing agents whose LUMO levels are energetically lower than than the HOMO levels of the semiconducting polymer. This leads to doping via integer charge transfer (ICT), where each dopant molecule removes an electron from the polymer π-system, producing both a cationic hole that can delocalize along the conjugated backbone (also referred to as a polaron) and a counterion formed from the reduced dopant. A variety of recent work has suggested that the ICT-separated hole and dopant counterion Coulomb interaction plays a fundamental role in determining the carrier behavior in doped conjugated polymers: the stronger the Coulomb interaction, the lower the polaron delocalization and carrier mobility.[2,40,43,44,46,58–61] The experimental evidence for charge carrier-counterion interactions, however, is indirect, based mostly on features observed in the polaron mid-IR absorption spectrum. Thus, one of the goals of this paper is to provide a means by which to directly measure the local electric fields experienced by polarons and dopant counterions in doped conjugated polymers.

The approach we take is enabled by the fact that the strength of the Coulomb interaction between polarons on the conjugated polymer backbone and dopant counterions is actually recorded in the vibrational spectra of certain dopant anions. Our first hint that this might be possible comes from previous work both by our group[12] and others[3,4,6,8,9,52,53,133,147,148] who have used the nitrile stretching vibrational spectrum of the 2,3,5,6-tetrafluoro-7,7,8,8-tetracyanoquinodimethane (F_4TCNQ) dopant as a diagnostic tool for tracking the doping mechanism in conjugated polymers, which takes place either via ICT or by the formation of charge transfer complexes (CTCs). These nitrile stretching modes have the advantage that they appear in a mid-IR spectral 'window' where no other molecular vibrations appear, so that they are relatively easy to measure and characterize. In the context of studying CTCs, the nitrile stretching modes of the neutral F_4TCNQ molecule undergo a predictable softening in their resonant vibrational energy that is roughly proportional to the oxidation state of the molecule. As a result, vibrational absorption at intermediate energies between the neutral and anionically-charged species is understood to represent a fractional charge transfer state for the dopant molecule.

Another clue comes from the work of Hase et al.,[7] who recently studied the nitrile stretching vibrational spectrum of the F_4TCNQ radical anion inside blend-doped films of poly(3-hexylthiophene-2,5-diyl) (P3HT). These workers showed that the amplitude of certain F_4TCNQ^- vibrational features can change quite dramatically (and even disappear) when the doped films are subjected to thermal annealing cycles. This demonstrates that the precise vibrational spectrum of the F_4TCNQ dopant anion is in fact dependent on the local structural morphology. As a result, it has become increasingly clear that the F_4TCNQ vibrational spectrum can change in subtle ways as a result of the charge state of the molecule and the local structural morphology in which it resides.

In this paper, we provide a comprehensive picture of the Coulomb interactions in F_4TCNQ-doped P3HT films that links the behavior of the F_4TCNQ nitrile vibrational spectrum to the degree of polaron delocalization in the doped polymer, the local structural disorder, and the polaron-dopant Coulomb interactions that ultimately affect the charge carrier mobility. We show that the counterion vibrational spectrum is directly influenced by the local electric field emanating from the nearby hole, and thus can serve as an exquisite reporter of the degree of polaron delocalization on the nearby conjugated polymer.

We then argue that the behavior of the F_4TCNQ^- nitrile stretching modes can be quantitatively described using the framework of the vibrational Stark effect (VSE). There is a rich existing literature using the vibrational Stark shifts for a variety of nitrile, carbonyl, and other groups to directly measure the local electric fields experienced in biological systems,[149–161] self assembled monolayers,[162–166] solvated ion pairs,[167–169] and other applicationas.[170–172] Thus, by measuring the vibrational Stark shift of the nitrile stretches on the F_4TCNQ anion across a range of doped P3HT environments, we are able to directly infer the anion-hole separation distance and to correlate the electric field experienced by the dopant anion directly with the degree of polaron coherence. Overall, we show in this work that the F_4TCNQ radical anion is more than just a dopant counterion, it also serves as a sensitive vibrational Stark probe, reporting directly on the strength of the local Coulomb interaction with polaronic charge carriers in doped P3HT.

4.2 The mid-IR Spectroscopy of F_4TCNQ-Doped P3HT Films

We have previously shown that sequential processing, casting the polymer film first and then infiltrating the dopant in a second solution- or gas-phase step, is a versatile technique capable of producing high-quality doped polymer films.[2,11,19,43,44,61,66,67] This method also allows for tuning the degree of crystallinity in doped conjugated polymer films. For example, doped P3HT crystallinity can be tuned either by changing the processing conditions of the pre-cast polymer film,[61] or by careful choice of the solvent used in the subsequent doping step.[12]

Figure 4.1a shows a series of mid-IR absorption spectra for F_4TCNQ-doped P3HT films where the solvent used to introduce the dopant is comprised of a mixture of chloroform (CF) and dichloromethane (DCM). By varying the blend ratio of these two solvents, we can exert a high degree of control over the resultant morphology. In previous work, we used grazing incidence wide-angle X-ray scattering (GIWAXS) to characterize the crystallinity of these films, and found that although the morphology and even the doping mechanism both become associated with increased amorphous regions as CF content increases in the doping solvent, the ordered regions that remain become more highly crystalline.[12] This is due to the strong dissolving power of the CF solvent, which effectively allows for recrystallization of the ordered fractions of the pre-cast P3HT film that remain following doping. Thus, the crystalline domains that do survive have a much higher average polaron coherence length than those in films prepared with doping solvents where redissolution does not occur.[12]

The crystallinity of F_4TCNQ-doped P3HT films also can be manipulated during the initial polymer spin-coating step, as shown in Figure 4.1b. In this case, we exploit both the polymer regioregularity and the polymer casting solvent drying kinetics to control the polymer order. We previously have used GIWAXS to show that when a commercial P3HT film is cast from CF, a fast-drying solvent, the resultant polymer film is highly amorphous with relatively little crystallinity.[61] In contrast, when commercially-available P3HT is cast from the more slowly-drying solvent *o*-dichlorobenzene (ODCB), the films have more time to order and become more crystalline. Finally, by using a specially-synthesized batch of P3HT with virtually 100% regioregularity,[61,146] cast from ODCB, we can obtain highly crystalline P3HT films (Please see appendix C for experimental details). We also showed that when the film crystallinity is tuned this way, the crystalline regions of the polymer dope first, and the amorphous regions only become doped at very high doping concentrations after the crystalline regions are filled.[61]

4.2.1 Spectral Signatures of P3HT Polaron Coherence Following Doping with F_4TCNQ

Spano and co-workers have developed a theory for doped conjugated polymers that describes how changes in the energetic and structural disorder of a polymer affect polaron coherence, that is, the degree to which the polaron is delocalized along the P3HT backbone or possibly between adjacent π-stacked P3HT chains.[40,58–61] The theory indicates that as the polaron coherence changes, there is a corresponding shift in both the position and shape of the mid-IR polaron electronic absorption spectrum. In this model, one of the primary features that affects the polaron coherence length is the strength of the Coulomb interaction between the positively-charged, delocalized hole on the polymer and the corresponding counter-charge located on the dopant molecule. The model is able to reproduce experiment remarkably well for a variety of conjugated polymer-dopant pairs.[40,58–61]

In the present work, the most crystalline of the F_4TCNQ-doped P3HT samples (Fig. 4.1 purple curve in panel a and light green curve in panel b) show characteristic P3HT polaron absorption from highly-ordered environments. Since the hole is better able to delocalize in such environments, there is less Coulomb attraction between the hole on the polymer and dopant counterion, as discussed further below in section 4.3.1. This weakened Coulomb interaction and larger coherence lengths are manifest spectroscopically by both increased relative absorption intensity for the ‘A’ peak (the rough

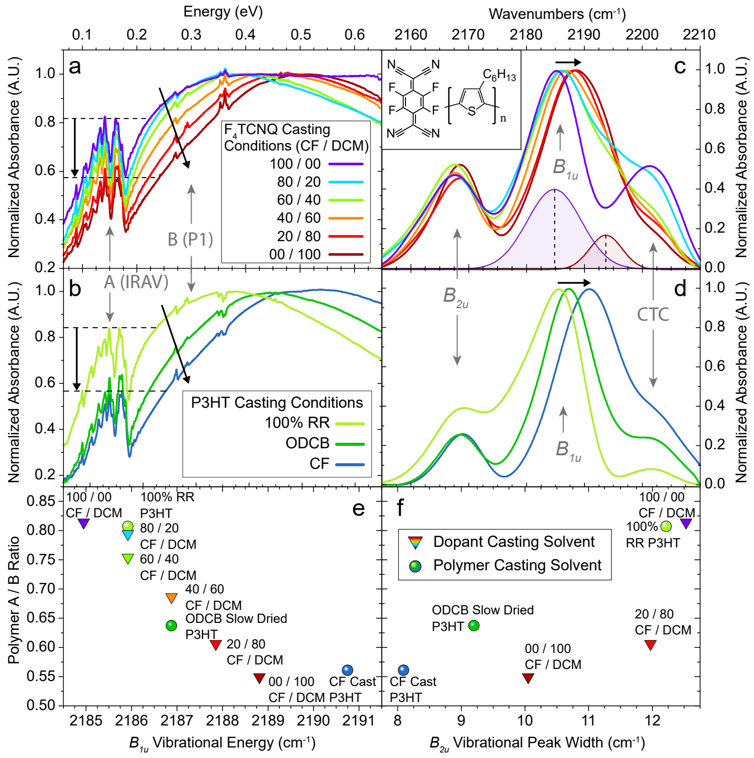

Figure 4.1: (a) Normalized mid-IR electronic absorption spectra for P3HT films sequentially doped with F_4TCNQ (1 mg mL^{-1}) from solvent blends comprised of CF and DCM. (b) Normalized mid-IR electronic absorption spectra of doped P3HT films where the initial films are created to have a range of crystallinities and then subsequently doped with F_4TCNQ (1 mg mL^{-1}) from DCM. For the blue and dark green curves, commercially-available P3HT with a regioregularity of $91-94\%$ was used, and the relative film crystallinity was controlled by varying the drying time of the casting solvent. A specially-synthesized batch of P3HT with virtually 100% regioregularity was cast from ODCB to obtain the most ordered conditions shown in light green. (See appendix C for x-ray-based structural characterization). The A/B spectral ratio (see text) for both panels a and b can be estimated on the vertical axis by following the horizontal dashed lines. (c) F_4TCNQ nitrile stretch vibrational spectra of the doped films in panel a (also directly visible in panel a as tiny peaks near 0.27 eV). The shaded gaussians correspond to peak fits for the conditions using 100% CF as the doping solvent, reduced to 0.3 intensity for ease of viewing (see appendix C for fitting details). (d) F_4TCNQ nitrile stretching vibrational spectra of the doped films in panel b. (e) Scatter plot displaying the experimentally-measured A/B ratio for the samples in panels a and b plotted against the vibrational energy of the F_4TCNQ^- B_{1u} mode. (f) Scatter plot displaying the A/B ratio for all the samples in panels a and b plotted against the peak width of the F_4TCNQ^- B_{2u} vibrational mode.

feature centered near $\sim$0.16 eV), and a shift to lower energies for peak 'B' (the main, smoother feature that peaks between 0.35 and 0.55 eV).

In contrast, the curves in maroon (panel a) and blue (panel b), which are for the most disordered doped P3HT films, show mid-IR absorption spectra characterized by a relatively low absorption intensity of the A peak and a shift of the B peak to higher energies. This is a hallmark of poor polaron coherence.[40,58–60] Because the amplitude of peak A decreases relative to peak B with increasing hole localization, the amplitude ratio of peaks A/B becomes a simple metric for tracking changes in polaron delocalization in doped conjugated polymers.[40,58–60]

For the method of controlling morphology by adjusting the doping solvent (panel a), the A/B ratio increases from A/B = 0.55 when casting F_4TCNQ from pure DCM, up to A/B = 0.81 when casting the dopant from pure CF. When altering the morphology during the polymer casting step (panel b), the change in the A/B ratio is nearly identical, with A/B = 0.56 when the polymer is cast from CF and A/B = 0.81 for slow-dried films fabricated from 100% regioregular P3HT. Due to the relatively small physical size of the F_4TCNQ anion, the Coulomb interaction between the anion and the hole polaron has enough strength that increasing the local order of the polymer can only tune the degree of polaron delocalization over a somewhat limited range compared to what is achievable with larger dopants.[2,43]

The theory developed by Spano and co-workers provides a direct connection between polaron coherence lengths and spectral A/B ratios.[59] In this work, we will quantitatively estimate the polaron coherence by measuring the strength of the electric field between the F_4TCNQ^- counterion and the hole polaron on P3HT. Our approach is possible because the theoretical relationship between the A/B spectral ratio and polaron coherence is predicted to be roughly linear across a wide range of coherence length values.[59] For our doped P3HT films with different degrees of order, the measured A/B ratios ranged from $\sim 0.55 \rightarrow 0.81$, which should correspond to a $\sim$25% increase in the average polaron coherence length.[59] In the sections that follow, we will show how shifts in the energy of the F_4TCNQ vibrational modes allow us to map out the local electrical fields in doped P3HT films to precisely determine the change in polaron coherence length.

4.2.2 The F_4TCNQ^- Nitrile Vibrational Spectrum in Doped P3HT Films

F_4TCNQ^- has two IR active vibrational modes with significant oscillator strength in the so-called transparent window between 1800 and 2500 cm^{-1}: these are C≡N stretching modes with B_{1u} and B_{2u} symmetry (Figure 4.2a) that in doped P3HT films occur near 2190 cm^{-1} and 2170 cm^{-1}, respectively. An example IR spectrum of F_4TCNQ-doped P3HT produced by sequential processing is shown in Figure 4.2b. Meneghetti and Pecile have noted that the location and geometry of the nitrile substituents on this molecule make these two vibrational modes uniquely susceptible to their local environment.[136] In fact, this susceptibility to local environment should make these modes relatively poor indicators for quantitatively measuring the degree of charge transfer, a subject of much recent interest.[4,6,8,9,12,52,53,133,147,148]

The literature on the vibrational spectroscopy of the F_4TCNQ radical anion inside films of doped P3HT shows that the two nitrile stretches can absorb at a variety of locations.[3–9] In Figure 4.2c, we have reproduced the IR spectra of F_4TCNQ^- in doped P3HT films taken from seven different recent sources in the literature; it is clear that different groups observe different F_4TCNQ anion vibrational spectra for what is nominally the same doped polymer system.

All of the data shown in Fig. 4.2c were taken on films prepared by blend doping, where the polymer and dopant were mixed together in solution prior to casting. This method has the advantage of providing a precise dopant to monomer ratio, but suffers from several drawbacks, including yielding a very poor film morphology, as we have discussed elsewhere.[11,19,61] We can see that for blend casting, the B_{1u} and B_{2u} modes usually appear near 2194 cm^{-1} and 2170 cm^{-1}, respectively. However, the spectra in Fig. 4.2c show an additional vibrational peak between these two modes, centered near 2185 cm^{-1}. The specific origin of this peak has been a topic of some debate.[3–6,8,9] In early work, this 2185 cm^{-1} peak was tentatively assigned to a C≡N stretching mode of A_g symmetry,[3,147] which would require a break in planarity of the F_4TCNQ anion. Such a non-planar geometry might occur if F_4TCNQ doped P3HT in a π-stacking arrangement.[142] The more recent consensus, however, is that F_4TCNQ^- resides in the lamellar side-chain regions of the doped P3HT crystallites,[7,11,21,29,34,42,44–46,53,55,61] so that the 2185 cm^{-1} mode must result from some other phenomenon.[9]

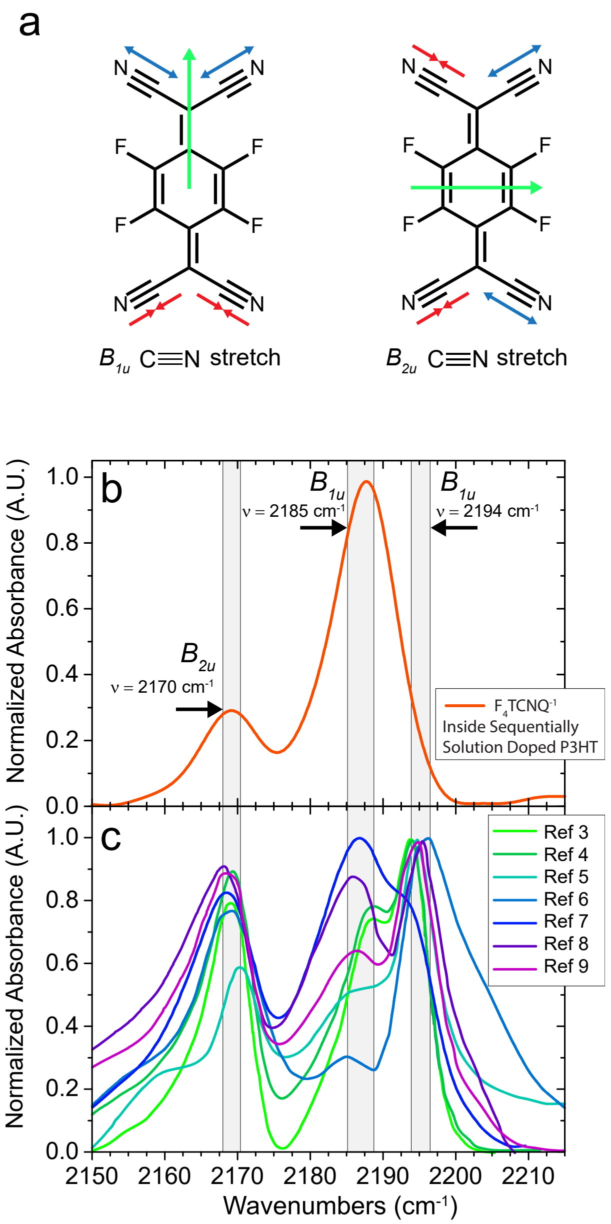

Figure 4.2: (a) Atomic displacement vectors for the two F_4TCNQ C≡N vibrational modes with B_{1u} and B_{2u} symmetry. Compression and expansion of the C≡N bonds is indicated red and blue arrows, respectively. The difference dipoles (green arrows) for these two modes point along the long axis of the molecule for the B_{1u} mode and across the short molecular axis for the B_{2u} mode. (b) FTIR spectrum of the F_4TCNQ^{-1} radical anion inside sequentially solution-doped P3HT (with the dopant cast from $1\,\mathrm{mg\,mL^{-1}}$ n-butyl acetate) and (c) inside blend-doped P3HT samples taken from various literature references, in descending order on the legend: Pingel et al. (3), Ghani et al. (4), Mendez et al. (5), Jacobs et al. (6), Hase et al. (7), Neelamraju et al. (8), Watts et al. (9).

One important clue to the assignment of the 2185 $\mathrm{cm^{-1}}$ peak comes from Hase et al.,[7] who showed that upon exposing F_4TCNQ-doped P3HT films to extended thermal annealing cycles, the B_{1u} absorption feature near 2194 $\mathrm{cm^{-1}}$ becomes reduced in amplitude, leaving behind the peak near 2185 $\mathrm{cm^{-1}}$ and the B_{2u} mode near 2170 $\mathrm{cm^{-1}}$. Watts et al. subsequently noted that if the unknown peak near 2185 $\mathrm{cm^{-1}}$ did belong to an A_g mode, then the two features near 2185 $\mathrm{cm^{-1}}$ and 2194 $\mathrm{cm^{-1}}$ should show similar behavior upon annealing.[9] The fact that annealing causes a loss in amplitude only for the 2194 $\mathrm{cm^{-1}}$ mode suggests that this vibrational feature is associated with a structure that can change upon annealing. Thus, it seems far more likely that the two features near 2185 $\mathrm{cm^{-1}}$ and 2194 $\mathrm{cm^{-1}}$ both belong to the B_{1u} mode, where the specific vibrational energies are reporting something about variations in the local structural environment.

With the idea that the F_4TCNQ^- nitrile stretching modes shift with their local environment, we can examine how the doped film processing method, which controls P3HT crystallinity and polaron delocalization, affects the resulting dopant nitrile vibrational spectrum. Figure 4.2b shows the intensity-normalized nitrile vibrational spectrum of the F_4TCNQ radical anion inside sequentially-doped P3HT using the relatively non-interacting solvent *n*-butyl acetate to infiltrate the dopant at a concentration of 1 $\mathrm{mg\,mL^{-1}}$. It's clear from comparing panels b and c in Fig. 4.2 that the dopant anion vibrational spectrum for sequentially-doped films is considerably different from those obtained from blend doping. Rather than seeing two peaks for the B_{1u} mode distributed between 2194 $\mathrm{cm^{-1}}$ and 2185 $\mathrm{cm^{-1}}$, the sequentially-doped film shows only a single feature centered at 2187 $\mathrm{cm^{-1}}$. This suggests that for sequential processing, which under these conditions produces more ordered doped P3HT films, the dopant molecules have a singular well-defined geometry in the polymer crystallites. The higher-energy B_{1u} peak near 2194 $\mathrm{cm^{-1}}$, in contrast, must belong to anions that Coulombically trap the hole in the morphologically-disordered polymer regions that predominate in blend-cast doped films.

4.2.3 Correlation Between Polaron Coherence and F_4TCNQ^- Vibrational Spectrum

Now that we have established a basis for understanding how the doped polymer structural environment should affect the vibrational spectrum of F_4TCNQ^-, we can consider how the local degree of order and polaron coherence affect the nitrile stretching frequencies. Figure 4.1c shows the vibrational spectrum of the F_4TCNQ radical anion inside P3HT films sequentially doped with F_4TCNQ cast from CF/DCM solvent blends. We see that when the dopant is infiltrated from pure CF, the principle B_{1u} nitrile absorption feature occurs with $\nu_{max} = 2185\,\mathrm{cm}^{-1}$ (purple curve). As the polaron becomes increasingly localized by increasing the fraction of DCM in the doping solvent, the B_{1u} vibrational peak monotonically shifts to $\nu_{max} = 2189\,\mathrm{cm}^{-1}$ (maroon curve). It is worth noting that even in these high-DCM processed P3HT films, which are the most disordered made by sequential doping, the B_{1u} mode is still five wavenumbers lower in energy than the $2194\,\mathrm{cm}^{-1}$ peak seen in the even more disordered blend-doped P3HT films.

When we analyze the principal vibrational features in the sequentially-doped films seen in Fig. 4.1c in more detail, we see that they are actually best fit to two gaussians: a dominant feature that shifts between 2188 and $2185\,\mathrm{cm}^{-1}$ (shaded purple curve reduced to 0.3 intensity) and a smaller shoulder (shaded maroon curve) located near $2194\,\mathrm{cm}^{-1}$ (see appendix C for fitting details). As the polarons in the crystalline regions become more delocalized by increasing the fraction of CF, the intensity of this small peak shoulder near $2194\,\mathrm{cm}^{-1}$ monotonically decreases and disappears entirely when the dopant is cast from 100% CF. The fact that the peak near $2194\,\mathrm{cm}^{-1}$ decreases with a higher fraction of CF solvent and thus increasing local crystalline order fits well with the notion that this higher-energy peak is associated with highly localized polarons, which are more likely to exist in more disordered polymer regions. This also helps to explain why the peak near $2194\,\mathrm{cm}^{-1}$ presents so prominently in films produced by blend doping, since blend-cast films are expected to have a broader distribution of morphological states.

A similar trend for the F_4TCNQ^- B_{1u} vibrational mode also occurs when the doped polymer crystallinity is tuned by changing the how the polymer film is cast (with the dopant solvent held constant), as shown in Figure 4.1d. When the underlying P3HT film is 100% regioregular and cast from ODCB, the F_4TCNQ^- B_{1u} mode has $\nu_{max} = 2186\,\mathrm{cm}^{-1}$. As the polaron becomes more localized when the initial P3HT film is cast from CF, we see the B_{1u} mode shift up to $\nu_{max} = 2191\,\mathrm{cm}^{-1}$.

For both sets of doped P3HT films, we see a remarkably strong correlation between the P3HT polaron coherence, as measured by the A/B spectral intensity ratio, and the position of the F_4TCNQ^-

B_{1u} nitrile stretch, as summarized in Fig. 4.1e. This correlation is one of the principal results of this work: the position of the B_{1u} stretching peak of the dopant provides a local measure of polaron coherence on the polymer.

As an aside, we note that in both sets of doped P3HT films, we see an increased amplitude for the F_4TCNQ CTC vibrational peak near 2200 cm^{-1} with increasing polymer disorder.[12] The reason the CTC peak becomes more prominent when the doping solvent has an increasing fraction of CF is because the use of CF as a sequential doping solvent causes significant disruption of the P3HT crystal lattice. This is what both increases the total fraction of disordered regions and also increases the order of the crystalline regions that remain.[12] When using more common and milder processing solvents however, it is clear that CTC formation is mostly limited by the amount of disordered polymer regions.

For the subset of our F_4TCNQ-doped P3HT samples where the F_4TCNQ$^-$ B_{2u} mode did not have a neighboring low-energy shoulder (which has been previously attributed to the B_{3g} mode near $\nu = 2160$ cm^{-1},[4,10] or simply remained an unassigned mode[8,9]) we can cleanly fit both the position and width of the B_{2u} peak. We find that the vibrational energy of this mode does not shift in different P3HT environments, always remaining within a 2 cm^{-1} range. However, we do see that the full width at half maximum (FWHM) of the F_4TCNQ$^-$ B_{2u} feature broadens from 8.1 cm^{-1} for doped P3HT films with the most localized polarons (lowest A/B ratio) up to 12.5 cm^{-1} for doped films with the most delocalized polarons (highest A/B ratio), as summarized in Figure 4.1f. The fact that it is the peak width of the B_{2u} mode that correlates with polaron coherence, not the peak vibrational energy, provides another crucial piece of information that will allow us to quantify both the orientation of the F_4TCNQ anion relative to the P3HT polaron and the degree of polaron delocalization.

Although the two series of doped P3HT films we have studied modify the local polymer crystalline order during different processing steps, they show a similar range of polaron coherence, as evidenced by the A/B spectral ratio, and a similar behavior of the B_{1u} and B_{2u} vibrational modes, summarized in Figures 4.1e and f. For the most locally-ordered P3HT films from each set (100% RR pre-cast P3HT film and commercial P3HT with the dopant cast from 100% CF) the mid-IR spectra have an identical A/B ratio of 0.81 and correspondingly similar B_{1u} vibrational peak positions of

$2185 - 2186\,\mathrm{cm}^{-1}$ as well as similarly broad B_{2u} vibrational peak widths of $\sim 12.2 - 12.5\,\mathrm{cm}^{-1}$. This represents the highest A/B ratio, smallest B_{1u} vibrational frequency and broadest B_{2u} peak width that we have observed for this polymer-dopant combination. Thus, it is likely these values are approaching the fundamental upper limit for polaron delocalization when F_4TCNQ is used to dope highly-ordered P3HT.

Why would there be a fundamental upper limit to polaron delocalization? We expect polaron delocalization to be determined by two primary factors: (i) the inherent energetic disorder due to structural imperfections in the polymer crystallites, and (ii) the strength of the Coulomb interaction between the hole and dopant counteranion.[40,58–60] Since the dopant preferentially occupies crystalline regions of P3HT films,[11,61] the distance between the anion and the polymer backbone, d_{anion}, depends mainly on the physical size of the anion.[2,43] For the doped P3HT samples whose properties are shown in Fig. 4.1, d_{anion} is essentially fixed, so the increases we see in polaron coherence and the corresponding changes in the vibrational modes must result from increases in the local structural order of the polymer.

All of this means that the extent of polaron delocalization in the most-ordered polymer regions is limited by the minimum possible strength for the hole-counterion Coulomb interaction. F_4TCNQ-doped P3HT has a lamellar spacing of 17Å,[12,61] so the maximum possible dopant-polaron distance is ∼8 Å. Because of this relatively short distance, the Coulomb interaction from $F_4\mathrm{TCNQ}^-$ always causes some localization of the polaron beyond what is intrinsically allowed by a highly ordered polymer structure.[59,61] This explains why the F_4TCNQ-doped P3HT system has a relatively limited doping efficiency and carrier delocalization,[16] and why the use of physically larger dopants that screen the coulomb interaction can produce polarons with even greater delocalization in P3HT (A/B ratios greater than unity).[2,43] The idea that dopant anions can only reside in a limited set of places also helps to explain why F_4TCNQ-doped P3HT films always display some absorption of the most weakly-shifted B_{1u} nitrile peak near $2185\,\mathrm{cm}^{-1}$: even in blend-cast films with a relatively poor overall morphology, there are always a few doped P3HT crystallites with a reasonable degree of order.

4.3 F_4TCNQ and the Vibrational Stark Effect

Now that we have established a clear correlation between the behavior of the C≡N vibrational stretches of F_4TCNQ^- and the degree of polaron coherence in doped P3HT films, we can turn our attention to considering the mechanisms that cause these changes to take place.

The central thesis of this paper is that the blueshift of the B_{1u} mode and broadening of the B_{2u} mode with increasing A/B ratio occur as a direct result of the vibrational Stark effect (VSE). The VSE arises from the interaction between a molecule's vibrational mode and an externally-applied electric field. If vibrational excitation of a particular mode changes the dipole of the molecule, then the difference dipole vector between the ground and excited vibrational states can interact with the aligned component of an external electric field, causing a shift in the resonant energy for that vibrational mode. Since external fields are usually weak relative to the internal fields that hold a molecule together, the VSE can be well described by first-order perturbation theory, and the shift of the vibrational frequency is roughly linear with the local field strength.

The VSE is well studied in the literature, and its primary use has been to better understand the electric fields present in biological systems.[149–161] The VSE also has been recently used to directly study ionic interactions in solution, allowing researchers to determine if dissolved salts exist as contact ion pairs, solvent-separated ion pairs, or truly free solvated ions.[167–169] In many applications, VSE probes are simple alkyl-nitrile substituents, for which the difference dipole is aligned along the internuclear axis of the C≡N triple bond. The F_4TCNQ anion, in contrast, has two pairs of nitrile groups arranged so that the ground state molecule has no net dipole moment. Figure 4.2a shows the atomic displacement vectors for the F_4TCNQ^- B_{1u} and B_{2u} nitrile stretching modes with bond compression indicated in red, bond expansion in blue, and the difference dipole vectors in green. The difference dipole vector for the B_{1u} mode points along the long axis of the molecule, while that of the B_{2u} mode points transversely across the short axis. So although F_4TCNQ was not specifically designed for this purpose, it's clear that this dopant molecule contains all of the essential machinery required to operate as a vibrational Stark probe.

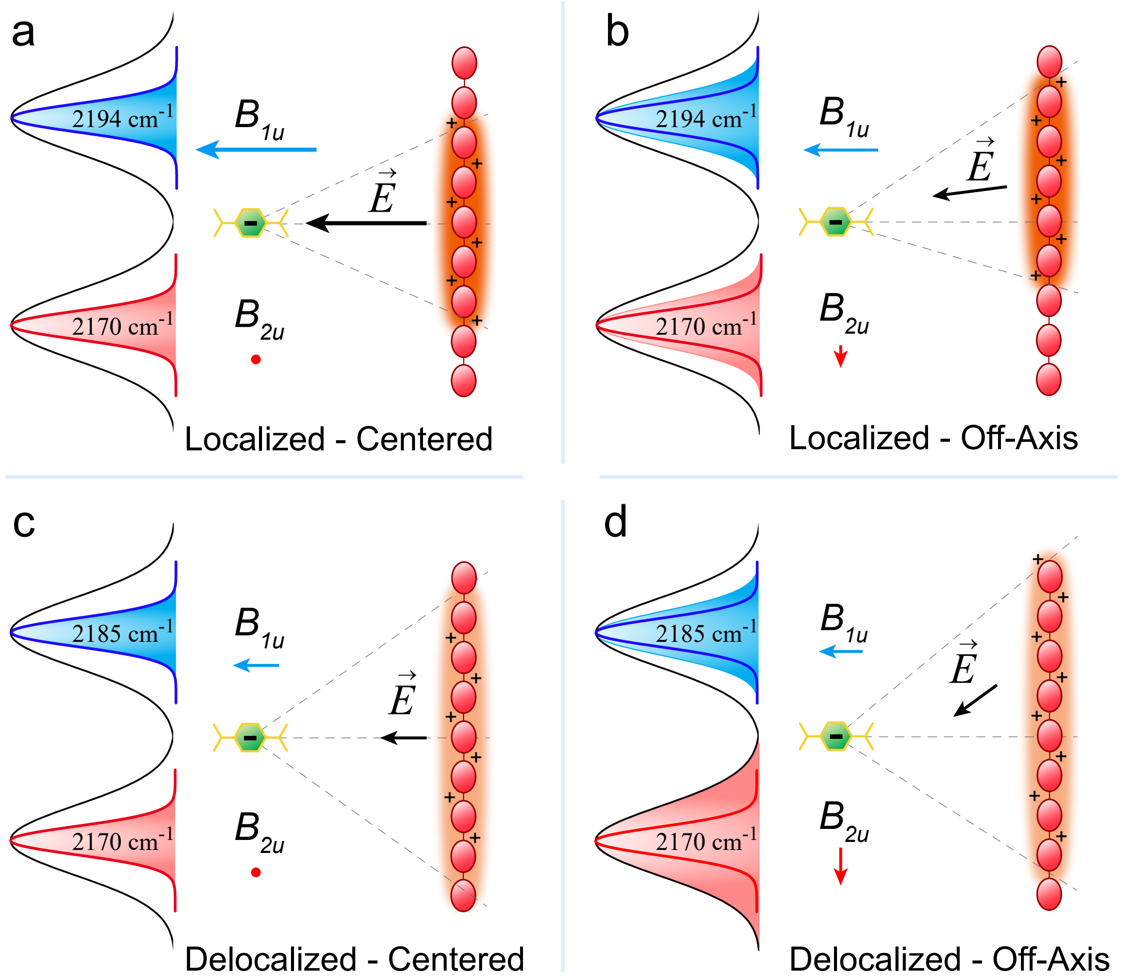

Figure 4.3: Cartoons illustrating how the electric field from a variety of polaron geometries influences the vibrations of the F_4TCNQ anion. (a) A localized P3HT polaron centered along the dopant-polymer axis produces a strong electric field aligned with the F_4TCNQ^- B_{1u} difference dipole, resulting in a VSE shift to a higher vibrational energy. The centered geometry has no electric field component aligned along the B_{2u} difference dipole, so there is no VSE shift of that mode. (b) A localized P3HT polaron with a slightly off-axis geometry slightly lowers the electric field component experienced by the B_{1u} vibration and slightly increases that experienced by the B_{2u} vibration, leading to a slight broadening of both modes. (c) A more delocalized P3HT polaron centered along the dopant-polymer axis exerts a lower field strength on the F_4TCNQ anion than the localized polaron case in panel a, resulting in a smaller VSE shift of the B_{1u} mode, which appears at a lower vibrational energy. (d) A more delocalized P3HT polaron with an off-axis geometry has little effect on the B_{1u} mode, but the increased electric field component along the B_{2u} mode leads to an increase in VSE broadening.

4.3.1 Coulomb Interactions and the Vibrational Stark Effect in F_4TCNQ-Doped P3HT Films

The fact that the difference dipoles of the B_{1u} and B_{2u} modes point in perpendicular directions allows us to directly infer the orientation of the dopant anion relative to the polaron on the polymer backbone that generates the local electric field. As mentioned above, X-ray diffraction work from several groups has determined that F_4TCNQ^- sits in the lamellar side-chain regions of the P3HT crystallites.[7,11,21,34,42,44–46,53,61] In addition, Brinkmann and co-workers, who study rub-aligned F_4TCNQ-doped P3HT films using polarized absorption spectroscopy, have shown that the long axis of the F_4TCNQ^- anion sits perpendicular to the polymer backbone.[29,55,57,68,69] This means that the difference dipole vector of the B_{1u} mode is oriented parallel to the electric field lines emanating from the hole on the polymer backbone (Figure 4.3), while that of the B_{2u} mode lies perpendicular to the local field.

Fig. 4.3a and c illustrate how the VSE shifts the resonant energy of the F_4TCNQ^- B_{1u} mode in direct response to changes in the magnitude of the P3HT hole-generated electric field. At fixed d_{anion}, the strength of the field will decrease as the polaron becomes increasingly delocalized. This provides a simple explanation as to why the frequency of the F_4TCNQ^- B_{1u} mode, whose difference dipole is oriented parallel with the field lines from the polaron, exhibits a strong vibrational Stark shift in response to changes in polaron coherence length (i.e., with A/B spectral ratio, as seen in Fig. 4.1e).

In contrast, the peak vibrational energy of the F_4TCNQ^- B_{2u} mode does not change with polaron coherence length, it only broadens. This is because the orientation of the B_{2u} mode difference dipole is mostly orthogonal to the hole-generated electric field. This means that any Coulomb interaction between the polaron and the difference dipole of this mode must originate from an off-axis electric field component. In the simplest case where the polaron is centered on the polymer-dopant axis (Fig. 4.3a and c), there is no net off-axis field component that might be aligned with the B_{2u} mode, explaining why this peak does not shift in response to changes in polaron coherence.

However, there is no guarantee that a polaron will always be centered along the dopant-polaron axis; in fact, we expect some degree of along-the-chain disorder of the dopant location relative to the polaron position in F_4TCNQ-doped P3HT films. When such lateral disorder is present, the F_4TCNQ anion is not exactly centered relative to the polaron. This means that the magnitude of the polaron E_{field} component aligned with the B_{2u} difference dipole will increase not only with the amount of off-center displacement, but also with the degree of polaron delocalization, as illustrated in Fig. 4.3b and d. If the total lateral disorder is modest, the result will be a net broadening of the B_{2u} mode rather than a shift, exactly as observed in Fig. 4.1f. This is because on average, the polaron is still centered relative to the location of the anion, so the off-axis component is relatively weak compared to the field strengths experienced along the B_{1u} difference dipole direction.

It makes sense that there should be a relatively strong correlation between the width of the F_4TCNQ^- B_{2u} nitrile stretch and the degree of polaron delocalization, but it is also possible that broadening of the B_{2u} mode might occur if the dopant anions had significant orientational disorder relative to the direction of the electric field from the polaron. If there were orientational disorder, however, the B_{2u} peak would be expected to narrow as the degree of local polymer crystalline order increased. Instead, we observe the opposite: the B_{2u} peak broadens as the polymer film becomes more ordered. This verifies that the observed correlation of the anion vibrational spectrum with the delocalization of the polaron indeed comes from the most ordered regions in the doped films and is not representative of orientationally-disordered areas of the film.

4.3.2 The Stark Tuning Rate: Quantifying Local Electric Field Strengths with Vibrational Mode Shifts

The above evidence strongly indicates that the VSE can explain all of the observed changes in the F_4TCNQ^- nitrile vibrations as resulting from changes in polaron delocalization in doped P3HT films. In the remaining sections, we will work to quantify the strength of these interactions to experimentally extract the anion-hole distance and degree of polaron delocalization.

It is well established that there is a linear relationship between the shift of a vibrational mode and the strength of the applied field. The magnitude of the vibrational shift per unit applied field is known as the Stark Tuning Rate (STR) parameter. To the best of our knowledge, the STR parameter for F_4TCNQ and its anions has not been experimentally measured. Thus in order to quantitatively determine the changes in electric field produced by different P3HT polaron coherence lengths, we must first determine the STR parameter for the relevant F_4TCNQ^- nitrile vibrational modes. One method is to pair the experimentally-measured vibrational shifts for these modes with detailed modeling of the predicted changes in E_{field} for the anion-hole Coulomb interaction. These methods consistently yield a STR of $\sim 2\,\text{cm}^{-1}/(\text{MV}\,\text{cm}^{-1})$ for the B_{1u} mode, and a STR of $\sim 4\,\text{cm}^{-1}/(\text{MV}\,\text{cm}^{-1})$ for the B_{2u} mode across a wide range of delocalization length changes, justifying their use here. These values are also within the range of STR parameters determined by others for similar molecules with multiple nitrile groups on a single carbon atom.[153,154,164]

4.3.3 Using the VSE to Directly Measure Polaron Delocalization in F_4TCNQ-Doped P3HT Films

With the Stark tuning rate parameters in hand, we can now use these values, along with the data presented in Fig. 4.1, to quantitatively determine how the polaron coherence length changes across the experimentally observed range of A/B values. We begin by considering how the electric field experienced by the different vibrational modes of F_4TCNQ^- change as a function of both P3HT polaron coherence length and the anion-hole separation distance, d_{anion}. For this calculation, we consider the field experienced by the anion at a single point located at d_{anion} away from the center of the P3HT chain. We then approximate polaron delocalization as a single positive charge spread out uniformly along a one-dimensional line of length L, given in units of the number of P3HT monomers. We then model changes in polaron coherence as n increases from $1 \rightarrow 9$ (Figure 4.4a), so that the one-dimensional polaronic charge density goes as $1/L$. Our model assumes a dielectric constant of unity, as the short-range interactions between the polaron and anion likely do not experience the dielectric value of the bulk material, an assumption which is consistent with what others have chosen for similar inquiries.[58,59,61] We note that our model ignores interchain polaron coherence, a choice made because we do not expect delocalization between neighboring chains to significantly affect the electric fields experienced by a nearby F_4TCNQ anion. Finally, even though we expect some along-the-chain disorder, we assume that on average, the anion is centered along the length of the delocalized polaron.

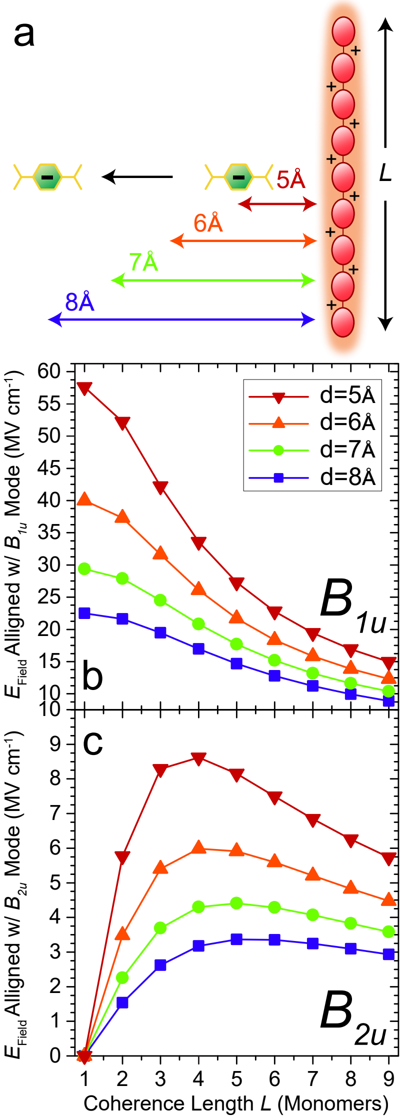

Figure 4.4: (a) Cartoon of hole polaron delocalization along the P3HT backbone, modeled as a line of uniform charge density q^+/L, where q^+ is the elementary charge and L is the delocalization length. (b) The electric field component experienced by the F_4TCNQ anion B_{1u} mode from the line of charge is calculated as a function of delocalization from a single monomer up to a length of 9 monomer units for a range of anion distances from $5\,\text{Å}$ up to $8\,\text{Å}$. (c) The electric field component from half of the delocalized polaron, chosen as a proxy to represent along-the-chain disorder, along the F_4TCNQ B_{2u} difference dipole. The magnitude of this component is an order of magnitude smaller than that along the B_{1u} direction

The main difficulty associated with quantitatively determining the change in P3HT polaron coherence length from the VSE of the F_4TCNQ nitrile stretching modes is that we only have access to the experimentally-measured vibrational shifts that occur within a range of externally applied fields: we do not know the absolute magnitudes of these fields because we do not know the position of the B_{1u} stretching mode inside a P3HT film in the absence of any external fields. Thus, the best we can do is use the measured shift in the B_{1u} peak vibrational energy, along with the calculated STR, to determine the change in electric field associated with the $\sim$25% increase in polaron coherence length measured by the spectral A/B ratio in Fig. 4.1. Once we have calculated the change in electric field experienced by the B_{1u} mode, we can then use the measured change in width of the B_{2u} mode, which experiences a field from the same delocalized polaron, to experimentally determine both the value of d_{anion} and the physical polaron coherence length increase that can explain the vibrational Stark features of both modes.

Figure 4.4b shows how the strength of the electric field aligned with the B_{1u} difference dipole is affected as polaron delocalization is increased from $1 \rightarrow 9$ monomer units. As argued above, the maximum possible dopant-polaron distance in a P3HT crystallite is half the lamellar spacing, or only $\sim$8 Å.[12,61] Thus, by examining a range of possible anion-hole distances up to 8 Å, we can narrow down the possible range of fields exerted by a P3HT polaron on the nitrile stretching modes of F_4TCNQ^-. In Figure 4.4b, the dark blue squares corresponding to $d_{\text{anion}} = 8$ Å show that increasing the degree of polaron delocalization diminishes the strength of the electric field experienced by the anion to $\sim$ 39% of its original value. Because this is the largest possible anion-hole distance, it also represents the minimum possible decrease in the relative field strength for a $1 \rightarrow 9$-unit change in polaron delocalization. For shorter anion-hole distances, such as $d_{\text{anion}} = 5$ Å (red triangles), the relative electric field strength drops to $\sim$ 26% of its starting value as the polaron delocalizes from $1 \rightarrow 9$ monomer units. We do not expect more sophisticated models to deviate significantly from these trends, since fundamentally this is an interaction described by Coulomb's law.

For the B_{2u} mode, our simplified model does not predict any net electric field alignment with the difference dipole. However, we can approximate the effects of along-the-chain disorder (cf. Fig. 4.3b and d) by considering the field contribution from just half of the delocalized polaron along the positive axis. Figure 4.4c shows the magnitude of the electric field component from half the delocalized charge that is aligned parallel with the B_{2u} mode as function of both polaron coherence length and d_{anion}. In this case, we see that the electric field does not vary monotonically with polaron delocalization because of competing effects. At shorter polaron coherence lengths, additional delocalization creates additional off-axis field alignment, which raises the overall magnitude of the field component along the B_{2u} difference dipole. However at longer coherence lengths, additional delocalization lowers the line charge density, which contributes to a net reduction in the total magnitude of the field.

In our simple model, the predicted magnitudes of the fields experienced by the $F_4\text{TCNQ}^-$ B_{2u} mode are nearly an order of magnitude lower compared to those experienced by the B_{1u} mode. This is indeed consistent with the fact that the B_{2u} mode only slightly broadens and does not shift with changing P3HT polaron delocalization, as measured by the A/B spectral ratio, while the B_{1u} mode shows a definite Stark shift as polaron delocalization changes.

With these curves it is now possible to quantify the degree of polaron coherence associated with a given A/B spectral ratio on the doped polymer. As mentioned above, theoretical work based on Spano's model[59] indicates that our range of measured A/B ratios corresponds to a $\sim$25% increase in P3HT polaron coherence length; this change of coherence is the same whether or not the delocalization is along or between the polymer chains, and as also mentioned above, we consider only the intrachain delocalization here. With the calculated B_{2u} STR of $\sim 4\,\text{cm}^{-1}/(\text{MV}\,\text{cm}^{-1})$ and the observed (single edge) vibrational peak broadening of $2.2\,\text{cm}^{-1}$, the observed 25% change in polaron delocalization corresponds to a change in electric field of $0.52\,\text{MV}\,\text{cm}^{-1}$. Note that because the E_{field} alignment does not change monotonically for this mode, we cannot determine the sign of this change or the distance of the delocalized polaron that exerts the field.

However, the same delocalized polaron electric fields that change the width of the B_{2u} mode also cause the simultaneous Stark shift of B_{1u} mode. The calculated STR parameter for the B_{1u} mode is $\sim 2\,\text{cm}^{-1}/(\text{MV}\,\text{cm}^{-1})$, so based on the experimentally-measured vibrational shift of $5.79\,\text{cm}^{-1}$, the electric field experienced by this mode decreases by $2.94\,\text{MV}\,\text{cm}^{-1}$ over this range of A/B ratios. Figure 4.4b and c shows that the only way for F_4TCNQ^- to experience both of these field components for a $\sim$25% change in polaron coherence at a single distance is when the intrachain coherence length increases from $3 \rightarrow 3.75$ monomer units with an anion-hole separation distance of 6 Å. Thus, using the VSE it is possible to make the first experimental measurement linking the spectral A/B ratio to a specific degree of intrachain polaron delocalization.

Rather than assuming the $\sim$25% change in delocalization length from theory, we can also do the same analysis by first assuming a fixed 6 Å distance for d_{anion} based on x-ray diffraction. The measured field-induced changes of the two F_4TCNQ^- modes are then consistent only with a coherence length change of $\sim$25% from 3 to 3.75 monomer units, verifying that we have experimentally determined the intrachain polaron coherence length with two independent but reasonable starting assumptions.

Thus, by using the two orthogonally-oriented nitrile vibrational modes of F_4TCNQ^- as independent measurements of the ranging electric field, we can build a comprehensive picture of the charge carrier-dopant interactions in F_4TCNQ-doped P3HT films. The experimentally-determined change in intrachain polaron coherence length from $3 \rightarrow 3.75$ monomer units is consistent with what has been put forward previously for this system.[58] The Stark-determined d_{anion} of 6 Å also fits well with the X-ray scattering determined lamellar stacking distances[12,61] (see appendix C table C.3) as well as previously modeled anion distances based on the profile shape of the mid-IR polaron absorbance of F_4TCNQ-doped P3HT system.[58,59,61]

4.4 Conclusions

In summary, we have shown that the nitrile stretches of the commonly-used dopant F_4TCNQ make an exquisite vibrational Stark probe of the local electric fields in doped conjugated polymer films, allowing us to uncover detailed information about P3HT polaron coherence. The fact that we observe one mode shift with polaron coherence while the other only broadens directly demonstrates that the dopant anion has a preferred orientation with respect to the polymer backbone. This is consistent with the idea that dopants prefer to reside in the lamellar regions of polymer crystallites, reinforcing conclusions in the literature reached by x-ray scattering[7,11,21,34,42,44–46,53,61] and by polarized spectroscopy of rub-aligned films.[29,55,57,68,69]

More importantly, we have provided the first experimental evidence that shows it is the degree of polaron delocalization that is directly responsible for the commonly seen changes in the F_4TCNQ^-

nitrile vibrational spectrum in doped P3HT films with varying degrees of crystalline order. This verifies theories that argue the polaron A/B spectral ratio (and position of the B polaron absorption band) are indeed direct experimental signatures of polaron coherence. With a simple model, we are able to use the magnitudes of the observed vibrational spectral shifts and broadening to pin down precisely how the local electric field changes with polaron delocalization in different P3HT environments. The field magnitudes experimentally prove that the anion-polaron distance in F_4TCNQ-doped P3HT films is $\sim$6 Å, and that intrachain polaron coherence lengths of roughly 3 to 4 monomer repeat units can be produced by varying the degree of local order through the film processing conditions.

Our results also allow us to explain the previous uncertainty over how to assign the vibrational spectrum of F_4TCNQ^- in doped P3HT films. The various vibrational lines that have been observed occur as a direct result of the unique preparation conditions and dopant/polymer blend ratios which produce a range of structural morphologies and polaron delocalization lengths. This in turn causes the dopant anions to experience a range of local electric fields, ultimately shifting the resonant vibrational energies. This also means that using the positions of the F_4TCNQ anion nitrile vibrations to determine the precise degree of charge transfer in charge-transfer complexes, usually associated with a feature near 2200 cm^{-1}, is potentially fraught with difficulty as electric fields from nearby integer charge-transferred polarons may also be responsible for shifts of this mode.

For the F_4TCNQ-P3HT materials combination studied here, the relatively short intrachain polaron coherence lengths we measure are a direct result of the fact that the F_4TCNQ anion always resides within 1 nm of the polaron, so that polaron coherence is always limited by the local Coulomb interaction with the anion, independent of how well ordered the P3HT crystallites are. Thus, although F_4TCNQ is certainly a useful molecular dopant for studying polaron behavior in conjugated polymers, the relatively strong Coulomb interaction it partakes in puts a fundamental limit on the degree of polaron coherence for this polymer-dopant combination. Fortunately, these issues can be avoided with the use of other dopants that better screen the polaron-counterion Coulomb interaction.[2,43]

We close by noting that in many ways, measuring the electric field landscape in doped semiconducting materials is precisely the kind of application that vibrational Stark probes were designed to explore. The nitrile groups that make this kind of analysis possible are commonly added to *p*-type dopants to make them stronger oxidizers. Thus, application of dopants as VSE probes is a natural use for these molecules. Although the current generation of nitrile containing dopants like F_4TCNQ were not designed to be used this way, it's exciting to imagine an entirely new class of *p*-type dopants that could be specifically engineered to fulfill the dual roles of being strong oxidizers that also map the electric fields from polarons in these materials. For these reasons, we are optimistic that the VSE will become a more generally applied principle in this area for probing the Coulomb interactions in doped conjugated polymers.

4.5 Supporting Information

Supporting Information includes detailed information on materials used, fabrication & doping of polymer films, FTIR measurements, peak fitting of the F_4TCNQ C≡N vibrational spectra, tabulated fitting parameters, dopant-polaron Coulomb modeling, and GIWAXS measurements of doped polymer films. These can all be found in Appendix C.

4.6 Acknowledgements

This work was supported by the National Science Foundation under grant number CHE-2003755.

APPENDIX A

Supporting Information for Chapter 2

A.1 Experimental Details

A.1.1 Organic Materials

All materials were purchased commercially and used as received. P3HT was purchased from Rieke Metals, Inc. (4002-EE; RR ∼91-94%, M_w = 46-57 kDa, PDI=2.3) and F_4TCNQ was purchased from TCI America.

A.1.2 Doping Fabrication Procedures

The first step in the fabrication process was cleaning glass substrates. First, the glass substrates were sonicated for approximately ten minutes in each cleaning solution (detergent, deionized water, acetone, and isopropanol). The substrates were dried with nitrogen gas before being put under vacuum for approximately 10 minutes.

P3HT solutions at concentrations of 0.5%, 2%, and 5% were prepared by respectively dissolving 5 mg, 20 mg, and 50 mg P3HT in 1 mL *ortho*-dichlorobenzene. The solutions were heated at 65 °C to dissolve the polymer and the solutions were cooled to room temperature before using. The solutions were used without any further preparation such as filtration. Films were prepared in a nitrogen atmosphere by spin-casting the P3HT solution on glass substrates at 1000 rpm for 60 s, followed by 3000 rpm for 5 s. The 0.5%, 2%, and 5% solutions respectively gave 25 nm, 110 nm, and 400 nm thick films. The 2 µm thick films were prepared by slow-drying: 30 µL of a 2% P3HT solution was drop-cast onto the glass substrate and placed into a covered Petri dish for two days for complete drying.

Evaporation sequential doping proceeded via thermal evaporation. F_4TCNQ was thermally evaporated onto P3HT films using an Angstrom Engineering Nexdep thermal evaporator: the F_4TCNQ powder was placed in an alumina crucible resistively heated at pressures $<1 \times 10^{-6}$ Torr to induce sublimation towards exposed P3HT samples fixed to an actively-cooled rotating sample stage; due to the high vapor pressure of F_4TCNQ, only low powers were needed to sublime the material, further ensuring the films were constantly cooled. The evaporation rate was 0.5 Å/s for the entire evaporation and the thickness of evaporated dopant was monitored using a quartz crystal microbalance located near the sample stage. Solution sequential doping proceeded via spin coating a solution of F_4TCNQ dissolved in dichloromethane (DCM) onto the P3HT film. The F_4TCNQ solution was cast directly on the P3HT film and spun at 4000 rpm for 10 s.

A.2 Optical Characterization

A.2.1 UV-Visible Spectroscopy

UV-Visible absorption experiments were carried out using a Lambda 25 UV-Vis spectrophotometer.

As shown in Figure A.3, there is close agreement in the spectral profiles for the solution- and evaporation-doped 110-nm- and 400-nm-thick pre-cast P3HT films that yield the highest electrical conductivities. We note that the 25-nm pre-cast P3HT film doped with the 1 mg/mL solution has the optimal conductivity, yet by UV-vis has a large F_4TCNQ neutral peak. This observation agrees with the report by Hamidi-Sakr et al. and our “overhead” analysis where some extra dopant is required for optimal doping.[29] Since this additional dopant is required to reorient and does not contribute to the doping, for thin films we expect to see a larger intensity for the F_4TCNQ neutral peak. We also note that the 25 nm evaporation-doped P3HT film does not have a large F_4TCNQ neutral peak, but instead has a high dopant:polymer thickness ratio. Thus, both evaporation and solution-sequential doping require extra F_4TCNQ, but the identification is different for each doping method. This highlights that despite the similarities in doping the film, some differences do exist and they are more apparent in the thinner films.

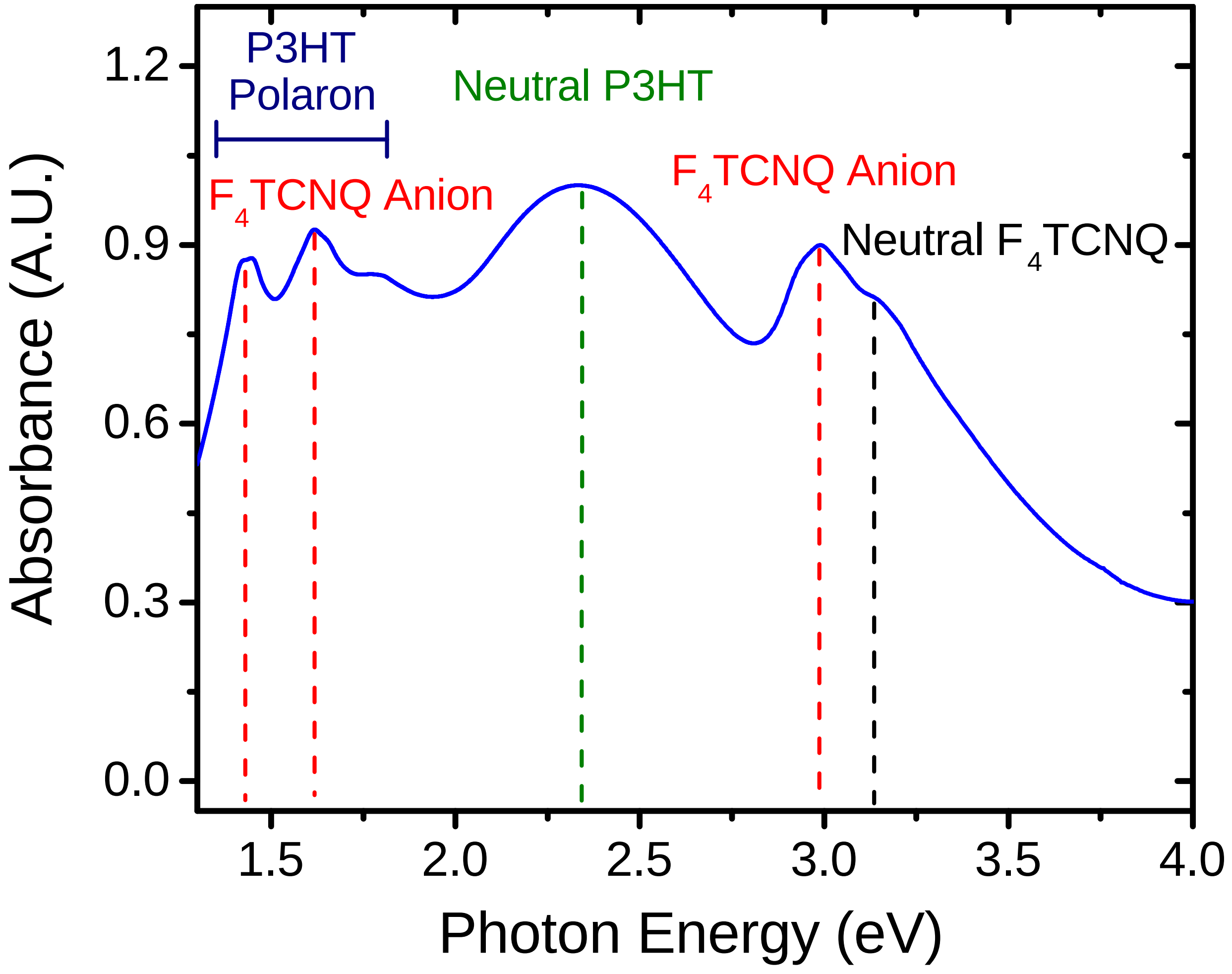

Figure A.1: Normalized UV-Visible spectra for a P3HT film doped with F_4TCNQ. Chemical doping results in the following peaks: P3HT polaron (navy), F_4TCNQ anion (red), neutral P3HT (green), and neutral F_4TCNQ, (black).

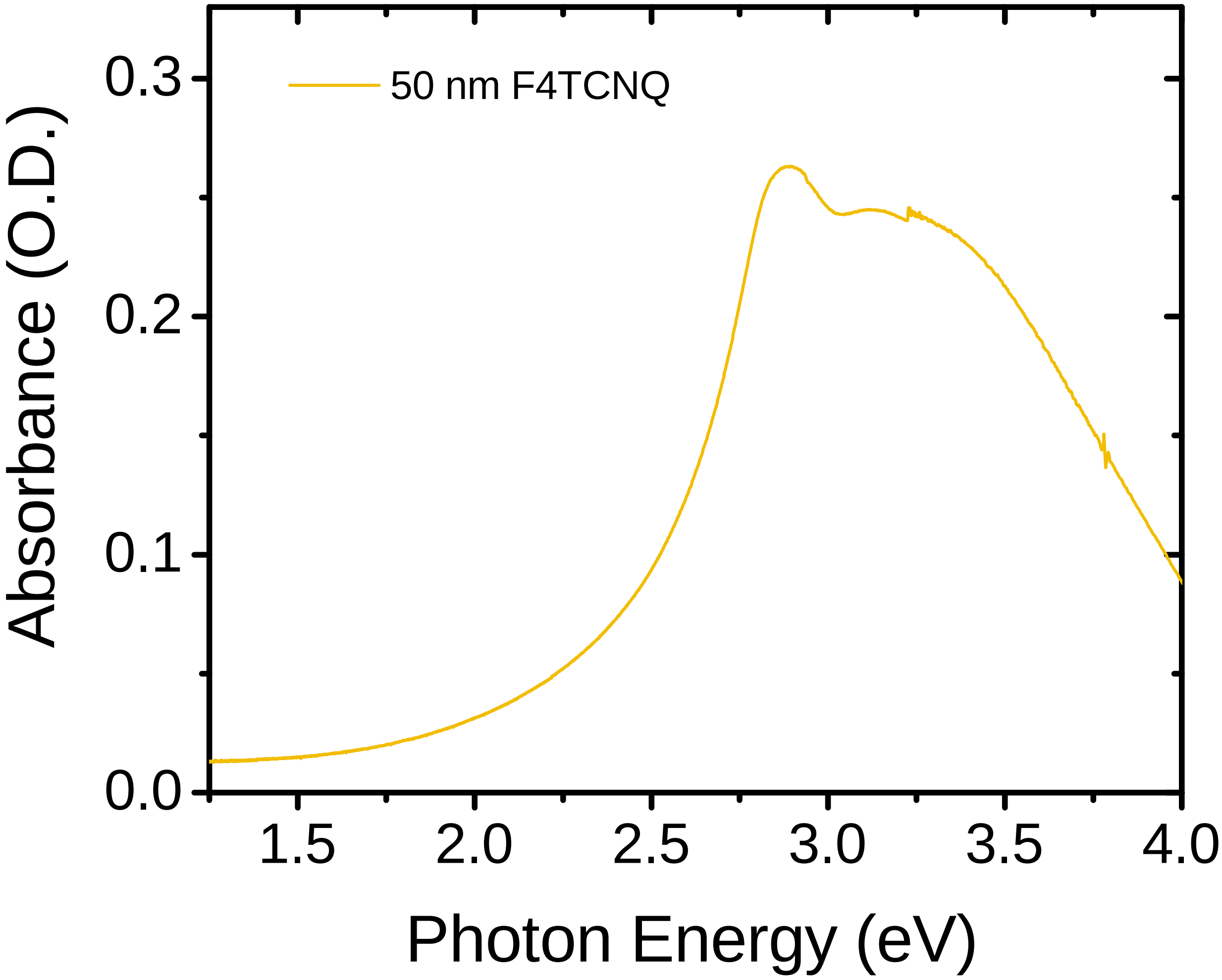

Figure A.2: UV-Visible spectrum of 50 nm evaporated F_4TCNQ on glass.

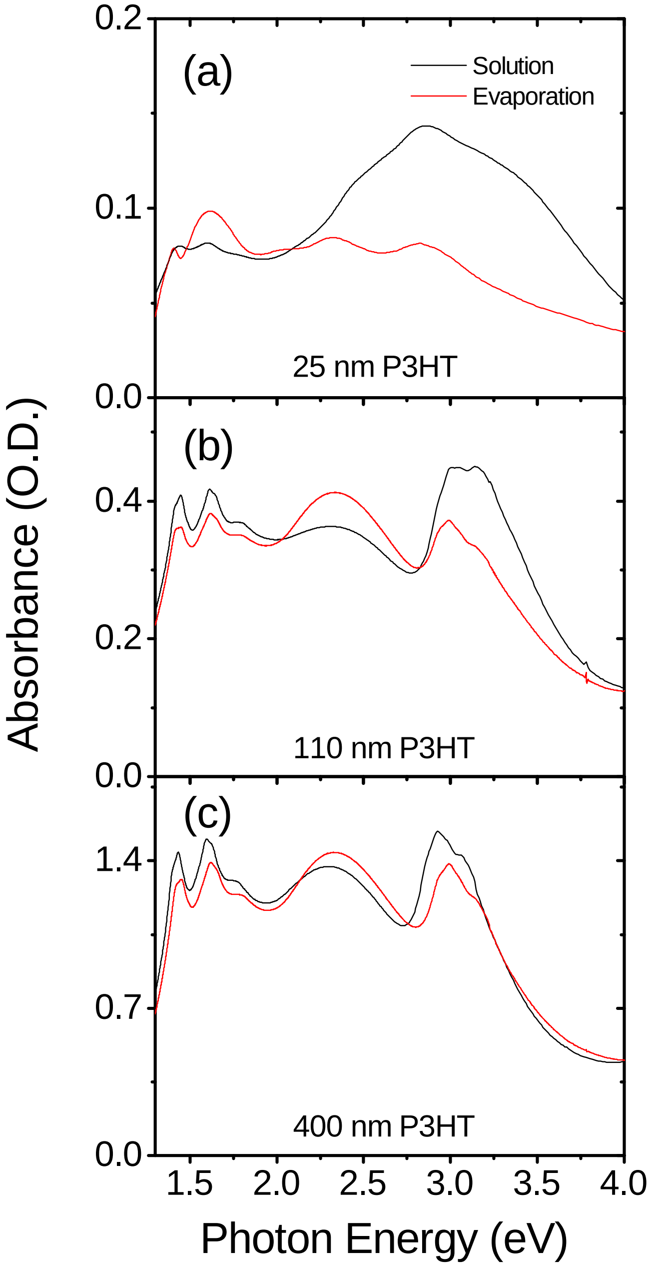

Figure A.3: UV-visible spectra for solution- and evaporation-doped P3HT films with the highest electrical conductivity. The films compared are (a) 25 nm pre-cast P3HT films, (b) 110 nm pre-cast P3HT films, and (c) 400 nm pre-cast P3HT films. Varying thicknesses of F_4TCNQ were evaporated on the P3HT films. As the thickness of P3HT increases, an increasing thickness of F_4TCNQ is required to effectively dope the film, as indicated by a decrease the in P3HT neutral peak and the increase of the F_4TCNQ anion peaks. For all films, as the film is saturated with F_4TCNQ, the neutral F_4TCNQ peak grows in as the primary feature.

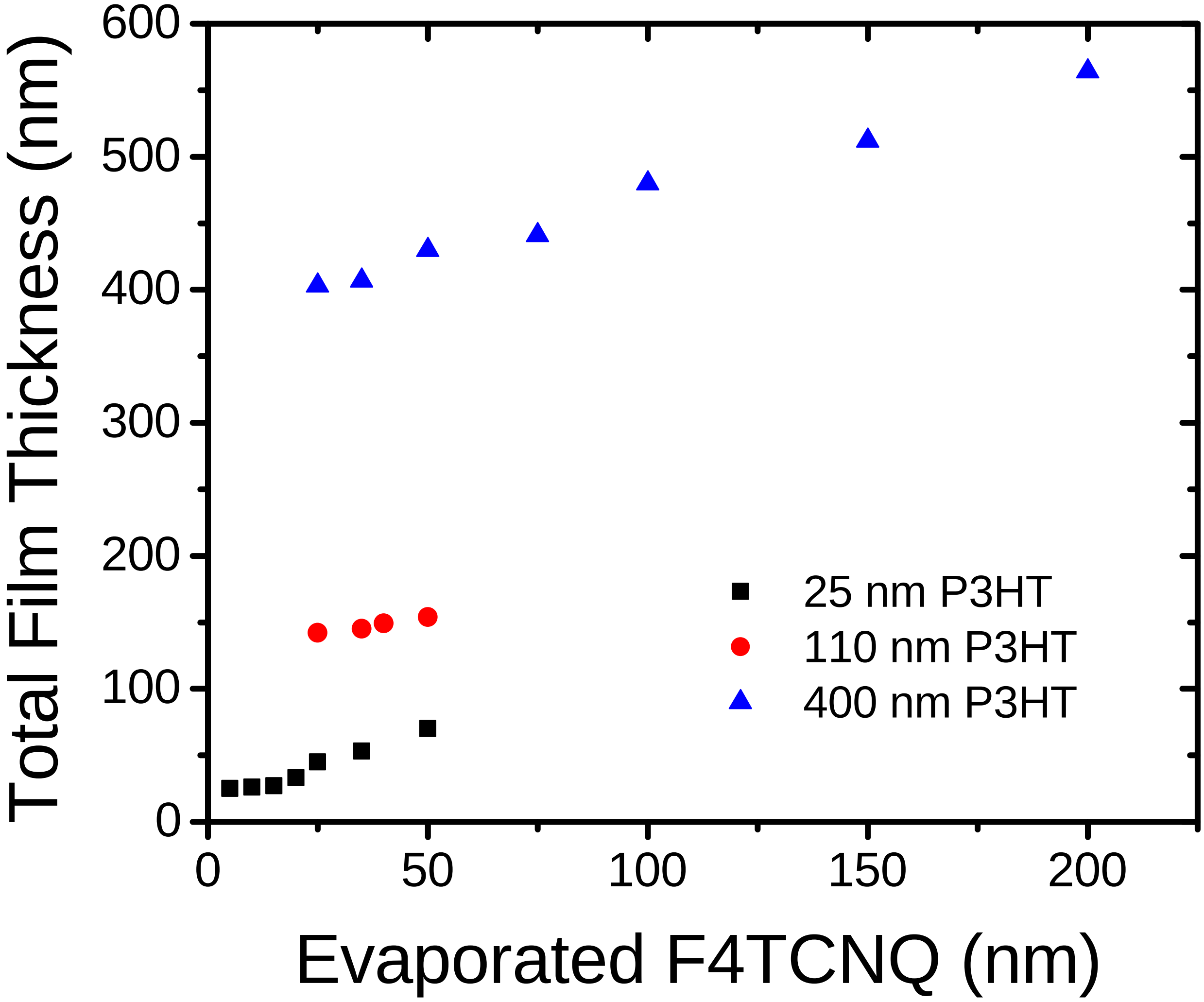

Figure A.4: Total film thickness for 25 nm (black squares), 110 nm (red circles), and 400 nm (blue triangles) pre-cast P3HT films after F_4TCNQ evaporation. For the initial evaporation of F_4TCNQ, the thickness change is very small.

A.3 Grazing Incidence Wide Angle X-Ray Scattering (GIWAXS)

2-D grazing incidence wide angle X-ray scattering (GIWAXS) experiments were performed at Stanford Synchrotron Light Source beamline 11-3. A wavelength of 0.9742 Å, incidence angle of 0.12°, and a 2-D charge-coupled device distance of 250 mm were used. 2-D diffractograms were radially integrated from 0-180° for full integration, 0-10° for in-plane curves, and 80-90° for out-of-plane curves. GIWAXS curves were reduced and processed using the WAXStools macro in IgorPro. Curves were thickness normalized based on the pre-doping thickness because only the polymer thickness contributes to diffraction intensity.

2-D images and 1-D integrated curves are shown in the figures A.5 and A.6 below demonstrating the orientation behavior relative to the substrate of all doped and undoped films discussed in this study.

A.4 Calculating the F_4TCNQ Overhead Thickness

Since the 25 nm, 110 nm, and 400 nm pre-cast P3HT films require, respectively, 15 nm, 40 nm, and 150 nm of evaporated F_4TCNQ in order to achieve optimal conductivity values, we can calculate the F_4TCNQ:P3HT thickness ratios: respectively, these values are 0.60, 0.36, and 0.38. The thickness required to orient the polymer, or "overhead" thickness can be calculated assuming that it does not contribute significantly to the conductivity. It is important to note that the dopant-to-polymer thickness ratios to maximize the electrical conductivity calculated above all assume each nm of dopant contributes to the conductivity. Once subtracting the "overhead" thickness, t, the optimal doping thicknesses for the 25 nm, 110 nm, and 400 nm films are, respectively, $15 - t$, $40 - t$, and $150 - t$. We find that when $t = 6$ nm, the dopant-to-polymer thickness ratios are, respectively, 0.36, 0.31, and 0.36.

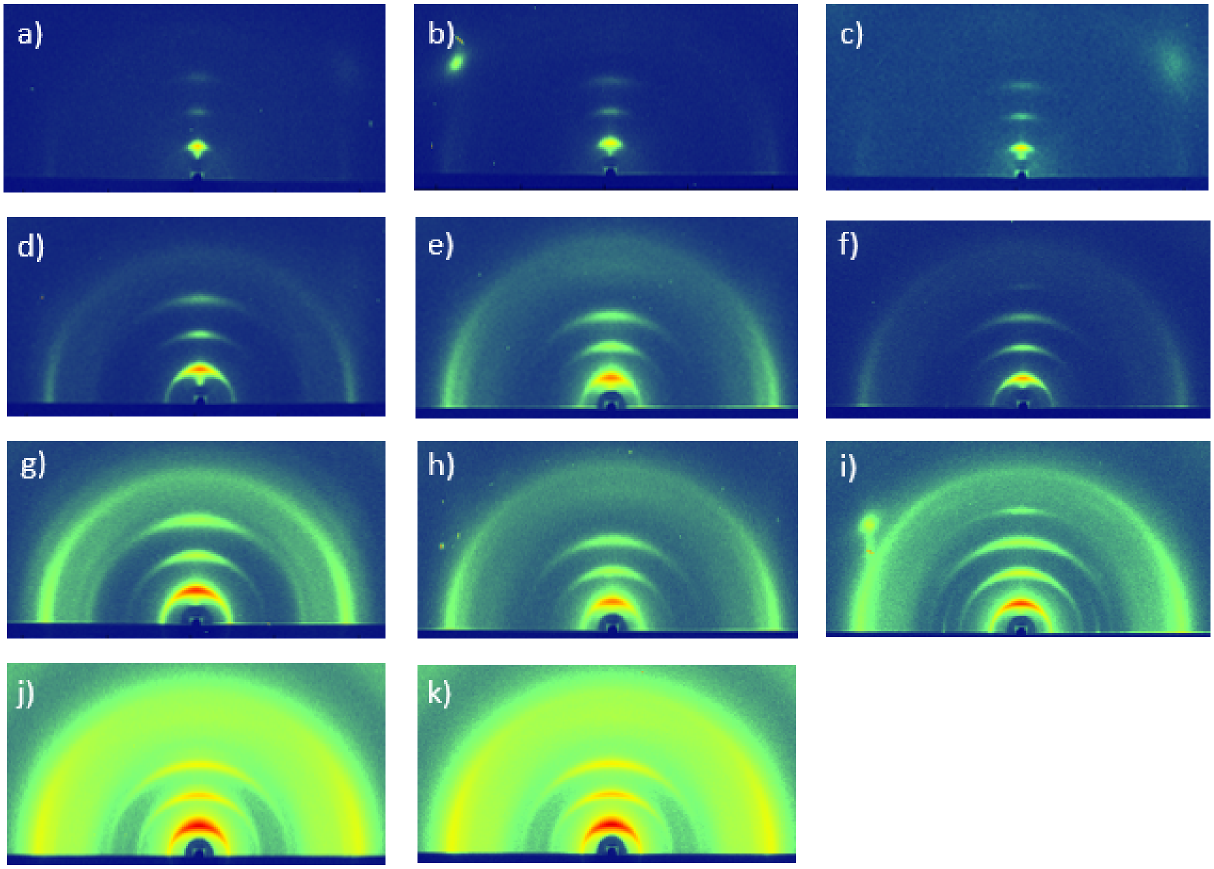

Figure A.5: Intensity color-mapped GIWAXS diffractograms for (a) Pure P3HT 25 nm, (b) solution-doped 25 nm, (c) vapor-doped 25 nm, (d) pure P3HT 110 nm, (e) solution-doped 110 nm, (f) vapor-doped 110 nm, (g) pure P3HT 400 nm, (h) solution-doped 400 nm, (i) vapor-doped 400 nm, (j) pure P3HT 2000 nm, and (k) solution-doped 2000 nm.

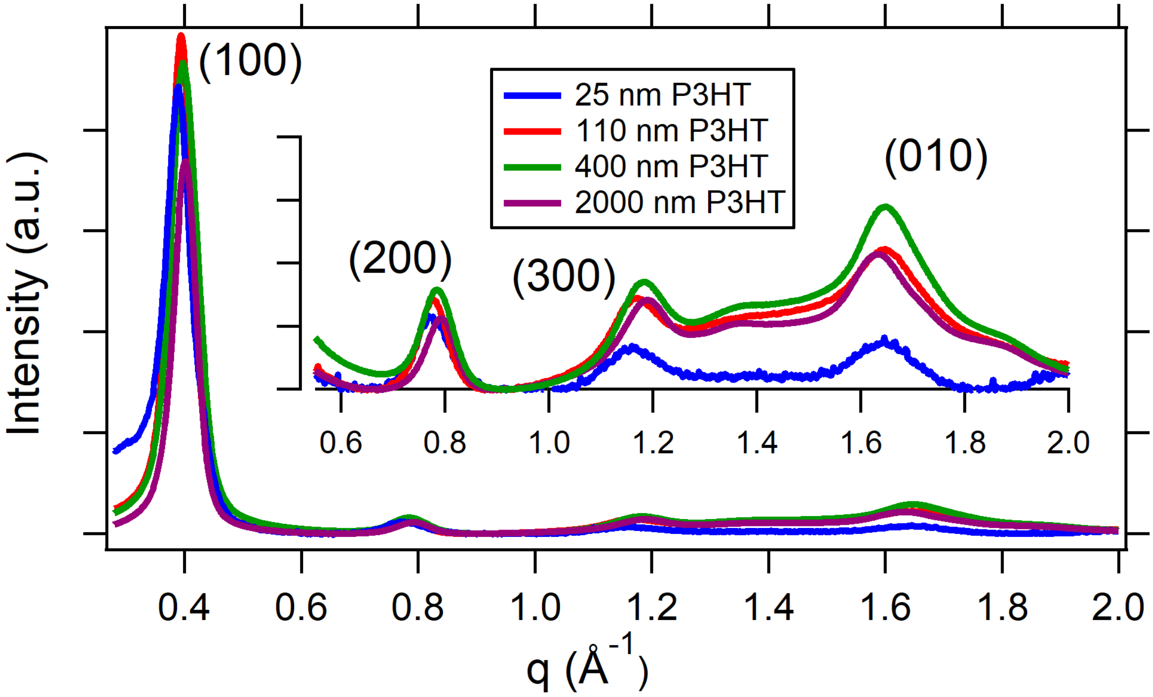

Figure A.6: Thickness-normalized full integrations of pure P3HT at various thickness demonstrating that there is little crystallinity difference between sample thicknesses. Crystallinity as demonstrated by the (100) peak intensity decreases slightly for thicker films.

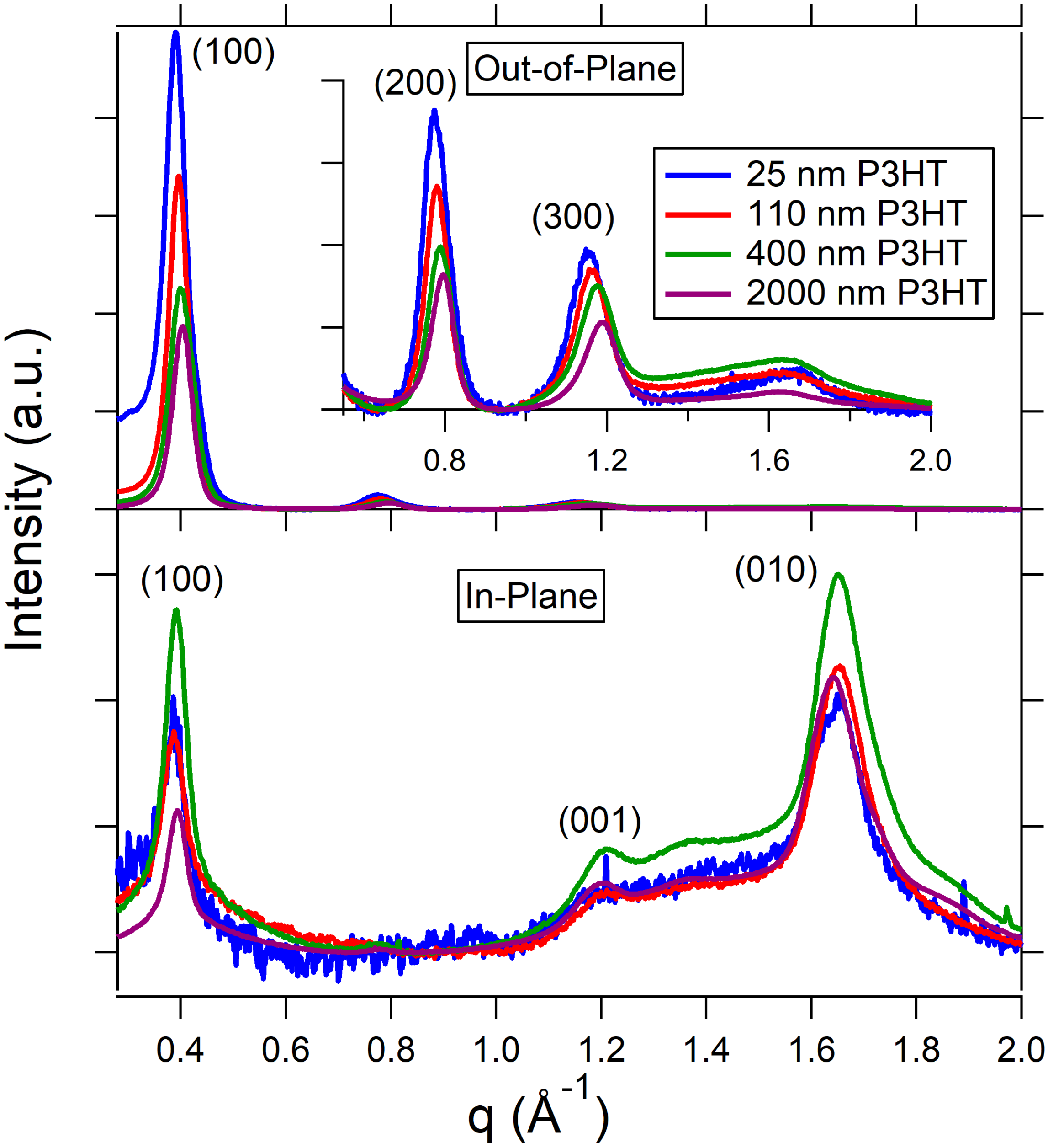

Figure A.7: Out-of-plane (top) and in-plane integrations of pure P3HT demonstrating predominantly edge-on orientation is preserved for all film thicknesses.

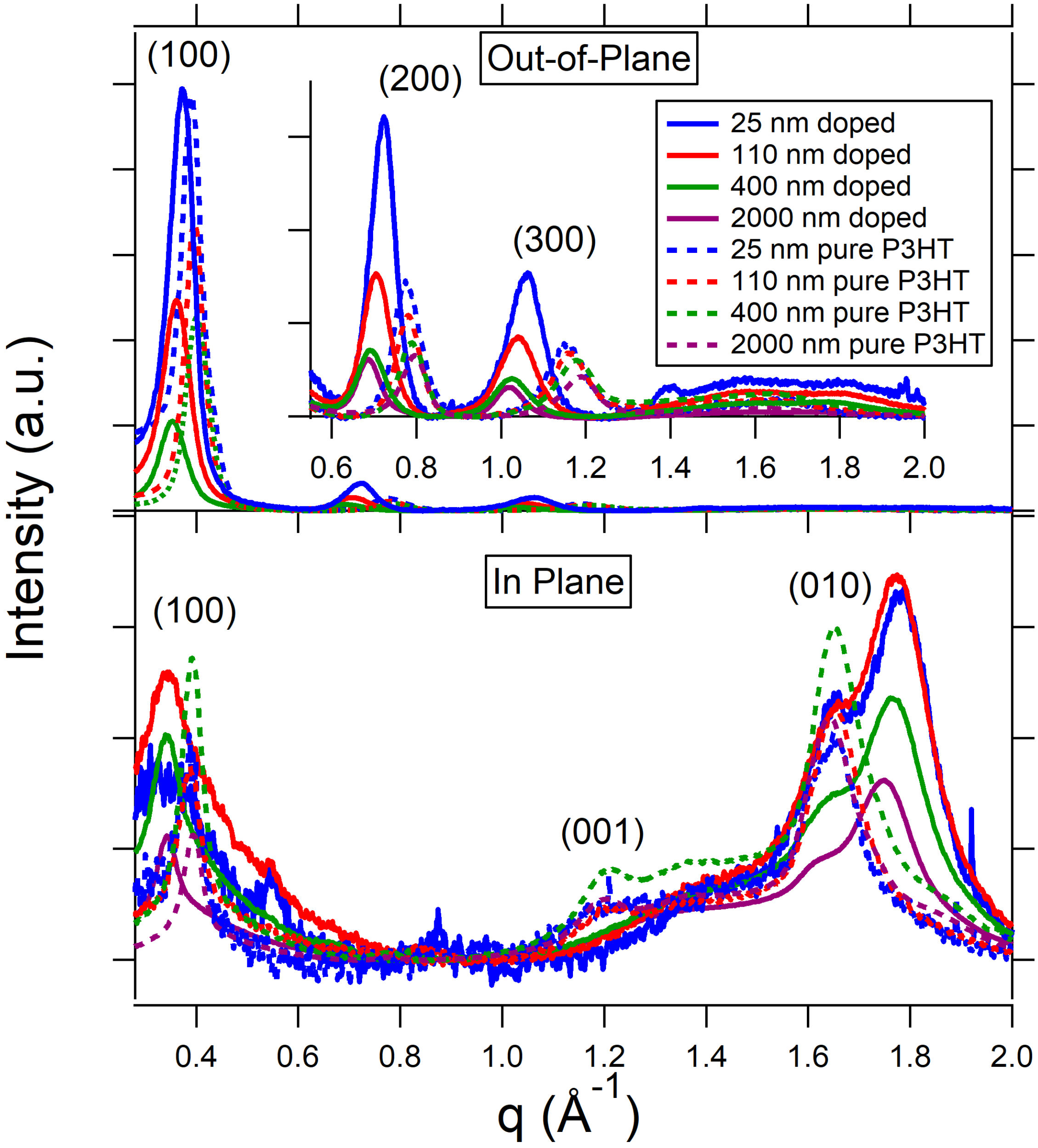

Figure A.8: Out-of-plane (top) and in-plane (bottom) integrations of solution-doped P3HT. This demonstrates that the edge-on orientation does not change upon SqP doping via solution processing.

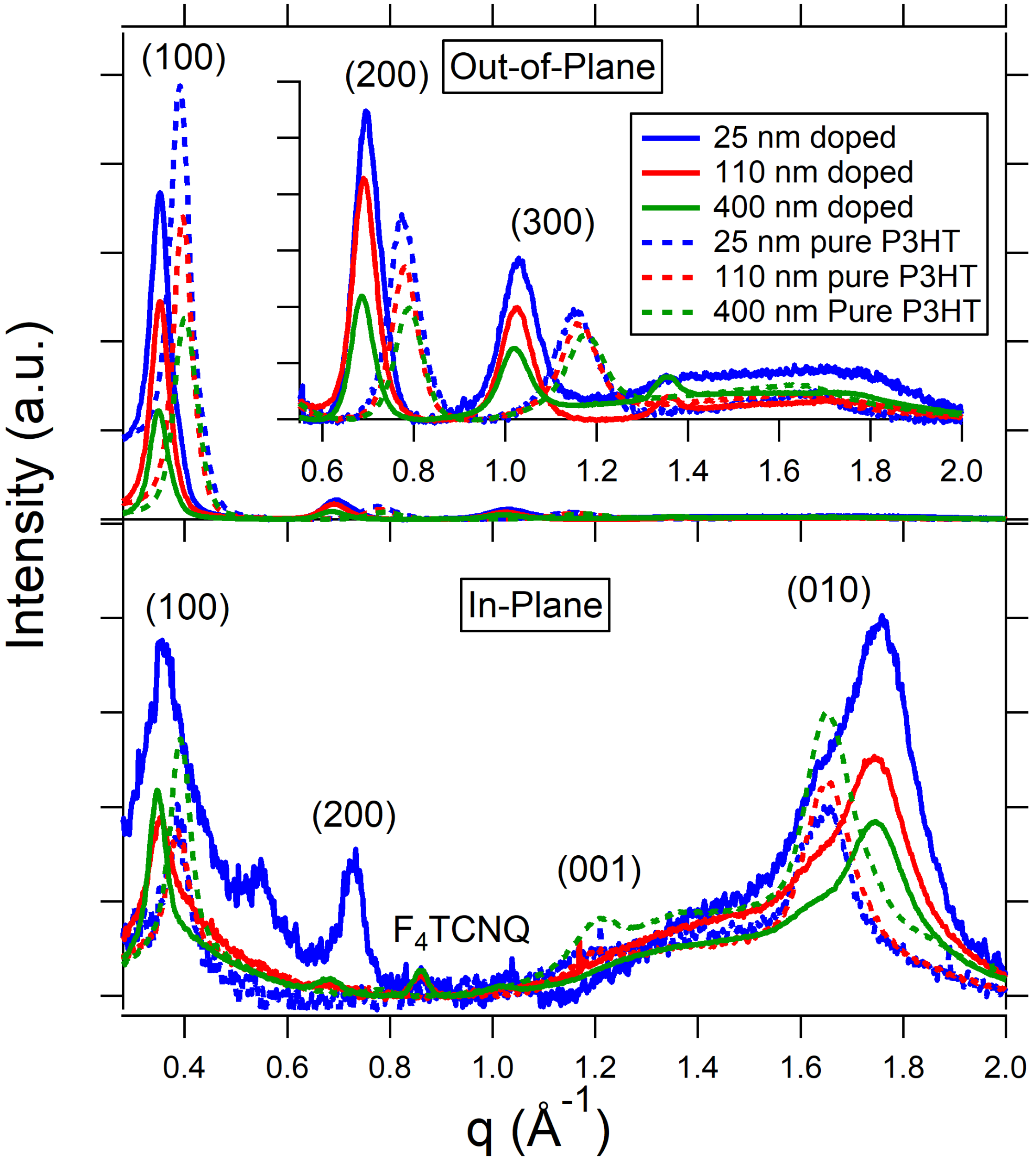

Figure A.9: Out-of-plane (top) and in-plane (bottom) integrations of vapor-doped P3HT. This demonstrates that the edge-on orientation does not change upon vapor-doping.

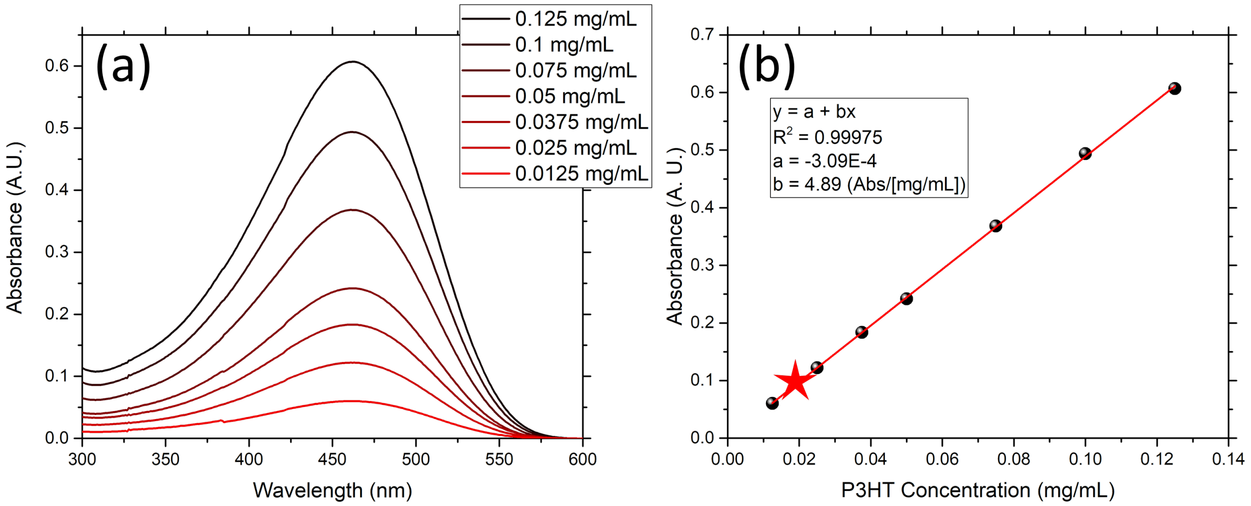

Figure A.10: (a) UV-Vis absorbance spectrum for known P3HT solution concentrations. (b) Calibration curve of P3HT dissolved in ODCB from the data in (a). The red star indicates the average absorbance for P3HT films re-dissolved in 1.00 mL ODCB.

A.5 Determination of Monomer:Dopant Ratio in Evaporation-Doped Films

The mass density of our P3HT films and evaporated F_4TCNQ films was determined using a previously-described method[108] that relies on UV-Vis spectroscopy and surface profilometry. First, a calibration curve was constructed of known concentrations of P3HT solutions dissolved in ODCB, as shown in Figure A.10. Next, we used profilometry and the fact that Volume = Thickness × Area, to obtain the total volume of a P3HT film on a $1.5 \times 1.5\,\mathrm{cm}^2$ substrate was obtained. In order to determine the average mass of a P3HT film of known volume, the film was dissolved in 1.00 mL of ODCB and the UV-Vis absorbance of the resulting solution was measured. This absorbance was then compared to a least-squares linear fit of the calibration solutions to obtain the mass of the dissolved P3HT. This procedure yielded a P3HT mass density of $\sim 1.29\,\mathrm{g\,cm^{-3}}$, in line with previously reported P3HT densities[173, 174] that range between $1.1\text{-}1.33\,\mathrm{g\,cm^{-3}}$.

For F_4TCNQ, we first followed a similar procedure as for P3HT films followed above. We note that the density of F_4TCNQ single crystals has been reported to be $1.68\,\mathrm{g\,cm^{-3}}$, which is quite a bit higher than that of P3HT. Figures A.11 and A.12 show that using the re-dissolution method, we arrived at an unexpectedly low mass density value for our evaporated F_4TCNQ films of only

$0.74\,\mathrm{g\,cm^{-3}}$, less than half that of the single crystal. Given how low the evaporated density came out, we worked to verify this number using an independent technique. Our thermal evaporator uses an SQC-310 Thin Film Deposition Controller from INFICON and the user manual details a standard procedure for refining the density value for a given material. Using a fresh QCM thickness monitor, setting the deposition tooling factor to 100%, Z-factor to 1.000 and inputting a "best guess" density, D_1, for the pure crystal value. After placing a sample directly adjacent to the QCM sensor, a 100-nm deposition, T_x, of F_4TCNQ was carried out as measured by the SQC-310, followed by a measurement of the actual film thickness, T_m, using profilometry. Using Eq. A.1, this procedure was performed 3 times, each with a successively more accurate "best guess" until the revised estimate gave $0.77\,\mathrm{g\,cm^{-3}}$, and a final iteration confirmed the value with $T_m = T_x$, and the same density $0.77\,\mathrm{g\,cm^{-3}}$.

$$\mathrm{Density}(\mathrm{g/cm^3}) = D_1 \left(\frac{T_x}{T_m}\right) \tag{A.1}$$

To further verify the validity of this method, we employed the Sauerbrey equation (Eq. A.2) relating the change in resonant frequency for an ideal AT-cut quartz crystal resonator to the change in mass, where here the mass of the added material is approximated to be part of the QCM itself. It is important to note that the relationship between these two quantities can only be assumed to be linear for the first 5% change in resonant frequency thus requiring the use of a new QCM sensor.

$$\Delta m = -\frac{\Delta f A \sqrt{\rho_q \mu_q}}{2 f_0^2} \tag{A.2}$$

Simply using the resonant frequency change, Δf, the piezoelectrically active crystal area (i.e., the QCM area exposed to the impinging material), A, the density and shear modulus of quartz for an AT-cut crystal, ρ_q, and μ_q, respectively, (Table A.1) and the profilometer measured thickness of 108 ± 8 nm, we obtained a calculated density of $0.77 \pm 0.06\,\mathrm{g\,cm^{-3}}$.

Note that the density obtained by the UV-Vis re-dissolution method, $0.74\,\mathrm{g\,cm^{-3}}$, is within the error of this presumably more trustworthy method which relies on very sensitive changes in QCM resonant frequency, so it appears that the density of evaporated F_4TCNQ is indeed about half that of the single crystal. We use $0.77 \pm 0.06\,\mathrm{g\,cm^{-3}}$ for our calculations of the monomer:dopant ratio presented in the main text. To further justify the validity of this abnormally low density, we

Table A.1: List of parameters used and calculated for the method relying on the Sauerbrey equation.

Parameter	Value
f_0	5 986 930.02 Hz
f_{final}	5 986 254.63 Hz
Δf	-675.39 Hz
Δm	4.027 µg
A	0.4869 cm^2
$T_{profilometer}$	108 ± 8 nm
Calculated Density	$0.77 \pm 0.06\,\mathrm{g\,cm^{-3}}$

performed the same set of experiments on an evaporated film of silver (114 ± 4 nm). It is typical for evaporated thin films to have somewhat lower densities when compared to their bulk values and this was indeed true for our silver sample. We calculated a density of $9.28 \pm 0.27\,\mathrm{g\,cm^{-3}}$ compared to the bulk value of $10.49\,\mathrm{g\,cm^{-3}}$.

A.6 Electrical Measurements

A.6.1 Conductivity Measurements

Conductivity measurements were collected in the Van der Pauw geometry using a custom-made apparatus. The measurements were collected in ambient atmosphere using a Keithley 2400 sourcemeter where the max current ranged from 10 µA to 100 µA. The current was swept from negative to positive, rotated 90 °, and repeated. The slope of the I–V curves were subsequently fit to the Van der Pauw equation. Note that our 4-point probe Van Der Pauw technique relies on a Keithley 2400 and is not capable of accurately measuring values with sheet resistances above $\sim 5 \times 10^8\ \Omega/\square$. This sheet resistance corresponds to conductivities far below what we have reported here. Samples in the Van der Pauw geometry were prepared as described in the main text, with silver paste applied at the corners of the film to act as contacts.

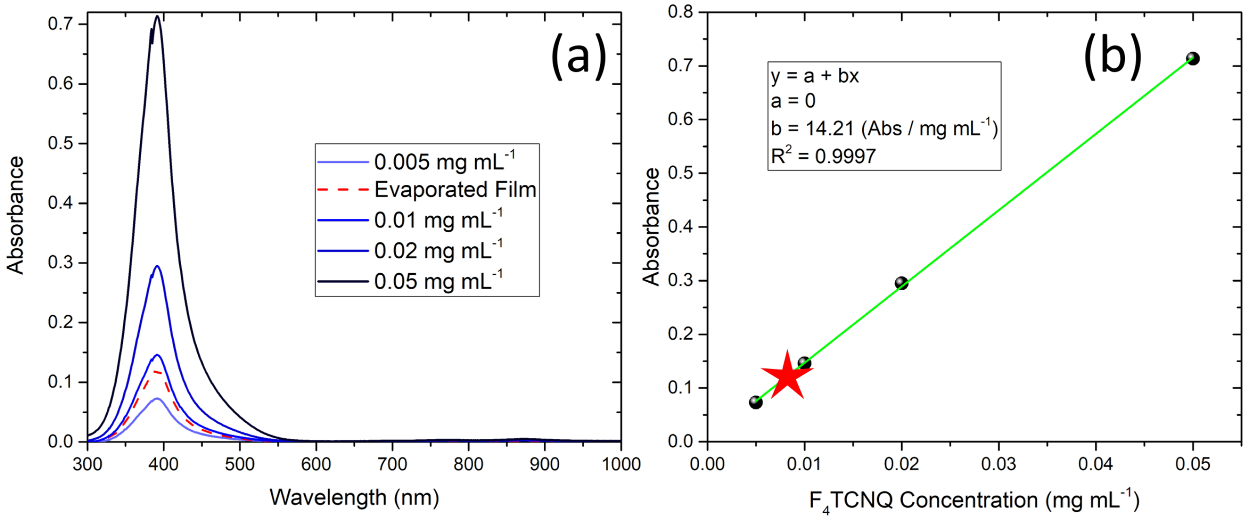

Figure A.11: (a) UV-Vis absorbance spectrum for each solution concentration. Red star indicates the average absorbance for F_4TCNQ films dissolved in 1 mL ODCB. (b) Calibration curve of F_4TCNQ dissolved in ODCB and serial diluted to obtain a range of concentrations.

A.6.2 Sheet Resistance Over Time

To verify that the vapor doped films were stable over time, we periodically tested sheet resistance over several hours. In Figure A.13 it can be seen that the film sheet resistance is largely unchanged over a period of 130 minutes, indicating the majority of dopants have already undergone charge transfer and films remain stable to degradation in air over a period of hours.

A.6.3 Thermoelectric Measurements

Samples for the Seebeck measurement were prepared as earlier described in the text. To reduce contact resistance at the electrodes, 15 nm molybdenum oxide (MoO_3) was first evaporated, followed by 60 nm of silver. To ensure reproducibility of the Seebeck measurement, the distance between electrodes was kept constant by evaporating the metal contacts through a shadow-mask with an active layer gap of 6.6 mm. The measurements were collected in an argon atmosphere.

The Seebeck measurement requires the use of an HP 6632A DC power supply to power both peltier heat pumps (the hot and cold sinks), a Keithley 2400 source meter to run the resistance temperature detectors (RTDs) that measure the temperature at each electrode, and a Keithley 2000

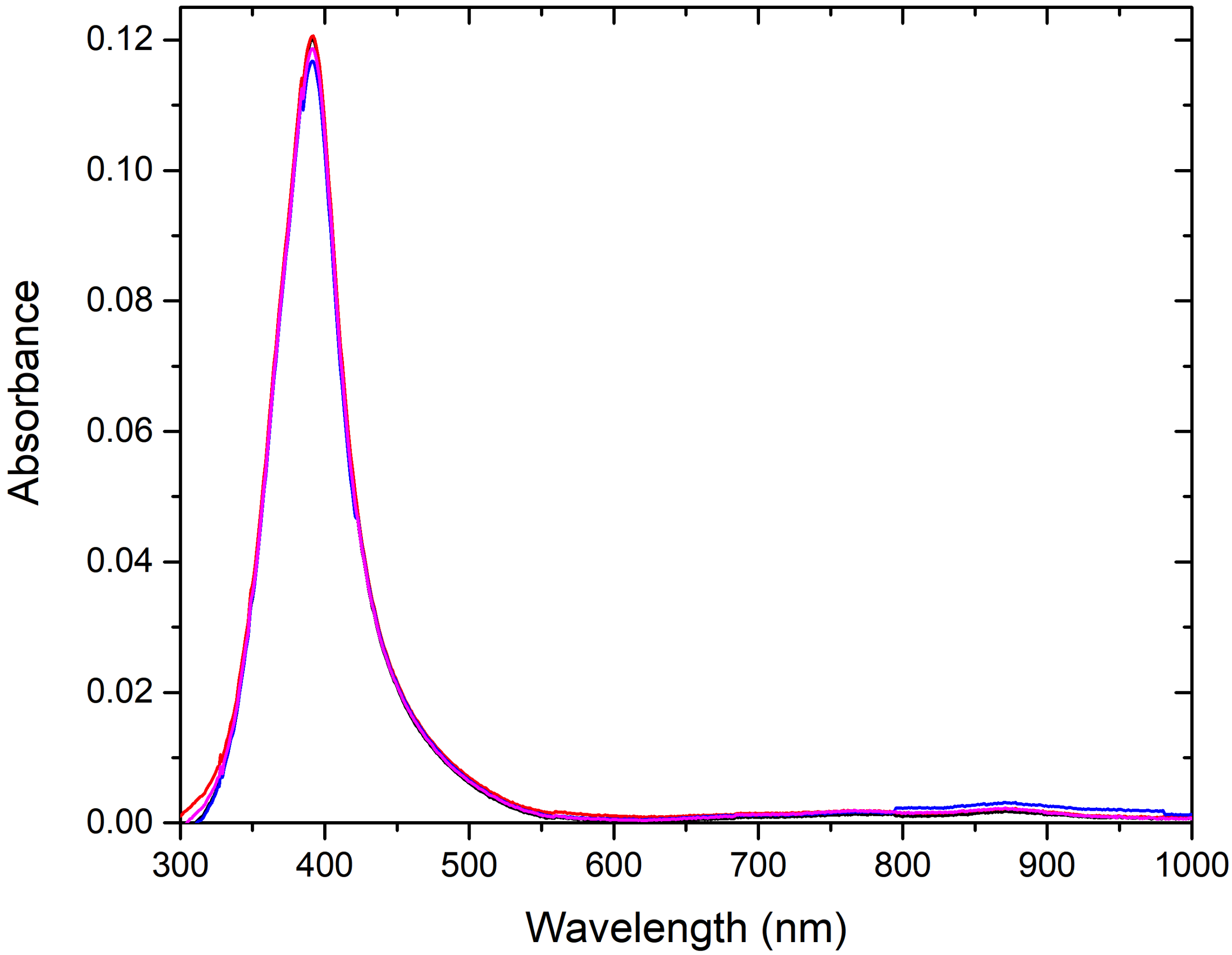

Figure A.12: An overlay of 5 samples with 50 nm of F_4TCNQ evaporated on 1.5 cm × 1.5 cm substrates. Samples were each dissolved in 1 mL ODCB prior to taking UV-VIS

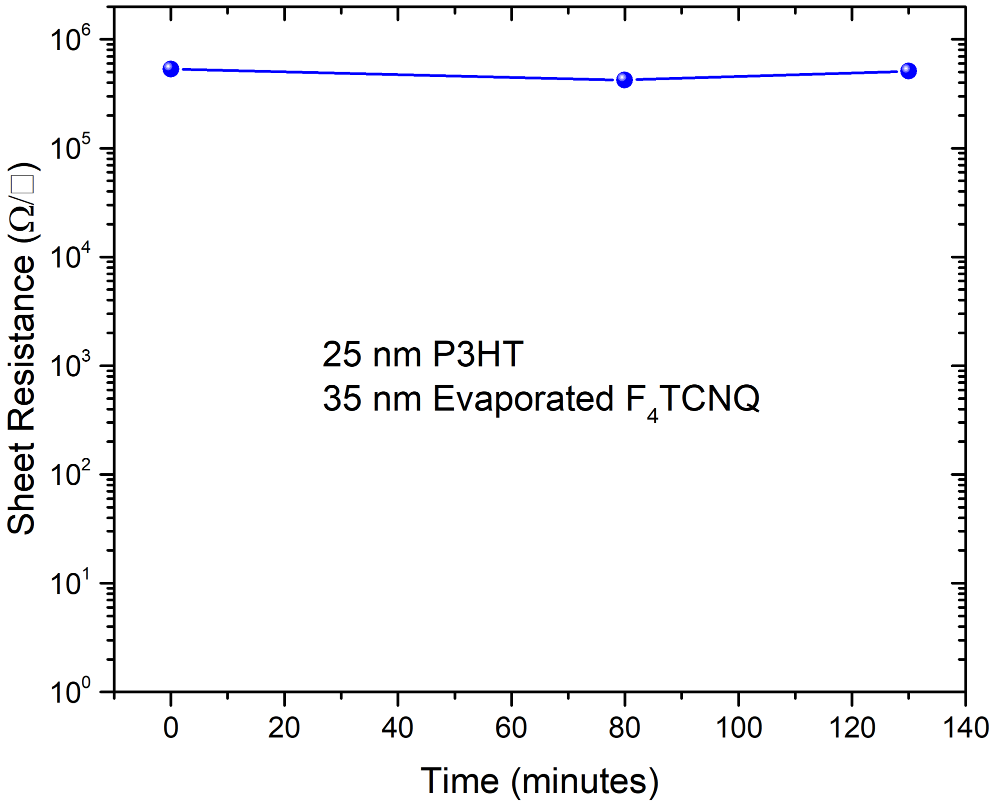

Figure A.13: Sheet resistance measured for a precast 25 nm P3HT film, vapor doped with 30 nm of F_4TCNQ.

digital multimeter to measure the induced thermoelectric voltage.

A home-built LabVIEW program controls the measurement and operates as follows. A temperature gradient is first established across the device using the two peltier devices. Once the temperature gradient stabilized, the induced voltage drop across the two electrodes is measured. Following this, a larger temperature gradient is defined and the process repeated until a satisfactory range of values can be recorded (thermovoltage vs. temperature difference). The thermovoltages sampled ranged from 2 °C to 9°C. The data was then fit to a least squares linear regression and the Seebeck coefficient was determined from the corresponding slope, where all $R^2 \geq 0.999$ with an example plot shown in Figure A.15.

A.6.4 Seebeck Empirical Power Law Fitting

It has been empirically observed that the Seebeck coefficient follows the proportionality $S \propto \sigma^{-1/4}$.[22,96] More, precisely the corresponding power law is defined as:

$$S = \frac{k_B}{e}\left(\frac{\sigma}{\sigma_\alpha}\right)^{-1/4}$$

where S is the Seebeck coefficient, k_B is the Boltzmann constant, e is the fundamental unit charge, σ is the electrical conductivity, and σ_α is an empirical constant fitted to $1\,\mathrm{S\,cm^{-1}}$.[96] For convenience, the term $\frac{k_B}{e}$ is represented in the unit of thermopower as $86.17\,\mu\mathrm{V\,K^{-1}}$. We plotted the Seebeck coefficient for both evaporation and solution sequential-doped as a function of the electrical conductivity. The data points used are from the samples that produced the highest electrical conductivities for each doping method, as shown in the main text. As shown in Figure A.17 the evaporation and solution sequential-doped films match the empirical power law well.

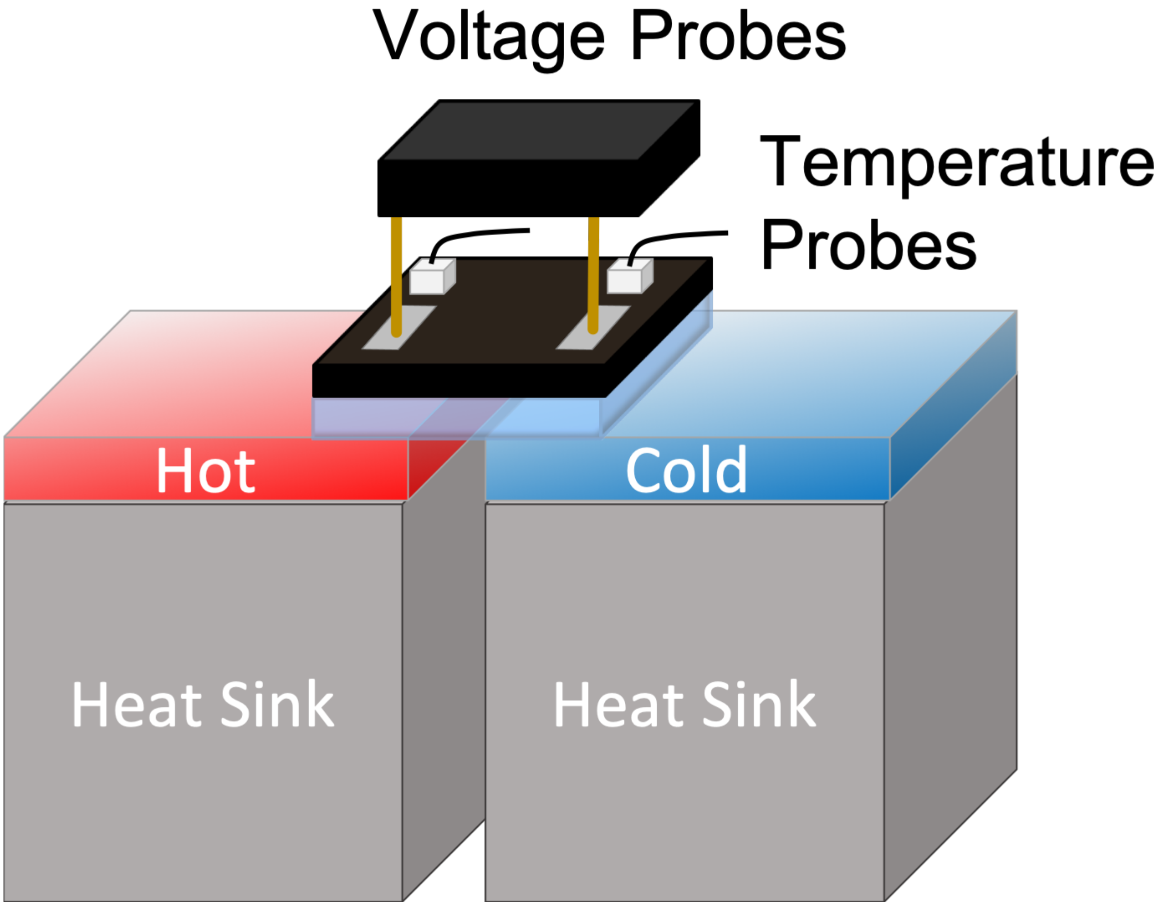

Figure A.14: A schematic of the home-built setup for taking Seebeck measurements. The temperature gradient was maintained by a set of Peltier devices attached to aluminum heat sinks. The distance between the sensing locations (6.6 mm) was kept constant across all devices tested. The RTDs were lowered down onto the film using a probe alignment head, ensuring they were always separated by the same distance as the electrical contacts.

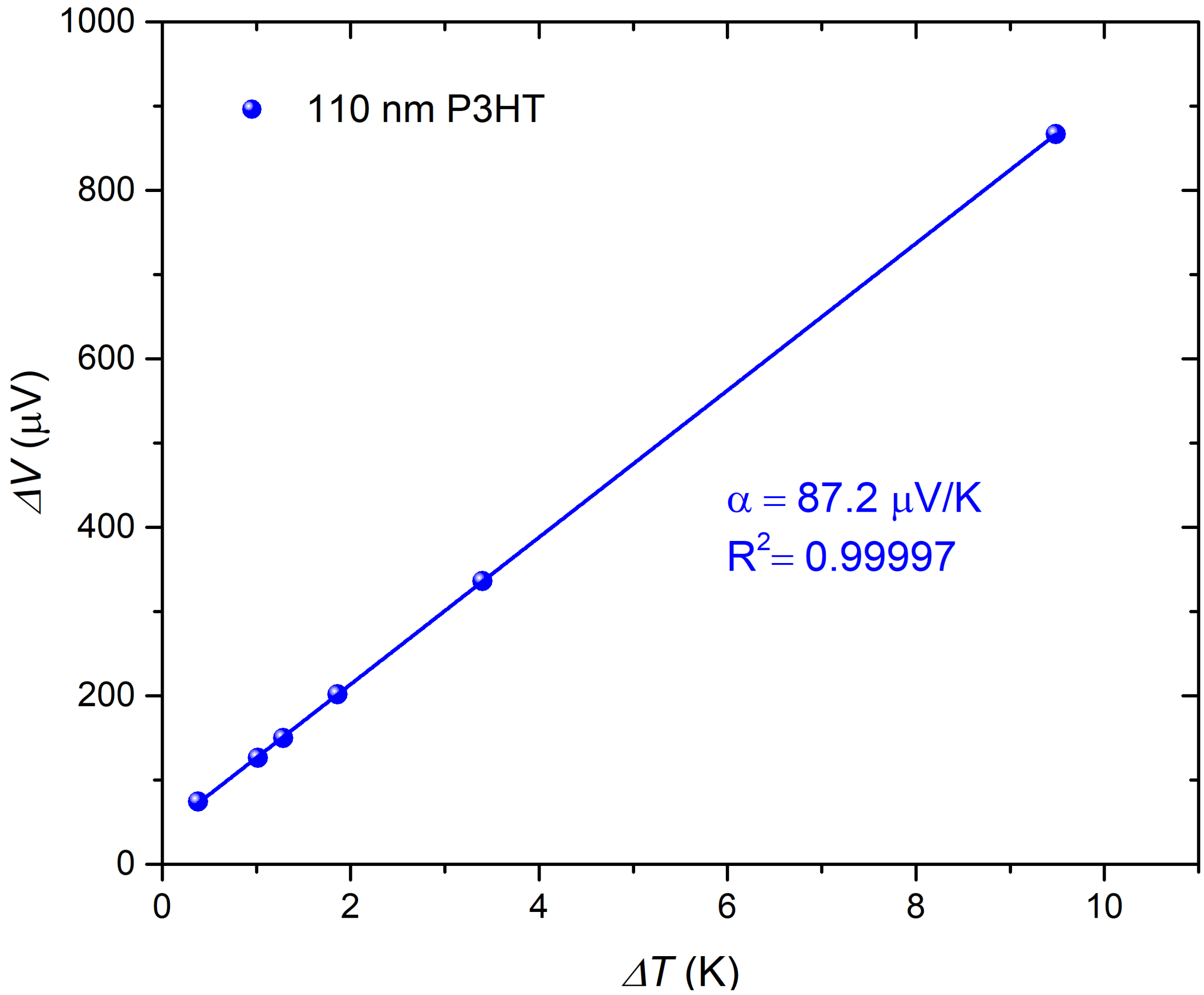

Figure A.15: Graphical determination of the Seebeck coefficient for a pre-cast 110 nm P3HT film doped with a 1 mg/mL F_4TCNQ solution. Two thermoelectrics (the hot and cold sinks) are powered to established a temperature difference (ΔT). For each temperature difference, the thermovoltage (ΔV) was measured, allowing a line to be constructed. Using the slope of the line, the Seebeck coefficient was determined.

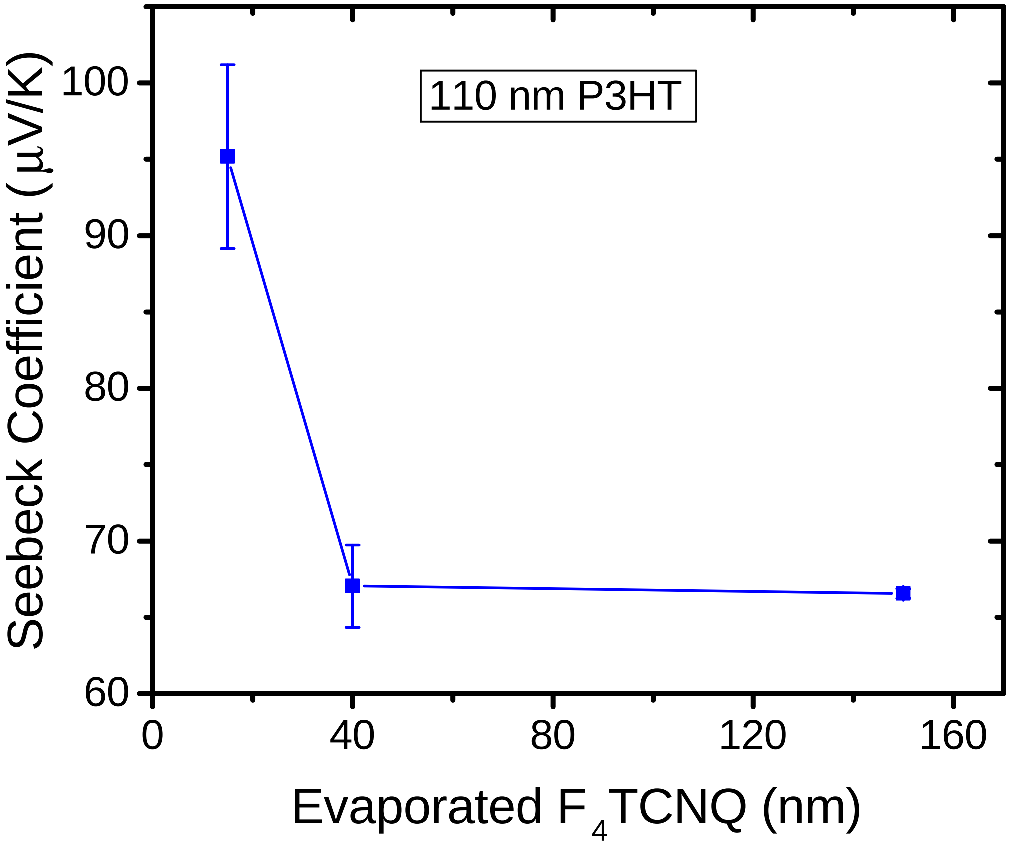

Figure A.16: Seebeck coefficients for pre-cast 110 nm P3HT films doped with 15 nm, 40 nm, and 150 nm of F_4TCNQ. The three thicknesses were selected to under-dope, optimally-dope, and over-dope with respect to the electrical conductivity. Once optimally doing the film with 40 nm of dopant, the Seebeck coefficient remains constant to higher doping levels.

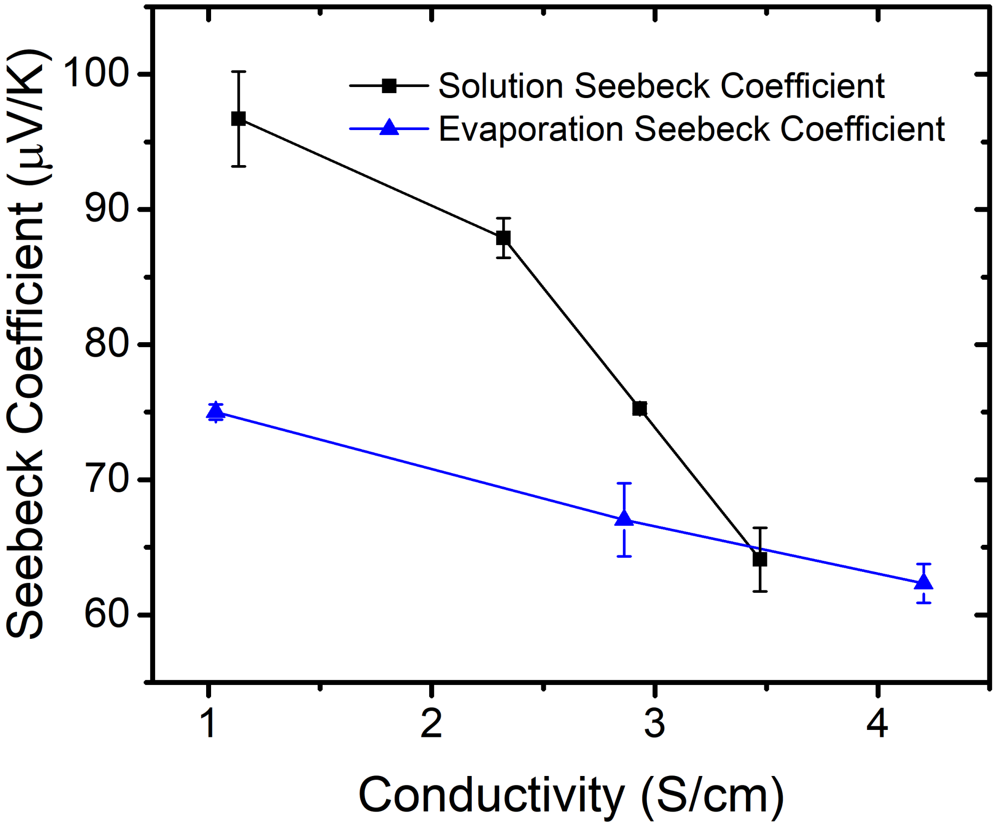

Figure A.17: Solution (black squares) and evaporation (blue triangles) Seebeck coefficient (*S*) plotted as a function of the electrical conductivity (σ). The negative correlation between these two properties can be better visualized when plotted against each other.

APPENDIX B

Supporting Information for Chapter 3

B.1 Experimental Methods

B.1.1 Optical & Electrical Measurements

UV-vis-NIR absorbance spectra were acquired between 300-2000 nm with a Shimadzu UV3101PC Scanning Spectrophotometer using polymer films prepared on glass substrates. FTIR absorbance of the P1 polaron band and F_4TCNQ C≡N stretching mode were acquired between 480-5000 cm^{-1} using a Jasco FT/IR-420 spectrometer. The corresponding polymer films were prepared on KBr plates.

Figure B.1 shows UV-vis spectra of P3HT films sequentially solution doped with F_4TCNQ (1 mg mL^{-1}) from solvents with a wide rage of solubilities towards P3HT: Acetonitrile (3×10^{-5} mg mL^{-1}), dichloromethane (0.818 mg mL^{-1}), and chloroform (38 mg mL^{-1}).[135] For dopant solvents with increased solubility towards P3HT, the neutral absorption of P3HT near 2.5 eV diminishes in the doped films. Once the solubility increases to a level like that of chloroform, the two peaks near 1.5 eV and third near 3.0 eV (dashed red lines) which are all indicative of ICT, become reduced in magnitude, while peaks near 2.0 eV and 3.3 eV (dashed green lines), which indicate new CTC transitions, increase in magnitude.

Figure B.2 shows an unrefined set of spectra for the (20/80) CF/DCM solvent blend conditions, to illustrate the method used for constructing the combined UV-vis-NIR / FTIR spectra, for example, in Figure 3.1 of the main text. UV-vis-NIR spectra were acquired on films using glass substrates and FTIR was acquired for the same film conditions cast on KBr plates. The two spectra were connected at 5000 cm^{-1} = 2000 nm = 0.619 eV in what is shown in the main text.

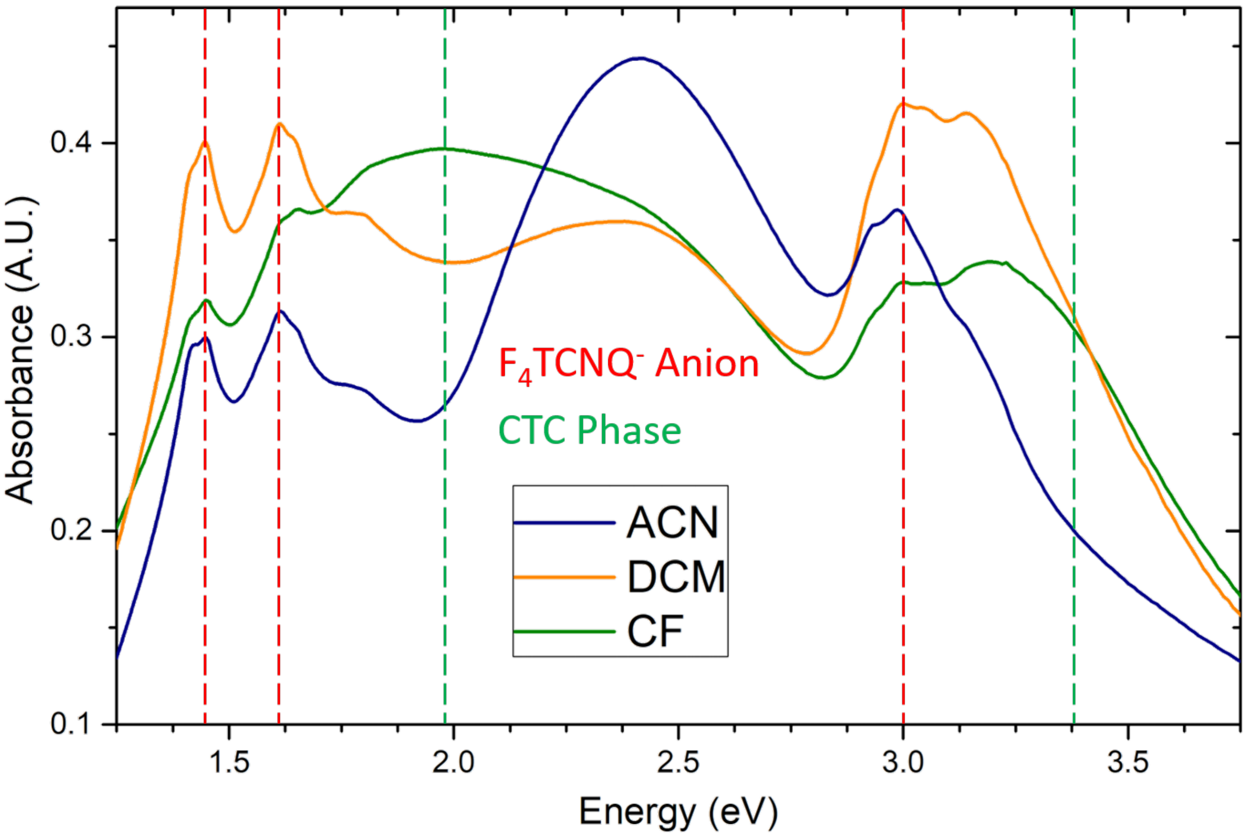

Figure B.1: Films sequentially solution doped with F_4TCNQ ($1\,\mathrm{mg\,mL^{-1}}$) from solvents with increasing solubility towards the underlying P3HT layer.

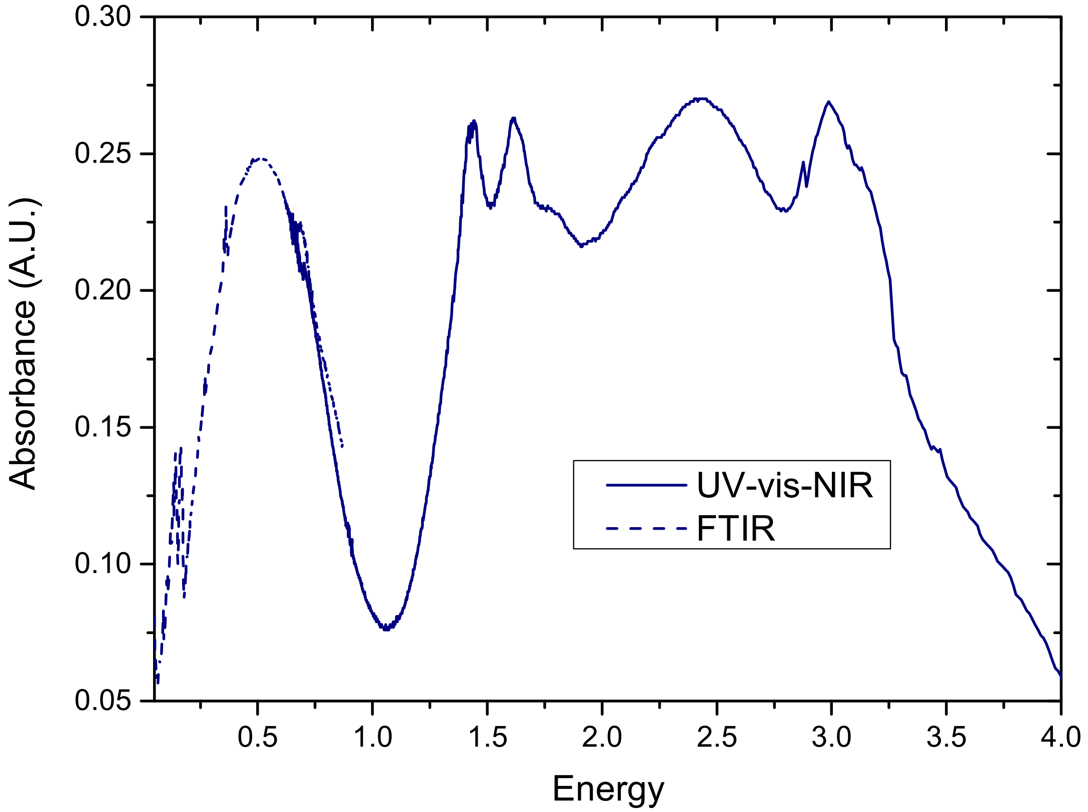

Figure B.2: (Dashed blue) raw absorption profile captured from FTIR spectrometer. (Solid blue) raw absorption profile captured from UV-vis-NIR spectrophotometer

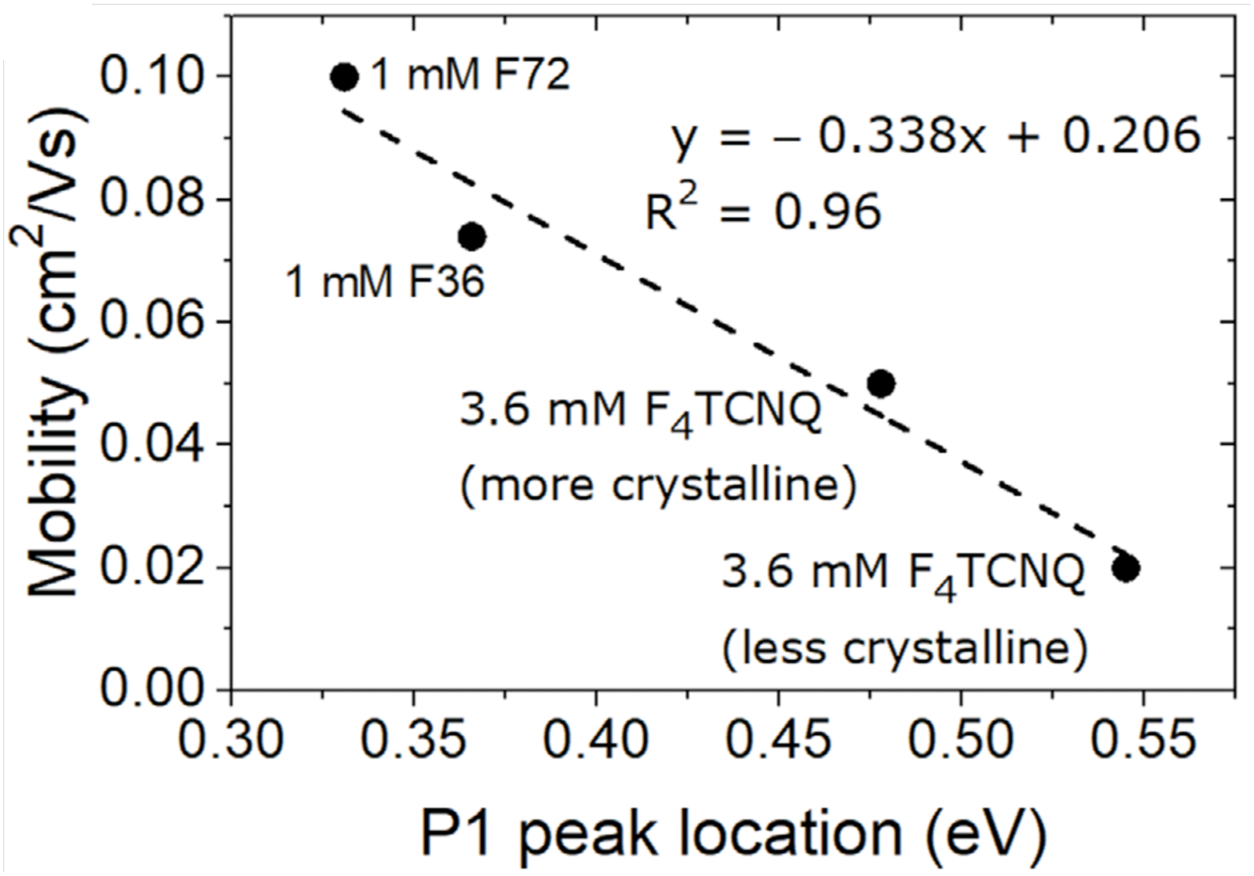

Figure B.3: (Borrowed from ref 2) AC Hall determined mobility vs fitted P1 peak absorption. A roughly linear relationship exists between the two in this regime.

Doped polymer film samples used for measuring electrical conductivity were prepared on 1.5×1.5 cm^2 glass substrates. Resistivity was measured via a home-built four-point probe setup using the Van der Pauw method with electrodes placed at the corners of the substrate. In order to convert resistivity to conductivity, the corresponding film thicknesses were also measured for each sample using a Dektak 150 surface profilometer. At least three samples were measured for each doping condition. We note that our use of a macroscopic, cm-scale conductivity measurement generally produces lower values of conductivity than measurements from other groups that use electrodes spaced in the mm or even µm length range. Thus, our values are likely underestimates compared to those from other groups.

In previous work, we have shown using AC Hall effect measurements that there is a roughly linear relationship between the peak energy of the P1 polaron band absorption and the corresponding

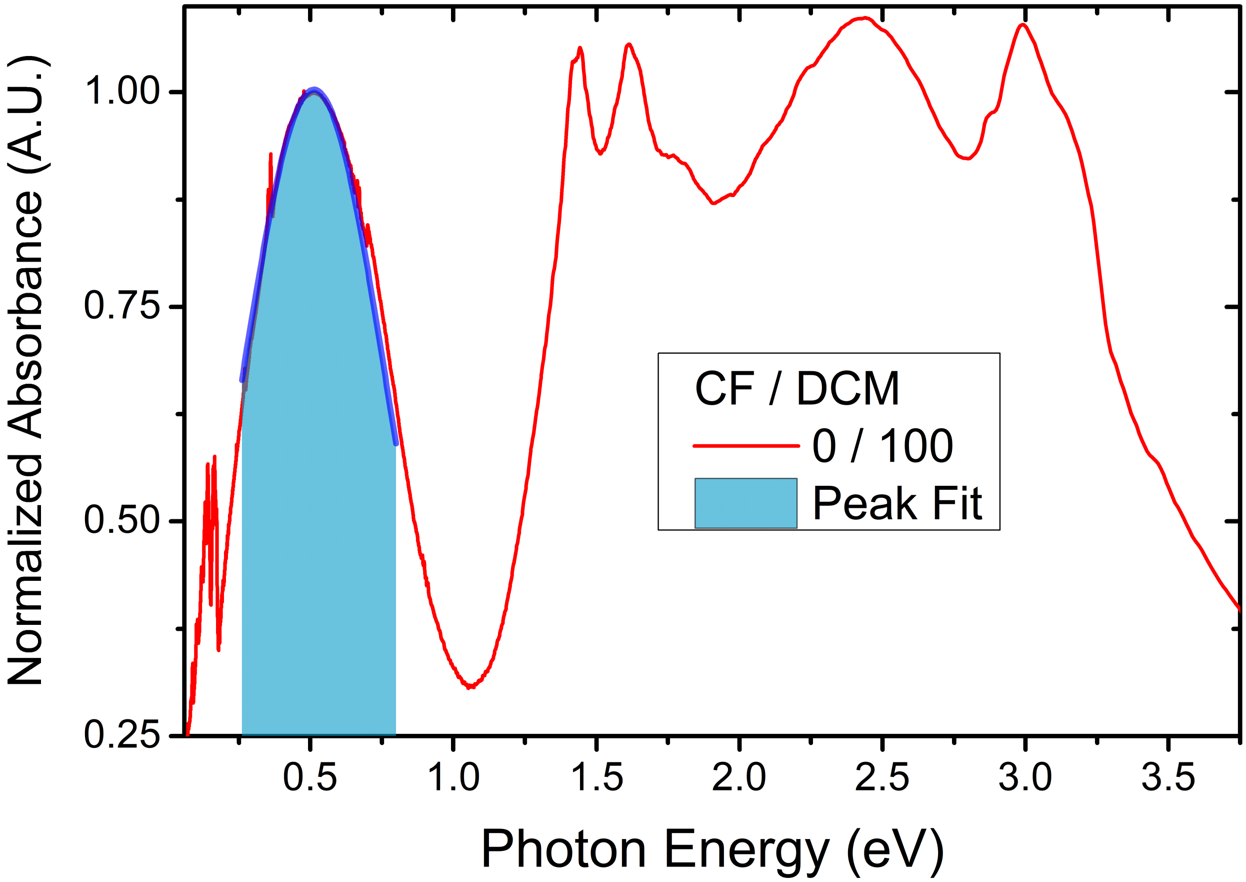

Figure B.4: Example UV-Vis-NIR / FTIR spectrum showing overlayed gaussian fit for the P1 peak absorption (blue). The energy for the best fit P1 peak intensity is then used to estimate the free carrier mobility.

Table B.1: P3HT film thicknesses after sequential doping from CF/DCM solvent blends.

CF / DCM	Thickness (nm)
00/100	148 ± 6 nm
40/60	143 ± 12 nm
60/40	107 ± 9 nm
80/20	91 ± 6 nm
100/00	83 ± 8 nm

free carrier mobility for chemically-doped P3HT (Figure B.3[2]) $\mu = -0.338\lambda_{max} + 0.206$, where λ_{max} is the P1 band peak position in eV and μ is given in $cm^2V^{-1}s^{-1}$. Thus, the IR spectrum of doped P3HT films also includes implicit information about the free carrier mobility for each set of preparation conditions. Figure B.4 shows an example of fitting the P1 band to a gaussian peak in the range of 0.25-0.6 eV to obtain a value for peak absorbance. We used this value to estimate the free carrier mobility. Then, using the known relationship between the electrical conductivity, σ, and carrier mobility, μ, shown in equation B.1 (which is also mentioned in section 3.3.2 of the main text), we were able to estimate the free carrier concentration, p; these values are what are shown in Fig. 3.2c of the main text.

$$\sigma = pe\mu \tag{B.1}$$

Because accurate determination of the in-plane conductivity also requires knowledge of the film thickness, we measured the film thickness of our P3HT films as the doping solvent was tuned from DCM to CF (Table B.1). A consistent loss in P3HT film thickness is observed as the fraction of CF is increased, due to the fact CF has a higher dissolving power for P3HT than does DCM. We see that the overall thickness when using pure CF as the doping solvent results in a doped film that is 44% smaller in thickness compared to using pure DCM as the doping solvent.

B.1.2 F_4TCNQ C≡N Vibrational Spectrum & Peak Fitting Details

F_4TCNQ contains only a limited number of vibrational modes with significant absorptivity above 2000 cm^{-1}. For neutral F_4TCNQ, there is a relatively weakly absorbing b_{1u} mode at 2227 cm^{-1} and a b_{2u} mode at 2214 cm^{-1}. Upon formation of the anionically charged species, these two modes gain significant oscillator strength, as well as soften to lower energy. We label these peaks of the F_4TCNQ anion as $b_{1u}\nu_{2185}$ and $b_{2u}\nu_{2168}$. We assign the peak corresponding to the fractional charge transfer species as belonging to the b_{1u} stretching mode, denoted here as $b_{1u}CTC$.

Peak fitting for all vibrational spectra was carried out by assigning three gaussian peaks and allowing the parameters (peak center of gravity, amplitude, and FWHM) to independently vary. Fitting was carried out by a non-linear least squares minimization following the Levenberg-Marquardt algorithm and allowed to iterate until converging with a χ^2 tolerance of at least 1×10^{-6}.

Table B.2 shows that the relative amplitude for the $b_{1u}CTC$ peak, which corresponds to partial charge transfer, monotonically increases as the fraction of CF is increased in the casting solvent. It's also interesting to point out that when only considering the ICT phase, peak $b_{1u}\nu_{2185}$ systematically redshifts from 2189 cm^{-1} from when pure DCM is used as the dopant casting solvent down to 2185 cm^{-1} when pure CF is used; this is nearly 10 cm^{-1} redshifted from the typically reported anion peak location at 2194 cm^{-1}. We believe this to be a consequence of the highly ordered, lamellar environment found for these sequential doping conditions, an idea further supported by the fact that the FWHM for this peak also decreases by $\sim$30% as the solvent is changed from DCM to CF, indicating a more homogeneous environment for the remaining ICT phase.

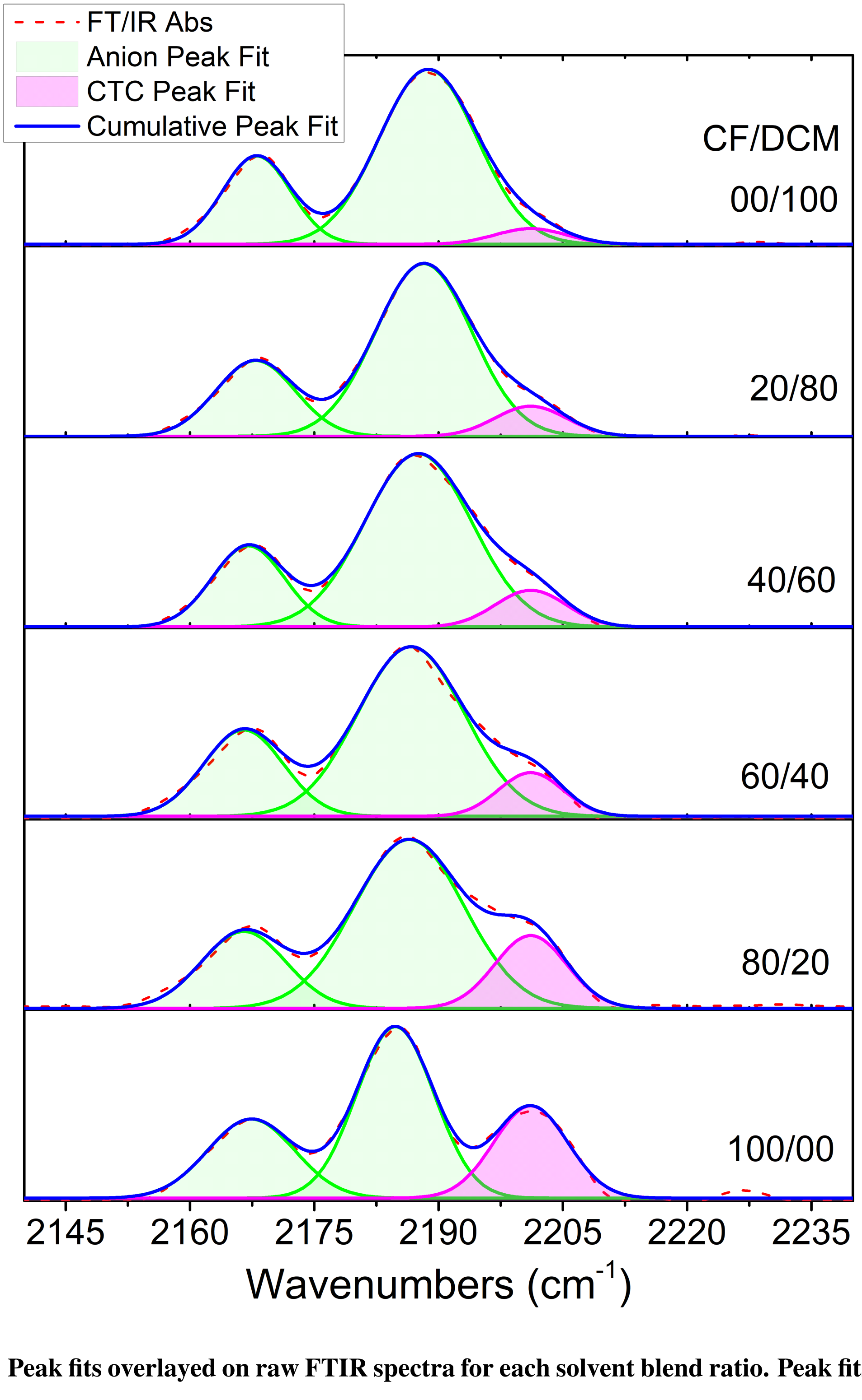

Figure B.5: Peak fits overlayed on raw FTIR spectra for each solvent blend ratio. Peak fits for $b_{2u}\nu_{2168}$ and $b_{1u}\nu_{2185}$, shown in green. Peak fits for the intermediate CTC phase $b_{1u}CTC$ shown in magenta.

Table B.2: Fitting parameters for the F_4TCNQ vibrational spectra, sequentially doped from CF/DCM solvent blends.

	CF/DCM	**00/100**	**20/80**	**40/60**	**60/40**	**80/20**	**100/00**
	Adj. R-Square	0.9983	0.9991	0.9980	0.9970	0.9974	0.9948
b_{2u} ν_{2168}	A	5.26	5.18	5.25	6.44	5.72	6.15
	c	2168.00	2167.84	2167.12	2166.75	2166.76	2167.38
	ω	9.65	11.09	10.42	12.10	12.07	12.53
b_{1u} ν_{2185}	A	15.49	15.02	13.65	13.60	15.09	11.68
	c	2188.92	2188.39	2186.68	2185.86	2186.07	2184.79
	ω	15.49	14.17	13.33	13.10	14.44	11.04
b_{1u}CTC	A	0.60	1.47	3.92	4.36	5.38	6.08
	c	2203.08	2202.22	2197.91	2198.41	2200.16	2201.14
	ω	6.14	8.54	12.60	11.92	11.03	10.62

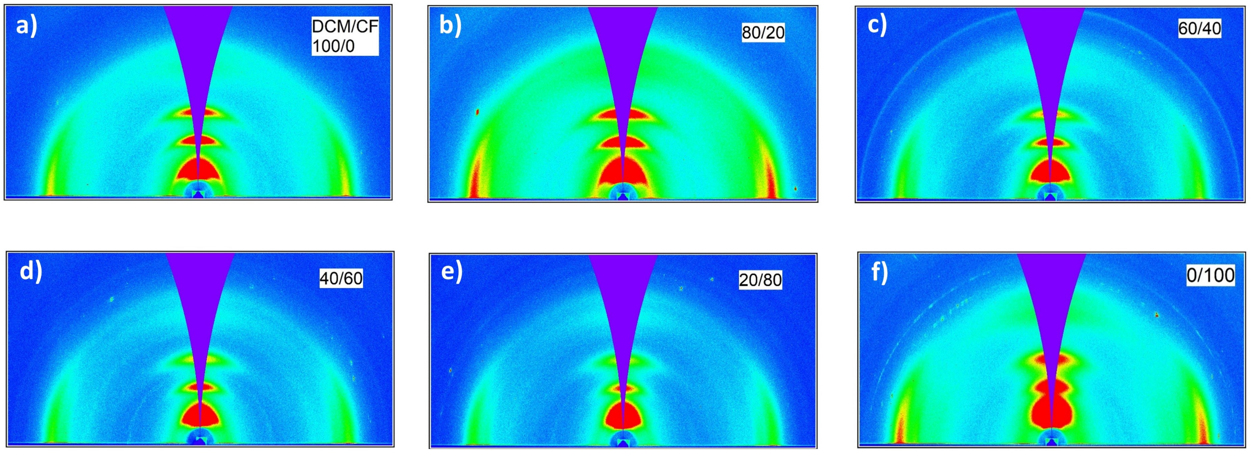

Figure B.6: 2D diffractograms of P3HT SqP doped with F4TCNQ from solvent mixture of DCM/CF with ratio of (a)100/00, (b) 80/20, (c) 60/40, (d) 40/60, (e) 20/80 and (f) 0/100. With increasing CF ratio, the lamellar diffraction peaks broaden. The π diffraction peak moves to higher q as well as broadens. The doped P3HT transits from Phase I(ICT) to Phase II(CTC).

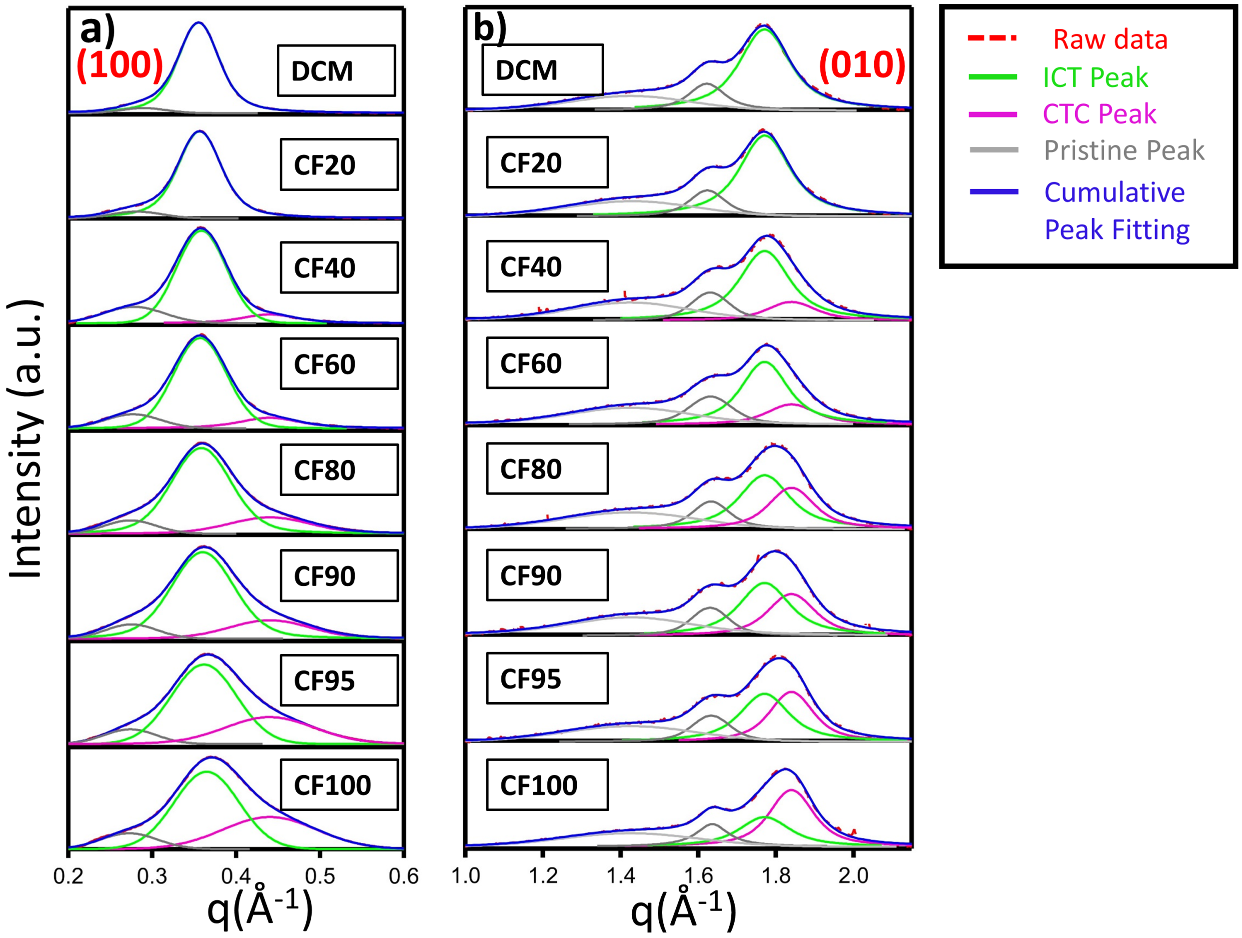

Figure B.7: Peak fitting of lamellar (a) and π-π(b) peaks of doped P3HT with F4TCNQ SqP from mixture of DCM and CF with different ratio. With increasing CF ratio, there is a new lamellar peak coming up at $0.44\,\mathring{A}^{-1}$ (pink curve,CTC peak) along with the commonly seen ICT peak(green curve). At the same time, the broadened π peak can be fitted to two peaks: an ICT peak (green curve) and a new peak located at $1.84\,\mathring{A}^{-1}$ (pink peak) that assigned to CTC peak. The new peaks in both lamellar and π direction correspond to a new doped P3HT phase(Phase II, CTC phase).

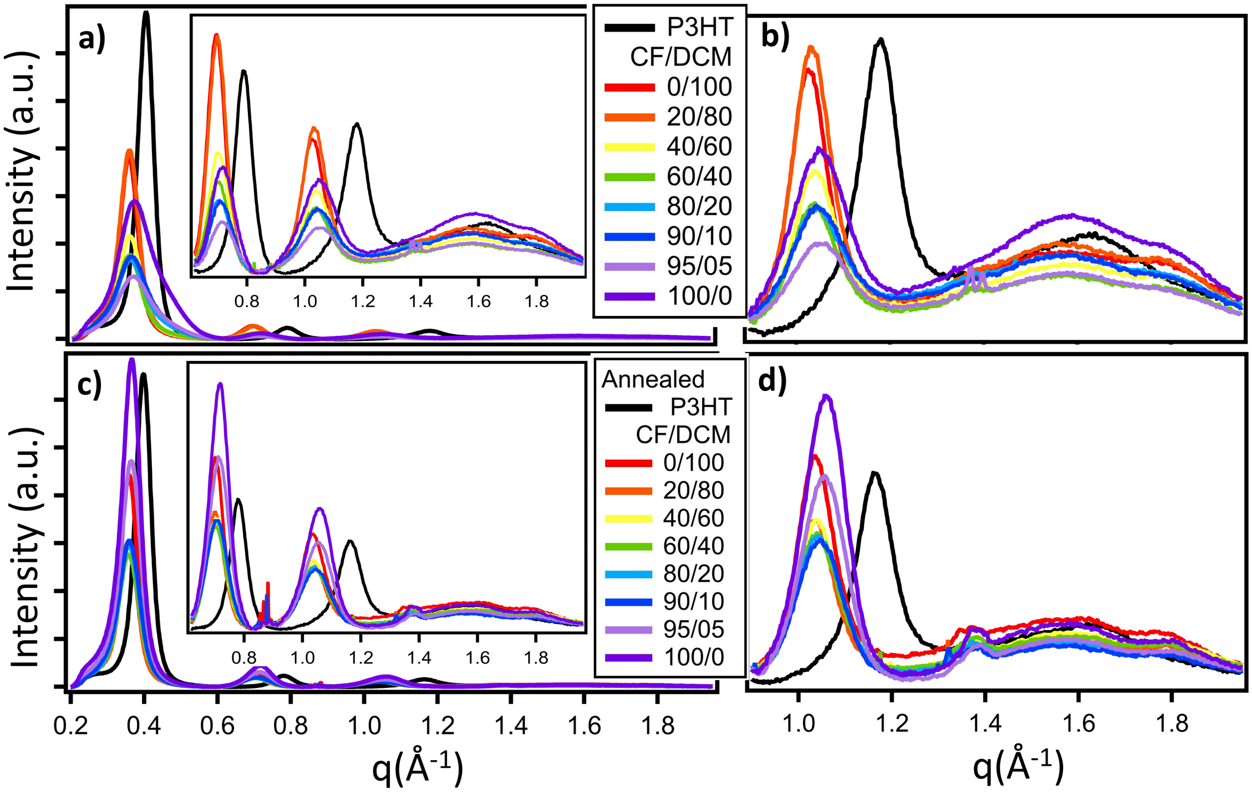

Figure B.8: Out-of-plane integrated thickness-normalized 2-D GIWAXS diffractograms for P3HT doped with F4TCNQ SqP from different CF/DCM ratio before (a)(b) and after (c)(d) thermal annealing. The inset in (a) and (c) show the higher q region expanded in vertical direction. Similarly, (b) and (d) show more expanded π stacking region in (a) and (c).

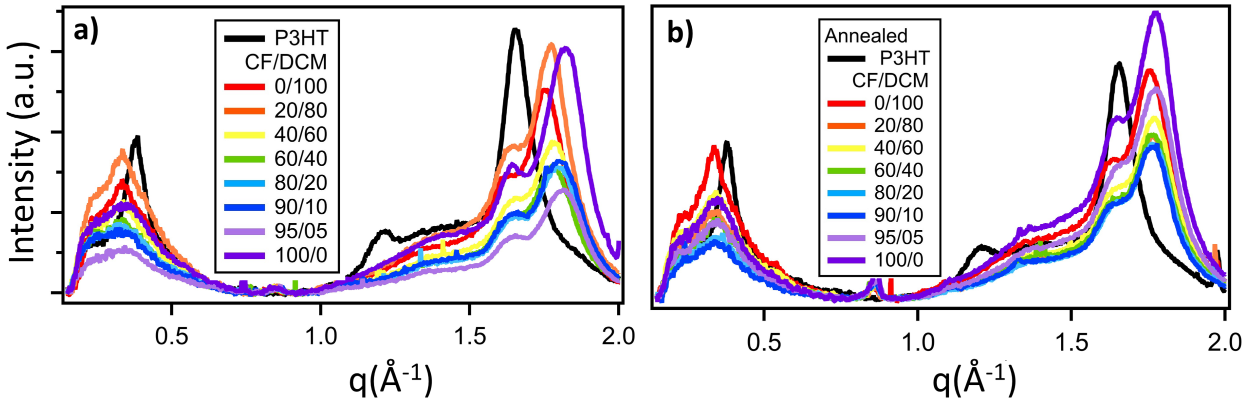

Figure B.9: In-plane integrated thickness-normalized 2-D GIWAXS diffractograms for P3HT doped with F4TCNQ SqP from different CF/DCM ratio before (a) and after (b) thermal annealing.

APPENDIX C

Supporting Information for Chapter 4

C.1 Experimental Methods

C.1.1 Materials

Electronic-grade Poly(3-hexylthiophene-2,5-diyl) (P3HT) (4002-EE; 91-94% RR, M_w=46–57 kg mol^{-1}, PDI=2.3) was purchased from Rieke metals. Sublimation grade F_4TCNQ (purity $> 98\%$) was purchased from TCI America. Synthesis, preparation, and characterization of the specially synthesized 100% RR P3HT has been described by us in prior work.[61] All materials and solvents were used as received without any further purification. Reusable KBr plates were used as substrates and first cleaned by polishing with a cotton swab soaked in chlorobenzene (CB). All subsequent fabrication steps described in sections below were carried out inside a N_2-filled glovebox.

C.1.2 Sequential Doping from CF/DCM Solvent Blends

For the polymer coating step, P3HT ($20\,\mathrm{mg\,mL^{-1}}$) in *o*-dichlorobenzene (ODCB) was spin-coated for 20 s at 1000 RPM to fully coat the substrate, while still keeping a thin layer of liquid ODCB dissolved P3HT intact. The wet films where then placed inside a petri dish with the lid *off*, so that the solvent vapor could still collect inside the petri dish volume but dissipate relatively quickly. This causes the solid polymer film to form over the course of 1-2 minutes. Subsequently, these pristine polymer films were solution doped with F_4TCNQ by spin-coating them using a doping solvent mixture of various ratios chloroform (CF) and dichloromethane (DCM) (F_4TCNQ concentration held at $1\,\mathrm{mg\,mL^{-1}}$) at 4000 RPM for 10 s.

C.1.3 Fabrication of Pristine Polymer Films of Controlled Crystallinity & Sequential Doping

To tune the crystallinity of the pristine polymer films, we exploited solvent evaporation kinetics to control the drying time of the polymer layer. For the most disordered films, commercially-available P3HT ($10\,\mathrm{mg\,mL^{-1}}$) was spin-coated out of chloroform (CF) (b.p.=61.2 °C) for 60 s at 1000 RPM. To produce films with more order in the P3HT crystallites, the same commercially-available P3HT ($20\,\mathrm{mg\,mL^{-1}}$) was spin-coated out of ODCB (b.p.=180.19 °C) for 20 s at 1000 RPM. The still-wet films were then placed inside a *closed* petri dish to prevent the solvent vapor from easily escaping, which extends the drying time to 3-4 hours.

Finally, P3HT films with the most crystalline order were fabricated from an in-house synthesized batch of P3HT with virtually perfect regioregularity, confirmed via ^{1}H NMR.[61] Because of the high degree of regioregularity, the solutions were first heated to 60 °C to prevent aggregation and then spin-coated out of ODCB ($20\,\mathrm{mg\,mL^{-1}}$) for 20 s at 1160 RPM. The still-wet films were then placed inside a *closed* petri dish to prolong the crystallization period.

C.1.4 Sequential Doping from *n*-butyl acetate

To form the pristine polymer films for sequential doping from *n*-butyl acetate (*n*BA), P3HT solutions ($20\,\mathrm{mg\,mL^{-1}}$) in *o*-dichlorobenzene (ODCB) were spin-coated for 60 s at 1000 RPM followed by 5 s at 3000 RPM to form a solid-phase polymer film of good quality. These films were then solution doped by spin-coating with F_4TCNQ solutions ($0.01\text{-}5\,\mathrm{mg\,mL^{-1}}$) out of *n*-butyl acetate (*n*BA), a solvent chosen because it adequately swells the underlying P3HT layer (to allow for dopant infiltration) without dissolving it.

C.1.5 Fourier-Transform Infrared Spectroscopy

FTIR absorbance was captured in a N_2-purged Jasco FT/IR-420 spectrometer, from $470\text{-}5200\,\mathrm{cm^{-1}}$. Both the mid-IR electronic absorption of doped P3HT and the vibrational modes for the F_4TCNQ radical anion were acquired from a single spectrum for each film, as shown in Figure C.1. The doped

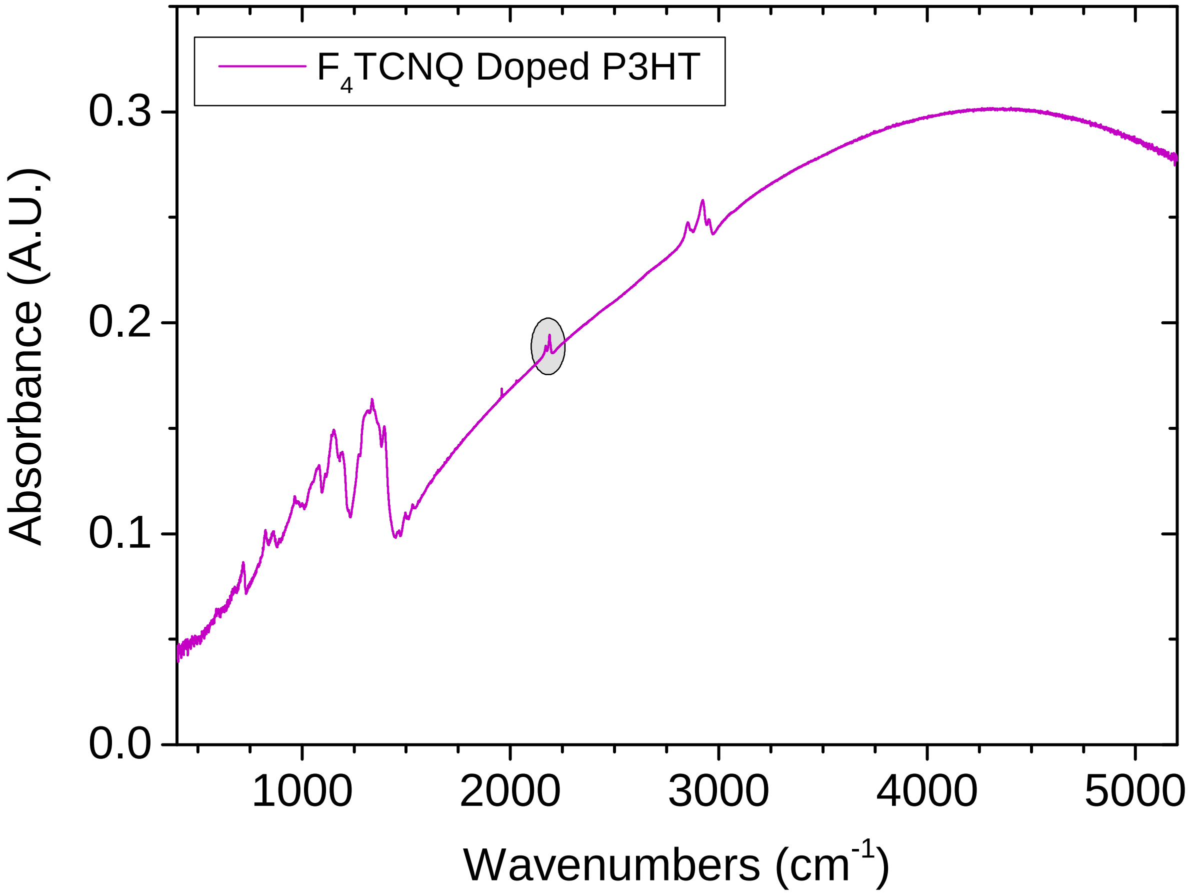

Figure C.1: Example of a raw FTIR absorbance spectrum for a sequentially solution doped P3HT film, fabricated on a 25 x 4 mm **circular KBr window. Note the absorbance of the F_4TCNQ nitrile stretching modes near** $\sim$2200 cm^{-1}**, which are indicated by the gray oval.**

polymer's A/B ratio was determined by taking the intensity of peak A at 0.160 eV and dividing it by the intensity of peak B. Due to the broad absorption profile of peak B, the precise energy for the true maximum peak intensity can be affected by noise intrinsic to the FTIR measurement. Thus, to accurately determine the point where peak B is centered, we fit the absorption feature to a gaussian function, allowing a wide range of measured data to be used in determination of the peak absorbance energy (Figure C.2).

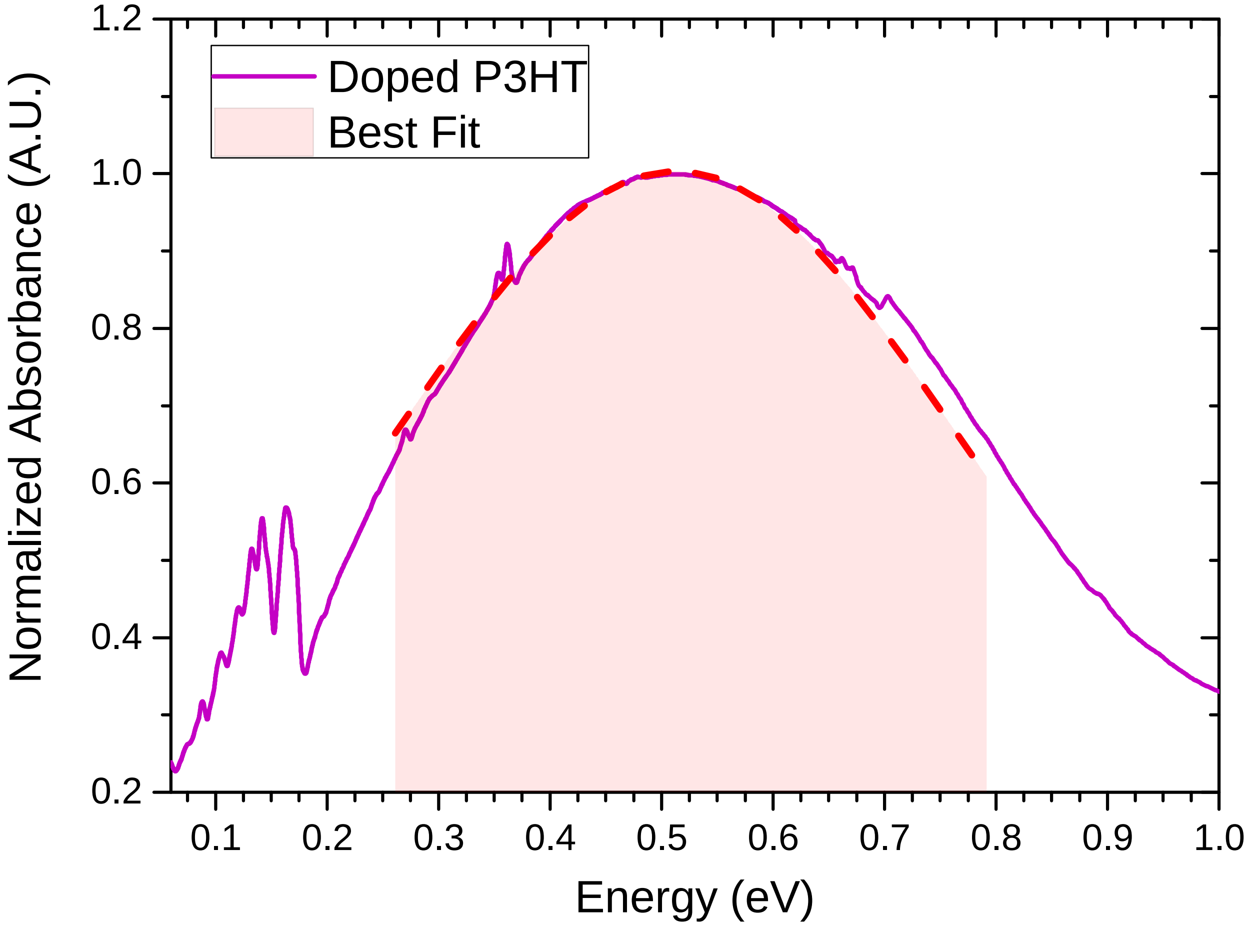

Figure C.2: The magenta curve shows an example FTIR absorbance spectrum for a sequentially solution doped P3HT film $(1\,\mathrm{mg\,mL^{-1}}$ **F_4TCNQ out of DCM). The dashed red curve with light red fill shows the best-fit gaussian function to the band, which aids in the reliable determination of the peak energy for peak B.**

C.2 Baseline Correction and Peak Fitting of the F_4TCNQ Vibrational Spectrum

C.2.1 Baseline Correction & the Christiansen Effect

Baseline correction for the F_4TCNQ nitrile-region vibrational spectra was carried out using the Peak Analyzer tool in OriginPro 9.1 software. The F_4TCNQ vibrational spectrum sits atop the broad, sloped electronic absorption due to peak B of the corresponding doped polymer. Due to this feature, the raw absorption spectrum of the F_4TCNQ radical anion is significantly skewed to higher absorbances at higher wavenumbers, making it necessary to remove this background before carrying out meaningful peak fitting (Figure C.3). Additionally, we and others[7] have noted a 'transmittance peak' in the raw absorption spectrum that has a dip in intensity on the high-energy side of the nitrile stretching modes near $2010\,\mathrm{cm}^{-1}$. This has been attributed to the Christiansen effect,[7] which appears as an anomalous increase in transmittance, or Christiansen peak. The Christiansen effect is typically seen in cases where a guest species is disbursed throughout a host matrix, and a Christiansen peak is expected where the index of refraction of the host and guest species happen to be equal.[175] For our F_4TCNQ-doped P3HT system, we consistently find the Christiansen peak located near $2010\,\mathrm{cm}^{-1}$, a location sufficiently separated from the closest vibronic features that it should not affect our understanding of the nitrile stretching peaks of interest. For clarity, the small dip in absorption due to the Christiansen effect has been carefully included in the background and subtracted accordingly before any fitting. We note that although the Christiansen peak is also expected to appear in blend-cast doped films, we are only aware of one other work in this area that mentions its presence,[7] so we surmise that it is likely a routine practice to subtract this feature.

C.2.2 Peak Fitting

Peak fitting for all vibrational spectra was performed using the Peak Analyzer tool in OriginPro 9.1. Fitting was carried out by assigning initial gaussian peak centers for each expected vibrational mode and subsequently allowing all lineshape parameters to freely vary (peak center (c), amplitude (A), FWHM (ω)). A non-linear least squares minimization was carried out using the

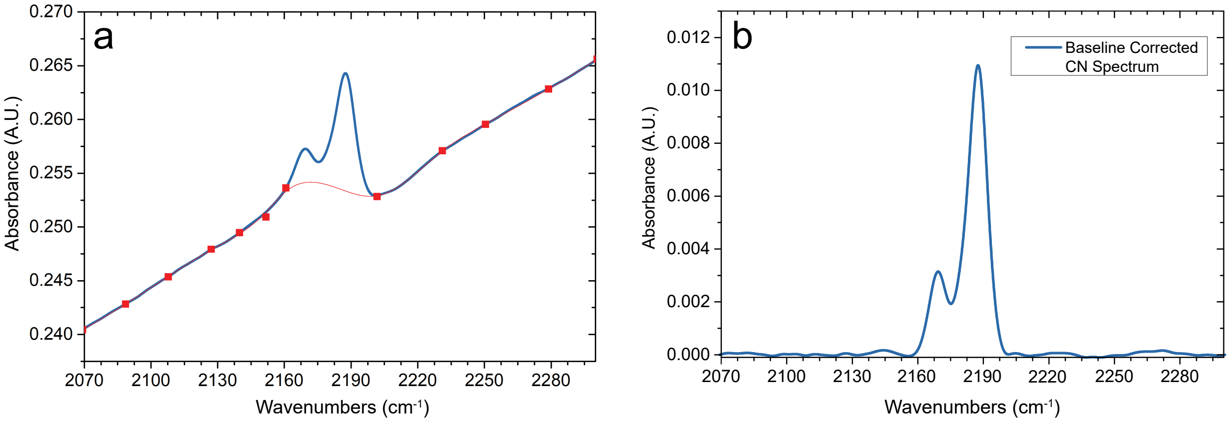

Figure C.3: (a) Raw absorbance data for the C≡N vibrational spectrum of the F_4TCNQ radical anion inside sequentially solution doped P3HT ($1\,\mathrm{mg\,mL^{-1}}$ **out of *n*BA) with baseline anchor points shown as red squares. The B-Spline function was used to connect anchor points, which allows for a smooth intensity transition between the low energy and high energy background regimes. (b) The corresponding background-subtracted dataset, shown with the expanded background regime used for baseline correcting.**

Levenberg–Marquardt algorithm and allowed to iterate until converging with a χ^2 tolerance of at least 1×10^{-6}.

Unless stated otherwise, we fit our measured vibrational spectra (cf. Fig. C.4) to four independently-varying gaussians that were initially centered at $2201\,\mathrm{cm^{-1}}$ (pink), $2194\,\mathrm{cm^{-1}}$ (dark green), $2185\,\mathrm{cm^{-1}}$, (light green) and $2168\,\mathrm{cm^{-1}}$ (orange). The peak center at 2201 $\mathrm{cm^{-1}}$ was chosen to represent the characteristic absorption energy for F_4TCNQ in a fractional charge transfer complex (CTC), a topic we have previously discussed in detail in Ref 12. The peak at $2194\,\mathrm{cm^{-1}}$ was chosen to represent the F_4TCNQ^- B_{1u} mode in a trapped polaronic environment, characteristic of more disordered P3HT crystallites. The peak closer to $2185\,\mathrm{cm^{-1}}$ was chosen to represent the B_{1u} mode in more ordered P3HT crystallites, where the electric field strengths from the more delocalized P3HT polaron are smaller.

The results of peak fitting in Figure C.4 show that the dominant ICT species in sequentially doped P3HT belongs to the peak we label here as $B_{1u}\nu_{2185}$, with only a small population of $B_{1u}\nu_{2194}$, which is otherwise usually the most intense absorbance peak found in blend-doped polymer films. It’s interesting to see that the peak near $2194\,\mathrm{cm^{-1}}$ manifests here as either a small shoulder or

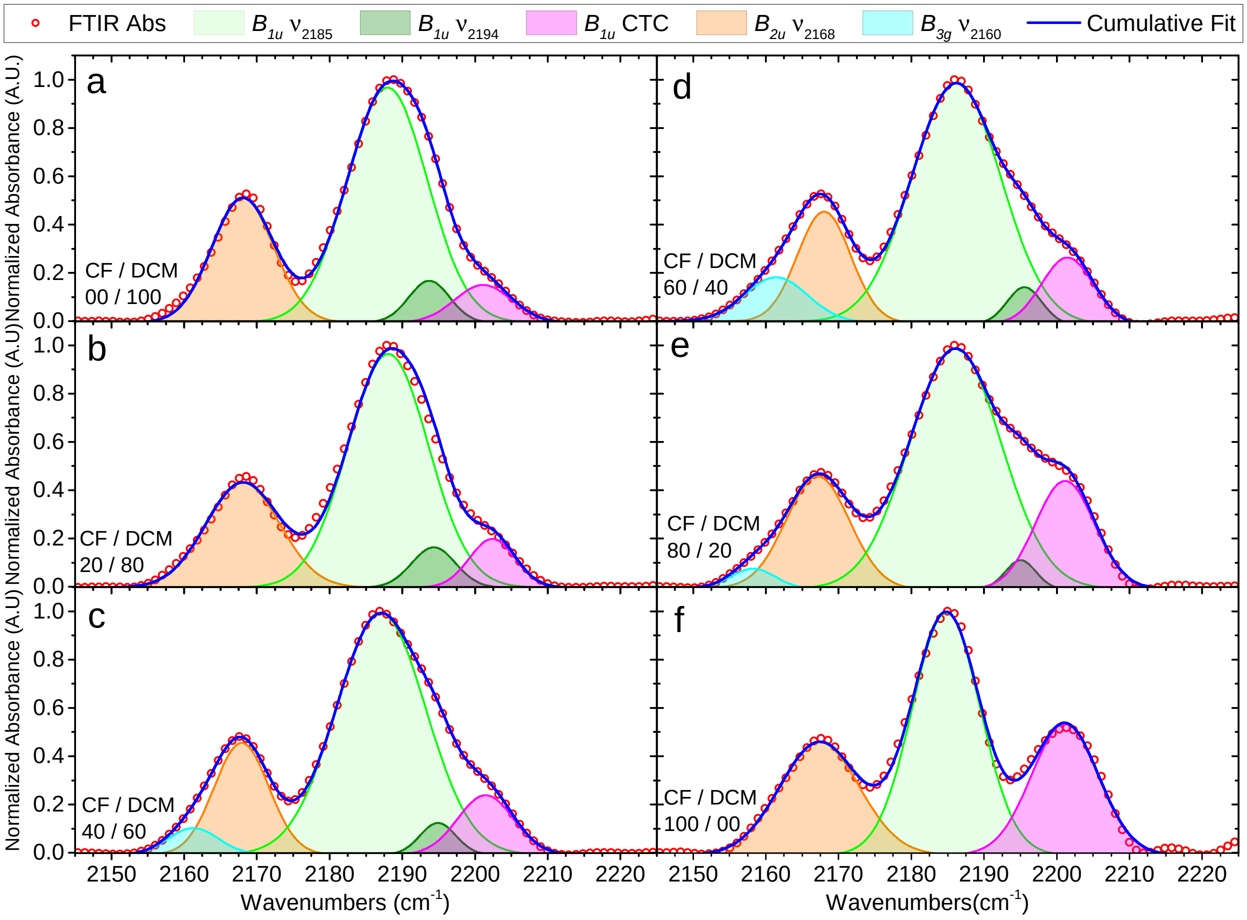

Figure C.4: Peak fits for the F_4TCNQ-doped P3HT vibrational spectra with the doping solvent comprised of blends of CF and DCM. Conditions c-e benefit from an improved fit by including a small amount of the B_{3g} mode (light blue) to account for the low energy tail in these spectra. We note that this assignment is in agreement with what others have sometimes found in this location as well.[4,8–10]

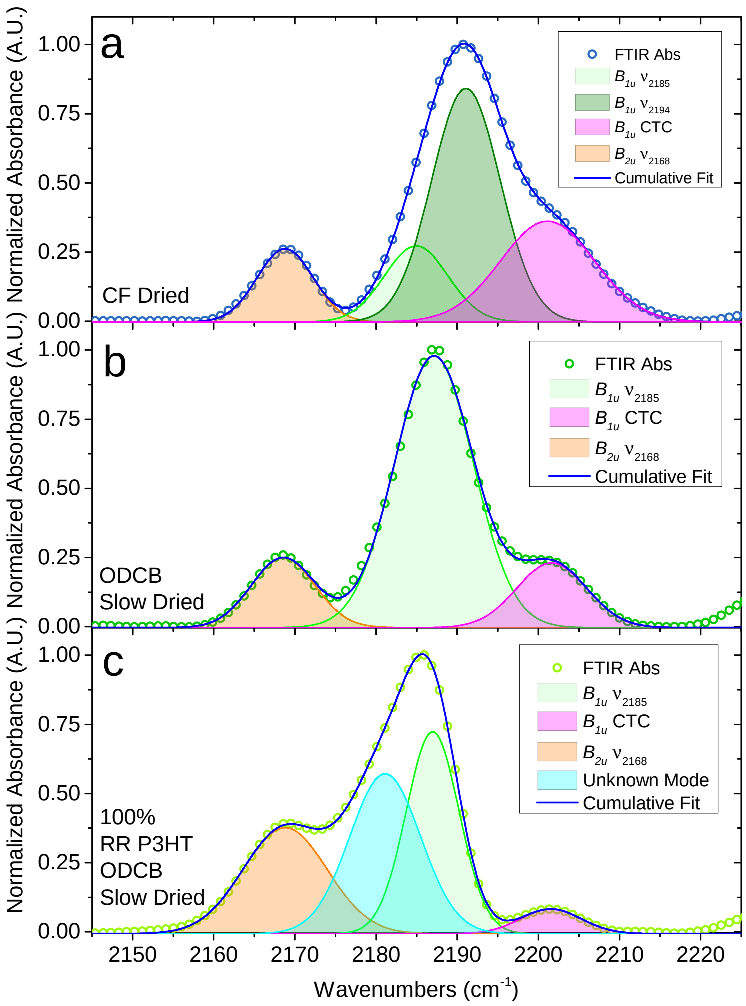

Figure C.5: (a) Vibrational peak fits for a CF-cast P3HT film sequentially solution doped with F_4TCNQ from DCM ($1\,\mathrm{mg\,mL^{-1}}$), which has the lowest degree of crystalline order of all the doped samples studied in this work. This is the only vibrational spectrum presented where the $B_{1u}\nu_{2194}$ vibrational mode corresponds to the principle absorption feature. This sample also has a correspondingly high CTC peak intensity, indicating an elevated degree of CTC states for these preparation conditions. (b) Peak fits for a P3HT film initially spin-coated from ODCB and slow-dried before being sequentially solution doped with F_4TCNQ from DCM ($1\,\mathrm{mg\,mL^{-1}}$). The spectrum could not be fit properly with any B_{1u} peak at 2194 cm^{-1}, further indicating the relatively high crystalline order. (c) Peak fits for solution doped highly crystalline P3HT films of essentially 100% regioregularity, which were subsequently doped with F_4TCNQ from DCM ($1\,\mathrm{mg\,mL^{-1}}$). This film also did not show any sign of the 2194 cm^{-1} peak, but an additional peak near 2181 cm^{-1} was required to explain the asymmetric shape of the tallest absorption feature.

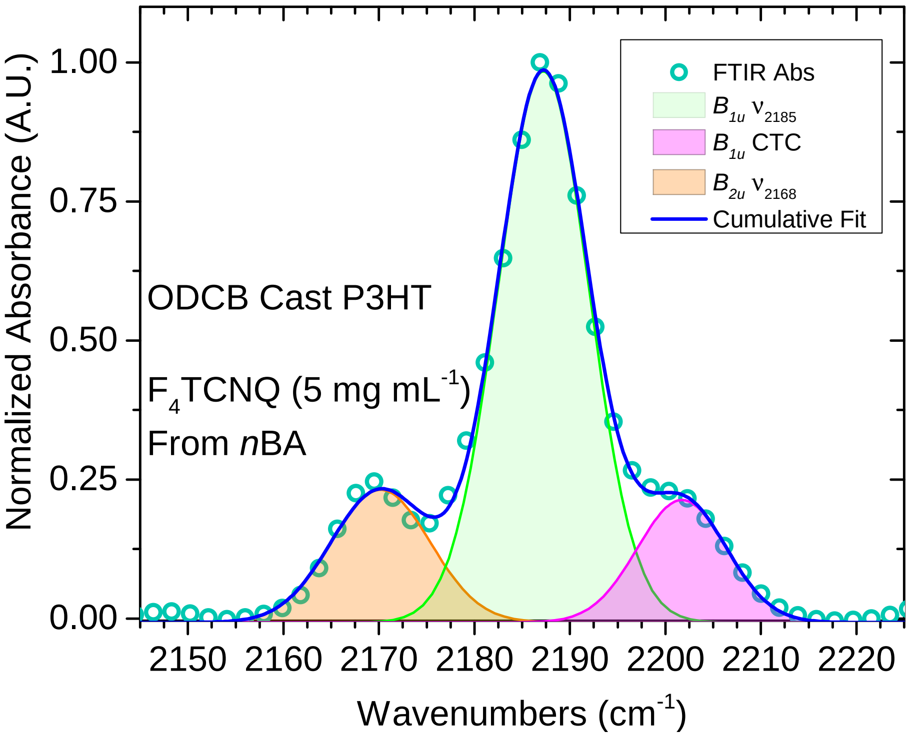

Figure C.6: Peak fits for an ODCB-cast P3HT film sequentially doped from the minimally-interacting solvent *n*-butyl acetate. $(5\,\mathrm{mg\,mL^{-1}})$**.**

change in inflection. The only film with a dominant peak near 2191 cm^{-1} belongs to the P3HT which was cast from CF (figure C.5a), which has the lowest degree of crystalline order. For films with a higher degree of crystalline order, it was not actually possible to obtain a plausible fit for the peak $B_{1u}\nu_{2194}$. This happened in the case of using (1) pure CF as the *dopant* casting solvent, (2) pre-cast P3HT cast from ODCB that was extensively slow-dried in a covered petri dish, and (3) the 100% RR P3HT. Each of these conditions are known to correlate with the most delocalized polaron spectra, which further supports the notion that the peak near 2194 cm^{-1} belongs to the B_{1u} mode inside the least-ordered P3HT crystallites. This peak near 2194 cm^{-1} was also missing for conditions where the minimally-interacting *n*BA solvent was used (Figures C.6 and C.13a) instead of DCM, which was applied for every other sample in this study except that using 100% CF as the doping solvent. DCM has excellent swelling properties towards P3HT and results in the highest doping levels per unit concentration that we are aware of. This suggests that DCM's swelling power also introduces some minor disorder to the crystallites in these films, as reflected in the presence of the disordered nitrile stretching peak near 2194 cm^{-1}. This is similar to a previous observation, which noted broader peak widths associated with doping of P3HT from DCM compared to relatively narrow peak widths seen when intercalating F_4TCNQ from the vapor phase.[11,12]

Figure C.7 details the relative loss in intensity of the $B_{1u}\nu_{2194}$ peak as the fraction of CF in the doping solvent increases; the greater the loss, the more the P3HT polaron is delocalized.

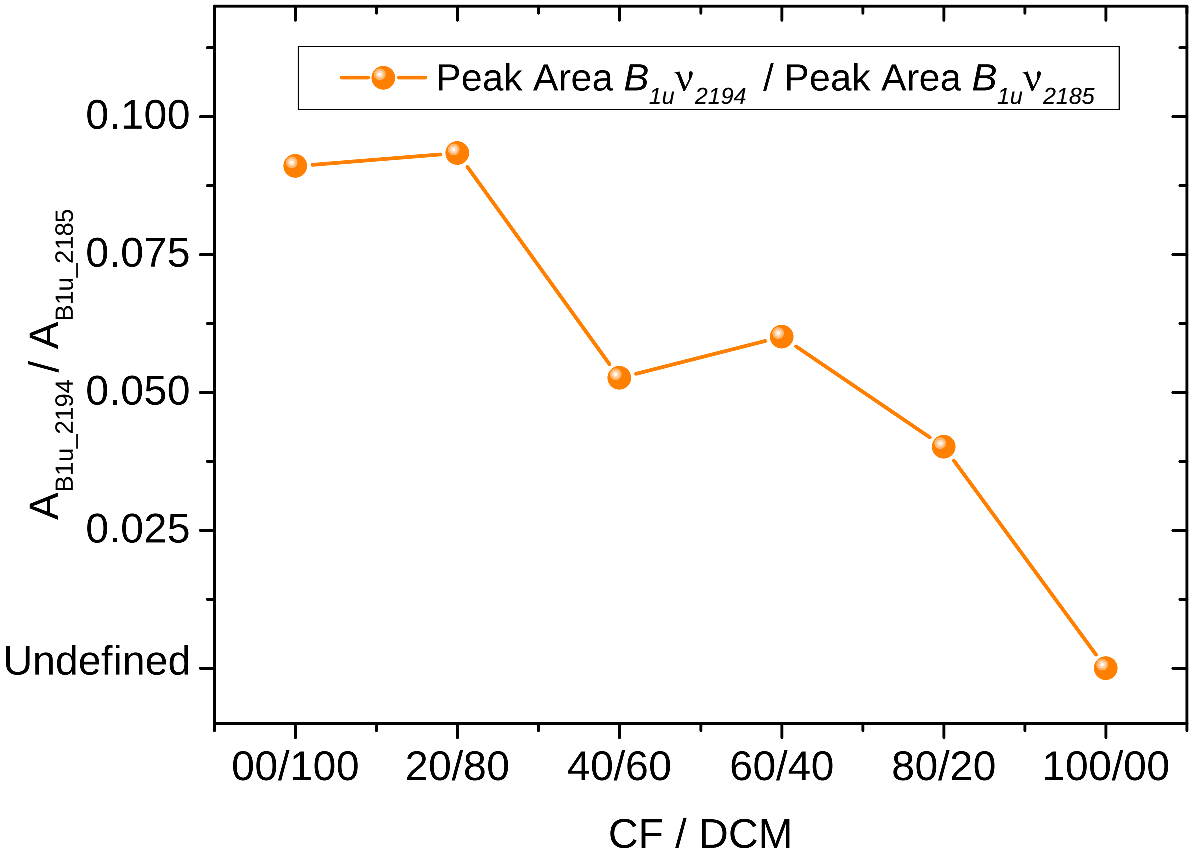

Figure C.7: Integrated peak area for $B_{1u}\nu_{2194}$ scaled against the integrated peak area for the principle $B_{1u}\nu_{2185}$ vibrational peak. The final data point at 00/100 (CF/DCM) has no plausible peak fit for $B_{1u}\nu_{2194}$ and so is listed as undefined.

For doping from the solvent blends with compositions of 40/60 through 80/20 CF/DCM (Figure C.4c-e), the cumulative peak fit can be improved by including an additional gaussian in the low-energy tail region near $B_{2u}\nu_{2168}$. This is similar to what has been found elsewhere, where the additional gaussian has simply remained an unassigned tail.[8,9] In Ref 4, it was argued that the peak we refer to here as $B_{2u}\nu_{2168}$ can be assigned to an additional, smaller vibrational mode of B_{3g} symmetry. This specific energy, along with the correspondingly low amplitude of this mode, are consistent with calculations in the literature,[10] so we believe it is acceptable to assign this additional peak as $B_{3g}\nu_{2160}$.

Figure C.8 shows that for the 100% RR P3HT, a reasonable fit can only be obtained when including an additional gaussian centered near 2181 cm^{-1}. The clear asymmetry in the tail on the lower frequency side of the B_{1u} mode suggests that there is indeed an additional peak here, which remains unassigned in the current work. It's interesting to speculate that this unknown peak could be associated with a further Stark-shifted B_{1u} mode where the Coulombic interaction with the polaron is either further reduced, or possibly this peak arises from the purely free F_4TCNQ anion, an idea that would fit with the fact that this mode is only present for the most ordered 100% RR P3HT samples.

C.3 Overview of E_{field} Calculation

To estimate the total net electric field from P3HT polarons along the difference dipole of the F_4TCNQ anion B_{1u} mode, we can use the general solution for the electric field near any line of uniform charge with length L, which is given by Eq. C.1 where $\mu = q^+/L$ is the 1-D line charge density and d_{anion} can take on any integer value between 5-8 Å. Figure C.9 depicts how the geometry is related to this equation, with a specific example for a chain length of 5 P3HT monomer units, or $5n$.

As the length of the line increases by increments of n, the total E_{field} can be calculated by subtracting the limits of Eq. C.2.

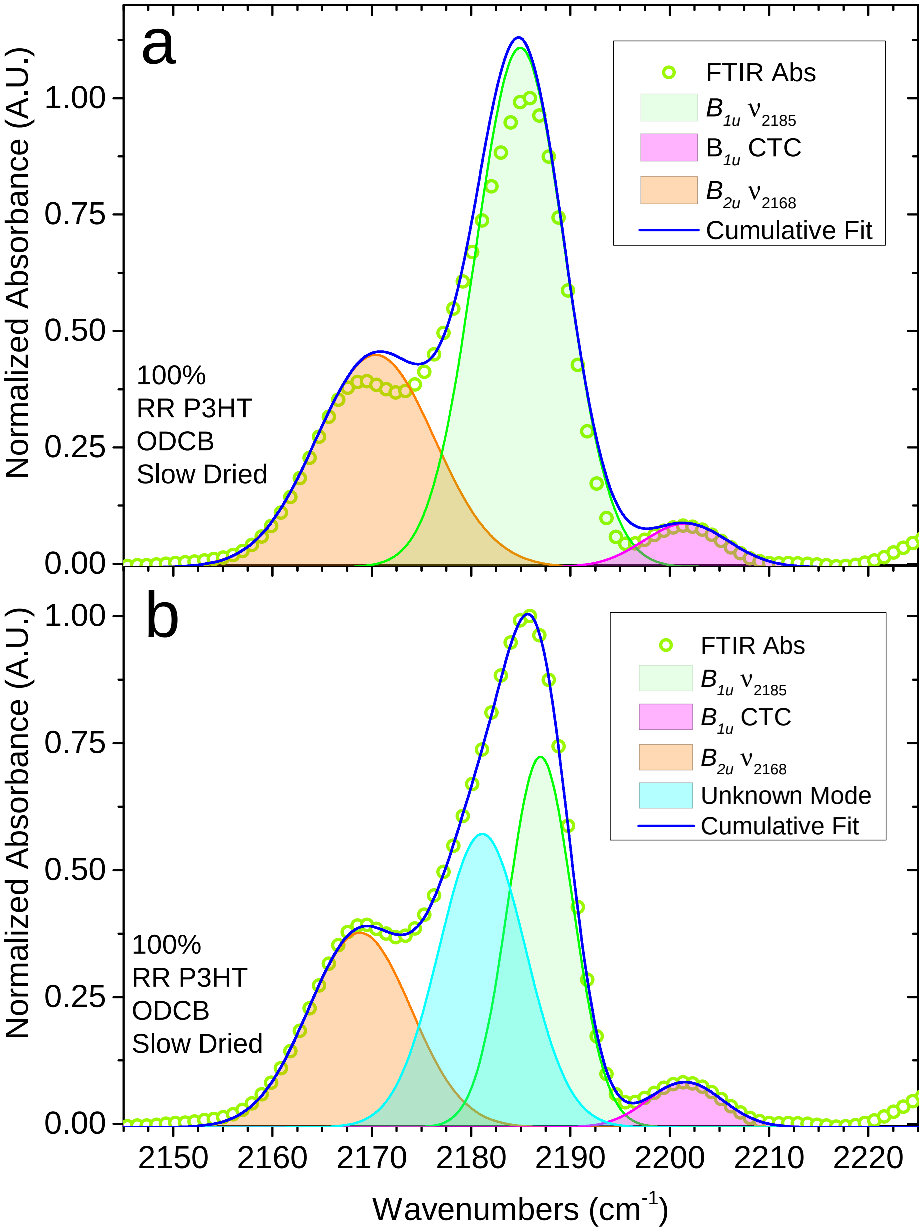

Figure C.8: Nitrile vibrational peak fits for solution-doped highly crystalline P3HT films with essentially 100% regioregularity (a) without including any extra vibrational modes, and (b) including the additional mode at $2181\ \mathrm{cm}^{-1}$. It's clear that the raw FTIR absorbance profile can only be reproduced when including the additional peak.

Table C.1: Fitting parameters for the F_4TCNQ vibrational spectra taken for sequential doping out of CF/DCM solvent blends. A, Integrated peak area percent of cumulative fit (%). c, peak center (cm^{-1}). ω, FWHM peak width (cm^{-1}).

	CF/DCM	**00/100**	**20/80**	**40/60**	**60/40**	**80/20**	**100/00**
	Adj. R-Square	0.9980	0.9965	0.9996	0.9990	0.9992	0.9948
$B_{3g}\nu_{2160}$	A	-	-	4.01	8.00	2.33	-
	c	-	-	2161.23	2161.41	2158.25	-
	ω	-	-	8.15	10.20	7.14	-
$B_{2u}\nu_{2168}$	A	25.41	25.32	18.24	16.88	19.20	25.71
	c	2168.07	2168.07	2167.91	2168.01	2167.14	2167.38
	ω	10.05	11.97	8.85	8.64	10.35	12.53
$B_{1u}\nu_{2185}$	A	61.90	61.70	64.46	61.53	59.04	48.87
	c	2187.95	2188.06	2187.06	2186.20	2186.06	2184.79
	ω	12.98	13.09	14.48	14.48	14.88	11.04
$B_{1u}\nu_{2194}$	A	5.63	5.76	3.39	3.70	2.37	-
	c	2193.71	2194.31	2194.90	2195.57	2195.03	-
	ω	6.63	7.11	5.79	5.64	4.94	-
B_{1u}CTC	A	7.06	7.22	9.90	9.90	17.06	25.42
	c	2201.13	2202.38	2201.44	2201.47	2201.13	2201.14
	ω	9.22	7.36	9.02	8.35	7.14	10.62

Table C.2: Fitting parameters for the F_4TCNQ vibrational spectra, inside films where the crystallinity was tuned via solvent evaporation kinetics during polymer spin-coating. A, Integrated peak area percent of cumulative fit (%). c, peak center (cm^{-1}). ω, FWHM peak width (cm^{-1}).

	Polymer Conditions	**CF Cast**	**ODCB Cast**	**100% RR**
	Adj. R-Square	0.9992	0.9890	0.9961
$B_{2u}\nu_{2168}$	A	11.83	14.61	27.48
	c	2168.78	2168.55	2168.79
	ω	8.09	9.20	12.22
Unknown Mode	A	-	-	34.94
	c	-	-	2181.12
	ω	-	-	10.30
$B_{1u}\nu_{2185}$	A	14.04	70.46	32.96
	c	2184.95	2187.14	2186.98
	ω	9.23	11.44	7.70
$B_{1u}\nu_{2194}$	A	46.60	-	-
	c	2191.08	-	-
	ω	9.97	-	-
B_{1u}CTC	A	27.54	14.93	4.62
	c	2201.13	2201.64	2201.53
	ω	13.67	10.18	8.82

$$E_{\text{field}||B_{1u}} = \frac{1}{4\pi\varepsilon_0}\frac{\mu}{d_{\text{anion}}}\int_{-\theta}^{+\theta}\cos\theta\, d\theta \tag{C.1}$$

$$E_{\text{field}||B_{1u}} = \frac{1}{4\pi\varepsilon_0}\frac{\mu}{d_{\text{anion}}}\sin\theta\Big|_{-\theta}^{+\theta} \tag{C.2}$$

To calculate the magnitude of the P3HT polaron's electric field along the B_{2u} mode difference dipole, we consider only the positive axis. As explained in the main text, most of the field along the B_{2u} difference dipole arises from along-the-chain disorder of the F_4TCNQ anion relative to the center of the polaron. To approximate the magnitude of the off-axis field associated with this disorder, we simply used only half of the line of charge, and then integrate over $\sin\theta$ instead of $\cos\theta$.

$$E_{\text{field}||B_{2u}} = \frac{1}{4\pi\varepsilon_0}\frac{\mu}{d_{\text{anion}}}\int_{0}^{+\theta}\sin\theta\, d\theta \tag{C.3}$$

$$E_{\text{field}||B_{2u}} = \frac{1}{4\pi\varepsilon_0}\frac{\mu}{d_{\text{anion}}} - \cos\theta\Big|_{0}^{+\theta} \tag{C.4}$$

C.4 Grazing-Incidence Wide-Angle X-ray Scattering (GIWAXS)

Figure C.10, with the data reproduced from reference 61, shows an example of the out-of-plane and in-plane diffraction patterns for sequentially F_4TNCQ-doped P3HT films where the P3HT crystallinity was varied by adjusting the casting conditions when putting down the polymer layer. The combination of in-plane and out-of-plane data for both the (100) and (010) diffraction peaks allowed us to conclude in previous work that for the pristine films, both the relative crystalline order and degree of edge-on crystallite orientation increase for both the pristine and doped samples in the order CF-cast, ODCB-cast, 100%RR.[61]

Figure C.11, which is based on data from reference 12, shows the full 2-D diffraction patterns for sequentially F_4TCNQ-doped P3HT films where the polymer morphology is modified by adjusting the ratio of CF/DCM in the doping solvent. In addition to altering the degree of crystalline order,

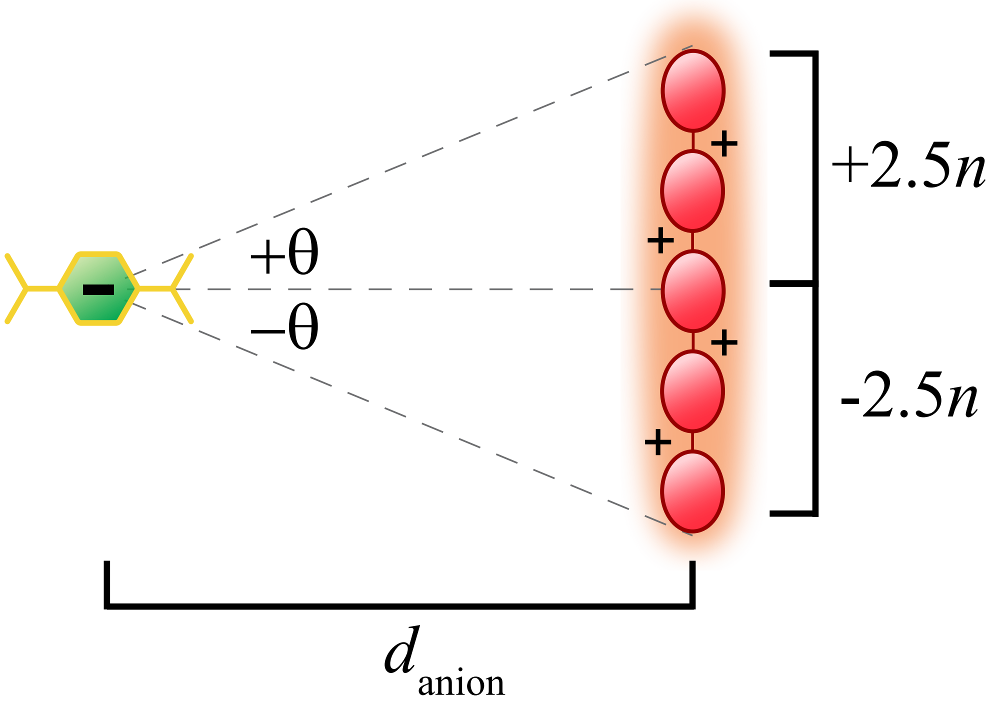

Figure C.9: Depiction of the needed parameters to calculate the total E_{field} alignment for a line of uniform charge which is 5 monomers in length for this example.

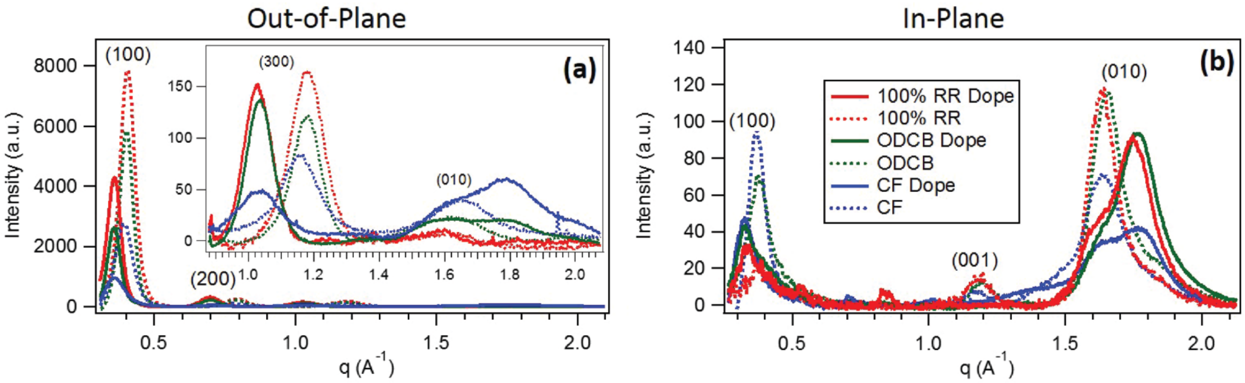

Figure C.10: Integrated (a) out-of-plane and (b) in-plane grazing-incidence wide-angle X-ray diffraction patterns for CF-cast (blue dashed curves), ODCB-cast (green dashed curves), and 100% RR ODCB-cast P3HT (red dashed curves). Solid curves of the same colors represent the same films after doping with F_4TCNQ from DCM ($1\,\mathrm{mg\,mL^{-1}}$). The inset in panel (a) shows the region around the out-of-plane (010) peak on an expanded scale.

varying the doping solvent in this way causes a significant increase in the number of fractional charge transfer complexes (CTCs) in the film. The use of CF as a dopant deposition solvent is

Table C.3: Measured d-spacings for doped P3HT Lamellar stacking direction.

Experimental Conditions	d-spacing (Å)
00/100 (CF/DCM)	17.6
100/00 (CF/DCM)	17.3
CF Cast P3HT	17.8
ODCB Slow Dried P3HT	17.5
100%RR P3HT	17.5

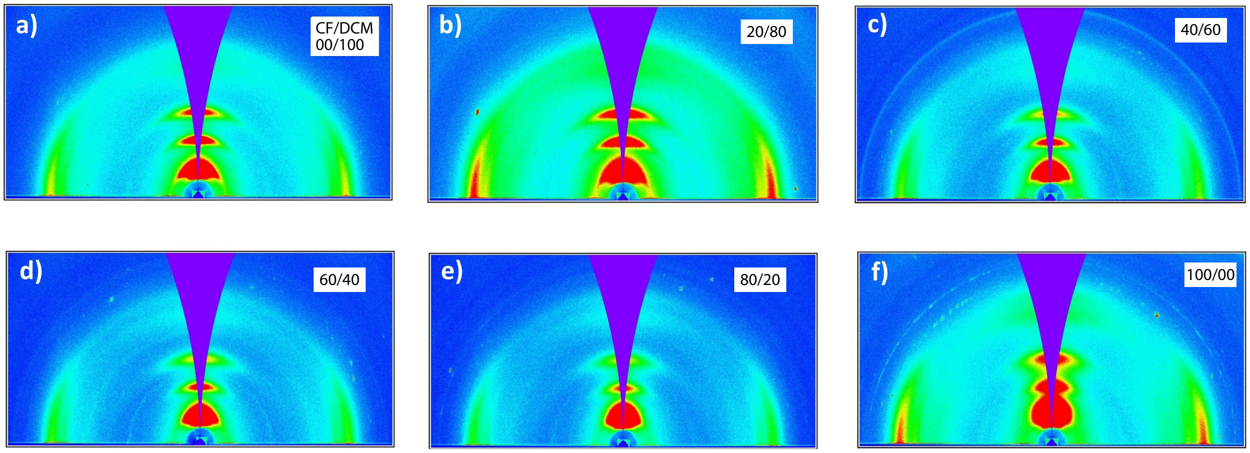

Figure C.11: 2-D GIWAXS diffractograms of P3HT sequentially doped with F$_4$TCNQ from solvent mixtures of CF/DCM (1 mg mL^{-1}) (a) 00/100, (b) 20/80, (c) 40/60, (d) 60/40, (e) 80/20 and (f) 100/00.

associated with a significant disruption of the preexisting polymer structure, increasing the fraction of amorphous polymer regions and CTC polymorphs in the film. However, the remaining ICT-doped regions that remain have more crystalline order than in the original undoped P3HT film. Figure C.12 is adapted from previous work in reference[12] and shows the in-plane and out-of-plane components of the data in Figure C.11. This data shows clearly that both the doping mechanism (CTC vs. ITC) and the fraction of amorphous regions increase as CF content increases in the doping solvent. At the same time, the ordered regions that remain become more highly crystalline.[12]

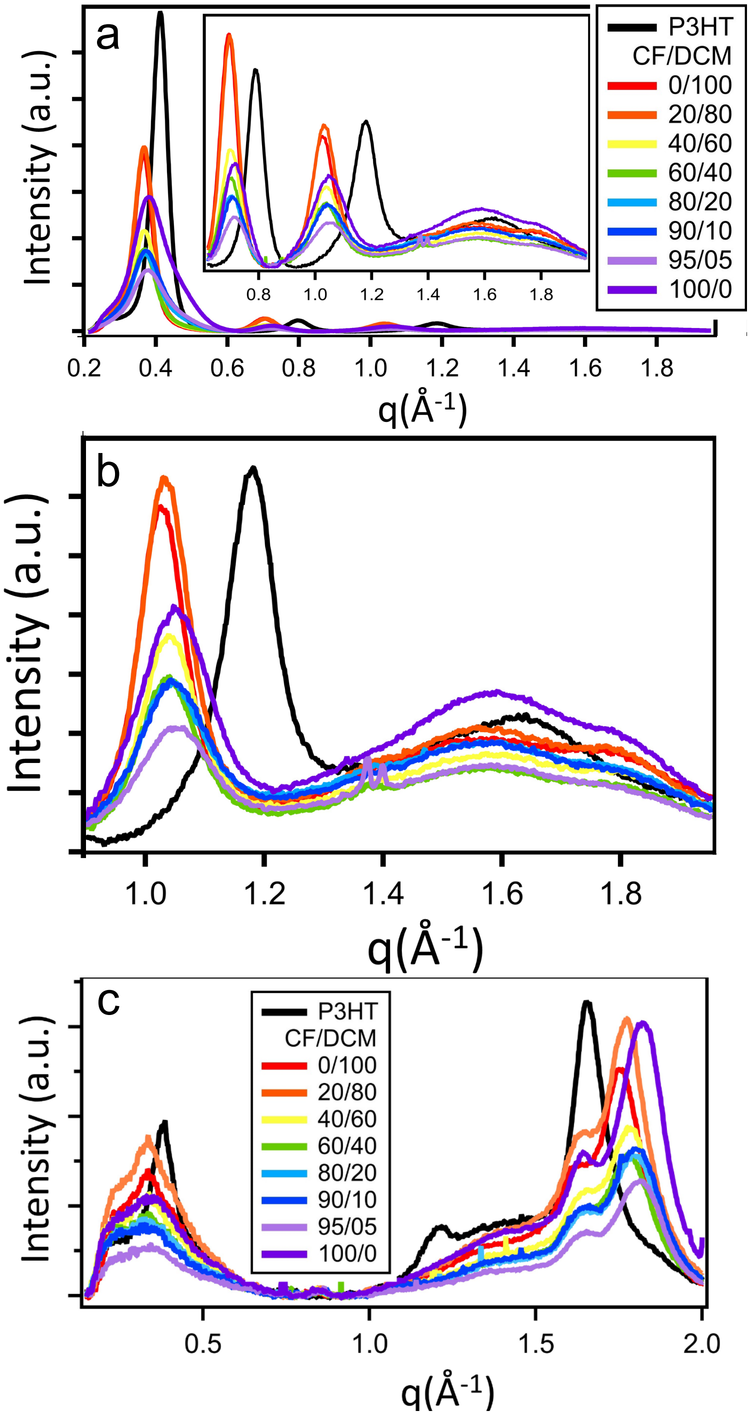

Figure C.12: Integrated thickness-normalized GIWAXS diffractograms for F$_4$TCNQ-doped P3HT from solvent mixtures of CF/DCM in-plane (a) full range and (b) just higher *q* segment. (c) in-plane. The inset in panel (a) shows the region around the out-of-plane (010) peak on an expanded scale.

C.5 Polaronic Coulomb Interactions and Doping Concentration

To investigate how the vibrational spectrum of films produced via sequential processing changes as a function of doping concentration, Figure C.13a shows intensity-normalized spectra of the F_4TCNQ^- B_{1u} vibrational mode in doped P3HT films spanning a solution doping concentration range over two orders of magnitude. For these films, the specific energy of the B_{1u} mode is not sensitive to the absolute doping level. At the highest doping levels we do see the appearance of a new peak located near $2202\,\mathrm{cm}^{-1}$, which is a signature of F_4TCNQ in a fractional charge-transfer complex (CTC).[4,6,8,9,12,52,133]

Figure C.13b shows that the mid-IR electronic absorption spectrum of these same films, normalized to the intensity of the 'B' peak, are essentially independent of dopant concentration. We can see that the degree of polaron delocalization stays virtually unchanged as a function of doping concentration; for these spectra, the A/B band amplitude ratio is 0.53 ± 0.01.

We thus see a set of five distinct conditions where the Stark shift for the F_4TCNQ radical anion yields $\nu_{max} = 2187\,\mathrm{cm}^{-1}$, which are each in direct correspondence with precisely the same mid-IR spectral shape, quantified by A/B ratio = 0.53 ± 0.01. This verifies the idea that doping happens in the crystalline polymer regions first, so that there is a relatively fixed anion-polaron geometry until the polymer crystallites are filled.

Figure C.14 shows an experimental example that demonstrates how the strength of the Coulombic interaction can profoundly affect the mid-IR hole polaron absorption in doped P3HT. When the electron acceptor is a small molecule such as F_4TCNQ (teal curve), the close proximity of the anionic charge provides for a relatively strong Coulomb interaction between the dopant anion and the P3HT polaronic charge carriers, limiting the extent to which the hole can delocalize. The spectral signatures of this interaction are characterized by peak B being shifted to higher energies, and a correspondingly small absorption for peak A below $\sim 0.17\,\mathrm{eV}$. In contrast, the magenta curve in Fig. C.14 shows the P3HT polaron absorption when the dopant anion is a very large (2 nm diameter) dodecaborane-based cluster (DDB-F_{72}).[2,43] Since the electron on the cluster anion localizes near the core of the molecule, there is very little Coulomb attraction between the hole on the polymer and the dopant counterion simply due to this counterion's large physical size.[2,43,59]

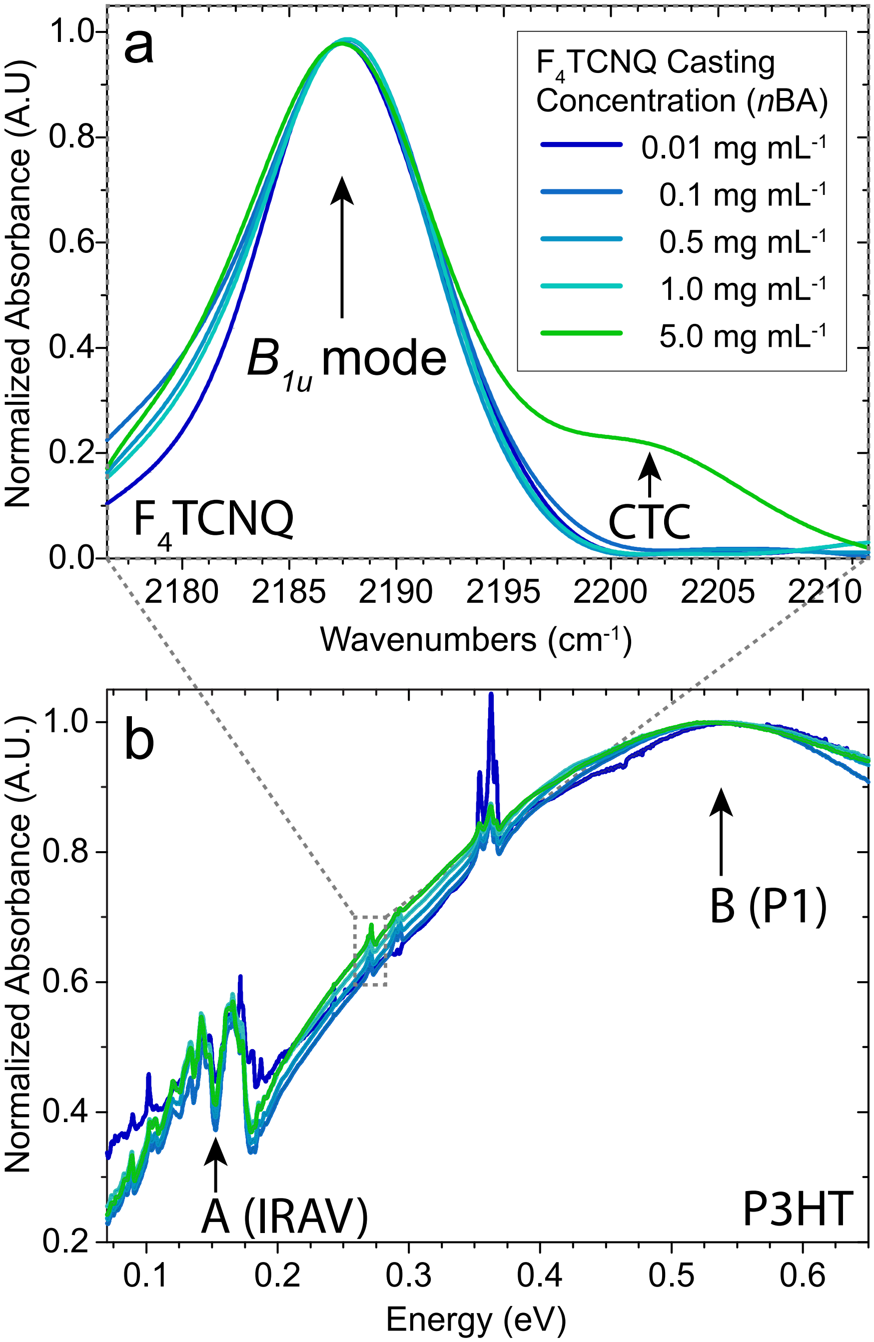

Figure C.13: (a) The F$_4$TCNQ radical anion vibrational spectrum in sequentially solution doped P3HT, normalized against peak intensity across a range of doping solvent concentrations. The dominant feature near $2187\,\mathrm{cm}^{-1}$ belongs to the B_{1u} vibrational mode. At sufficiently high doping levels, an additional peak emerges near $2202\,\mathrm{cm}^{-1}$, indicating the presence of some additional charge transfer complex doping with P3HT. (b) The mid-IR electronic absorbance spectrum for the corresponding P3HT films, normalized against peak intensity for peak B.

This significantly weakened Coulomb interaction produces polarons with large coherence lengths in P3HT, as evidenced by the broad 'B' peak shifting to lower energies and by the increased intensity for the IRAV 'A' peak. These conditions are also associated with significantly higher charge carrier mobilities, a factor of two higher than the most crystalline P3HT doped with F_4TCNQ.[2] As such, there is a clear relationship between the hole-dopant Coulomb interaction and the resulting mid-IR spectral shape.

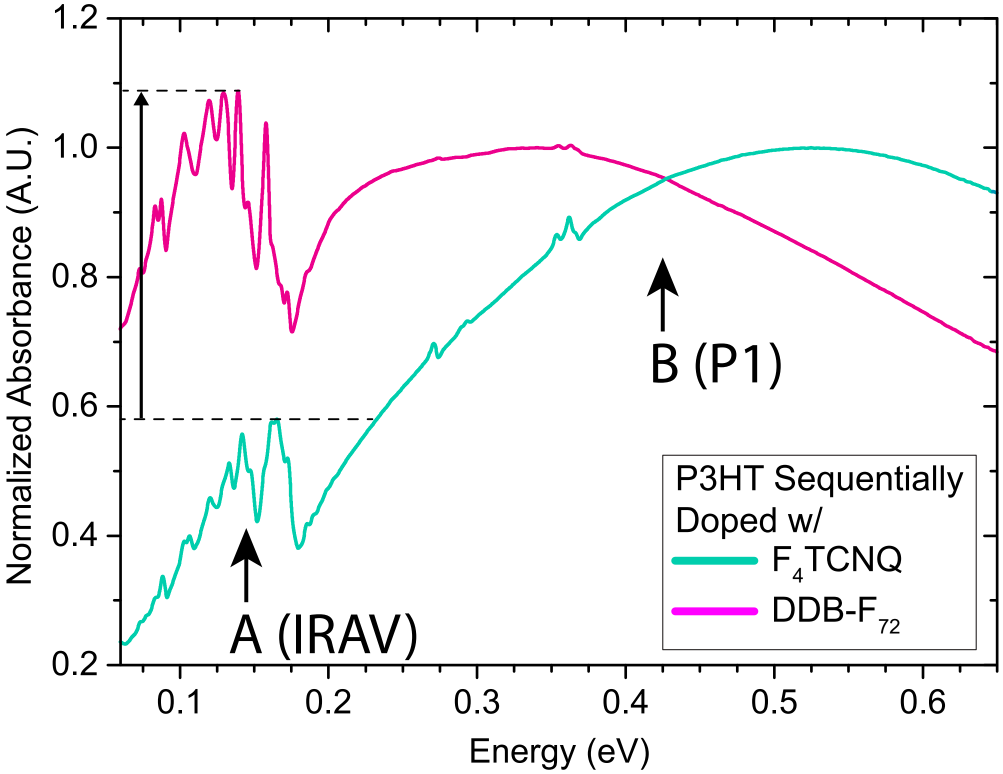

Figure C.14: Mid-IR electronic absorbance spectra for P3HT sequentially solution doped with the small molecule, F_4TCNQ (teal), compared to the bulky dodecaborane cluster, DDB-F_{72} (magenta).

APPENDIX D

Laboratory Specific Experimental Methods

D.1 Introduction

The purpose of this appendix is to guide lab members to successful operation of existing Schwartz Group lab equipment and LabVIEW programs used for device testing. There are additional tutorial videos that have been assembled to aid in the data processing work flow. These tutorials cover concepts related to connecting spectral data for samples acquired on FTIR and UV-Vis-NIR instruments, the baseline correction of vibrational spectra with a highly sloped background, Savitsky-Golay filtering of data (when necessary), peak fitting methods, and construction of publication quality figures using OriginPro 9.1 software which is available to students in the Department of Chemistry & Biochemistry for free. These videos can be found on the internal Schwartz group website under the `'Tutorials'` panel.

D.2 Veeco Dektak 150 Surface Profilometer

The user manual for this instrument can be found at the link https://www.equipx.net/uploads/Veeco/Veeco-Dektak-150-user-manual.pdf , and should be the first resource used to answer questions concerning normal operation of this instrument. An image of our profilometer for reference can be seen in Figure D.1

There are currently two known issues with our particular profilometer and these can be divided into problems with (1) software and (2) hardware. In the below subsections D.2.1 and D.2.2, we will discuss how these issues present themselves and what can be done to mitigate / work around them. By following these guidelines, it is possible this profilometer will continue to be operational for a

Figure D.1: View of our Veeco Dektak 150 Surface Profilometer from the front.

very long time. If these guidelines are ignored, it could lead to serious damage of the stage motor, stylus tip, and possibly instrument death.

D.2.1 Software Related Issues

When first beginning to operate the instrument, always be sure that the the mechanical switch is first illuminated with the 'ON' button clicked in (small control box located at the back right section of the vibration isolation table in Figure D.1). The software can then be opened on the computer. From the perspective of the software, the instrument should always be physically 'ON' when in use. To safely turn off the instrument (without throwing software errors that require a reboot), first be sure that the tower is fully raised, then close the software completely before changing the mechanical switch on the instrument to the 'OFF' position.

By far the most limiting software issue has come up during the last academic year of 2020-2021. It was first noted that the software would sometimes throw a 'Critical Error' message when initializing to begin taking a scan. In the moments directly after the beginning of the scan, the surface profile will fail to post any curve to the screen and shortly thereafter the dreaded 'Critical Error' box will display on the screen as shown in Figure D.2. Once the error is displayed, the instrument will not communicate properly with the software until both the instrument and computer have been fully power cycled.

The critical error only displays for certain combinations of scan parameters. Table D.1 shows a list of combinations of scan distances / length, and the corresponding scan rate. Table D.1 makes it clear that for a wide range of distances and durations, scan rates that are slower than $\sim$15 $\mu\mathrm{m\,s^{-1}}$, are likely to result in a 'Critical Error'. At the same time, any combination of scan distance and duration greater than this value will likely complete the scan normally without any indication of a problem. The specific cause behind this issue is not known, but it appears to be software related. In any case, this issue can be entirely negated by choosing scan rates above $\sim$15 $\mu\mathrm{m\,s^{-1}}$.

The scan parameters can be adjusted by first going 'Window' $\rightarrow$ 'Scan Routine' (Figure D.3). On the subsequent window, the 'Scan Length' and 'Scan Duration' can be adjusted as shown in Figure D.4. Unfortunately the scan rate must be calculated manually from these two values,

Table D.1: List of combinations of scan distance and scan duration, alongside the corresponding scan rate. Scans parameters that caused the error are shown in red and those that did not cause a critical error are shown in green.

Scan Distance / Duration	Scan Rate
1000 µm / 30 s	33.3 $\mu m\,s^{-1}$
800 µm / 30 s	26.66 $\mu m\,s^{-1}$
600 µm / 30 s	20.00 $\mu m\,s^{-1}$
500 µm / 30 s	16.67 $\mu m\,s^{-1}$
450 µm / 30 s	15.00 $\mu m\,s^{-1}$
300 µm / 30 s	10.00 $\mu m\,s^{-1}$
250 µm / 30 s	8.33 $\mu m\,s^{-1}$
1500 µm / 100 s	15 $\mu m\,s^{-1}$
250 µm / 17 s	15 $\mu m\,s^{-1}$

since it is not displayed anywhere in the software as far as I know. For taking standard thickness measurements on polymer films, a scan distance of 450 µm and 20 s (scan rate = 22.5 $\mu m\,s^{-1}$) provides a wide enough distance to capture a reasonable background needed for leveling the scan in the subsequent processing step.

D.2.2 Hardware Related Issues

In addition to some software issues, there is also a mechanical issue related to the motor which raises the tower along the vertical z-axis of the instrument. Due to apparent age related wear of the motor or gears related to this mechanism, under certain circumstances when raising the tower to the fully retracted position, the tower will make an audible grinding sound while skipping in place, without making progress towards lifting itself. The issue can be temporarily alleviated by carefully placing a hand through the front window to the area near the back of the instrument where the large screw is located (obviously be careful where your hand is touching and do not bump the stage or

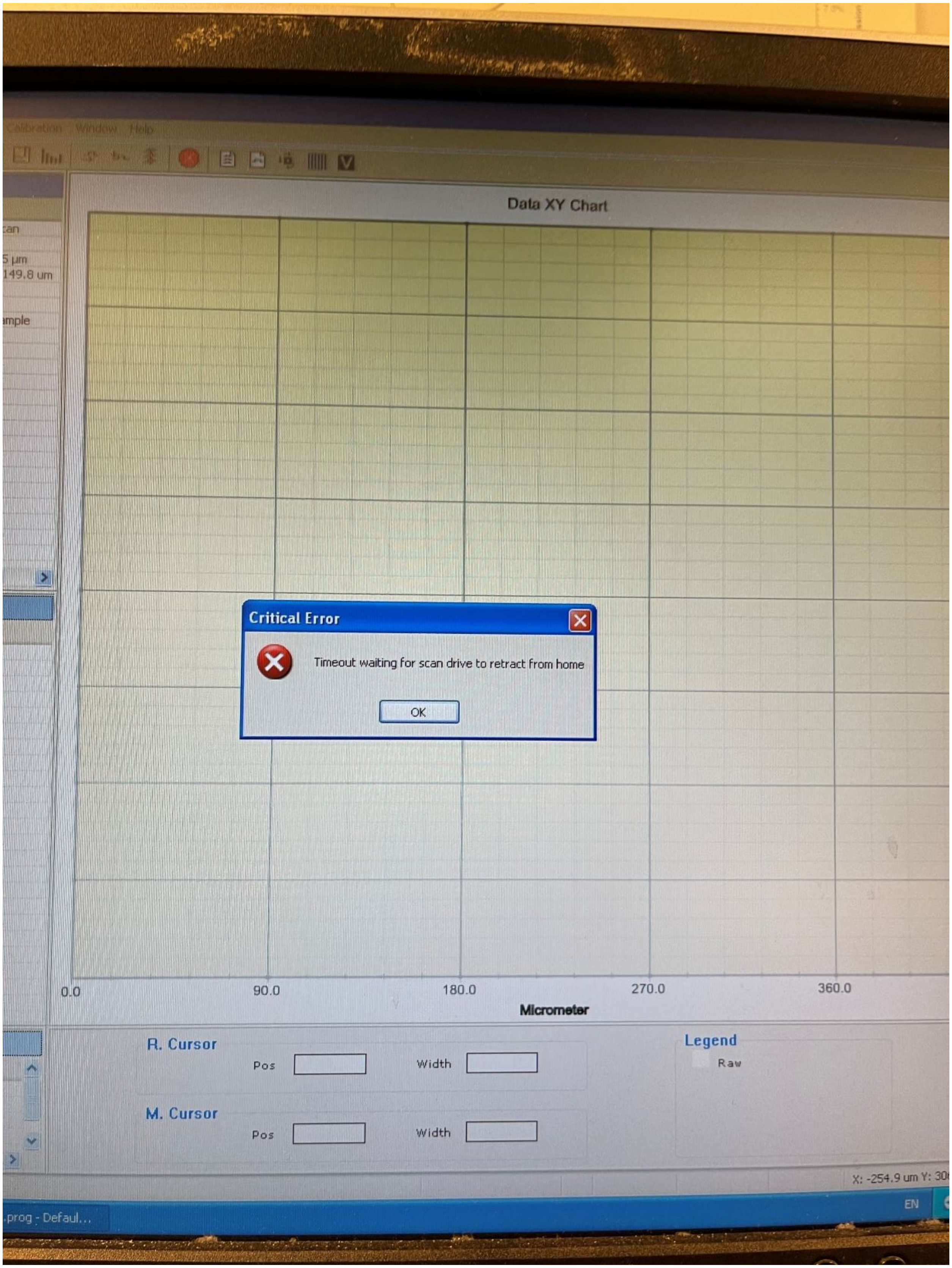

Critical Error

Timeout waiting for scan drive to retract from home

Figure D.2: The ‘Critical Error’ that’s displayed when scanning at a rate below $15\,\mu\mathrm{m\,s^{-1}}$

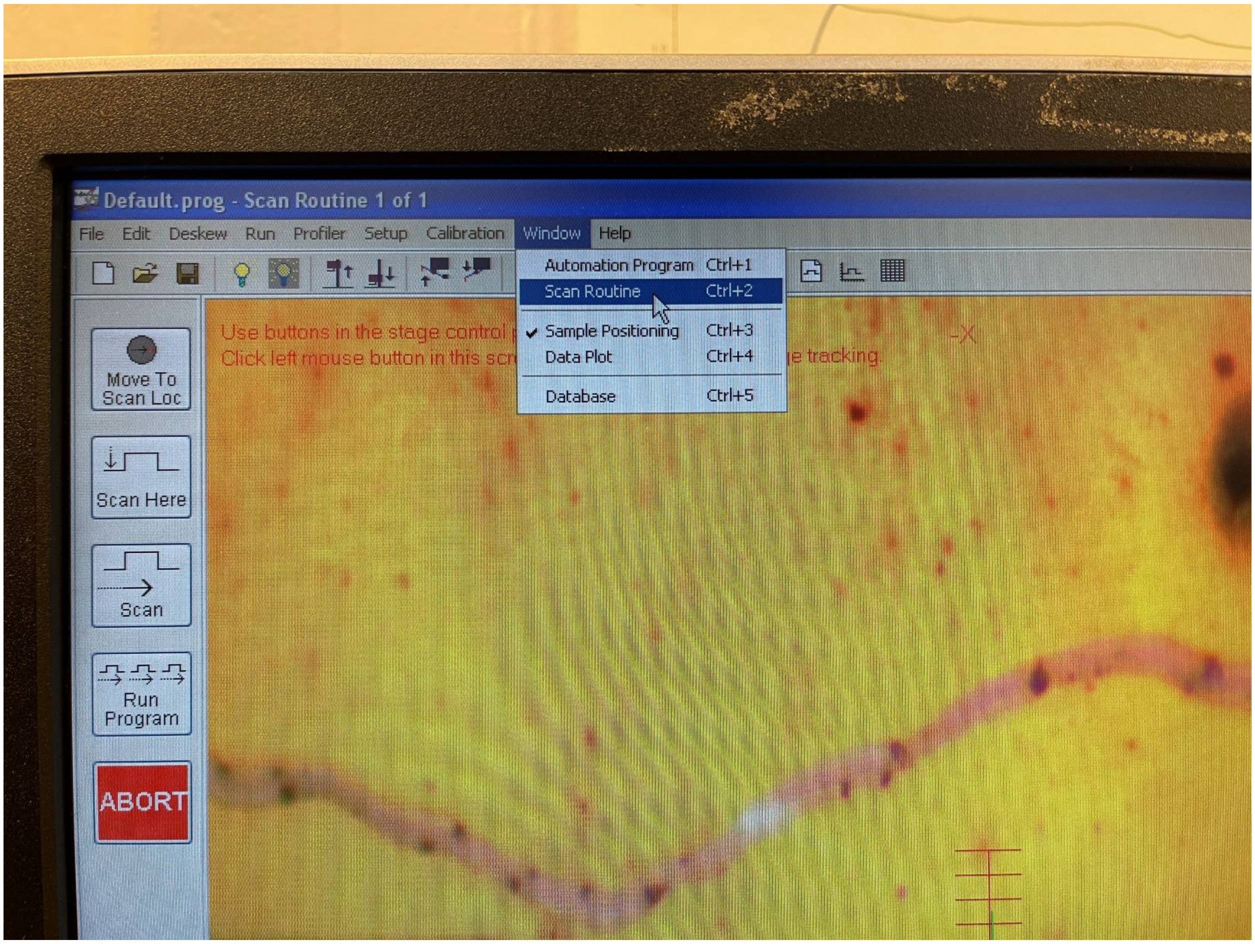

Figure D.3: Go to 'Window' → 'Scan Routine' to access the scan routine settings shown in figure D.4

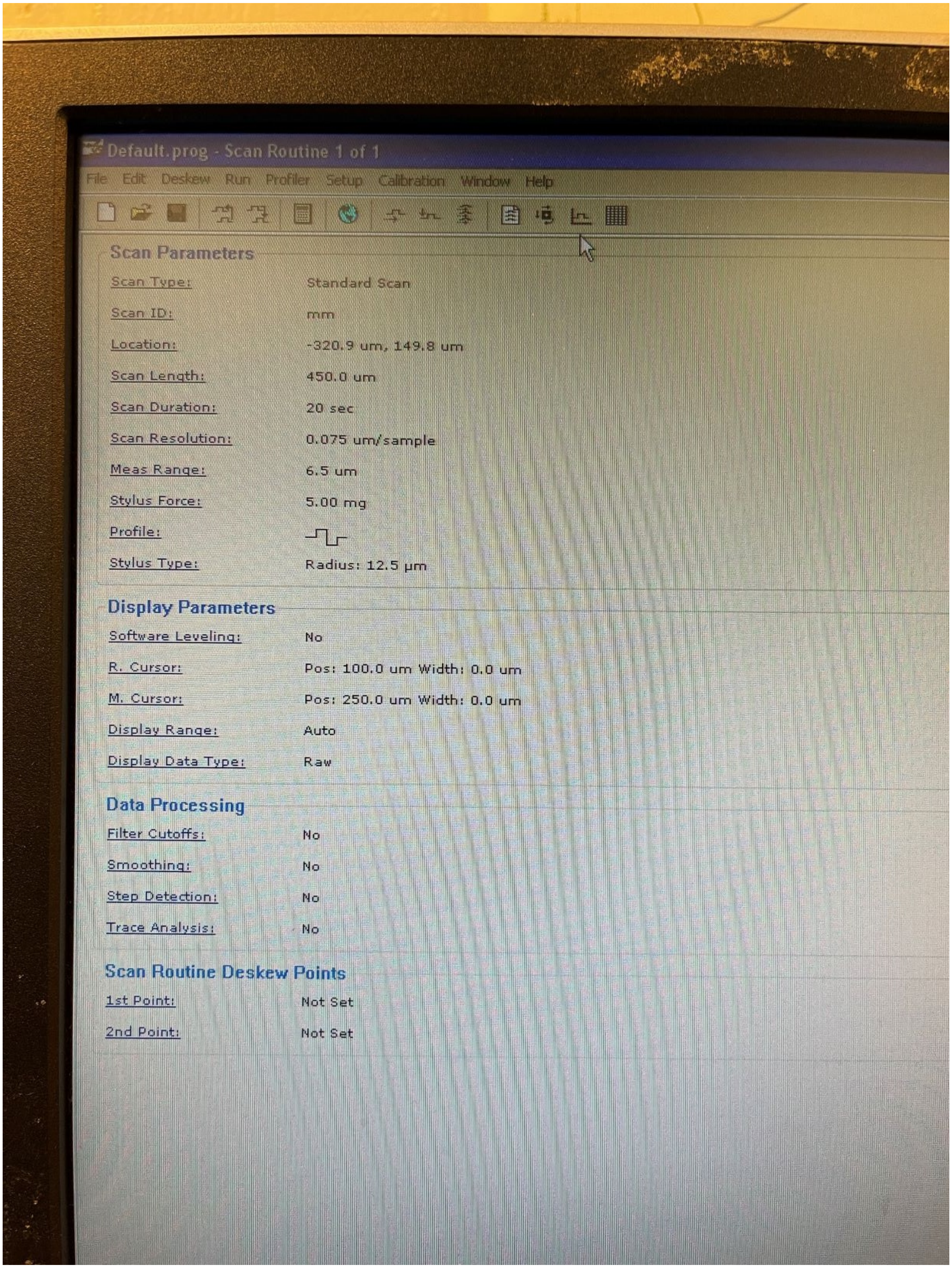

Scan Parameters

Scan Type: Standard Scan
Scan ID: mm
Location: -320.9 um, 149.8 um
Scan Length: 450.0 um
Scan Duration: 20 sec
Scan Resolution: 0.075 um/sample
Meas Range: 6.5 um
Stylus Force: 5.00 mg
Profile:
Stylus Type: Radius: 12.5 µm

Display Parameters

Software Leveling: No
R. Cursor: Pos: 100.0 um Width: 0.0 um
M. Cursor: Pos: 250.0 um Width: 0.0 um
Display Range: Auto
Display Data Type: Raw

Data Processing

Filter Cutoffs: No
Smoothing: No
Step Detection: No
Trace Analysis: No

Scan Routine Deskew Points

1st Point: Not Set
2nd Point: Not Set

Figure D.4: ‘Scan Routine’ dialogue, displaying all of the adjustable scan parameters.

tower which may result in stylus tip damage). Figure D.5 shows with red arrows the location where your hand should be hovering just underneath, ready to intervene if the tower begins to grind. With your right hand still free, click the ‘Tower Up’ icon in the software to begin moving the tower to the fully retracted position. If you begin to hear any grinding sound, promptly apply gentle but firm pressure upwards in the direction the tower should be moving. Your hand should be pressing on the light gray section indicated by the red arrows, and continue slowly applying additional pressure up until the grinding stops. This might only be 1-2 seconds as the grinding issue appears to only happen when the tower is fully extended to the lowest position. As the grinding noise stops, you can gently release pressure and allow the tower to raise under its own power. *Only apply pressure as needed and whenever possible, allow the tower to retract under its own power.* The idea here is we want to relieve whatever excess strain is being exerted on the motor. Helping it by reducing the weight it has to lift tends to put things back on track. If this issue happens once, it will likely happen again on the subsequent scan, so the instrument tends to stick with what it has done recently in the past (both good and bad behavior). I have had some success with exiting the software, turning off the instrument and then starting the instrument up again and opening the software. Doing this procedure forces the instrument to reinitialize itself, which may allow it to fix itself in some way. It is very possible that the instrument will retract without issue for extended periods of time, however if it begins to show signs of grinding, follow the above steps to minimize wear and tear.

You can gain a sense for if the instrument will be behaving this way on a given day, by carefully observing its behavior when moving the tower down to the null position, close to the sample. Sometimes, it will display some subtle ‘skipping’ behavior in the last moments before reaching the null position on the way down.

If you suspect that the motor will grind when trying to move the tower up, preemptively place a hand hovering near the back to minimize the time spent grinding (if it happens). Doing it this way also means you won’t be thrusting your hand into the instrument enclosure *during* the grinding, which if you are panicked could cause your arm to bump into things causing other damage.

This small skipping on the way down is also typically associated with some skipping when the tower is moving down to actually begin taking a scan. In this case, the tower will skip forwards along your line path by an unpredictable amount, so adding some additional length to your scan to

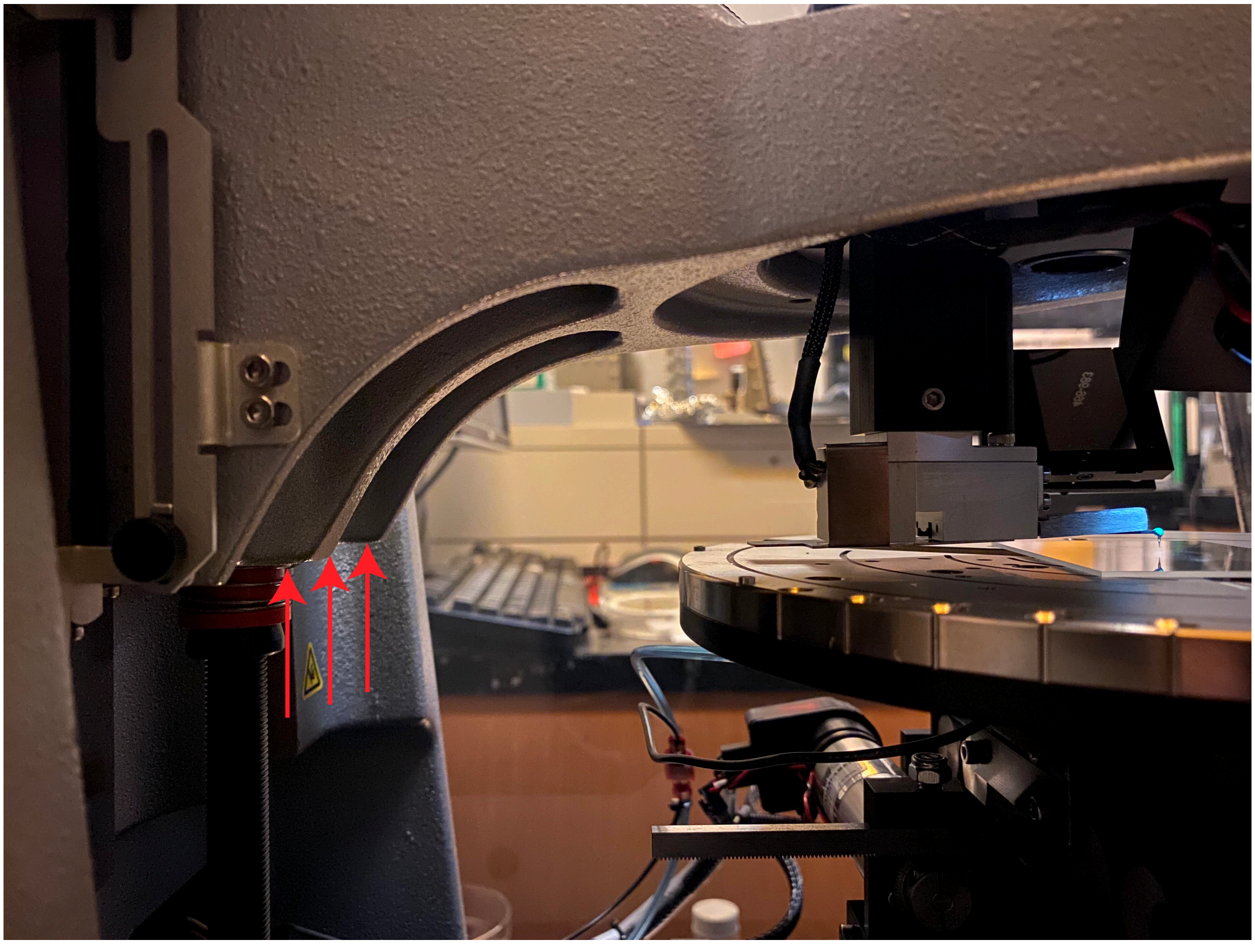

Figure D.5: Red arrows indicate the location where your hand should be hovering just underneath, ready to intervene applying gentle upwards pressure if the tower begins to grind.

anticipate this shift can be a useful practice. If you observe that the tower is behaving this way with small skips that appear fine on the way down, it is much more likely (but not a certainty) that the tower will have a grinding event when you go to fully retract the stage so this would be an indication you may want to place your hand ready near the back (Figure D.5).

D.2.3 Changing the Stylus Tip and Completing the Stylus Force Calibration

If for some reason the stylus needs to be changed or the force that it applies needs to be recalibrated (e.g. replacing a broken tip) a video demonstrating how this is done can be found on YouTube at the following the url, https://www.youtube.com/watch?v=JqPQThHB6_s&ab_channel=davesatiesdavesaties

Dektak 150 Simplified Force Calibration

1. In Dektak program menu, go to Calibration → Stylus Force.
2. Set Measurement range to 524um.
3. Close environmental enclosure door.
4. Click on Balance and wait about a minute until the balanced value (D0) shows up. Do this 3 times and enter the average of these values in D0.

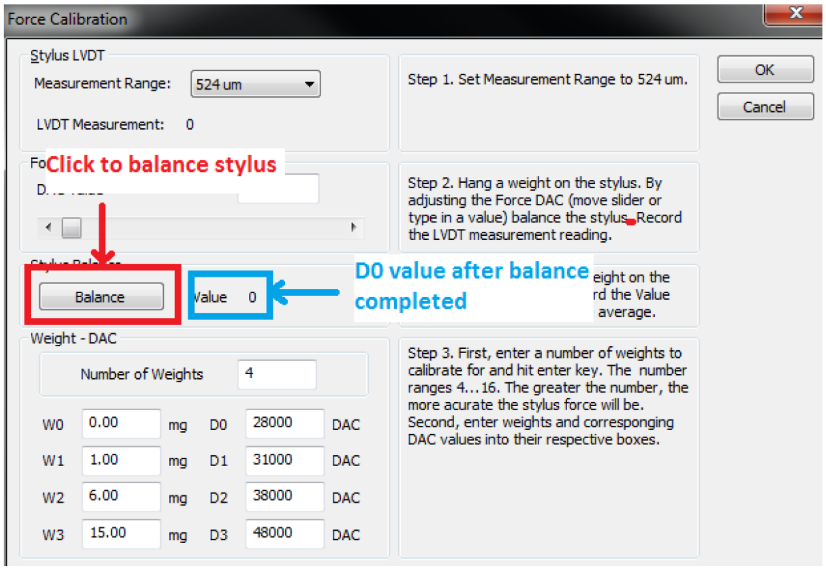

Click to balance stylus

D0 value after balance completed

Measurement Range: 524 um

LVDT Measurement: 0

Value 0

Step 1. Set Measurement Range to 524 um.

Step 2. Hang a weight on the stylus. By adjusting the Force DAC (move slider or type in a value) balance the stylus. Record the LVDT measurement reading.

eight on the
rd the Value
average.

Step 3. First, enter a number of weights to calibrate for and hit enter key. The number ranges 4...16. The greater the number, the more acurate the stylus force will be. Second, enter weights and corresponging DAC values into their respective boxes.

Number of Weights 4

W0	0.00	mg	D0	28000	DAC
W1	1.00	mg	D1	31000	DAC
W2	6.00	mg	D2	38000	DAC
W3	15.00	mg	D3	48000	DAC

5. Derive D1, D2 and D3 using the formulas below.

D0 = balance function will give this number
D1 = D0 +1731
D2 = D1 +7010
D3 = D2 +11195
Set the weight values as follow:
W0 =0
W1 = 1.11
W2 = 5.93
W3 = 16

6. Click OK to accept new force calibration values.

Figure D.6: Procedure for recalibrating the stylus force, as provided by Bruker (which now owns Veeco).

What is not mentioned in that video is that upon installing a tip (either brand new, or just resituating an old one), the stylus force needs to be recalibrated. An Excel calculator displaying this procedure can be found on the argon box computer by searching for '`Dektak 150 Simplified Force Calibration`' but I've also reproduced an image of it here in Figure D.6 for ease of access.

D.3 Electrical Measurements and LabVIEW Programs

Photovoltaics, light emitting diodes and other devices adopt a layered thin film structure where layers are put down in a particular order with the need for a transparent electrode on one side. In the Schwartz Group, we have accumulated a large number of reusable conductive ITO, transparent substrates from the days of making bulk heterjunction (BHJ) solar cells. The additional electrodes for these types of devices can be deposited using our thermal evaporator and the corresponding shadow mask, as depicted in Figure D.7. The specific evaporation recipes for a variety of small molecule depositions designed for OLED device fabrication (as well as electrode deposition recipes) can be found in Dane's lab notebook as well as in the Inficon thermal evaporator software.

Once electrodes have been deposited, the final step is to characterize the electrical quality of these devices. In Figures D.7 and D.8b, the four pads that show a bulb near the top and bottom represent the device cathode (-). When driving the device, electrons are injected into the sample through this electrode. On the far left, the fifth electrode which looks different from the others makes contact directly with the ITO substrate by previously scraping away the polymer layer here or masking off this section with tape when evaporating small molecule layers. In this way, the aluminum based anode (+) makes direct physical contact with the underlying ITO. The charges from this electrode on the anode side are holes which are injected from the ITO directly into the active layer of the device. Electrical characterization is carried out using various LabVIEW programs that are located on the argon box computer. There have been many different LabVIEW programs developed over the years, and many improved iterations based on similar underlying virtual instruments (VIs). Below is a non comprehensive list of the most useful LabVIEW VIs you may want to choose from during electrical characterization. Many of these are located on the computer desktop, but they can of course also be found by doing a search from the windows start menu.

- `Van der Pauw Ke2400_v2.0`
- `Resistance vs time`
- `New J-V Sweep`
- `2 point IV sweep`
- `OFET sweep`
- `LIV_OLED`
- `CELIV`
- `Seebeck Measurement v2.0`
- `EQE_V2.1`

Inside the argon box there is a control box with rainbow colored wires connected to a 3M clip. This can be used to secure the gold pronged electrodes on the clip to the actual device electrodes, as shown in Figure D.8b. There is a circular white teflon sample holder with a metal bracket that this 3M clip fits snuggly into which is not shown, but is currently fastened to the small optical table inside the argon box. The electrical signal is carried outside the argon box through the rainbow wire indicated by the orange arrows in Figures D.8a and D.9a. Unfortunately, for unknown reasons, the positive and negative leads are routed through the BNC cable backwards so to ensure the device anode (+) is connected to the Keithley 2400 source meter properly, be sure that the GRND banana plug (indicated by the notch that says GRND) is actually connected to the red (+) terminal on the Keithley 2400 as shown in Figure D.9b. You can check if this setup is working properly by running a J-V sweep from 0-3V using a test LED stored on the shelves of the argon box. The longer electrode on the LED is the anode (+) and thus clips to the first gold lead on the 3M clip (electrode on the far left in Figure D.8b). The control box near the computer is shown in Figure D.9 and has a black dial that allows for switching between a series of channels. You can see that the dial begins counting from channel 2, and this is because channel 1 is dedicated to carrying the (+) anode signal from the device on pad 1. In this way, the dial allows simple switching between pads 2-5 from

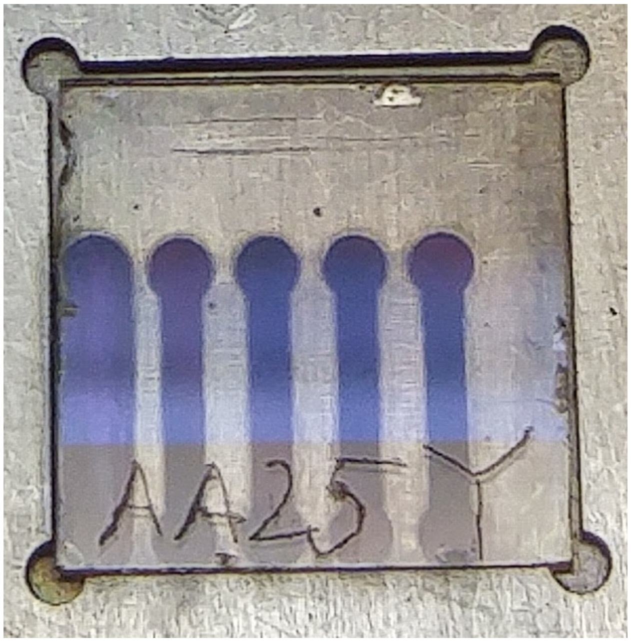

Figure D.7: An ITO substrate showing thin film interference with the reflected light inside the argon box. The section at the bottom does not show thin film interference because it is electrically insulated and does not contain any ITO. This way, when attaching the electrode clip, the electrodes can punch through the pad without risk of shorting directly through to the ITO. The substrate here is located inside a custom made shadow mask. The aluminum will travel through the negative part of the 'shadow' and deposit an image of the electrodes on top of the sample.

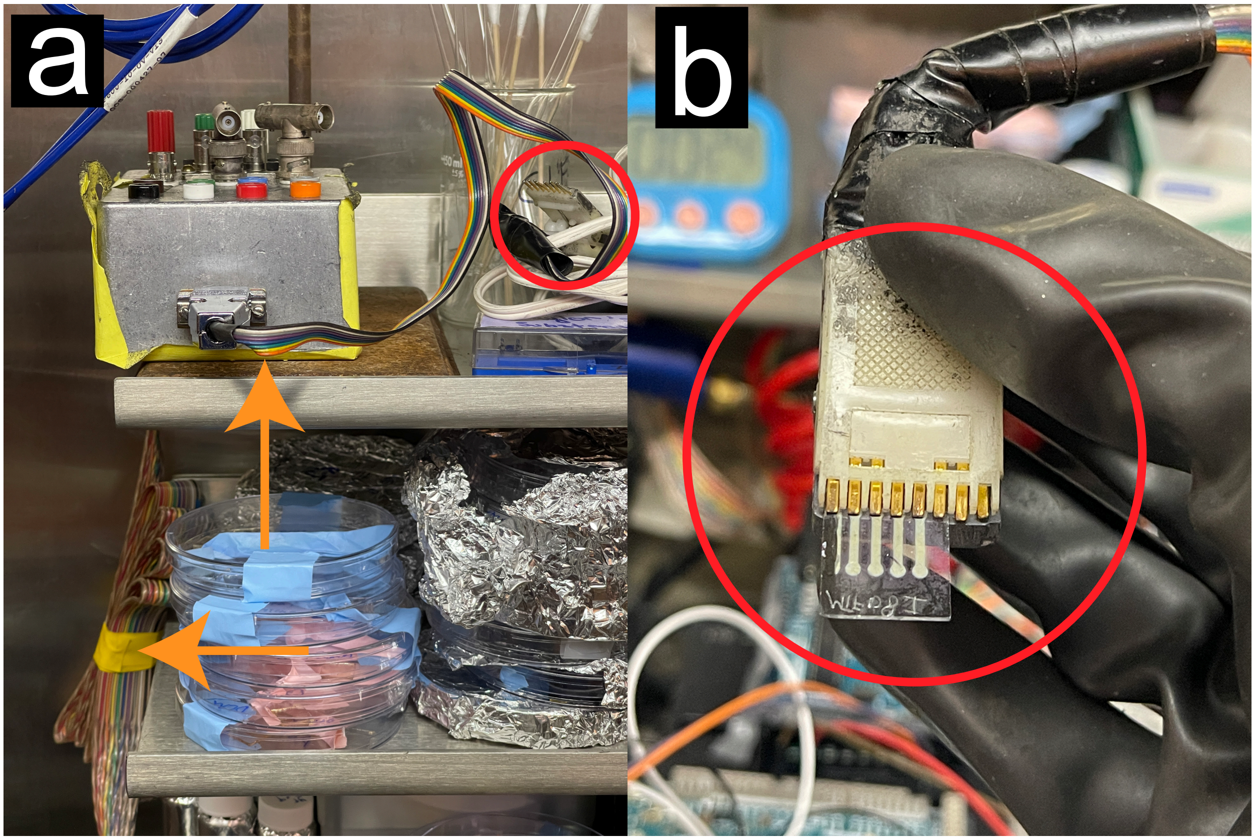

Figure D.8: Depiction of the old school device testing arrangement for ITO based samples in the 'sandwich structure' (a) A complete image showing the wiring for this arrangement on the side that's inside the argon box. The rainbow colored cable exits the box and runs directly to the small control switch box near the argon box PC. (b) A closeup image of the 3M clip device holder with gold prongs, clipped to an ITO based sample.

outside the box, without having to disturb the sample. By investigating the behavior of 4 different pads on a single ITO slide, the chances of finding an idealized trace are much higher.

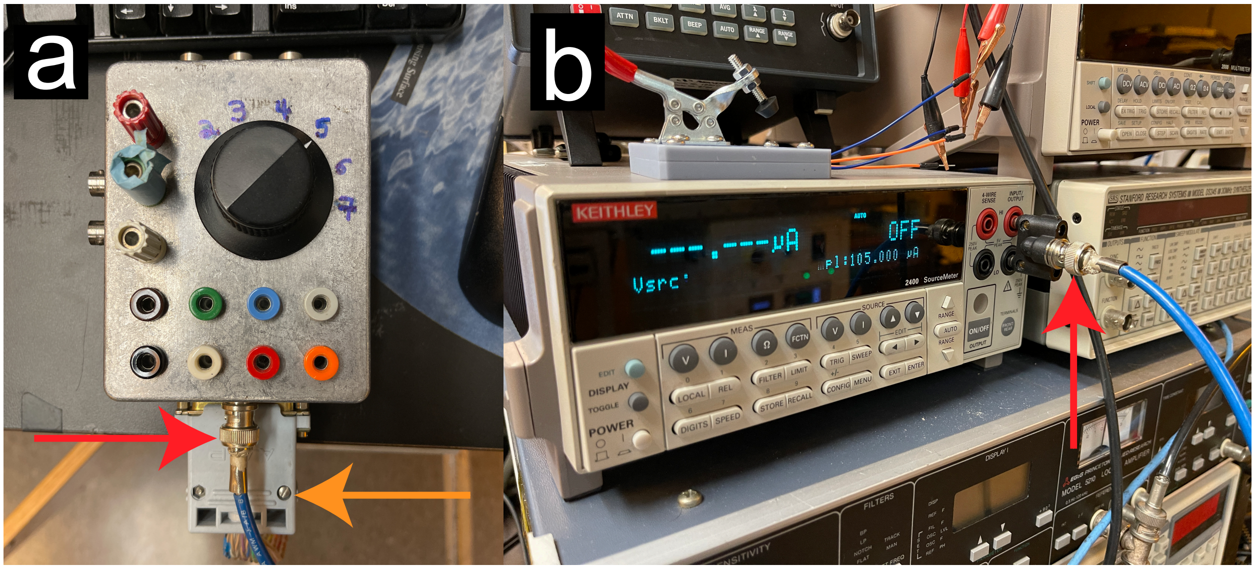

Figure D.9: (a) The control switch box that is connected directly via the rainbow colored cable indicated by the orange arrows here as well as in Figure D.8. The specific pad (2-5) gets selected by adjusting the channel as shown by the black dial on the center of the control box. The anode (+) lead that is connected to the ITO on pad 1 remains in place, and the dial adjusts which pad becomes electrically connected as the device cathode (-). The positive and negative leads are then routed through a BNC cable indicated by the arrow in red, and ultimately connected to the Keithley 2400 shown in panel b. For this measurement, be sure that the bannan clip is plugged in *backwards*, with the GRND lead plugged into the red (+) terminal and the other clip plugged into the black (-) terminal. If you are not sure, test your setup with a commercial LED found on the argon box shelves.

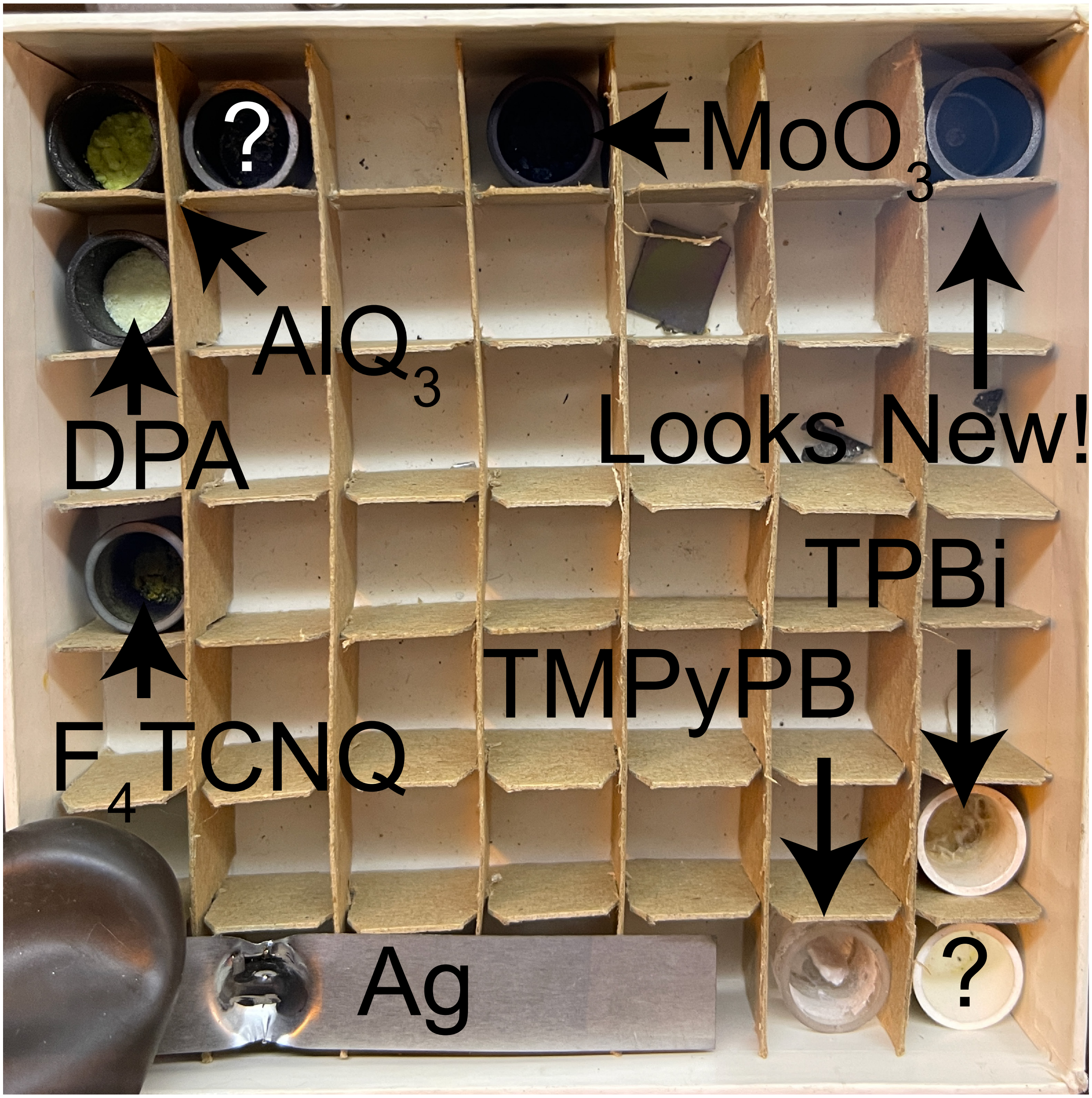

Figure D.10: A snapshot of the current arrangement of crucibles for evaporating non metal species. Many of these molecules are used as layers in the fabrication of light emitting diodes, and so the corresponding vials these were taken from can be found by matching the short hand name with the structure found online (e.g. search for 'ALQ$_3$ OLED' to match the short hand name to the specific structure listed on the bottle.) At the time of this writing, the commercial bottles for these small molecules are stored in the large antechamber area with the additional supplies of metals.

REFERENCES

[1] P. Stallinga, *Electrical Characterization of Organic Electronic Materials and Devices*. Chichester, UK: John Wiley & Sons, Ltd, oct 2009.

[2] T. J. Aubry, K. J. Winchell, C. Z. Salamat, V. M. Basile, J. R. Lindemuth, J. M. Stauber, J. C. Axtell, R. M. Kubena, M. D. Phan, M. J. Bird, A. M. Spokoyny, S. H. Tolbert, and B. J. Schwartz, "Tunable Dopants with Intrinsic Counterion Separation Reveal the Effects of Electron Affinity on Dopant Intercalation and Free Carrier Production in Sequentially Doped Conjugated Polymer Films," *Advanced Functional Materials*, vol. 30, p. 2001800, jul 2020.

[3] P. Pingel, L. Zhu, K. S. Park, J.-O. Vogel, S. Janietz, E.-G. Kim, J. P. Rabe, J.-L. Brédas, and N. Koch, "Charge-Transfer Localization in Molecularly Doped Thiophene-Based Donor Polymers," *The Journal of Physical Chemistry Letters*, vol. 1, pp. 2037–2041, jul 2010.

[4] F. Ghani, A. Opitz, P. Pingel, G. Heimel, I. Salzmann, J. Frisch, D. Neher, A. Tsami, U. Scherf, and N. Koch, "Charge transfer in and conductivity of molecularly doped thiophene-based copolymers," *Journal of Polymer Science, Part B: Polymer Physics*, vol. 53, no. 1, pp. 58–63, 2015.

[5] H. Méndez, G. Heimel, S. Winkler, J. Frisch, A. Opitz, K. Sauer, B. Wegner, M. Oehzelt, C. Röthel, S. Duhm, D. Többens, N. Koch, and I. Salzmann, "Charge-transfer crystallites as molecular electrical dopants," *Nature Communications*, vol. 6, p. 8560, dec 2015.

[6] I. E. Jacobs, C. Cendra, T. F. Harrelson, Z. I. Bedolla Valdez, R. Faller, A. Salleo, and A. J. Moulé, "Polymorphism controls the degree of charge transfer in a molecularly doped semiconducting polymer," *Materials Horizons*, vol. 5, no. 4, pp. 655–660, 2018.

[7] H. Hase, K. O. Neill, J. Frisch, A. Opitz, and N. Koch, "Unraveling the Microstructure of Molecularly Doped Poly(3-hexylthiophene) by Thermally Induced Dedoping," *The Journal of Physical Chemistry C*, vol. 122, pp. 25893–25899, 2018.

[8] B. Neelamraju, K. E. Watts, J. E. Pemberton, and E. L. Ratcliff, "Correlation of Coexistent Charge Transfer States in F 4 TCNQ-Doped P3HT with Microstructure," *Journal of Physical Chemistry Letters*, vol. 9, no. 23, pp. 6871–6877, 2018.

[9] K. E. Watts, B. Neelamraju, E. L. Ratcliff, and J. E. Pemberton, "Stability of Charge Transfer States in F 4 TCNQ-Doped P3HT," *Chemistry of Materials*, vol. 31, pp. 6986–6994, sep 2019.

[10] N. L. Haworth, J. Lu, N. Vo, T. H. Le, C. D. Thompson, A. M. Bond, and L. L. Martin, "Diagnosis of the Redox Levels of TCNQF 4 Compounds Using Vibrational Spectroscopy," *ChemPlusChem*, vol. 79, pp. 962–972, jul 2014.

[11] M. T. Fontana, D. A. Stanfield, D. T. Scholes, K. J. Winchell, S. H. Tolbert, and B. J. Schwartz, "Evaporation vs Solution Sequential Doping of Conjugated Polymers: F 4 TCNQ Doping of Micrometer-Thick P3HT Films for Thermoelectrics," *The Journal of Physical Chemistry C*, vol. 123, pp. 22711–22724, sep 2019.

[12] D. A. Stanfield, Y. Wu, S. H. Tolbert, and B. J. Schwartz, “Controlling the Formation of Charge Transfer Complexes in Chemically Doped Semiconducting Polymers,” *Chemistry of Materials*, p. acs.chemmater.0c04471, mar 2021.

[13] A. O. Patil, A. J. Heeger, and F. Wudl, “Optical properties of conducting polymers,” *Chemical Reviews*, vol. 88, pp. 183–200, jan 1988.

[14] Y. Furukawa, “Electronic Absorption and Vibrational Spectroscopies of Conjugated Conducting Polymers,” *The Journal of Physical Chemistry*, vol. 100, pp. 15644–15653, jan 1996.

[15] H. Méndez, G. Heimel, A. Opitz, K. Sauer, P. Barkowski, M. Oehzelt, J. Soeda, T. Okamoto, J. Takeya, J.-B. Arlin, J.-Y. Balandier, Y. Geerts, N. Koch, and I. Salzmann, “Doping of Organic Semiconductors: Impact of Dopant Strength and Electronic Coupling,” *Angewandte Chemie International Edition*, vol. 52, pp. 7751–7755, jul 2013.

[16] P. Pingel and D. Neher, “Comprehensive picture of p-type doping of P3HT with the molecular acceptor F4TCNQ,” *Physical Review B*, vol. 87, no. 11, p. 115209, 2013.

[17] J. E. Cochran, M. J. N. Junk, A. M. Glaudell, P. L. Miller, J. S. Cowart, M. F. Toney, C. J. Hawker, B. F. Chmelka, and M. L. Chabinyc, “Molecular Interactions and Ordering in Electrically Doped Polymers: Blends of PBTTT and F4TCNQ,” *Macromolecules*, vol. 47, pp. 6836–6846, 2014.

[18] R. A. Schlitz, F. G. Brunetti, A. M. Glaudell, P. L. Miller, M. A. Brady, C. J. Takacs, C. J. Hawker, and M. L. Chabinyc, “Solubility-Limited Extrinsic n-Type Doping of a High Electron Mobility Polymer for Thermoelectric Applications,” *Advanced Materials*, vol. 26, pp. 2825–2830, may 2014.

[19] D. T. Scholes, S. A. Hawks, P. Y. Yee, H. Wu, J. R. Lindemuth, S. H. Tolbert, and B. J. Schwartz, “Overcoming Film Quality Issues for Conjugated Polymers Doped with F4TCNQ by Solution Sequential Processing: Hall Effect, Structural, and Optical Measurements,” *The Journal of Physical Chemistry Letters*, vol. 6, pp. 4786–4793, 2015.

[20] J. Yamamoto and Y. Furukawa, “Electronic and Vibrational Spectra of Positive Polarons and Bipolarons in Regioregular Poly(3-hexylthiophene) Doped with Ferric Chloride,” *The Journal of Physical Chemistry B*, vol. 119, pp. 4788–4794, apr 2015.

[21] K. Kang, S. Watanabe, K. Broch, A. Sepe, A. Brown, I. Nasrallah, M. Nikolka, Z. Fei, M. Heeney, D. Matsumoto, K. Marumoto, H. Tanaka, S.-i. Kuroda, and H. Sirringhaus, “2D Coherent Charge Transport in Highly Ordered Conducting Polymers Doped by Solid State Diffusion,” *Nature Materials*, vol. 15, no. 5, pp. 896–903, 2016.

[22] B. Russ, A. Glaudell, J. J. Urban, M. L. Chabinyc, and R. A. Segalman, “Organic Thermoelectric Materials for Energy Harvesting and Temperature Control,” *Nature Reviews Materials*, vol. 1, no. 10, pp. 1–14, 2016.

[23] I. E. Jacobs, E. W. Aasen, J. L. Oliveira, T. N. Fonseca, J. D. Roehling, J. Li, G. Zhang, M. P. Augustine, M. Mascal, and A. J. Moulé, "Comparison of Solution-Mixed and Sequentially Processed P3HT:F4TCNQ Films: Effect of Doping-Induced Aggregation on Film Morphology," *Journal of Materials Chemistry C*, vol. 4, no. 16, pp. 3454–3466, 2016.

[24] S. N. Patel, A. M. Glaudell, D. Kiefer, and M. L. Chabinyc, "Increasing the Thermoelectric Power Factor of a Semiconducting Polymer by Doping from the Vapor Phase," *ACS Macro Letters*, vol. 5, no. 3, pp. 268–272, 2016.

[25] V. A. Kolesov, C. Fuentes-Hernandez, W.-F. Chou, N. Aizawa, F. A. Larrain, M. Wang, A. Perrotta, S. Choi, S. Graham, G. C. Bazan, T.-Q. Nguyen, S. R. Marder, and B. Kippelen, "Solution-Based Electrical Doping of Semiconducting Polymer Films Over a Limited Depth," *Nature Materials*, vol. 1, no. December, pp. 1–8, 2016.

[26] N. Engel, S. I. Bokarev, A. Moguilevski, A. A. Raheem, R. Al-Obaidi, T. Möhle, G. Grell, K. R. Siefermann, B. Abel, S. G. Aziz, O. Kühn, M. Borgwardt, I. Y. Kiyan, and E. F. Aziz, "Light-Induced Relaxation Dynamics of the Ferricyanide Ion Revisited by Ultrafast XUV Photoelectron Spectroscopy," *Physical Chemistry Chemical Physics*, vol. 19, no. 22, pp. 14248–14255, 2017.

[27] M. N. Gueye, A. Carella, N. Massonnet, E. Yvenou, S. Brenet, J. Faure-Vincent, S. Pouget, F. Rieutord, H. Okuno, A. Benayad, R. Demadrille, and J.-P. Simonato, "Structure and Dopant Engineering in PEDOT Thin Films: Practical Tools for a Dramatic Conductivity Enhancement," *Chemistry of Materials*, vol. 28, pp. 3462–3468, may 2016.

[28] L. Müller, D. Nanova, T. Glaser, S. Beck, A. Pucci, A. K. Kast, R. R. Schröder, E. Mankel, P. Pingel, D. Neher, W. Kowalsky, and R. Lovrincic, "Charge-Transfer-Solvent Interaction Predefines Doping Efficiency in p-Doped P3HT Films," *Chem. Mater.*, vol. 28, no. 12, pp. 4432–4439, 2016.

[29] A. Hamidi-Sakr, L. Biniek, J. L. Bantignies, D. Maurin, L. Herrmann, N. Leclerc, P. Lévêque, V. Vijayakumar, N. Zimmermann, and M. Brinkmann, "A Versatile Method to Fabricate Highly In-Plane Aligned Conducting Polymer Films with Anisotropic Charge Transport and Thermoelectric Properties: The Key Role of Alkyl Side Chain Layers on the Doping Mechanism," *Advanced Functional Materials*, vol. 27, no. 25, pp. 1–13, 2017.

[30] L. Müller, S.-Y. Rhim, V. Sivanesan, D. Wang, S. Hietzschold, P. Reiser, E. Mankel, S. Beck, S. Barlow, S. R. Marder, A. Pucci, W. Kowalsky, and R. Lovrincic, "Electric-Field-Controlled Dopant Distribution in Organic Semiconductors," *Advanced Materials*, vol. 29, p. 1701466, aug 2017.

[31] I. E. Jacobs and A. J. Moulé, "Controlling Molecular Doping in Organic Semiconductors," *Advanced Materials*, vol. 29, p. 1703063, nov 2017.

[32] K. Broch, D. Venkateshvaran, V. Lemaur, Y. Olivier, D. Beljonne, M. Zelazny, I. Nasrallah, D. J. Harkin, M. Statz, R. D. Pietro, A. J. Kronemeijer, and H. Sirringhaus, "Measurements of Ambipolar Seebeck Coefficients in High-Mobility Diketopyrrolopyrrole Donor-Acceptor Copolymers," *Advanced Electronic Materials*, vol. 3, p. 1700225, nov 2017.

[33] Y. Karpov, T. Erdmann, M. Stamm, U. Lappan, O. Guskova, M. Malanin, I. Raguzin, T. Beryozkina, V. Bakulev, F. Günther, S. Gemming, G. Seifert, M. Hambsch, S. Mannsfeld, B. Voit, and A. Kiriy, "Molecular Doping of a High Mobility Diketopyrrolopyrrole-Dithienylthieno[3,2-b]thiophene Donor-Acceptor Copolymer with F6TCNNQ," *Macromolecules*, vol. 50, no. 3, pp. 914–926, 2017.

[34] S. N. Patel, A. M. Glaudell, K. A. Peterson, E. M. Thomas, K. A. O'Hara, E. Lim, and M. L. Chabinyc, "Morphology Controls the Thermoelectric Power Factor of a Doped Semiconducting Polymer," *Science Advances*, vol. 3, no. 6, pp. 24–26, 2017.

[35] J. Hynynen, D. Kiefer, L. Yu, R. Kroon, R. Munir, A. Amassian, M. Kemerink, and C. Müller, "Enhanced Electrical Conductivity of Molecularly p-Doped Poly(3-hexylthiophene) Through Understanding the Correlation with Solid-State Order," *Macromolecules*, vol. 50, no. 20, pp. 8140–8148, 2017.

[36] Y. Karpov, N. Kiriy, M. Al-Hussein, M. Hambsch, T. Beryozkina, V. Bakulev, S. C. Mannsfeld, B. Voit, and A. Kiriy, "Hexacyano-[3]-Radialene Anion-Radical Salts: A Promising Family of Highly Soluble p-Dopants," *Chemical Communications*, vol. 54, no. 3, pp. 307–310, 2018.

[37] J. Hynynen, D. Kiefer, and C. Müller, "Influence of crystallinity on the thermoelectric power factor of P3HT vapour-doped with F4TCNQ," *RSC Advances*, vol. 8, no. 3, pp. 1593–1599, 2018.

[38] J. Euvrard, A. Revaux, S. S. Nobre, A. Kahn, and D. Vuillaume, "Toward a better understanding of the doping mechanism involved in Mo(tfd-COCF 3) 3 doped PBDTTT-c," *Journal of Applied Physics*, vol. 123, p. 225501, jun 2018.

[39] A. Jha, H.-G. Duan, V. Tiwari, M. Thorwart, and R. J. D. Miller, "Origin of Poor Doping Efficiency in Solution Processed Organic Semiconductors," *Chemical Science*, vol. 9, p. 4468, 2018.

[40] R. Ghosh, A. R. Chew, J. Onorato, V. Pakhnyuk, C. K. Luscombe, A. Salleo, and F. C. Spano, "Spectral Signatures and Spatial Coherence of Bound and Unbound Polarons in P3HT Films: Theory Versus Experiment," *Journal of Physical Chemistry C*, vol. 122, no. 31, pp. 18048–18060, 2018.

[41] Z. Fan, D. Du, X. Guan, and J. Ouyang, "Polymer films with ultrahigh thermoelectric properties arising from significant seebeck coefficient enhancement by ion accumulation on surface," *Nano Energy*, vol. 51, pp. 481–488, sep 2018.

[42] E. Lim, K. A. Peterson, G. M. Su, and M. L. Chabinyc, "Thermoelectric Properties of Poly(3-hexylthiophene) (P3HT) Doped with 2,3,5,6-Tetrafluoro-7,7,8,8-tetracyanoquinodimethane (F4TCNQ) by Vapor-Phase Infiltration," *Chemistry of Materials*, vol. 30, no. 3, pp. 998–1010, 2018.

[43] T. J. Aubry, J. C. Axtell, V. M. Basile, K. J. Winchell, J. R. Lindemuth, T. M. Porter, J. Y. Liu, A. N. Alexandrova, C. P. Kubiak, S. H. Tolbert, A. M. Spokoyny, and B. J. Schwartz,

"Dodecaborane-Based Dopants Designed to Shield Anion Electrostatics Lead to Increased Carrier Mobility in a Doped Conjugated Polymer," *Advanced Materials*, vol. 31, no. 11, pp. 1–8, 2019.

[44] D. T. Scholes, P. Y. Yee, G. R. Mckeown, S. Li, H. Kang, R. Lindemuth, X. Xia, S. C. King, D. S. Seferos, S. H. Tolbert, and B. J. Schwartz, "Designing Conjugated Polymers for Molecular Doping : The Roles of Crystallinity , Swelling , and Conductivity in Sequentially-Doped Selenophene-Based Copolymers," *Chemistry of Materials*, no. 31, pp. 73–82, 2019.

[45] E. Lim, A. M. Glaudell, R. Miller, and M. L. Chabinyc, "The Role of Ordering on the Thermoelectric Properties of Blends of Regioregular and Regiorandom Poly(3-hexylthiophene)," *Advanced Electronic Materials*, vol. 5, p. 1800915, nov 2019.

[46] D. Kiefer, R. Kroon, A. I. Hofmann, H. Sun, X. Liu, A. Giovannitti, D. Stegerer, A. Cano, J. Hynynen, L. Yu, Y. Zhang, D. Nai, T. F. Harrelson, M. Sommer, A. J. Moulé, M. Kemerink, S. R. Marder, I. McCulloch, M. Fahlman, S. Fabiano, and C. Müller, "Double doping of conjugated polymers with monomer molecular dopants," *Nature Materials*, vol. 18, pp. 149–155, feb 2019.

[47] I. Enokida and Y. Furukawa, "Doping-level dependent mobilities of positive polarons and bipolarons in poly(2,5-bis(3-hexadecylthiophen-2-yl)thieno[3,2-b]thiophene) (PBTTT-C16) based on an ionic-liquid-gated transistor configuration," *Organic Electronics*, vol. 68, pp. 28–34, may 2019.

[48] Y. Yamashita, J. Tsurumi, M. Ohno, R. Fujimoto, S. Kumagai, T. Kurosawa, T. Okamoto, J. Takeya, and S. Watanabe, "Efficient molecular doping of polymeric semiconductors driven by anion exchange," *Nature*, vol. 572, pp. 634–638, aug 2019.

[49] B. Yurash, D. X. Cao, V. V. Brus, D. Leifert, M. Wang, A. Dixon, M. Seifrid, A. E. Mansour, D. Lungwitz, T. Liu, P. J. Santiago, K. R. Graham, N. Koch, G. C. Bazan, and T. Q. Nguyen, "Towards understanding the doping mechanism of organic semiconductors by Lewis acids," *Nature Materials*, vol. 18, no. 12, pp. 1327–1334, 2019.

[50] J. F. Ponder, A. K. Menon, R. R. Dasari, S. L. Pittelli, K. J. Thorley, S. K. Yee, S. R. Marder, and J. R. Reynolds, "Conductive, Solution-Processed Dioxythiophene Copolymers for Thermoelectric and Transparent Electrode Applications," *Advanced Energy Materials*, vol. 9, p. 1900395, jun 2019.

[51] A. Mazaheripour, E. M. Thomas, R. A. Segalman, and M. L. Chabinyc, "Nonaggregating Doped Polymers Based on Poly(3,4-Propylenedioxythiophene)," *Macromolecules*, vol. 52, no. 5, pp. 2203–2213, 2019.

[52] O. Zapata-Arteaga, B. Dörling, A. Perevedentsev, J. Martín, J. S. Reparaz, and M. Campoy-Quiles, "Closing the Stability-Performance Gap in Organic Thermoelectrics by Adjusting the Partial to Integer Charge Transfer Ratio," *Macromolecules*, vol. 53, no. 2, pp. 609–620, 2020.

[53] E. M. Thomas, K. A. Peterson, A. H. Balzer, D. Rawlings, N. Stingelin, R. A. Segalman, and M. L. Chabinyc, "Effects of Counter-Ion Size on Delocalization of Carriers and Stability of

Doped Semiconducting Polymers," *Advanced Electronic Materials*, vol. 6, p. 2000595, dec 2020.

[54] A. E. Mansour, D. Lungwitz, T. Schultz, M. Arvind, A. M. Valencia, C. Cocchi, A. Opitz, D. Neher, and N. Koch, "The optical signatures of molecular-doping induced polarons in poly(3-hexylthiophene-2,5-diyl): individual polymer chains versus aggregates," *Journal of Materials Chemistry C*, vol. 8, no. 8, pp. 2870–2879, 2020.

[55] V. Untilova, T. Biskup, L. Biniek, V. Vijayakumar, and M. Brinkmann, "Control of Chain Alignment and Crystallization Helps Enhance Charge Conductivities and Thermoelectric Power Factors in Sequentially Doped P3HT:F 4 TCNQ Films," *Macromolecules*, vol. 53, pp. 2441–2453, apr 2020.

[56] S. E. Yoon, Y. Kang, S. Y. Noh, J. Park, S. Y. Lee, J. Park, D. W. Lee, D. R. Whang, T. Kim, G.-H. Kim, H. Seo, B.-G. Kim, and J. H. Kim, "High Efficiency Doping of Conjugated Polymer for Investigation of Intercorrelation of Thermoelectric Effects with Electrical and Morphological Properties," *ACS Applied Materials & Interfaces*, vol. 12, pp. 1151–1158, jan 2020.

[57] V. Vijayakumar, P. Durand, H. Zeng, V. Untilova, L. Herrmann, P. Algayer, N. Leclerc, and M. Brinkmann, "Influence of dopant size and doping method on the structure and thermoelectric properties of PBTTT films doped with F6TCNNQ and F4TCNQ," *Journal of Materials Chemistry C*, vol. 8, no. 46, pp. 16470–16482, 2020.

[58] A. R. Chew, R. Ghosh, Z. Shang, F. C. Spano, and A. Salleo, "Sequential Doping Reveals the Importance of Amorphous Chain Rigidity in Charge Transport of Semi-Crystalline Polymers," *Journal of Physical Chemistry Letters*, vol. 8, no. 20, pp. 4974–4980, 2017.

[59] R. Ghosh, C. K. Luscombe, M. Hambsch, S. C. B. Mannsfeld, A. Salleo, and F. C. Spano, "Anisotropic Polaron Delocalization in Conjugated Homopolymers and Donor–Acceptor Copolymers," *Chemistry of Materials*, vol. 31, pp. 7033–7045, sep 2019.

[60] R. Ghosh and F. C. Spano, "Excitons and Polarons in Organic Materials," *Accounts of Chemical Research*, vol. 53, pp. 2201–2211, oct 2020.

[61] D. T. Scholes, P. Y. Yee, J. R. Lindemuth, H. Kang, J. Onorato, R. Ghosh, C. K. Luscombe, F. C. Spano, S. H. Tolbert, and B. J. Schwartz, "The Effects of Crystallinity on Charge Transport and the Structure of Sequentially Processed F4TCNQ-Doped Conjugated Polymer Films," *Advanced Functional Materials*, vol. 1702654, pp. 1–13, 2017.

[62] S. D. D. V. Rughooputh, S. Hotta, A. J. Heeger, and F. Wudl, "Chromism of soluble polythienylenes," *Journal of Polymer Science Part B: Polymer Physics*, vol. 25, pp. 1071–1078, may 1987.

[63] L. Dou, J. You, Z. Hong, Z. Xu, G. Li, R. A. Street, and Y. Yang, "25th anniversary article: A decade of organic/polymeric photovoltaic research," *Advanced Materials*, vol. 25, no. 46, pp. 6642–6671, 2013.

[64] M. Kuik, G. J. A. Wetzelaer, H. T. Nicolai, N. I. Craciun, D. M. De Leeuw, and P. W. Blom, “25th anniversary article: Charge transport and recombination in polymer light-emitting diodes,” *Advanced Materials*, vol. 26, no. 4, pp. 512–531, 2014.

[65] W. T. Neo, Q. Ye, S.-J. Chua, and J. Xu, “Conjugated polymer-based electrochromics: materials, device fabrication and application prospects,” *Journal of Materials Chemistry C*, vol. 4, no. 31, pp. 7364–7376, 2016.

[66] P. Y. Yee, D. T. Scholes, B. J. Schwartz, and S. H. Tolbert, “Dopant-Induced Ordering of Amorphous Regions in Regiorandom P3HT,” *The Journal of Physical Chemistry Letters*, vol. 10, pp. 4929–4934, sep 2019.

[67] M. G. Voss, D. T. Scholes, J. R. Challa, and B. J. Schwartz, “Ultrafast transient absorption spectroscopy of doped P3HT films: Distinguishing free and trapped polarons,” *Faraday Discussions*, vol. 216, pp. 339–362, 2019.

[68] V. Vijayakumar, Y. Zhong, V. Untilova, M. Bahri, L. Herrmann, L. Biniek, N. Leclerc, and M. Brinkmann, “Bringing Conducting Polymers to High Order- Toward Conductivities beyond 10 5 S cm-1 and Thermoelectric Power Factors of 2 mW m-1 K ,” *Advanced Energy Materials*, vol. 9, p. 1900266, jun 2019.

[69] V. Vijayakumar, E. Zaborova, L. Biniek, H. Zeng, L. Herrmann, A. Carvalho, O. Boyron, N. Leclerc, and M. Brinkmann, “Effect of Alkyl Side Chain Length on Doping Kinetics, Thermopower, and Charge Transport Properties in Highly Oriented F 4 TCNQ-Doped PBTTT Films,” *ACS Applied Materials & Interfaces*, vol. 11, pp. 4942–4953, feb 2019.

[70] T. P. Kaloni, P. K. Giesbrecht, G. Schreckenbach, and M. S. Freund, “Polythiophene: From Fundamental Perspectives to Applications,” *Chemistry of Materials*, vol. 29, no. 24, pp. 10248–10283, 2017.

[71] F. C. Krebs, “Fabrication and Processing of Polymer Solar Cells : A Review of Printing and Coating Techniques,” *Solar Energy Materials and Solar Cells*, vol. 93, pp. 394–412, 2009.

[72] Y. Li, “Molecular Design of Photovoltaic Materials for Polymer Solar Cells: Toward Suitable Electronic Energy Levels and Broad Absorption,” *Accounts of Chemical Research*, vol. 45, no. 5, pp. 723–733, 2012.

[73] L. Lu, T. Zheng, Q. Wu, A. M. Schneider, D. Zhao, and L. Yu, “Recent Advances in Bulk Heterojunction Polymer Solar Cells,” *Chemical Reviews*, vol. 115, pp. 12666–12731, 2015.

[74] R. Søndergaard, M. Hösel, D. Angmo, T. T. Larsen-Olsen, and F. C. Krebs, “Roll-to-Roll Fabrication of Polymer Solar Cells,” *Materials Today*, vol. 15, no. 1-2, pp. 36–49, 2012.

[75] B. McCulloch, V. Ho, M. Hoarfrost, C. Stanley, C. Do, W. T. Heller, and R. A. Segalman, “Polymer Chain Shape of poly(3-alkylthiophenes) in Solution Ssing Small-Angle Neutron Scattering,” *Macromolecules*, vol. 46, no. 5, pp. 1899–1907, 2013.

[76] A. J. Spakowitz and Z. G. Wang, “Exact Results for a Semiflexible Polymer Chain in an Aligning Field,” *Macromolecules*, vol. 37, no. 15, pp. 5814–5823, 2004.

[77] C. Deibel and V. Dyakonov, “Polymer-Fullerene Bulk Heterojunction Solar Cells,” *Reports Prog. Phys.*, no. 73, p. 96401, 2010.

[78] C. Duan, F. Huang, and Y. Cao, “Recent Development of Push-Pull Conjugated Polymers for Bulk-Heterojunction Photovoltaics: Rational Design and Fine Tailoring of Molecular Structures,” *Journal of Materials Chemistry*, vol. 22, no. 21, p. 10416, 2012.

[79] U. Giovanella, C. Botta, F. Galeotti, B. Vercelli, S. Battiato, and M. Pasini, “Perfluorinated Polymer with Unexpectedly Efficient Deep Blue Electroluminescence for Full-Colour OLED Displays and Light Therapy Applications,” *Journal of Materials Chemistry C*, vol. 1, pp. 5322–5329, 2013.

[80] A. J. Heeger, “25th Anniversary Article: Bulk Heterojunction Solar Cells: Understanding the Mechanism of Operation,” *Advanced Materials*, vol. 26, pp. 10–28, 2014.

[81] F. J. Céspedes-Guirao, S. García-Santamaría, F. Fernández-Lázaro, A. Sastre-Santos, and H. J. Bolink, “Efficient Electroluminescence from a Perylenediimide Fluorophore Obtained from a Simple Solution Processed OLED,” *Journal of Physics D: Applied Physics*, vol. 42, no. 10, p. 105106, 2009.

[82] E. Kozma, W. Mróz, F. Villafiorita-Monteleone, F. Galeotti, A. Andicsová-Eckstein, M. Catellani, and C. Botta, “Perylene Diimide Derivatives as Red and Deep Red-Emitters for Fully Solution Processable OLEDs,” *RSC Advances*, vol. 6, no. 66, pp. 61175–61179, 2016.

[83] G. J. Snyder and E. S. Toberer, “Complex Thermoelectric Materials,” *Nature Materials*, vol. 7, no. 2, pp. 105–114, 2008.

[84] J. Sun, M. L. Yeh, B. J. Jung, B. Zhang, J. Feser, A. Majumdar, and H. E. Katz, “Simultaneous Increase in Seebeck Coefficient and Conductivity in a Doped Poly(alkylthiophene) Blend with Defined Density of States,” *Macromolecules*, vol. 43, no. 6, pp. 2897–2903, 2010.

[85] B. T. McGrail, A. Sehirlioglu, and E. Pentzer, “Polymer Composites for Thermoelectric Applications,” *Angewandte Chemie - International Edition*, vol. 54, no. 6, pp. 1710–1723, 2015.

[86] S. Hwang, W. J. Potscavage, R. Nakamichi, and C. Adachi, “Processing and Doping of Thick Polymer Active Layers for Flexible Organic Thermoelectric Modules,” *Organic Electronics*, vol. 31, pp. 31–40, 2016.

[87] D. Kiefer, L. Yu, E. Fransson, A. Gómez, D. Primetzhofer, A. Amassian, M. Campoy-Quiles, and C. Müller, “A Solution-Doped Polymer Semiconductor:Insulator Blend for Thermoelectrics,” *Advanced Science*, vol. 4, no. 1, p. 1600203, 2017.

[88] H. Yao, Z. Fan, H. Cheng, X. Guan, C. Wang, K. Sun, and J. Ouyang, “Recent Development of Thermoelectric Polymers and Composites,” *Macromolecular Rapid Communications*, vol. 39, no. 6, p. 1700727, 2018.

[89] J. P. Heremans, “Thermoelectricity: The Ugly Duckling,” *Nature*, vol. 508, no. 1, pp. 327–328, 2008.

[90] M. T. Fontana, H. Kang, P. Y. Yee, Z. Fan, S. A. Hawks, L. T. Schelhas, S. Subramaniyan, Y. J. Hwang, S. A. Jenekhe, S. H. Tolbert, and B. J. Schwartz, "Low-Vapor-Pressure Solvent Additives Function as Polymer Swelling Agents in Bulk Heterojunction Organic Photovoltaics," *Journal of Physical Chemistry C*, vol. 122, no. 29, pp. 16574–16588, 2018.

[91] K.-H. Yim, G. L. Whiting, C. E. Murphy, J. J. M. Halls, J. H. Burroughes, R. H. Friend, and J.-S. Kim, "Controlling Electrical Properties of Conjugated Polymers via a Solution-Based p-Type Doping," *Advanced Materials*, vol. 20, no. 17, pp. 3319–3324, 2008.

[92] Y. Zhang, B. de Boer, and P. W. M. Blom, "Controllable Molecular Doping and Charge Transport in Solution-Processed Polymer Semiconducting Layers," *Advanced Functional Materials*, vol. 19, no. 12, pp. 1901–1905, 2009.

[93] D. T. Duong, C. Wang, E. Antono, M. F. Toney, and A. Salleo, "The Chemical and Structural Origin of Efficient p-Type Doping in P3HT," *Org. Electron.*, vol. 14, no. 5, pp. 1330–1336, 2013.

[94] C. K. Chiang, C. R. Fincher, Y. W. Park, A. J. Heeger, H. Shirakawa, E. J. Louis, S. C. Gau, and A. G. MacDiarmid, "Electrical Conductivity in Doped Polyacetylene," *Physical Review Letters*, vol. 39, no. 17, pp. 1098–1101, 1977.

[95] I. Salzmann and G. Heimel, "Toward a Comprehensive Understanding of Molecular Doping Organic Semiconductors (Review)," *Journal of Electron Spectroscopy and Related Phenomena*, vol. 204, pp. 208–222, 2015.

[96] A. M. Glaudell, J. E. Cochran, S. N. Patel, and M. L. Chabinyc, "Impact of the Doping Method on Conductivity and Thermopower in Semiconducting Polythiophenes," *Advanced Energy Materials*, vol. 5, no. 4, p. 1401072, 2015.

[97] J. Gao, J. D. Roegling, Y. Li, H. Guo, A. J. Moulé, and J. K. Grey, "The Effect of 2,3,5,6-Tetrafluoro-7,7,8,8-tetracyanoquinodimethane Charge Transfer Dopants on the Conformation and Aggregation of Poly(3-hexylthiophene)," *Journal of Materials Chemistry C*, vol. 1, no. 36, pp. 5638–5646, 2013.

[98] J. Gao, E. T. Niles, and J. K. Grey, "Aggregates Promote Efficient Charge Transfer Doping of Poly(3-hexylthiophene)," *Journal of Physical Chemistry Letters*, vol. 4, no. 17, pp. 2953–2957, 2013.

[99] F. Deschler, D. Riedel, A. Deák, B. Ecker, E. von Hauff, and E. Da Como, "Imaging of Morphological Changes and Phase Segregation in Doped Polymeric Semiconductors," *Synthetic Metals*, vol. 199, pp. 381–387, 2015.

[100] G. Zuo, O. Andersson, H. Abdalla, and M. Kemerink, "High Thermoelectric Power Factor from Multilayer Solution-Processed Organic Films," *Applied Physics Letters*, vol. 112, no. 8, pp. 2–6, 2018.

[101] Y. Xuan, X. Liu, S. Desbief, P. Leclère, M. Fahlman, R. Lazzaroni, M. Berggren, J. Cornil, D. Emin, and X. Crispin, "Thermoelectric Properties of Conducting Polymers : The case of Poly(3-hexylthiophene)," *Physical Review B*, vol. 82, p. 115454, 2010.

[102] S. A. Gregory, A. K. Menon, S. Ye, D. S. Seferos, J. R. Reynolds, and S. K. Yee, “Effect of Heteroatom and Doping on the Thermoelectric Properties of Poly (3-alkylchalcogenophenes),” *Advanced Energy Materials*, vol. 1802419, p. 1802419, 2018.

[103] S. A. Hawks, J. C. Aguirre, L. T. Schelhas, R. J. Thompson, R. C. Huber, A. S. Ferreira, G. Zhang, A. A. Herzing, S. H. Tolbert, and B. J. Schwartz, “Comparing Matched Polymer:Fullerene Solar Cells Made by Solution-Sequential Processing and Traditional Blend Casting: Nanoscale Structure and Device Performance,” *J. Phys. Chem. C*, vol. 118, pp. 17413–17425, 2014.

[104] J. C. Aguirre, S. A. Hawks, A. S. Ferreira, P. Yee, S. Subramaniyan, S. A. Jenekhe, S. H. Tolbert, and B. J. Schwartz, “Sequential processing for organic photovoltaics: Design rules for morphology control by tailored semi-orthogonal solvent blends,” *Advanced Energy Materials*, vol. 5, no. 11, p. 1402020, 2015.

[105] J. Li, G. Zhang, D. M. Holm, I. E. Jacobs, B. Yin, P. Stroeve, M. Mascal, and A. J. Moulé, “Introducing Solubility Control for Improved Organic P-Type Dopants,” *Chemistry of Materials*, vol. 27, no. 16, pp. 5765–5774, 2015.

[106] A. L. Ayzner, C. J. Tassone, S. H. Tolbert, and B. J. Schwartz, “Reappraising the Need for Bulk Heterojunctions in Polymer-Fullerene Photovoltaics: The Role of Carrier Transport in All-Solution-Processed P3HT/PCBM Bilayer Solar Cells,” *J. Phys. Chem. C*, vol. 113, pp. 20050–20060, 2009.

[107] J. C. Aguirre, A. Ferreira, H. Ding, S. A. Jenekhe, N. Kopidakis, M. Asta, L. Pilon, Y. Rubin, S. H. Tolbert, B. J. Schwartz, B. Dunn, and V. Ozolins, “Panoramic View of Electrochemical Pseudocapacitor and Organic Solar Cell Research in Molecularly Engineered Energy Materials,” *Journal of Physical Chemistry C*, vol. 118, pp. 19505–19523, 2014.

[108] C.-M. Che, V. A. L. Roy, H.-F. Xiang, P. T. Lai, and Z.-X. Xu, “Method for measurement of the density of thin films of small organic molecules,” *Review of Scientific Instruments*, vol. 78, no. 3, p. 034104, 2007.

[109] NIST, “Resistivity and Hall Reasurements,” 2018.

[110] J. Hynynen, E. Järsvall, R. Kroon, Y. Zhang, S. Barlow, S. R. Marder, M. Kemerink, A. Lund, and C. Müller, “Enhanced Thermoelectric Power Factor of Tensile Drawn Poly(3-hexylthiophene),” *ACS Macro Letters*, vol. 8, no. 1, pp. 70–76, 2019.

[111] P. Reiser, L. Müller, V. Sivanesan, R. Lovrincic, S. Barlow, S. R. Marder, A. Pucci, W. Jaegermann, E. Mankel, and S. Beck, “Dopant Diffusion in Sequentially Doped Poly(3-hexylthiophene) Studied by Infrared and Photoelectron Spectroscopy,” *Journal of Physical Chemistry C*, vol. 122, no. 26, pp. 14518–14527, 2018.

[112] J. Li, C. Koshnick, S. O. Diallo, S. Ackling, D. M. Huang, I. E. Jacobs, T. F. Harrelson, K. Hong, G. Zhang, J. Beckett, M. Mascal, and A. J. Moulé, “Quantitative Measurements of the Temperature-Dependent Microscopic and Macroscopic Dynamics of a Molecular Dopant in a Conjugated Polymer,” *Macromolecules*, vol. 50, no. 14, pp. 5476–5489, 2017.

[113] C. Wang, D. T. Duong, K. Vandewal, J. Rivnay, and A. Salleo, "Optical Measurement of Doping Efficiency in Poly(3-hexylthiophene) Solutions and Thin Films," *Physical Review B - Condensed Matter and Materials Physics*, vol. 91, no. 8, p. 085205, 2015.

[114] M. G. Voss, D. T. Scholes, J. R. Challa, and B. J. Schwartz, "Ultrafast transient absorption spectroscopy of doped P3HT films: distinguishing free and trapped polarons," *Faraday Discussions*, vol. 216, pp. 339–362, 2019.

[115] Z. M. Beiley, E. T. Hoke, R. Noriega, J. Dacuña, G. F. Burkhard, J. A. Bartelt, A. Salleo, M. F. Toney, and M. D. McGehee, "Morphology-Dependent Trap Formation in High Performance Polymer Bulk Heterojunction Solar Cells," *Advanced Energy Materials*, vol. 1, no. 5, pp. 954–962, 2011.

[116] Y. Liu, J. Zhao, Z. Li, C. Mu, W. Ma, H. Hu, K. Jiang, H. Lin, H. Ade, and H. Yan, "Aggregation and morphology control enables multiple cases of high-efficiency polymer solar cells," *Nature Communications*, vol. 5, p. 5293, dec 2014.

[117] E. Verploegen, R. Mondal, C. J. Bettinger, S. Sok, M. F. Toney, and Z. Bao, "Effects of Thermal Annealing Upon the Morphology of Polymer-Fullerene Blends," *Advanced Functional Materials*, vol. 20, no. 20, pp. 3519–3529, 2010.

[118] U. Zhokhavets, T. Erb, H. Hoppe, G. Gobsch, and N. S. Sariciftci, "Effect of Annealing of Poly(3-hexylthiophene)/Fullerene Bulk Heterojunction Composites on Structural and Optical Properties," *Thin Solid Films*, vol. 496, no. 2, pp. 679–682, 2006.

[119] A. Salleo, R. J. Kline, D. M. DeLongchamp, and M. L. Chabinyc, "Microstructural Characterization and Charge Transport in Thin Films of Conjugated Polymers," *Advanced Materials*, vol. 22, no. 34, pp. 3812–3838, 2010.

[120] M. Wohlgenannt, X. M. Jiang, and Z. V. Vardeny, "Confined and Delocalized Polarons in π-conjugated Oligomers and Polymers: A Study of the Effective Conjugation Length," *Physical Review B - Condensed Matter and Materials Physics*, vol. 69, no. 24, p. 241204, 2004.

[121] C. M. Pochas and F. C. Spano, "New Insights on the Nature of Two-Dimensional Polarons in Semiconducting Polymers: Infrared Absorption in Poly(3-hexylthiophene)," *Journal of Chemical Physics*, vol. 140, no. 24, p. 244902, 2014.

[122] R. Ghosh, C. M. Pochas, and F. C. Spano, "Polaron Delocalization in Conjugated Polymer Films," *Journal of Physical Chemistry C*, vol. 120, no. 21, pp. 11394–11406, 2016.

[123] J. S. Cowart, C. Liman, A. Garnica, Z. A. Page, E. Lim, R. R. Zope, T. Baruah, C. J. Hawker, and M. L. Chabinyc, "Donor-fullerene dyads for energy cascade organic solar cells," *Inorganica Chimica Acta*, vol. 468, pp. 192–202, 2017.

[124] L. Hou, X. Zhang, G. F. Cotella, G. Carnicella, M. Herder, B. M. Schmidt, M. Pätzel, S. Hecht, F. Cacialli, and P. Samorì, "Optically switchable organic light-emitting transistors," *Nature Nanotechnology*, 2019.

[125] Z. Liang, Y. Zhang, M. Souri, X. Luo, A. M. Boehm, R. Li, Y. Zhang, T. Wang, D. Y. Kim, J. Mei, S. R. Marder, and K. R. Graham, "Influence of dopant size and electron affinity on the electrical conductivity and thermoelectric properties of a series of conjugated polymers," *Journal of Materials Chemistry A*, vol. 6, no. 34, pp. 16495–16505, 2018.

[126] J. B. Torrance and B. D. Silverman, "Charge transfer and ionic bonding in organic solids with segregated stacks," *Physical Review B*, vol. 15, no. 2, pp. 788–801, 1977.

[127] J. B. Torrance, B. A. Scott, and F. B. Kaufman, "Optical properties of charge transfer salts of tetracyanoquinodimethane (TCNQ)," *Solid State Communications*, vol. 88, no. 11-12, pp. 971–975, 1993.

[128] C. D. Bryan, A. W. Cordes, R. M. Fleming, N. A. George, S. H. Glarum, R. C. Haddon, R. T. Oakley, T. T. Palstra, A. S. Perel, L. F. Schneemeyer, and J. V. Waszczak, "Conducting charge-transfer salts based on neutral π-radicals," *Nature*, vol. 365, no. 6449, pp. 821–823, 1993.

[129] J. Ferraris, D. O. Cowan, V. Walatka, and J. H. Perlstein, "Electron Transfer in a New Highly Conducting Donor-Acceptor Complex," *Journal of the American Chemical Society*, vol. 95, no. 3, pp. 948–949, 1973.

[130] I. Shokaryev, A. J. Buurma, O. D. Jurchescu, M. A. Uijttewaal, G. A. De Wijs, T. T. Palstra, and R. A. De Groot, "Electronic band structure of tetracene-TCNQ and perylene-TCNQ compounds," *Journal of Physical Chemistry A*, vol. 112, no. 11, pp. 2497–2502, 2008.

[131] K. P. Goetz, D. Vermeulen, M. E. Payne, C. Kloc, L. E. McNeil, and O. D. Jurchescu, "Charge-transfer complexes: New perspectives on an old class of compounds," *Journal of Materials Chemistry C*, vol. 2, no. 17, pp. 3065–3076, 2014.

[132] J. Fuzell, I. E. Jacobs, S. Ackling, T. F. Harrelson, D. M. Huang, D. Larsen, and A. J. Moulé, "Optical Dedoping Mechanism for P3HT:F4TCNQ Mixtures," *Journal of Physical Chemistry Letters*, vol. 7, no. 21, pp. 4297–4303, 2016.

[133] E. M. Thomas, E. C. Davidson, R. Katsumata, R. A. Segalman, and M. L. Chabinyc, "Branched Side Chains Govern Counterion Position and Doping Mechanism in Conjugated Polythiophenes," *ACS Macro Letters*, vol. 7, pp. 1492–1497, 2018.

[134] I. Salzmann, G. Heimel, M. Oehzelt, S. Winkler, and N. Koch, "Molecular Electrical Doping of Organic Semiconductors: Fundamental Mechanisms and Emerging Dopant Design Rules," *Accounts of Chemical Research*, vol. 49, pp. 370–378, mar 2016.

[135] M. Roesing, J. Howell, and D. Boucher, "Solubility characteristics of poly(3-hexylthiophene)," *Journal of Polymer Science, Part B: Polymer Physics*, vol. 55, no. 14, pp. 1075–1087, 2017.

[136] M. Meneghetti and C. Pecile, "Charge–transfer organic crystals: Molecular vibrations and spectroscopic effects of electron–molecular vibration coupling of the strong electron acceptor TCNQF 4," *The Journal of Chemical Physics*, vol. 84, pp. 4149–4162, apr 1986.

[137] N. Kayunkid, S. Uttiya, and M. Brinkmann, “Structural model of regioregular poly(3-hexylthiophene) obtained by electron diffraction analysis,” *Macromolecules*, vol. 43, no. 11, pp. 4961–4967, 2010.

[138] A. L. Sutton, B. F. Abrahams, D. M. D’Alessandro, T. A. Hudson, R. Robson, and P. M. Usov, “Structural and optical investigations of charge transfer complexes involving the radical anions of TCNQ and F4TCNQ,” *CrystEngComm*, vol. 18, no. 46, pp. 8906–8914, 2016.

[139] Q. Qin, J. T. Mague, K. Z. Moses, E. M. Carnicom, and R. J. Cava, “Structure and characterization of charge transfer complexes of benzo[1,2-: B:3,4-b:5,6-b]trithiophene [C3h-BTT],” *CrystEngComm*, vol. 19, no. 42, pp. 6355–6364, 2017.

[140] R. Sato, M. Dogishi, T. Higashino, T. Kadoya, T. Kawamoto, and T. Mori, “Charge-Transfer Complexes of Benzothienobenzothiophene with Tetracyanoquinodimethane and the n-Channel Organic Field-Effect Transistors,” *Journal of Physical Chemistry C*, vol. 121, no. 12, pp. 6561–6568, 2017.

[141] A. M. Valencia and C. Cocchi, “Electronic and Optical Properties of Oligothiophene-F4TCNQ Charge-Transfer Complexes: The Role of the Donor Conjugation Length,” *Journal of Physical Chemistry C*, vol. 123, no. 14, pp. 9617–9623, 2019.

[142] E. F. Aziz, A. Vollmer, S. Eisebitt, W. Eberhardt, P. Pingel, D. Neher, and N. Koch, “Localized Charge Transfer in a Molecularly Doped Conducting Polymer,” *Advanced Materials*, vol. 19, pp. 3257–3260, sep 2007.

[143] T. F. Harrelson, Y. Q. Cheng, J. Li, I. E. Jacobs, A. J. Ramirez-Cuesta, R. Faller, and A. J. Moulé, “Identifying Atomic Scale Structure in Undoped/Doped Semicrystalline P3HT Using Inelastic Neutron Scattering,” *Macromolecules*, vol. 50, no. 6, pp. 2424–2435, 2017.

[144] F. C. Spano, “Modeling disorder in polymer aggregates: The optical spectroscopy of regioregular poly(3-hexylthiophene) thin films,” *The Journal of Chemical Physics*, vol. 122, p. 234701, jun 2005.

[145] F. C. Spano, J. Clark, C. Silva, and R. H. Friend, “Determining Exciton Coherence from the Photoluminescence Spectral Line Shape in poly(3-hexylthiophene) Thin Films,” *Journal of Chemical Physics*, vol. 130, no. 7, p. 074904, 2009.

[146] H. Bronstein and C. K. Luscombe, “Effect of Initiators on the Kumada Catalyst-Transfer Polycondensation Reaction,” *Macromolecules*, vol. 42, pp. 7670–7677, oct 2009.

[147] L. Zhu, E.-G. Kim, Y. Yi, and J.-L. Brédas, “Charge Transfer in Molecular Complexes with 2,3,5,6-Tetrafluoro-7,7,8,8-tetracyanoquinodimethane (F 4 -TCNQ): A Density Functional Theory Study,” *Chemistry of Materials*, vol. 23, pp. 5149–5159, dec 2011.

[148] K. Kondratenko, Y. Boussoualem, D. P. Singh, R. Visvanathan, A. E. Duncan, N. A. Clark, C. Legrand, and A. Daoudi, “Molecular p-doping in organic liquid crystalline semiconductors: influence of the charge transfer complex on the properties of mesophase and bulk charge transport,” *Physical Chemistry Chemical Physics*, vol. 21, no. 34, pp. 18686–18698, 2019.

[149] A. Chattopadhyay and S. G. Boxer, “Vibrational Stark Effect Spectroscopy,” *Journal of the American Chemical Society*, vol. 117, pp. 1449–1450, feb 1995.

[150] S. S. Andrews and S. G. Boxer, “Vibrational Stark effects of nitriles. I. Methods and experimental results,” *Journal of Physical Chemistry A*, vol. 104, no. 51, pp. 11853–11863, 2000.

[151] E. S. Park, M. R. Thomas, and S. G. Boxer, “Vibrational Stark Spectroscopy of NO Bound to Heme: Effects of Protein Electrostatic Fields on the NO Stretch Frequency,” *Journal of the American Chemical Society*, vol. 122, pp. 12297–12303, dec 2000.

[152] I. T. Suydam and S. G. Boxer, “Vibrational Stark Effects Calibrate the Sensitivity of Vibrational Probes for Electric Fields in Proteins,” *Biochemistry*, vol. 42, no. 41, pp. 12050–12055, 2003.

[153] S. H. Brewer and S. Franzen, “A quantitative theory and computational approach for the vibrational Stark effect,” *The Journal of Chemical Physics*, vol. 119, pp. 851–858, jul 2003.

[154] S. D. Dalosto, J. M. Vanderkooi, and K. A. Sharp, “Vibrational Stark Effects on Carbonyl, Nitrile, and Nitrosyl Compounds Including Heme Ligands, CO, CN, and NO, Studied with Density Functional Theory,” *The Journal of Physical Chemistry B*, vol. 108, pp. 6450–6457, may 2004.

[155] P. A. Sigala, A. T. Fafarman, P. E. Bogard, S. G. Boxer, and D. Herschlag, “Do Ligand Binding and Solvent Exclusion Alter the Electrostatic Character within the Oxyanion Hole of an Enzymatic Active Site?,” *Journal of the American Chemical Society*, vol. 129, pp. 12104–12105, oct 2007.

[156] W. Hu and L. J. Webb, “Direct Measurement of the Membrane Dipole Field in Bicelles Using Vibrational Stark Effect Spectroscopy,” *The Journal of Physical Chemistry Letters*, vol. 2, pp. 1925–1930, aug 2011.

[157] S. D. Fried and S. G. Boxer, “Measuring Electric Fields and Noncovalent Interactions Using the Vibrational Stark Effect,” *Accounts of Chemical Research*, vol. 176, no. 1, pp. 100–106, 2016.

[158] J. D. Slocum and L. J. Webb, “Nitrile Probes of Electric Field Agree with Independently Measured Fields in Green Fluorescent Protein Even in the Presence of Hydrogen Bonding,” *Journal of the American Chemical Society*, vol. 138, pp. 6561–6570, may 2016.

[159] R. Adhikary, J. Zimmermann, and F. E. Romesberg, “Transparent Window Vibrational Probes for the Characterization of Proteins With High Structural and Temporal Resolution,” *Chemical Reviews*, vol. 117, pp. 1927–1969, feb 2017.

[160] J. D. Slocum and L. J. Webb, “Measuring Electric Fields in Biological Matter Using the Vibrational Stark Effect of Nitrile Probes,” *Annual Review of Physical Chemistry*, vol. 69, pp. 253–271, apr 2018.

[161] D. R. Martin and D. V. Matyushov, “Why are Vibrational Lines Narrow in Proteins?,” *The Journal of Physical Chemistry Letters*, vol. 11, pp. 5932–5937, aug 2020.

[162] Y. Li, P. Zolotavin, P. Doak, L. Kronik, J. B. Neaton, and D. Natelson, “Interplay of Bias-Driven Charging and the Vibrational Stark Effect in Molecular Junctions,” *Nano Letters*, vol. 16, pp. 1104–1109, feb 2016.

[163] J. K. Staffa, L. Lorenz, M. Stolarski, D. H. Murgida, I. Zebger, T. Utesch, J. Kozuch, and P. Hildebrandt, “Determination of the Local Electric Field at Au/SAM Interfaces Using the Vibrational Stark Effect,” *The Journal of Physical Chemistry C*, vol. 121, pp. 22274–22285, oct 2017.

[164] A. Ge, P. E. Videla, G. L. Lee, B. Rudshteyn, J. Song, C. P. Kubiak, V. S. Batista, and T. Lian, “Interfacial Structure and Electric Field Probed by in Situ Electrochemical Vibrational Stark Effect Spectroscopy and Computational Modeling,” *The Journal of Physical Chemistry C*, vol. 121, pp. 18674–18682, aug 2017.

[165] G. Zwaschka, M. Wolf, R. K. Campen, and Y. Tong, “A Microscopic Model of the Electrochemical Vibrational Stark Effect: Understanding VSF Spectroscopy of (bi)Sulfate on Pt(111),” *Surface Science*, vol. 678, pp. 78–85, dec 2018.

[166] J. H. K. Pfisterer, U. E. Zhumaev, W. Cheuquepan, J. M. Feliu, and K. F. Domke, “Stark effect or coverage dependence? Disentangling the EC-SEIRAS vibrational shift of sulfate on Au(111),” *The Journal of Chemical Physics*, vol. 150, p. 041709, jan 2019.

[167] T. Mani, D. C. Grills, and J. R. Miller, “Vibrational Stark Effects To Identify Ion Pairing and Determine Reduction Potentials in Electrolyte-Free Environments,” *Journal of the American Chemical Society*, vol. 137, pp. 1136–1140, jan 2015.

[168] J. Hack, D. C. Grills, J. R. Miller, and T. Mani, “Identification of Ion-Pair Structures in Solution by Vibrational Stark Effects,” *The Journal of Physical Chemistry B*, vol. 120, pp. 1149–1157, feb 2016.

[169] J. Donon, S. Habka, V. Vaquero-Vara, V. Brenner, M. Mons, and E. Gloaguen, “Electronic Stark Effect in Isolated Ion Pairs,” *The Journal of Physical Chemistry Letters*, vol. 10, pp. 7458–7462, dec 2019.

[170] M. Cho, “Vibrational solvatochromism and electrochromism: Coarse-grained models and their relationships,” *The Journal of Chemical Physics*, vol. 130, p. 094505, mar 2009.

[171] H. Kang, J. Maurais, Y. Park, P. Ayotte, and H. Kang, “Electric Field Effect on Condensed-Phase Molecular Systems. VIII. Vibrational Stark Effect and Dipolar Inversion in a Carbon Monoxide Crystal,” *The Journal of Physical Chemistry C*, vol. 123, pp. 31262–31271, dec 2019.

[172] H. Kang, Y. Park, S. Shin, and H. Kang, “Electric Field Effect on Condensed-Phase Molecular Systems. X. Interconversion Dynamics and Vibrational Stark Effect of Hydrogen Chloride Clusters in an Argon Matrix,” *The Journal of Physical Chemistry B*, vol. 124, pp. 4581–4589, jun 2020.

[173] J. Zhu, F. Bebensee, W. Hieringer, W. Zhao, J. H. Baricuatro, J. A. Farmer, Y. Bai, H. P. Steinrück, J. M. Gottfried, and C. T. Campbell, “Formation of the calcium/poly(3-hexylthiophene) interface: Structure and energetics,” *Journal of the American Chemical Society*, vol. 131, no. 37, pp. 13498–13507, 2009.

[174] Y. Sun, Y. C. Han, and J. G. Liu, “Controlling PCBM aggregation in P3HT/PCBM film by a selective solvent vapor annealing,” *Chinese Science Bulletin*, vol. 58, no. 22, pp. 2767–2774, 2013.

[175] R. Prost, “The Influence of the Christiansen Effect on I.R. Spectra of Powders,” *Clays and Clay Minerals*, vol. 21, no. 5, pp. 363–368, 1973.